Silicon Nanomembranes for Advanced Microvascular Mimetics

by

Tejas Suresh Khire

Submitted in Partial Fulfillment of the

Requirements for the Degree

Doctor of Philosophy

Supervised by
Professor James L. McGrath and Professor Richard E. Waugh

Department of Biomedical Engineering

School of Arts, Sciences & Engineering

University of Rochester

Rochester, New York

2018

The author wishes to thank his friends, family, and colleagues for their immeasurable support.

Table of Contents

Biographical Sketch **x**

Acknowledgments **xiii**

Abstract **xv**

Contributors and Funding Sources **xvii**

List of Tables **xx**

List of Figures **xxi**

1 Introduction **1**

1.1 Introduction 1

1.2 Inflammation and Vascular Permeability 4

1.2.1 Microcirculation 4

1.2.2 Endothelial Cells 5

1.2.3 Regulators of Endothelial Permeability 8

1.2.4 Neutrophil-Endothelial Interactions: Setting up the Stage 12

1.3 Neutrophils and Endothelial Permeability 18
1.4 *In vitro* Models of Microvasculature 25
1.4.1 Factors Influencing Endothelial Growth *In Vitro* 26
1.4.2 *In Vitro* Platforms: Requirements and Considerations . 32
1.4.3 Existing Platforms and Technologies 35
1.5 Silicon Nanomembranes 41
1.5.1 Applications of Silicon Nanomembranes for Tissue Barrier Models 42
1.6 *In vitro* Blood-Brain Barrier (BBB) Models 46
1.6.1 *In Vitro* Models to Study Immune Cell Activation . . . 47
1.6.2 *In Vitro* Models to Study Nanoparticle Translocation Across BBB 50
1.7 Thesis Overview 52

2 Finite Element Modeling to Analyze TEER Values Across Silicon Nanomembranes 53

2.1 Abstract 53
2.2 Introduction 54
2.3 *In vivo* Characterization of Endothelial Permeability: Standards and Conventions 57
2.4 Materials and Methods 61
2.4.1 Fabrication of Silicon Nanomembranes and Transwell Assembly 61

2.4.2 Effects of Membrane Geometry on Baseline TEER Values 61
2.4.3 Cell Culture 62
2.4.4 Evolution of TEER Values in Cell Culture 62
2.4.5 COMSOL Simulations 63
2.5 Results 66
2.5.1 Effects of Membrane Geometry on Resistance 66
2.5.2 Development and Validation of a FEA Model 68
2.5.3 Modeling Cell Growth 72
2.5.4 Mapping Function 75
2.6 Discussion 76
2.7 Conclusion 85

3 Vascular Microphysiological System to Study Neutrophil-Endothelial Interactions 87

3.1 Introduction 87
3.2 Materials and Methods 96
3.2.1 Manufacturing of Microporous Silicon Nanomembranes 98
3.2.2 Microvessel Mimetic (MVM) Platform Fabrication . . . 98
3.2.3 Flow Circuit Optimization 105
3.2.4 Cell Culture Protocols 106
3.2.5 Neutrophil Assays 107
3.2.6 TEER and Impedance Measurement 109
3.2.7 Macromolecular Permeability Characterization Assays . 110

3.2.8 Electron Microscopy 111
3.2.9 Finite Element Analysis in COMSOL Multiphysics® . 113
3.3 Results 113
3.3.1 MVM Device Assembly and Flow Characterization . . 114
3.3.2 Flow-conditioned Cell Culture 119
3.3.3 TEER Results 123
3.3.4 Mathematical Analysis of TEER Values 127
3.3.5 Impedance Spectroscopy in MVM Platform 128
3.3.6 Neutrophil Diapedesis in MVM Platform 131
3.3.7 Electron Microscopy to Image Neutrophil Transmigration 136
3.3.8 Influence of Blocking Neutrophil Basement Membrane Migration 138
3.3.9 Neutrophil Migration - Impedance Analysis 143
3.3.10 Neutrophil Migration - Dextran Permeability 146
3.4 Discussion 149
3.5 Conclusion 159

4 A Silicon Nanomembrane-based *in vitro* Platform to Visualize Immune Cell Trafficking across the Human Blood Brain Barrier 160
4.1 Abstract 160
4.2 Introduction 162
4.3 Results 168

4.3.1 Live Cell Imaging on Commercial Supports 168
4.3.2 Culturing CD34$^+$-derived ECs on Silicon Nanomembranes 172
4.3.3 Impact of Pericyte Conditioned Medium 174
4.3.4 CD34$^+$-derived ECs establish BBB Characteristics on NPN 178
4.3.5 Introduction of the μSiM-CVB Flow System 185
4.3.6 T-cell Extravasation in μSiM-CVB 187
4.4 Discussion 191
4.5 Methods 200
4.5.1 Device Fabrication 200
4.5.2 Isolation and differentiation of CD34$^+$ cells from human umbilical cord blood 202
4.5.3 Induction of BBB characteristic in CD34$^+$-derived endothelial cells 203
4.5.4 Endothelial Permeability (Pe) Measurements 204
4.5.5 Stimulation of BLECs with the pro-inflammatory cytokine TNF-α 205
4.5.6 Immunofluorescence staining of BLECs 205
4.5.7 Human peripheral blood T-cells 207
4.5.8 *In vitro* live cell imaging 208
4.5.9 Statistical Analysis 209
4.5.10 Ethics approval and consent to participate 210

4.6 Author's Contribution 210

5 Porous Silicon Nitride Membranes for *in situ* Optical Analysis of Translocation of Nanoparticles across the Blood-Brain Barrier 212

5.1 Abstract 212

5.2 Introduction 214

5.3 Results and Discussion 215

5.3.1 Coculture Device Prototype for *In Vitro* BBB Model . 215

5.3.2 Nanoparticle Transport in the BBB Model 217

5.4 Conclusion 220

5.5 Materials and Methods 223

5.5.1 Nanomembrane Fabrication 223

5.5.2 Device Assembly 224

5.5.3 Routine Cell Culturing 224

5.5.4 BBB Cocultures on Transwell Inserts 225

5.5.5 BBB Coculture on SiN-based Devices 226

5.5.6 Immunocytochemistry 227

5.5.7 Paracellular Permeability Assays 228

5.5.8 Nanoparticle Characterization 228

5.5.9 Subcellular Localization and Translocation Studies on NPs in SiN-based Devices 229

6 Summary 232

Bibliography **241**

Biographical Sketch

The author was born in the city of Dombivli in suburbs of Mumbai in India. He attended Indian Institute of Technology at Kharagpur, India, and graduated with a Bachelor of Technology degree in Biotechnology and Biochemical Engineering in 2010. He completed his Master of Science degree in Biomedical Engineering at the University of Rochester in 2012 under the supervision of Professor James McGrath and Professor Richard Waugh. He continued his doctoral studies at the University of Rochester and pursued research on developing novel microphysiological systems for studying vascular disorders. He was awarded a Howard Hughes Medical Institute Med-into-Grad Fellowship in Cardiovascular Science in 2014-2015.

The following publications were a result of work conducted during doctoral study:

T. S. Khire, K. S. Lucas, A. T. Salminen, E. Luke, R. E. Waugh, and J. L. McGrath. Silicon Nanomembranes to Engineer Vascular Microphysiological System (MPS) to Study Neutrophil-Endothelial Interactions. Manuscript in preparation.

A. Salminen, J. Zhang, G. Madejski, **T. S. Khire**, R. Waugh, J. McGrath, T. Gaborski. Dual-Scale Porous Ultrathin Nanomembranes for Vascular Transmigration Models, Manuscript under review, SMALL.

D. Hudecz, **T. S. Khire**, H. L. Chung, E. Luke, K. A. Dawson, J. L. McGrath, Y. Yan. Porous Silicon Nitride Membranes for *in situ* Optical Analysis of Translocation of Nanoparticles across the Blood-Brain Barrier, Manuscript in preparation.

M. Rosito & A. Mossu, **T. S. Khire**, H.L. Chung, H. Nishihara, I. Gruber, E. Luke, F. Gosselet, J. L. McGrath, and B. Engelhardt. A silicon nanomembrane-based *in vitro* platform to visualize immune cell trafficking across the live human blood-brain barrier, Manuscript accepted, Journal of Cerebral Blood Flow & Metabolism.

T. S. Khire, B. J. Nehilla, J. Getpreecharsawas, M. E. Gracheva, R. E. Waugh, and J. L. McGrath. Finite element modeling to analyze teer values across silicon nanomembranes. Biomedical Microdevices, 20(1):11, Jan 2018.

H. H. Chung, C. K. Chan, **T. S. Khire**, G. A. Marsh, A. Clark, R. E. Waugh, and J. L. McGrath. Highly permeable silicon membranes for shear free chemotaxis and rapid cell labeling. Lab on a Chip, 14(14):2456-2468, 2014.

J. DesOrmeaux, J. Winans, S. Wayson, T. Gaborski, **T. Khire**, C. Striemer, and J. McGrath. Nanoporous silicon nitride membranes fabricated from porous nanocrystalline silicon templates. Nanoscale, 6(18):10798-10805, 2014.

D. G. Johnson, **T. S. Khire**, Y. L. Lyubarskaya, K. J. Smith, J.-P. S. DesOrmeaux, J. G. Taylor, T. R. Gaborski, A. A. Shestopalov, C. C. Striemer, and J. L. McGrath. Ultrathin silicon membranes for wearable dialysis. Advances in chronic kidney disease, 20(6):508-515, 2013.

T. S. Khire, J. Kundu, S. C. Kundu, and V. K. Yadavalli. The fractal self-assembly of the silk protein sericin. Soft Matter, 6(9):2066-2071, 2010.

Acknowledgments

I want to sincerely thank all the people who helped me, without whom I could not have done this work. My family is the solid foundation that gave me the necessary support and encouragement, and their belief in me is solely the reason why I was able to achieve anything in my life. No words can express my gratitude to them and I owe every bit of my success to them.

I am ever thankful to my advisors Professors James McGrath and Richard Waugh for accepting me in their lab, and perpetually believing in me and my work!

Many thanks to old and new friends in Rochester for cherishing the happy moments with me, tolerating me at my bad times, and giving me life-lasting memories.

I want to thank all my current and previous labmates for their experimental support, intellectual help, Danforth lunches, game nights, frisbee sessions, and all other fun events that kept me mentally sane while in the basement.

Special thanks to Ms. Donna Porcelli for rescuing me from some of the toughest situations I had encountered during my PhD.

Finally, I want to thank the Medical Center squash community for introducing me to the 'fittest' sport and acting as a necessary stress buster after a long day in the lab.

Abstract

Current *in vitro* models of the microvasculature remain limited in their ability to provide live-cell imaging and monitor barrier function under physiological shear stress. In this thesis, we employ silicon nanomembrane (SN) technology and microdevice fabrication strategies to engineer an advanced vascular mimetic platform. SNs are highly porous and permeable substrates with thickness <100 nm and offer superior phase and fluorescence imaging characteristics.

Our microvascular mimetic (MVM) platform enables microfluidic and biochemical stimulation of human endothelial cell (ECs) with simultaneous optical and electronic measurements. This system enables the growth of ECs under physiological shear levels and in the close proximity to extracellular matrix components. We also developed a complementary mathematical model that characterizes the electrical resistance of SNs and the MVM platform. This model enables the interpretation of cellular barrier function in the context of abundant published results featuring conventional Transwell® inserts.

To simulate inflammatory conditions, we introduced bacterial chemoattractants (abluminal stimulus) to compel neutrophil extravasation across the endothelium. We found a modest decrease in the electrical impedance and an increase in the permeability of fluorescent dextran during neutrophil diapedesis. The treatment of neutrophils with anti-CD29 blocking antibody reduced neutrophil subendothelial migration and mitigated the loss of barrier function, thus, demonstrating a potential therapeutic role of anti-CD29 treatment in reducing edema.

Our MVM platform was also adapted to study the blood-brain barrier (BBB) in two collaborations. In one collaboration, we found that $CD34^{+}$-derived ECs establish BBB properties with the abluminal introduction of pericytes-conditioned medium. Our MVM-BBB was then used to image and characterize the migration of patient-derived T-cells in an *in vitro* model of Multiple Sclerosis. In the second collaboration, we adapted our MVM platform to image the translocation of 100 nm nanoparticles (NPs) across more traditional BBB coculture. Using high-resolution confocal microscopy of live cultures, we detected very rare examples (0.04%) of NPs translocating across the BBB. These results suggest the value of a BBB platform compatible with high-resolution live-cell imaging for the design of drug-containing NPs that can breach the BBB to target central nervous system disorders such as Alzheimer's and Parkinson's disease.

Contributors and Funding Sources

This work was supported by a dissertation committee consisting of Professor James L. McGrath (co-advisor), Professor Richard Waugh (co-advisor), and Professor Diane Dalecki, all of the Department of Biomedical Engineering, Professor Lisa DeLouise of the Department of Dermatology, and Professor Angela Glading of the Department of Pharmacology and Physiology at the University of Rochester.

Chapter 2 is previously published in the Biomedical Microdevices journal, and is included as is with permission from the Springer Nature publishing house. Tejas Khire is the co-first author of this publication along with Barrett Nehilla. Barrett Nehilla was responsible for cell culture studies, and Thomas Andolsek was helpful in acquiring acellular resistance measurements. Design of studies, mathematical modeling, finite element analysis, data interpretation, and COMSOL simulations were performed by Tejas Khire. Manuscript was primarily written by Tejas Khire and edited by the remaining authors.

Chapter 3 is developed as a manuscript currently in preparation. Tejas Khire, James McGrath and Richard Waugh were responsible for design-

ing experiments. Alec Salminen was responsible for shear-stress verification experiment; Kilean Lucas was responsible for scanning electron microscopy imaging; Henry Chung was helpful in developing programming code to quantify cell alignment; Thomas Andolsek, Emma Luke, and Robert Breidenstein were helpful in device fabrication. Remaining experiments were performed by Tejas Khire. Tejas Khire wrote the chapter and James McGrath and Richard Waugh edited.

Chapter 4 is adapted from a manuscript accepted in Journal of Cerebral Blood Flow & Metabolism. The work presented in this chapter is a collaborative research between the labs of James McGrath (University of Rochester) and Britta Engelhardt (University of Bern, CH). The microfluidic platform incorporating silicon nanomembrane technology that is central to the studies in this paper was designed, developed, and optimized by Tejas Khire. All the experiments and gathered data directly involve the application of this platform, hence the entire study has been presented in this chapter. Tejas Khire is the second author of this manuscript and was responsible for data curation, formal analysis, investigation, methodology and writing the original draft.

Chapter 5 is lightly adapted from a manuscript currently in preparation. The work presented in this chapter is a collaborative research between the labs of James McGrath (University of Rochester) and Kenneth Dawson (University College Dublin, IE). The microfluidic platform incorporating silicon nanomembrane technology that is central to the studies in this paper was de-

signed, developed, and optimized by Tejas Khire. Only the results obtained from this platform and that are relevant to the main theme of this thesis has been presented in this chapter. Tejas Khire is the second author of this manuscript and was responsible for data curation, analysis, troubleshooting, and writing the original draft.

All other work conducted for the dissertation was completed by the student independently.

Graduate study was supported by National Institutes of Health (NIH) program project grant number: 5 Grant R01 HL125265, and Howard Hughes Medical Institute (HHMI) Med-into-Grad Fellowship in Cardiovascular Science.

List of Tables

1.1 Structural Characteristics of Endothelium 7

1.2 Leukocyte Adhesion Cascade Molecules 16

3.1 Neutrophilic Granules 90

3.2 Gasket Dimensions 99

3.3 ECM Ligands of β1 Integrins 140

4.1 Inserts Tested 171

5.1 Paracellular Permeability of 4 kDa FITC-dextran 217

List of Figures

1.1 Leukocyte Adhesion Cascade 15
1.2 Fabrication of Silicon Nanomembranes 43
1.3 Confocal Imaging on Silicon Nanomembranes 45

2.1 *In vivo* measurement of capillary resistance 58
2.2 Effect of Membrane Geometry on TEER Values 67
2.3 COMSOL model of EndOhm chamber 69
2.4 Validation of COMSOL Model 70
2.5 Electric field lines for track-etched membranes 71
2.6 Electric field lines for silicon nanomembranes 72
2.7 Comparison of experimental and simulated TEER values in different membrane-systems 73
2.8 Ratio of simulated resistance in different membrane-systems . 77
2.9 Overlapping of the mapped data across different membrane-systems 78
2.10 Difference in electric field lines in confluent culture in different membrane-systems 79

3.1 Leukocyte Adhesion Cascade 89
3.2 Assembly and Operation Flowchart 97
3.3 Device Schematic 100
3.4 Designs for Precision Cutting 101
3.5 3D CAD Model 102
3.6 Assembled Device 104
3.7 Indium Tin Oxide Electrode 105
3.8 Fluidic Capacitor 106
3.9 FITC-Dextran Permeability Assay 112
3.10 Flow Setup 116
3.11 Pulsation Dampening 117
3.12 Flow Verification 118
3.13 Effect of Shear Stress on Endothelial Cells 120
3.14 Detachment of Endothelial Cells 122
3.15 Alignment Characterization 123
3.16 TEER vs Endothelial Growth 126
3.17 TEER Prediction in COMSOL Multiphysics 129
3.18 Electric Fieldlines in the MVM 129
3.19 Equivalent Circuit for Impedance Analysis 130
3.20 Growth Characterization Using Impedance Analysis 132
3.21 Neutrophil Migration Schematic 133
3.22 Neutrophil Transendothelial Migration 135
3.23 Scanning Electron Microscopy (SEM) 137

3.24 Collagen Gel under SEM 138
3.25 3D Migration of Neutrophils under SEM 139
3.26 Blocking Neutrophil Migration 142
3.27 Effects of β1 Blocking on Neutrophil Migration 143
3.28 Effects of β1 Blocking on HUVECs Alone 144
3.29 Impedance Analysis During Neutrophil Migration 145
3.30 Fluorescence Analysis During Neutrophil Migration 147
3.31 3D Migration of Antibody-treated Neutrophils under SEM . . 148

4.1 $CD34^+$-derived ECs grow to confluent monolayers on the nanoporous silicon nitride membrane 173
4.2 Endothelial cell adhesion under shear stress 175
4.3 Induction of BBB characteristics in $CD34^+$ ECs by pericyte-conditioned medium 179
4.4 $CD34^+$-derived ECs grown on nanoporous silicon nitride membranes establish BLECs characteristics 183
4.5 Assembly of the μSiM-CVB flow system 188
4.6 *In vitro* live cell imaging of the T-cell-BBB interactions under flow 192

5.1 Schematic and Expression of BBB Markers *In Vitro* 218
5.2 Nanoparticle Translocation Across BBB 221

6.1 Systemic Inflammation *In Vitro* 240

Chapter 1

Introduction

1.1 Introduction

Definition

The word 'inflammation' is derived from the ancient Latin word 'inflammare' meaning to 'to set on fire'. The science of inflammation is one of the most widely studied subjects historically, and the definition of inflammation has evolved significantly over the course of time [1]. Terms such as *edema*, which are widely used in medical textbooks and research materials even today, have been attributed to Hippocrates belonging to 5th century BC [2]. One of the earliest definitions of inflammation was proposed by Roman scholar Cornelius Celsus around 1st century AD. He described inflammation on the basis of 4 cardinal signs visible: *rubor et tumor cum calore et dolore* - redness and swelling with heat and pain [1]. Although this definition encompasses the clinical symptoms of inflammation, the four events do not always occur

simultaneously. The fifth sign of inflammation was proposed by the Roman physician Galen almost two centuries after Cornelius, and he described it as *functio laesa*, or the loss of function. He, for the first time, associated inflammation with the bodily fluids, also known as 'humor', which is still a widely accepted view of acute inflammation [3]. (This definition is also attributed to German scientist Virchoff and the credit remains controversial [4].)

The invention of microscopy allowed the scientists to study the role of (white) blood cells during the inflammatory response that further enhanced our mechanistic understanding of inflammation. In 1824, French biologist Dutrochet reported the observation of the egress of white blood cells, also known as leukocytes, from small blood vessels [5]. One of the most elaborate pictures of leukocyte migration in inflammation was provided by Arnold Heidelberg in 1870s, where he used silver stain to label endothelial junctions and observed leukocyte escape through the junctional spaces. He also schematized the process of the junctional migration of leukocytes for the first time [6]. However, the most important contribution to the theory that the inner walls of the blood vessel, i.e., endothelium or endothelial cells, affect the propensity of leukocyte migration (which we now know is mediated by adhesion molecules) was first formulated and established by Julius Cohnheim in 1880s [1, 4, 5, 7]. His interpretation of the phenomenon was quite interesting, and laid down the foundations of modern innate immunity, as stated below: *" ...We hold fast the conviction which was forced on us by our experi-*

ments and reflection that inflammation is the expression and consequence of a molecular alteration in the vessel walls. By it, adhesion between the vessel wall and the blood is increased..." [5]. His interpretation of the leukocyte emigration from the blood vessel was solely attributed to the blood vessel wall without assuming any significant role for leukocytes themselves. Further work by Metchnikoff around the same era was responsible for coining the word 'chemotaxis' - directed migration of leukocytes towards the source of chemoattractant - and assumed an equally important contribution by leukocytes in determining their overall migratory fate [2]. In the 20th century, our understanding of the physical and life sciences advanced exponentially.

Development of radioactive and fluorescent tracer molecules, with simultaneous improvements in the resolution offered by optical microscopy, development of *in vivo* imaging, and advancements in scanning and electron microscopy rapidly ushered in a new era of hypothesis-testing and experimental execution. All these efforts changed our understanding of the human immune system and its role in regulating inflammation. In a review by Rocha Silva published in 1978, one of the most comprehensive definitions of inflammation was conceptualized, which is more or less accepted in its original form until today: *"...Inflammation is a multi-factorial mediated phenomenon, in which different mediators appear and vanish at the appropriate time and space and are responsible for increasing vascular permeability, attracting leukocytes, inducing pain, edema, and necrosis..."* [8]. The work presented in this thesis revolves around this definition of inflammation and aims to address ques-

tions associated with leukocyte migration and their effects in altering vessel permeability.

1.2 Inflammation and Vascular Permeability

1.2.1 Microcirculation

Microvasculature and microcirculation play an important role in the inception and sustainment of the inflammatory insult. The pervasiveness of the microcirculation throughout the entire body makes it a key element in the inflammatory cascade. Microvessels can be classified into three major categories that are preserved regardless of the vascular bed: arterioles, capillaries, and venules [9]. Large arteries narrow down to smaller arteries that further split and distribute the blood supply into arterioles. The smallest pre-capillary arterioles are ∼15-20 microns in diameter and provide the most resistance to the blood flow, hence, known as 'resistance' microvessels. These arterioles give rise to capillary vessels with diameters less than 10 microns. The capillary vessels form a massive network with a large surface to volume ratio [2]. These capillaries allow for easy transport of hydrophilic and lipophilic molecules, as well as facilitate the transport of water, nutrients, and oxygen across the individual blood-tissue barrier. Capillaries then merge and drain the deoxygenated blood into post-capillary venules. Each of these three microvessel structures contributes to inflammation differently.

Arterioles are surrounded by smooth muscle cells that control vascular tone. During inflammation arterioles are responsible for reduced blood flow by vasoconstriction, and this in turn causes reduced flow in inflamed capillaries and may result in leukocyte plugging of the capillary lumen [10]. However, the most important role during inflammation is played by the post-capillary venules. Upregulation of adhesion molecules on the endothelial surface (as hypothesized by Cohnheim), and the simultaneous release of chemoattractant molecules trigger the activation of leukocytes, which adhere to the vessel walls and extravasate through the walls of post-capillary venules during inflammation [11]. The work presented in this thesis focuses on understanding the responses of post-capillary venules due to their eminent role during inflammatory responses in the body.

1.2.2 Endothelial Cells

Endothelial cells (ECs) constitute the inner lining of the blood and lymphatic vessels, and are the one of the most important constituents of the vascular system. Unlike the classical view that assumed homogeneity in the types of ECs, these cells are extremely heterogeneous and differ significantly in different vascular beds as well as within the same bed depending on their location and stipulated functions [12]. These differences can be attributed to genetic (intrinsic) factors that are determined during the development and/or to environmental (extrinsic) factors that contribute to the phenotype of endothelial cells [13]. Micro-structural analysis revealed that the notice-

able differences in the ECs of different origin and vascular beds are exhibited at their intercellular junctions, as indicated in Table 1.1. Regardless of these structural differences, the pathophysiological responses of ECs to inflammatory insults can be generalized. The strategic positioning of the ECs acting as a physical barrier between the blood supply and the surrounding tissue, as well as their ability to synthesize and secrete vasoactive substances, cytokines, adhesion molecules, and endothelin (vasoconstrictor) make ECs the master regulators of homeostasis [14]. The structural configuration of endothelial cells imparts on them diverse functionality. Polarization of endothelial cells allows them to express different adhesion receptors on the luminal side and focal adhesion complexes on the abluminal (basolateral) side, with junctional moieties providing cell-cell cohesive interactions at the cell edges. Under homeostatic conditions, ECs act as a selectively permeable barrier that regulates the transport of fluids, solutes, proteins, and other macromolecules, controls vascular tone (in conjunction with the mural cell surrounding the endothelium), and exhibits highly anti-inflammatory and anti-thrombogenic/anti-coagulatory properties [2]. The checkpoints that regulate the trafficking of different elements across the ECs under normal conditions is disturbed during inflammation and leads to an increase in the permeability of the endothelium. It needs to be noted that, although inflammation-induced permeability is a pathological response, it is necessary for the body to supply the necessary armamentarium such as nutrients, immunoglobulins, albumin and other plasma proteins required to neutralize, repair, and heal the site of

Table 1.1: Structural Characteristics of Endothelium. Adapted from [16].

Type of Endothelial Cells	Representative Vascular Bed	Pore sizes
Non-sinusoidal, non-fenestrated with tight junctions	Retina, Brain-spinal cord, Enteric nervous system	$<$1 nm
Non-sinusoidal, non-fenestrated with loose junctions	Skin, Muscle, Cortical bone, Adipose Tissue, Lung	$\sim$ 5 nm
Non-sinusoidal with diaphragmed fenestrate	Testis, Connective Tissue, Endocrine/exocrine Glands, Intestinal mucosa	6-12 nm
Non-sinusoidal with open fenestrate	Kidney Glomerulus	$\sim$ 15 nm
Reticulo-endothelial Sinusoids	Liver	$\sim$ 105 nm
Non reticulo-endothelial Sinusoids	Spleen	$\sim$ 5 μm

inflammation [15]. Pathological conditions where this fine balance between *good* & *bad* aspects of inflammatory response is lost result into conditions called 'hyperpermeability', which is often referred to as 'permeability'. The following sections review briefly the different layers of barrier offered by the endothelium to prevent and mitigate (hyper)permeability.

1.2.3 Regulators of Endothelial Permeability

Endothelial Glycocalyx

Endothelial permeability is an important characteristic of microcirculation that is affected during inflammation. There are hierarchical structures and mechanisms in place to cope with the increasing permeability that mitigate the loss of vascular tone and plasma exudate in the extravascular spaces. The foremost barrier offered by ECs is the expression of endothelial surface layer (ESL), also known as endothelial glycocalyx. This layer is about ∼200-500 nm thick and is expressed on the luminal surface of endothelial cells. It consists of multiple proteoglycans and glycoproteins rendering a net negative charge to the glycocalyx layer [17]. Glycocalyx influences homeostasis by modulating vascular tone and flow patterns, and preventing the adhesion of immune cells on the endothelial surface by charge mediated repulsion and steric hindrance [18]. Inflammatory mediators such as tumor necrosis factor-alpha (TNF-α) are responsible for the degradation of this glycocaylx layer, and 'prepares' the endothelial cells for an anti-inflammatory response.

Endothelial Junctions

The second and probably the most important barrier in regulating the endothelial permeability is the endothelial cell-body itself. There are two distinct paths of transport - transcellular and paracellular - i.e. through and between the endothelial cells respectively. The paracellular route of trans-

port occurs through the intercellular cleft (space) between adjacent endothelial cells, and allows for passive diffusion of molecules less than 3 nm in size [19]. This includes substances such as water, glucose, urea, and ionic species. All other macromolecules with size more than 3 nm face obstruction from the interendothelial junctions (IEJ). There are three main types of junctional complexes, adherens junctions, tight junctions, and gap junctions, although, only the first two are known to be involved in the regulation of permeability. Adherens junctions are composed of vascular endothelial (VE)-cadherin complexes, and are found in almost all types of vascular beds. Dynamic interactions between VE-cadherin and their cytoskeletal anchoring proteins are extremely important for the regulation of a tight barrier, and disruption of these *intracellular* interactions has a direct impact on the breakdown of *intercellular* homotypic cadherin interactions ultimately leading to a rise in the endothelial permeability [20]. Tight junctions, unlike the adherens junctions, are less ubiquitous and mainly consist of proteins such as occludins (cytoskeletal adaptor protein) and claudins (expressed on the endothelial surface). These junctions are responsible for very high resistances to the transport of molecular and cellular species, which is crucial for immune-privileged sites such as the brain and central nervous system.

Transcellular pathways of transport are receptor mediated and are recognized for their ability to transport macromolecules such as albumin, lipids, insulin etc. from the luminal side to the abluminal side. Caveolae are the vesicular structures involved in endocytosis (as well as transcytosis) of these

macromolecular species. Proteins associated with caveolae, such as caveolin-1, dynamin etc., are the primary regulators of transcellular permeability [19]. Transcellular pathways for water molecules also exist and are facilitated by aquaporin channels embedded in the lipid bilayer of ECs. While transcellular mechanisms offer high selectivity for transporting species across the blood-tissue barriers, paracellular routes are energetically less expensive for the cells, thus, increasing overall efficiency of transport [21].

Endothelial Extracellular Matrix

The last entity that acts as a barrier for molecular and cellular trafficking across the blood vessel-wall is the basal lamina and the subjacent extracellular matrix (ECM). ECM is a voluminous, insoluble, three dimensional structure, which consists of proteins with structurally independent domains and highly conserved sequences and arrangements [22]. Electron microscopy studies have discovered that basement membrane (BM) is a $\sim$ 50-100 nm thick, dense, and amorphous sheet-like structure that is morphologically distinct from the surrounding fibrillar ECM [23]. While the endothelial cells belonging to arteries, arterioles, and veins have a basement membrane secreted by the ECs, capillary and post-capillary venular endothelial cells share this responsibility with the surrounding pericytes that are in fact embedded within the secreted BM structure [24]. BM is composed of interwoven networks of collagen IV and laminins. These self-assemble into large polymeric structures and are stabilized and connected to each other through a variety of macro-

molecules such as nidogen, perlecan, entactin, and other non-collagenous proteins [25]. Around 50 different macromolecules in the size range of 75-400 nm are present in the BM assembly, creating an effective pore size on the order of ∼50 nm for the passive diffusion of small molecules through it [26]. These pore sizes are about 40 times smaller than the necessary gap required by the leukocytes required for exiting the blood vessel. These structural characteristics essentially make BM an important factor not only for regulating the molecular permeability, but also in acting as an extra level of barrier for the trafficking of immune cells across the subendothelial layer. The interstitial matrix, typically dominated by collagen I in most connective tissues, along with non-collagenous proteins such as fibronectin and vitronectin, contribute to a reduced baseline permeability under normal conditions. These networks within the ECM can be disrupted by matrix metalloproteinases (MMPs) that are activated by the action of TNF-α, leading to increases in the permeability of the endothelial monolayer *in vitro* [27]. The MMPs, often secreted by various immune cells during an inflammatory response, are known to lyse the ECM proteins to allow for easier migration across the tissue. In our own experience, we observe slower diffusion of fluorescent dextran across intact collagen gels as compared to the fluid cell media, confirming the reduced permeability of such viscous gels.

In summary, different luminal and junctional structural elements of the endothelial cells and their surrounding ECM contribute to the overall barrier established at the blood vessel wall for cellular and molecular transport.

Damage to either one of these barriers can increase the net permeability of the endothelial monolayer. In this work, we focus on the effects of leukocyte activation on endothelial permeability. The following sections describe the different aspects of leukocyte migration responsible for increasing endothelial permeability.

1.2.4 Neutrophil-Endothelial Interactions: Setting up the Stage

The word 'neutrophil' is derived from the phrases *neutro* + *phile*, because neutrophils are neutral towards acidic and basic dyes used for histological staining (unlike basophils and eosinophils, other types of leukocytes, which selectively stain for basic and acidic dyes respectively). Neutrophils are the most dominant population of leukocytes in the blood circulation in the human body, and are the first responders to any sterile or infection-mediated inflammatory response. Neutrophils originate from pluripotent hematopoietic stem cells, and are continuously produced in the bone marrow from myeloid progenitor cells. They undergo differentiation through multiple stages before terminally differentiating to become polymorphonuclear (PMN) granulocytes [28]. (Hereafter, neutrophils might be alternately referred to as PMN). Upon maturation, neutrophils exit bone marrow following the gradients of granulocyte-colony stimulating factor (G-CSF), which is in turn triggered by the production of different cytokines (interleukins) secreted by T-cells of different types and functions [29]. Under normal physiological con-

ditions, circulating neutrophils can be found in different organs such as bone marrow, spleen, liver and lung (with the highest propensity for staying in the lungs), and are cleared in bone marrow, spleen, and liver. Neutrophils in circulation have a half-life of 6-8 hours, with this duration extending during the persistence of an inflammatory response.

Neutrophil Activation

Inflammation is responsible for the activation of neutrophils that undergo 'respiratory or oxidative burst' - a process in which neutrophils generate and secrete reactive oxygen and other free radical species responsible for the destruction of the bacteria [30]. During this process, neutrophils secrete numerous granules, which are responsible for the production of myeloperoxidase enzymes, proteases, MMPs (as described above), adhesion receptors, complement proteins, heparin-binding proteins, and cytokines for different effector functions [15]. Neutrophils possess the ability to engulf an entire bacterium in an elaborate process called phagocytosis. Neutrophils can also release neutrophil extracellular traps (NETs), composed of genomic DNA and degrading enzymes that can immobilize and/or engulf and/or kill the targeted pathogen. In all, neutrophils possess an excessive armamentarium to neutralize the source of a bacterial infection giving rise to an acute inflammation.

Neutrophil Migration

The most studied aspect of neutrophil activation revolves around their migration and egress from the blood vessel towards the site of infection or an insult. This elaborate multi-step process terminates with neutrophils leaving endothelium, and is referred to as 'diapedesis' or extravasation. Figure 1.1 highlights the main steps involved in the neutrophil/leukocyte adhesion cascade. This entire cascade is well characterized and numerous reviews can be found in the literature [11, 29, 31–33]. Neutrophils adhere, arrest, crawl, and transmigrate on endothelial surface in a regulated fashion, which requires dedicated sets of receptor-ligand interactions as summarized in Table 1.2.

Neutrophil Luminal Migration

It is important to consider the different roles of these surface molecules to understand the ability of neutrophils to migrate on the endothelial surface and undergo diapedesis. Briefly, neutrophils employ L-selectin receptors to roll on the vessel walls, whereas they use CD18 or $\beta 2$ integrins to arrest and crawl on the endothelial surface [35]. The $\beta 2$ integrin pairs with different α units - CD11a and CD11b - to constitute LFA-1 and MAC-1 integrins respectively, both of which recognize and bind to intercellular adhesion molecule 1 (ICAM-1). Different chemoattractants are responsible for inducing the differential activation of these integrins, and this allows the neutrophils to *'choose'* their direction of migration when two competing gradients of chemoattractants

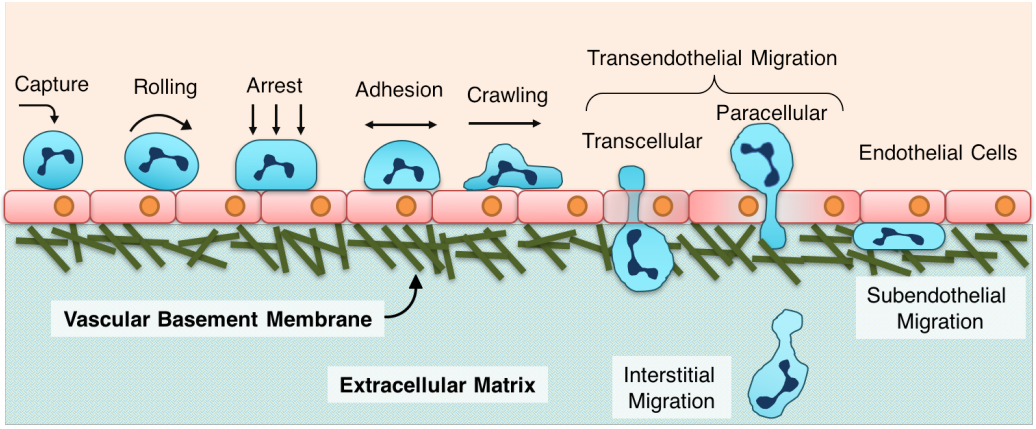

Figure 1.1: Leukocyte Adhesion Cascade: Circulating neutrophils marginate and slow down near the surface of vessel wall, which captures them and they begin the rolling motion. After getting arrested on the surface, neutrophils transform their shape and spread on the endothelial surface triggering enhanced adhesion between neutrophils and endothelial cells. Post-adhesion, neutrophils start crawling on the endothelial cells until they reach the 'hot spot' for egress to undergo transmigration either through the endothelial cell body (transcellular) or around them in between the interendothelial cleft (paracellular). Transmigrated neutrophils further migrate in the subendothelial space between the basal side of the endothelium and its subjacent basement membrane. Following the breach of basement membrane, activated neutrophils then begin their final lap of interstitial migration to reach their targeted destination.

Table 1.2: Leukocyte Adhesion Cascade Molecules: Interactions between different adhesion molecules on neutrophil and endothelial surfaces. Adapted from [34].

Stage in the Cascade	**Molecules on Endothelial Cells**	**Molecules on Neutrophil**
Tethering & Rolling	P-selectin, E-selectin, PSGL1, GlyCam	PSGL1, ESL1, CD44, L-selectin
Slow Rolling	ICAM-1, E-selectin	LFA1 (PSGL1-induced), PSGL1, ESL1, CD44
Arrest & Adhesion	ICAM1, VCAM1	LFA1, VLA4
Crawling	ICAM1	MAC1
Transmigration	ICAM1/2, VCAM1, CD99, PECAM1, JAMA/B/C	LFA1, MAC1, VLA4, CD99, PECAM1, JAMA

present in the vasculature [36]. Chemokines activate neutrophils through G protein coupled receptor (GPCR) pathways, which mediate inside-out signaling and activation of the (CD11/CD18) integrins and facilitate luminal migration of neutrophils [31]. The absence of either of these CD18 integrins can significantly delay the migration process [37], and complete knockout of CD18 can completely inhibit neutrophil diapedesis resulting in a compromised immune response [38]. The process of neutrophils locating the site for egress is dependent on the nature and source of chemoattractant, as well as the expression of ICAM, and their relative proximity with the 'closest'

available site for diapedesis. For example, it has been found that there exists a haptotatic gradient of ICAM-1 molecules on the epithelial surface that leads the neutrophils to the junctional sites of egress in a clinically healthy gingiva [39]. Whether such immobilized gradients exist elsewhere in the vascular endothelium needs to be discovered, but teleologically, the presence of surface-bound molecular gradient attracting and leading neutrophils to the site of egress is an efficient mechanism to achieve faster diapedesis. It has been also hypothesized and observed in certain studies that this guided migration of neutrophils further encourages them to egress through tricellular junctions (junctions formed at the intersection of 3 cells, instead of only 2 adjacent cells) [7, 40].

Neutrophil Abluminal (Subendothelial) Migration

After neutrophils cross the endothelial junctions, they need to traverse the basement membrane (BM) before they can invade the interstitial matrix and the deep tissue. *In vivo* animal studies have been instrumental in investigating the BM migration of neutrophils. Nourshargh et al. have identified regions in the BM that express lower amounts of BM proteins such as collagen and laminin, particularly laminin 10 (also known as laminin 511) [41]. These regions (also known as low expression regions LERs) are formed due to the patchy deposition of BM by pericytes, which offer paths of lower resistance for the egress of the neutrophils [42]. In another study by Sorokin and colleagues, authors observed that neutrophils spend more time in crossing

the BM (40 minutes) compared to the time required to traverse the endothelium (4 minutes) suggesting that BM migration is the rate-limiting step in the extravasation cascade [43]. The verification of these results in a *human* system is yet to be achieved due to the lack of sophisticated *in vitro* models of BM [44]. It has been found in different studies that neutrophils use $\beta 3$ and $\beta 1$ integrins to migrate on the BM surface [45], and the inhibition of these integrins can caused arrest of neutrophils in the subendothelial layers as shown both *in vivo* [38, 46] as well as *in vitro* [47]. Neutrophil migration beyond the BM into the ECM *can* be integrin-independent, where the traction forces provided by the ECM can facilitate actomyosin contractions within the neutrophil body and allow them to further 'swim' through the matrix towards the source of inflammation [48]. The work presented in this thesis is more focused in the subendothelial migration of neutrophils, and how the physical motion of neutrophils on the BM surface affects the overall endothelial permeability. The following sections briefly summarize the influence of neutrophil activation on endothelial barrier functions.

1.3 Neutrophils and Endothelial Permeability

Neutrophil (leukocyte) induced vascular leakage has been widely observed and reported previously [15, 49–53]. In the 1882 handbook of physiology, Cohnheim reported the following: *"Keeping pace with this exodus, emigration, or, as it is also called, extravasation of corpuscular elements there oc-*

curs an increased transudation of fluid, in consequence of which the meshes of the mesentery, or the tissues of the tongue, are infiltrated and swell..” [7]. Unlike this classical observation, which associated neutrophil migration as the key to increasing endothelial permeability, we now know that neutrophil migration is/can be independent of permeability, and that the migration and hyperpermeability are not necessarily coupled events [54]. Adhesion of neutrophils to the endothelial surface is sufficient to induce structural changes in endothelial cytoskeleton causing a rise in the net permeability [55]. Sarelius and colleagues have shown that rolling and adhesion events in the early stages of the leukocyte adhesion cascade can cause an increase in the leakage of labeled albumin in an animal model [56]. An excellent review discussing the intracellular signaling mechanisms associated with the rolling and adhesion events has been published recently [57] and is recommended for further reading. Adhesion events triggered by $\beta 2$ integrin-ICAM-1 interactions have been shown to increase endothelial permeability to macromolecules and decrease electrical resistance in an *in vitro* model [49]. Further studies proved that this neutrophil-endothelial adhesive interactions leads to the release of heparin-binding proteins, which causes a rapid and transient increase in the cytosolic calcium within the endothelial cells [50]. This sudden burst of free calcium ions causes actomyosin contraction leading to a retraction in cell-cell junctions and causing the increase in the net permeability. Different secretory products following neutrophil activation, as explained above, along with the generation of reactive oxide and nitride species also increase endothelial

permeability.

Neutrophil Transmigration-induced Permeability: Controversies and Resolution

The contribution of the actual process of transmigration (paracellular and transcellular) to endothelial permeability is unclear, and has been a controversial topic in literature [58]. This controversy seems to stem from the inconsistencies involved in the type of model used in the study (*in vivo* vs *in vitro*), the mode of initiating neutrophil transmigration (bacterial peptide vs endogenous chemoattractant vs sterile injury), and the method used for measuring permeability (ionic species vs fluorescent albumin vs fluorescent dextran molecules of different molecular weights). While animal models provide us with the most representative picture of the actual biological processes *in vivo*, the differences between animal (often mouse) and human pathophysiology make for an uncertain extrapolation of the results to human disease [59]. Similarly, the source of inflammation can be also responsible for activating different signaling cascades even though the final outcome is *still* neutrophil migration. For example, while fMLP directly activates the neutrophil machinery, endogenous mediators such as TNF-α and interleukin-8 promote chemotaxis by activating endothelial cells. Pre-activation of endothelial cells leads to the expression of ICAM-1, which is known to trigger transcellular (rather than paracellular) transmigration. Treatments with other bacterial products such as lipopolysaccharide (LPS), often used to study sepsis

in a mouse model, trigger systemic inflammation by inducing a cytokine storm [60]. Permeability measurement under such conditions can yield even more confusing results, as the neutrophils now experience much shallower chemokine gradients than usual and are known to respond differently [34].

One can expect a greater level of consistency within *in vitro* models due to the ability to regulate the inflammatory conditions in a much more precise manner. However, the mode of measuring permeability greatly affects this consistency. Transendothelial electrical resistance (TEER) is a metric used to quantify the leakage of ionic species across the endothelial monolayer, and hence, is very sensitive to even the smallest gaps present between the cells. It has been shown in electron microscopy studies that endothelial cells grown (under static conditions) *in vitro* exhibit visible gaps within the monolayer unlike their *in vivo* counterparts [61]. This will provide a reduced pre-inflammatory baseline measurement of TEER, which will understandably decrease only slightly in the presence of neutrophils. Macromolecular species need a wider gap to permeate, and are slightly insensitive to the finer gaps in the cultured endothelium. However, the variability in the size of tracer molecules used (typically dextran) can yield variable measures of permeability. The permeability of the macromolecules falls off sharply and non-linearly with increasing molecular size [19], and hence, using different molecular weight tracers can yield significantly different results. Furthermore, using labeled albumin for *in vitro* permeability measurement can complicate the results, because albumin is also transported actively through transcytosis

mechanisms along with its leakage through the gaps in the monolayer.

So, what do we know?

Regardless of these above-mentioned variabilities, it has been generally accepted that neutrophil transmigration can cause an increase in the endothelial permeability both *in vivo* and *in vitro*. One of the very few studies that concluded otherwise found that neutrophil transmigration through endothelial monolayer does not cause any increase in the trans endothelial electrical resistance (TEER) [62]. Authors facilitated chemotaxis by adding fMLP in the abluminal compartment and neutrophils in the luminal compartment atop endothelial cells. They had to increase the neutrophil-to-endothelial cells ratio up to 25 to observe any noticeable changes in TEER. The downside of this study was that the authors used amniotic membranes to grow the ECs, which suffer from low permeability to begin with [61]. Also the rate of data sampling was low, and since transmigration is a very transient process, it is highly likely that they failed to capture the events during data acquisition. On the contrary, in the study published by Gautam et al., authors found a sharp decrease in the electrical resistance in a similar setup over the course of 30 minutes [49, 50]. Another *in vitro* study implementing impedance spectroscopy also found a significant decay in the impedance values offered by the endothelial barrier as neutrophils transmigrated through the ECs [53]. Even *in vivo*, neutrophil transmigration was found to be responsible for an increase in fluorescent albumin flux across the mouse endothelium [37]. In this study,

authors forced neutrophils to transmigrate through both routes (trans-, and paracellular), and found that the increase in vascular permeability is almost similar for both the routes of transmigration. Very recently, Lim and colleagues discovered that extravasating neutrophils release microparticles that may act as a 'plug' to reduce vascular leakage [63]. Indeed, inhibiting the microparticle-formation can cause increased permeability *in vivo*. In summary, neutrophil transmigration, along with other upstream events related to their adhesion to endothelium, cause changes in endothelial barrier properties (to different degrees with varying kinetics), and these changes are sensitive to the input conditions responsible for facilitating the transmigration process.

Neutrophil Basement Membrane Migration-induced Permeability

While limited, a number of investigations have addressed the important question of how BM properties affect endothelial permeability. One of the classic studies was performed by Huber and Weiss in the 1980s. Authors grew human umbilical vein endothelial cells on top of collagen gel for ∼21 days under static condition. After 3 weeks of culturing, the authors induced neutrophil chemotaxis by adding neutrophils in the apical compartment and zymogen (a chemoattractant) in the basal compartment. After transmigration experiments, they fixed the basement membrane structure and imaged using scanning electron microscopy. They observed distorted structures of basement membrane upon imaging, with some samples showing perforated

matrix with clearly demarcated holes in them. Permeability studies of the denuded basement membrane also showed massive leakage of colloidal particles after neutrophils emigrated through the BM structure. This indicated that neutrophil migration affects the net endothelial permeability by attacking the integrity of its deposited basal lamina. While multiple studies have been performed in last 2 decades to explore the subendothelial migration of neutrophils, not much is known about the ability of neutrophils to alter BM integrity and increase net vascular permeability. Integrins present on neutrophil surface recognize different ligands (proteins) present in the BM, such as laminin isoforms, and the inability of neutrophils to recognize them can inhibit their migration on BM [43]. In a recent study on septic mouse, inhibition of $\alpha 3 \beta 1$ integrins on mouse neutrophils was responsible for the hampered migration of neutrophils in the BM region, and improved the survival rate in the septic animals [38]. Pharmacological blocking of this integrin also significantly reduced the migratory phenotype of neutrophils *in vitro*. Since microvascular permeability is one of the most detrimental factors in increasing morbidity and mortality in sepsis patients [64], one possible explanation can be that the inhibition of neutrophils reduced the (hyper)permeability in mouse microvasculature. The inability to invade the interstitial matrix might have arrested the progression of edema at the subendothelial layer, effectively preventing tissue ischemia and organ failure. While the exact reason behind the improved survival of treated mice is not yet known, the link between inhibited neutrophil migration and reduction in permeability might be the

missing piece in the puzzle. Thus, we sought out to ask the question: *how does the BM migration of neutrophils affect the overall permeability, and what are the molecular mechanisms involved in regulating this migration-induced permeability?*

To address this question, we aim to recreate the pathological conditions present during inflammation that stimulate neutrophil extravasation. We chose an *in vitro* model over *in vivo* to enable experimentation with human cells. The following sections describe currently available *in vitro* systems to study microvessel biology, their advantages and their limitations, and then we describe the advanced silicon nanomembrane technology used to engineer a novel microvessel mimetic (MVM) platform.

1.4 *In vitro* Models of Microvasculature

In vitro models of microvasculature provide a robust platform to study and address fundamental questions regarding blood vessels such as angiogenesis, inflammation, cancer metastasis, blood-based diagnostics, drug delivery etc., and their application has led to tremendous increases in our understanding of vascular function. Using reductionist approaches, it is possible to simplify the microenvironments present inside the body and identify key biological elements responsible for specific phenotypic activity. Platforms capable of growing endothelial cells enable detailed study of their biological responses to a wide range of stimuli, including mechanical perturbations,

normoxia/hypoxia, immune cell infiltration, substrate interactions, etc. The ultimate achievement of these *in vitro* models would be to construct a physiologically representative model of human microvasculature, and be able to replace, reduce, and refine the use of animal models in biomedical research (3Rs) [65]. While the definition of an '*in vitro*' model is very broad and can be include developments such as new stem cell lines or a new synthetic ECM construct, the definition of *in vitro* models in this study is limited to engineered platforms used to study endothelial cell biology outside the body. The following sections address the important factors to be kept under consideration while designing platforms *de novo* to study microvessel functions and describe the state-of-the-art models available commercially or published recently.

1.4.1 Factors Influencing Endothelial Growth *In Vitro*

Substrate Compliance

Endothelial cells (ECs) are very mechanosensitive cells, and the underlying growth substrate plays an important role in determining the growth and differentiation properties of the cells [66]. Substrate properties such as stiffness, porosity, permeability, and surface charge all affect the ECs, and optimizing these cell-substrate interactions is critical for physiologically representative *in vitro* models. To recreate the mechanical properties of tissues *in vitro*, it is necessary to fine-tune the stiffness of the growth substrate. Capillary walls

have stiffnesses in the range of kilo pascals [67] that are lower than commonly used artificial substrates such as glass (modulus in the range of GPa) or tissue culture plastic. On stiffer substrates, ECs can form stronger focal adhesion complexes that enhances cell-substrate interactions [68]. However compliant substrates allow for stronger cell-cell cohesive interactions that increases the monolayer barrier integrity [69]. Furthermore, the stiffening of vessel walls (as observed in atherosclerotic lesions) is associated with enhanced endothelial permeability and increased leukocyte migration [70]. These studies conclude that while stiffer substrates promote enhanced cell-surface adhesion, it can be at the expense of increased vascular permeability. Thus, it is necessary to use compliant substrates for the development of stronger cell-cell junctions and enhanced barrier properties.

Substrate Permeability and Thickness

Another important feature of the substrate that determines endothelial cell growth is the substrate porosity and permeability. It has been shown in numerous studies in the past that porous substrates are required for a more physiological growth of (endothelial) cells [68, 71–77]. Porosity of thin films supporting cell growth has wide-ranging effects as studied in our lab for the last decade. In a recent study by Gaborski et al., it was found that endothelial cells form fewer focal adhesions and express shorter fibronectin fibrils while grown on porous membranes, which resembled to their behavior on softer substrates [68]. Further investigations found that cells can spread better on

substrates with larger pore spacings that allowed for better fibrillogenesis and enhanced cell attachment [74]. Apart from pore spacing, the capability to fine-tune the pore sizes of these membranes will add an extra level of utility to the *in vitro* models. While red blood cells can squeeze through sub micron pores, neutrophils need a pore size of ∼3 microns for migration, whereas T-cells need even wider openings. Increasing pore sizes without reducing cell substrate interactions or compromising mechanical strength is an important aspect to be considered while designing novel substrates for cell culturing.

While conventionally, biologists have used glass or tissue culture plastic for cell culturing due to convenience associated in handling them, these flat substrates restrict the growth only to 2 dimensions and fail to capture the basolateral signaling that contributes to overall cell development. The phenomenon of apical and basolateral polarization is responsible for critical functions of endothelial cells including migration, lumen formation, barrier maturation [78], and is an important characteristic of endothelial/epithelial cultures. Despite their 2D nature, permeable substrates facilitate cellular signaling from the basal side effectively rendering a 3D growth environment. Furthermore, coculturing of ECs and mural cells also needs a permeable interface for unhindered cell-cell communication. In the past, we used highly permeable silicon nanomembrane (discussed below) for the growth and differentiation of adipose derived stem cells (ADSCs) with pericyte cocultures on two sides of the membrane. Not only did we observe the expression of endothelial markers on ADSCs triggered by the pericyte-mediated signaling,

but we also noticed a close-to-orthogonal arrangement of pericytes, which is consistent with their *in vivo* function of *wrapping* the microvessel from the outside [72]. In another study by Ryu and colleagues, the authors cocultured mesenchymal stem cells (MSCs) atop an ultrathin and highly permeable substrate in a close proximity with cardiomyoblasts [76]. Upon analysis, they found an enhanced expression of cardiac transcription factors in MSCs, which was absent in the case of low permeability polymer membranes available commercially. The permeability of the cell-culture substrate is even more important while studying a leaky barrier. For instance, in hepatic circulation, hepatocytes and sinusoidal endothelial cells are separated by a highly porous and permeable membrane (Table 1.1) to allow for easy trafficking of drugs and their metabolites across the blood-liver barrier.

Apart from being permeable, the substrates also need to be thin, preferably with a thickness similar to that of the physiological barriers. Basement membrane is $\sim$100 nm thick, and hence the substrate (membrane) used for cell culturing should be equal or lesser in thickness to reduce any membrane-limited transport of proteins and nutrients. The capillary endothelial cells in the brain and central nervous system are surrounded by foot processes extended by astrocytes, which essentially requires a direct physical contact between the two cell types. Thus, a thin membrane for coculturing is required to recreate this structural configuration *in vitro*. Having a thin membrane is also important for studying neutrophil chemotaxis across the endothelial-ECM barrier to avoid extra migratory distances for neutrophils.

Presence of Shear Stress

One of the most important factors that determines the fate of endothelial cells is the presence of shear stress during growth and maturation. Endothelial cells are mechanotransducers that can convert the mechanical stimuli into intracellular signaling cascades that can have significant effects on their functions including gene expression, growth and remodeling, apoptosis, migration, and permeability [79]. Mechanotransduction begins at the apical surface, which experiences shear stress and transmits the signals downstream to alter the cytoskeletal structures that link ECs with their adjacent cells and with their substrate. The most noticeable change is the reorganization of the cell orientation along the axis of shear stress, also known as 'alignment' phenomenon. In a classic study by Flaherty et al., the authors excised a piece of canine artery along the long axis, re-closed the open artery in the perpendicular axis and sutured it back in the animal. The cells in the sutured vessel significantly realigned in the direction of flow as estimated by measuring the ratio of major to minor axes [80]. After this study, the alignment phenomenon has been thoroughly observed in numerous studies published *in vivo* and *in vitro*, and is often considered as a hallmark of shear-conditioned endothelial cultures.

In addition to the ability of shear stress to align the endothelial cells in the direction of flow, the most significant effect of shear stress is in its ability to enhance the barrier properties of the endothelium both *in vivo* and

in vitro [81]. In our lab, we have found increased expression of glycocalyx layer with enhanced mechanical properties when HUVECs are subjected to shear stress for 24+ hours [Waugh Lab, unpublished data]. Shear stress also plays a key role in the formation and remodeling of tight junctions [82] and adherens junctions [83], and in reducing apoptosis and mitosis that lead to leaky junctions [81]. Further studies by King and colleagues have shown that shear stress has cooperative effects with the substrate stiffness. Compliant substrates enhance the shear-mediated alignment of endothelial cells and increase the barrier integrity *in vitro* [69].

Furthermore, not only are ECs capable of responding to the shear stress, they are also able to differentiate in response to the types of flow they are subjected to: laminar, oscillatory, and disturbed flow. While a net laminar flow is known to inhibit cell proliferation and trigger cell elongation in the direction of the flow, oscillatory flow with zero net directionality has no inhibitory effects on cell growth [79]. In the case of disturbed flow, the cells fail to show elongated morphology, but instead develop pathological lesions as in the case of atherosclerosis [84]. This makes sense in the light of the facts that these atherosclerotic plaques are predominantly formed at the bifurcation of large vessels, where the flow is disturbed. In summary, laminar shear stress is crucial for the physiological growth of microvascular endothelial cells, and the ability of an *in vitro* system to condition ECs under physiologically relevant shear stress is an important characteristic that needs to be incorporated in the design and development of new platforms.

1.4.2 *In Vitro* Platforms: Requirements and Considerations

Apart from the above mentioned substrate requirements, there are many other factors that need to be considered while designing a superior microvessel mimetic platform for *in vitro* studies. The substrate, along with being porous/permeable, (appropriately) compliant, and biocompatible, should preferably be optically transparent to allow for live phase imaging without fluorescent labeling. This is particularly important for neutrophil and other leukocyte migration studies because transmigration events can be observed and quantified in phase contrast imaging. Being able to capture the live dynamics of neutrophil-endothelial interactions is key to enhance the utility of the *in vitro* platforms. Most of the polymer membranes that are porous and available commercially for cell culture applications have significant autofluorescence, and lack sub micron features resulting in reduced optical transparency due to diffraction-mediated losses. Second, the substrate must support coculture applications, i.e. be amenable with various (micro)fabrication approaches to develop an operational (micro)fluidic system around the substrate. Since most of the fabrication approaches employ silicon or other inorganic materials, using organic materials will require additional functionalization steps to enable device fabrication. In addition to coculture, the presence of dual compartments will also facilitate the addition of ECM, which plays an important role in physiological growth and development of the endothelial cells.

As discussed earlier, the *in vitro* system must be capable of conditioning ECs under shear stress, preferably for long durations (hours to days) of cell culturing. While syringe pumps typically provide a smooth flow devoid of any pulsations, they cannot sustain longer durations due to defined syringe volumes. Peristaltic pumps can address this issue, but might create oscillatory flow patterns absent in microvasculature. Similarly, the geometrical design needs to be carefully optimized for reduced flow requirements to avoid unnecessary volumes of (expensive) cell culture media. A related parameter that needs to be considered in designing the flow chambers is the pattern of flow streamlines generated atop the endothelial cells. Fluidic parameters such as 'forward and backward' facing steps result in incompletely developed flow, and (oscillatory) disturbed flow patterns can cause pathological lesions. To avoid such design ramifications, the fluidics need to be modeled mathematically and appropriate design parameters needs to be implemented accordingly.

Finally, the platform needs to be equipped with *in situ* permeability measurement tools. There are, broadly speaking, two different ways to quantify endothelial permeability *in vitro* - tracer methods that employ fluorescent (macro)molecules and dyes, and electrical methods that record ionic permeability in the presence of an electric field. Each of these methods have their distinct benefits and limitations. Chemical methods rely on the diffusion/transport of fluorescent albumin or dextran of different molecular weights through the endothelium, and estimate the permeability by mea-

suring the increase in the fluorescent signal using fluorescence spectroscopy. The choice of macromolecule for permeability studies greatly improves the scope of application. Macromolecules can be used to determine the size of the 'opening'; for example the difference in the permeability values of 4kDa vs 10 kDa vs 70kDa dextran can be very informative in understanding the nature of pores present in the endothelial monolayer. Combining dextran with albumin tracers, one can further map the transcellular transport (albumin transport) in addition with the paracellular route (dextran transport). In order to obtain time-dependent data points, one has to continuously collect the fractions from the receiving chamber, and replenish it with the same amount of control media. This process provides limited temporal resolution and involves invasive interventions (fluid injections/aspirations) that might disturb the diffusion equilibrium within the apical and basal compartments. These problems are further aggravated for microfluidic devices, where the device volumes are often less than the minimum amount required for standard plate readers ($\sim$50 μl for a 96 well plate). Also, because these assays are fluorometric, they are typically end-point measurements, and not suitable for multiple studies in long term cultures.

Electrical methods, on the other hand, provide a non-invasive method to estimate the monolayer permeability by injecting a small magnitude of alternating current (I) and recording the corresponding potential drop (V) to calculate the trans endothelial electrical resistance (TEER) using Ohm's law (TEER=V/I). Continuous data acquisition is possible because low frequency

AC in the micro-ampere range does not harm the biological tissues. This allows us to capture the transient changes in monolayer permeability, such as those caused by neutrophil transmigration. Furthermore, advanced versions of electrical methods such as impedance spectroscopy allow for measuring cell confluency, cell-substrate gaps, and other electrochemical parameters that are difficult to measure otherwise [85]. However, as discussed earlier, electrical methods demand the fabrication and assembly of biocompatible electrodes within the main device. While there are standalone TEER measurement instruments, integrating the microsystem with these instruments can be a challenging engineering problem.

Thus, while both electrical and chemical assays have their unique advantages, the best strategy is to adopt a complementary combination of both these approaches for a robust readout of endothelial permeability [86]. An *in vitro* platform that can allow for both these assays in parallel is very beneficial for studying microvessel biology.

1.4.3 Existing Platforms and Technologies

In vitro Platforms for Microvessel Studies

Numerous platforms and devices are available commercially and have been published in the literature that focus on studying microvessel biology *in vitro*. Advancement in the fields of microfabrication and microelectromechanical systems (MEMS), polymer/material science, 3D printing, and rapid proto-

typing technologies have made it possible to design sophisticated systems addressing custom requirements [87]. An exhaustive list of these devices is beyond the scope of this thesis, and we present, briefly, the basic concepts and applications of the commonly used available systems. Fundamentally, these *in vitro* systems can be mono-compartmental or bi-compartmental depending on their design. While the single-compartment devices are easier to assemble and operate, they don't allow for coculture, chemotaxis assays, and 3D cell migration. In devices with two compartments, scaffold-less platforms have been developed that recreate the 3D environment without the use of a membrane [88]. In these devices, the extracellular matrix (ECM) can be patterned using appropriate methods that is responsible for the mechanical compartmentalization. Template-based patterning is the straight forward approach, where a 3D scaffold is used to polymerize ECM (mainly collagen 1 gel), and then the template is removed to yield micro-channels for cell seeding [88]. Alternatively, collagen gel is polymerized surrounding a simple optical fiber or a thin needle, and after gel polymerization, the needle or the fiber is removed and ECs are seeded inside the gel [89]. The devices are rotated for uniform seeding, and the microchannels can then be perfused with media to grow ECs under shear stress. Similar approaches have been implemented using polydimethylsiloxane (PDMS) gels in place of collagen [90].

In an advanced application of sacrificial template-based patterning, 3D printing is used to create a scaffold in the shape of a bifurcating microvessel networks, which can be then used to seed cells and recreate more physiolog-

ical branching patterns. Bhatia and colleagues used carbohydrate glass as a base material for 3D printing the scaffold that can be dissolved upon ECs' seeding, adhesion and maturation [91]. Another similar approach to create these networks is to use soft-lithography to first create the patterns using appropriate photoresist, and then using the resulting mold to cast collagen gels for cell seeding [92]. Both these approaches provide a 3D environment for endothelial growth and also recreate the necessary ECM composition that provides ECs with appropriate basolateral signaling. Unfortunately, these 3D printing and lithography based platforms are not suitable for chemotaxis assays and also require sophisticated instrumentation to achieve the fabrication. Yet another approach to achieve the growth of ECs in collagen gels exploits the self-assembling properties of endothelial cells in a 3D matrix like environment. ECs are suspended in gelatin spheroids and then embedded within collagen gels. After the gelatin is dissolved, the endothelial cells assume a spherical shape and merge with adjacent spheroids (due to surface tension) to form a conduit of endothelial cells within collagen gel [93]. This self assembly approach is simpler to execute but is limited by sizes of the gelatin spheroids, typically producing microchannels wider than 500 microns. In another study by Dalecki and colleagues, the authors embedded ECs in collagen gel of optimized concentrations, and subjected the structures to ultrasound standing waves [94]. The cells responded to the pressure nodes and antinodes forming regions with high cell concentrations where they could proliferate and form networks and branches. In our lab, we have attempted

to create dissolvable silicon filters in the presence of acidic pH generated by cell metabolism, and use these thin films as scaffold-less platforms for cell culture applications [71].

Other than these published systems, many commercial platforms are also available that allow for barrier tissue studies (with or without a membrane) such as EmulateBio (Boston, MA), MIMETAS (Leiden, Netherlands), Hesperos Inc. (Orlando, FL), Nortis Inc. (Woodinville, WA), CN BioInnovations (Hertfordshire, UK), SynVIVO (Huntsville, AL), ibidi GmbH (Munich, Germany) etc. These systems employ advanced 'assembly line' fabrication approaches and facilitate high throughout studies, but often at the expense of reduced physiological relevance. For instance, while 'Emulate' and 'Hesperos' platforms used membranes for dual compartmentalization, they are limited by their choices in using thick polymer membranes. 'MIMETAS' platforms allow for adding ECM gel and study permeability assays, but they are not suitable for shear stress experiments. 'ibidi' platforms allow for shear stress but are mono-compartmental and require expensive supporting equipments for operation. 'CNBio' and 'Nortis' allow for multiplexing but also require expensive and dedicated setups and have single chambers for cell culture. Thus, while the commercial platforms aim to address the limitations of the published technologies, they fail to achieve desired functionalities *in toto*.

In vitro Platforms for Permeability Studies

Development of *in vitro* platforms to study barrier tissues has a long history, and some of the earliest studies were published in 1940s/50s by Hans Ussing and others. In his seminal study, Ussing et al. suspended a thin layer of frog epithelial tissues across two compartments with isolated fluid compartments, and each compartment had a pair of electrodes - one for current injection, and other for voltage sensing [95]. By applying a known potential and measuring the short circuit, he was able to estimate the ionic permeability of frog epithelia. This technique was later commercialized and the devices used for measuring permeability are commonly known as Ussing Chambers. The compact version of these chambers was developed in 1970s and 80s. These included plastic buckets hanging over the wells of a multi-well tissue culture plate, hence, known as 'transwell inserts' or simply 'transwells'. Earlier iterations of these designs included an amniotic membrane to grow the cells on a porous substrate [62], but the modified versions (still being used today) consist of polymer track-etched (TE) membranes made out of polycarbonate (PC) or polyethylene terephthalate (PET) materials. These systems have been widely used for the last 3 decades and numerous adaptor systems have been developed to measure the permeability of the endothelial/epithelial cells growing on the suspended membrane filters. The 4-probe electrodes for TEER measurement are immersed in either side of the transwell chamber for resistance measurement, commonly known as 'chopstick'

electrodes (STX2, World Precision Instruments, Sarasota, FL). Due to the non-uniformities in the electric field created, the resistance values are often overestimated in this setup [85]. An alternate version consists of a standalone chamber with two embedded electrodes in the base of the chamber and two electrodes located in a screw-on cap (EndOhm Chamber- WPI Inc., Sarasota, FL). This configuration allows for more uniform electric field lines and better accuracy. The TEER value is calculated by multiplying the raw resistance values with the membrane area. To gain further information about cellular barrier properties, impedance spectroscopy instruments have been commercially manufactured, including the ECIS platform (Applied Biophysics, Troy NY), cellZScope (nanoAnalytics GmbH, Munster, Germany), xCELLigence (ACEA Biosciences, San Diego, CA). Also, numerous studies have been published that use either single frequency TEER measurements or impedance spectroscopy for permeability assessments in barrier tissues [96–108].

Given the abundance of the literature in the field of *in vitro* platforms for permeability research, one question sensibly arises: *what are the unmet needs of the scientific community, why so many systems, and what's the need for yet another system?* As mentioned earlier, the basic requirements from an *in vitro* system for endothelial biology studies are: 1) compliant, permeable and transparent substrate, 2) ability to introduce relevant shear levels, 3) non-invasive method to assess barrier permeability, 4) 3D microenvironment for neutrophil migration and chemotaxis, and 5) robust, reproducible, and relatively inexpensive. While the state-of-the-art systems can combinatori-

ally achieve all these desired aspects, there doesn't exist a single integrated system that is capable of simultaneously achieving all of them. This unmet need is the key motivation of the work presented in this thesis. Towards this end, we employ advanced silicon nanomembrane technology to engineer an integrated microvessel mimetic (MVM) platform to study neutrophil activation in an acute inflammatory response. The following sections describe the technology, its evolution, its current status, and our efforts in building this microsystem.

1.5 Silicon Nanomembranes

Silicon nanomembranes are a new type of ultrathin nanomaterials discovered and developed at University of Rochester. The first generation of these materials were serendipitously discovered during silicon manufacturing processes, but later on were characterized for their exceptional charge- and size-based filtration and separation properties [109]. The freestanding nanomembranes consist of porous nano crystalline Silicon, henceforth referred to as pncSi. Molecular level thinness and the absence of tortuous paths make these membranes ideal for filtering applications. Their fabrication process can further be modified to fine-tune the pore sizes and porosities. A unique characteristic of these membranes is their 1:1 aspect ratio, i.e. the pore diameter and their height (or membrane thickness) are almost identical. Due to this feature, time-scales for molecular diffusion across these membranes are negligible.

The entire fabrication process is very elaborate (Figure 1.2), and has already been published [109]. Briefly, a 300 micron bulk silicon wafer is coated with thin layers of oxide that define the inactive area for further etching. Photoresists are deposited to protect and demarcate the etched regions. After patterning, a 3-stack layers of 40 nm SiO_2/ 30 nm amorphous Si/ 40 nm SiO_2 are deposited on the bulk silicon. Rapid thermal annealing of these layers at a rapid ramp rate of 100°C/s up to 1000°C is achieved using a susceptor for uniform heating. This annealing transforms the amorphous silicon into crystalline structure, and also leads to the formation of void pores, which are formed due to the entrapment of (argon) gases sandwiched within the oxide layers. After pore formation is complete, the backside is released using ethylenediamine pyrocatechol (EDP) etch to remove the bulk silicon, and buffered oxide etch (BOE) to remove the oxide films to expose the freestanding window. This process is performed at a wafer scale to produce hundreds of these silicon membrane 'chips' after fabrication, as shown in the bottom-right panel of Figure 1.2. Note that these steps represent the fabrication of first-generation silicon nanomembranes (pncSi), and the current family of nanomembranes involve more advanced manufacturing processes.

1.5.1 Applications of Silicon Nanomembranes for Tissue Barrier Models

Silicon nanomembranes have been used in a variety of applications since their discovery, including bioseparations and filtration [110–115], hemodialy-

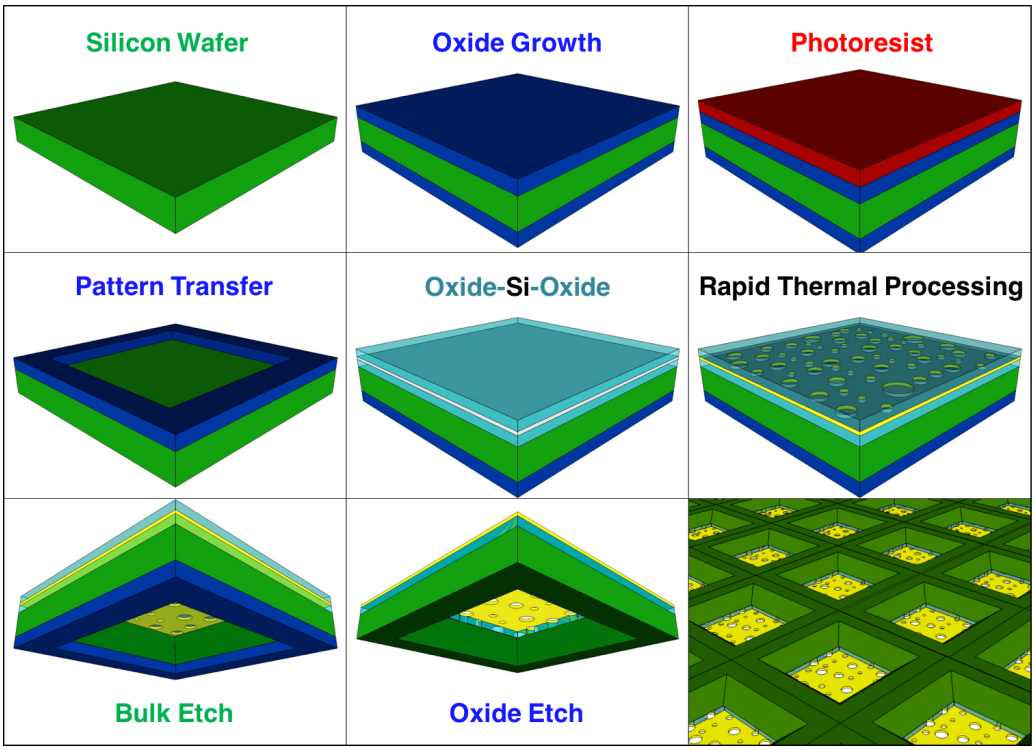

Figure 1.2: Fabrication of Silicon Nanomembranes: Major steps involved in the manufacturing of pncSi membranes [109]. Refer to text for further description. Schematic courtesy: Dr. Dave Fang.

sis [116, 117], extracorporeal blood purification [118], electrochemistry [119–121], biosensing [122], electron microscopy and tomography [123], rapid cell labeling [124], and bacterial infection studies [125]. However, the most extensive applications of these materials, due to their biocompatibility and superior imaging characteristics, have been in the area of endothelial cell biology to study different aspects of cell biology and barrier models.

Biocompatibility Studies: Agrawal et al. first demonstrated the biocompatibility of these materials and their application for barrier studies. The

thinness of silicon nano-films, and their susceptibility to dissolution under acidic conditions (as created by cell metabolism) present an unique opportunity for scaffold-less coculture applications [71].

TEER Measurement Studies: Khire and Nehilla et al. used pncSi membranes to study blood brain barrier by establishing monocultures and cocultures of brain endothelial cells with and without brain astrocytes [77] (also unpublished data, McGrath Lab). Figure 1.3 is a representative confocal image highlighting the thinness of the porous membranes for coculture applications. This was also the first study to use pncSi membranes to characterize tissue permeability and included development of the first iterations of *in vitro* microsystems to measure TEER using silicon nanomembranes. An important contribution of the work was the development of a quantitative model to understand the effects of different membrane geometries on TEER values that enables a robust way of interpreting and comparing TEER values from different systems.

Neutrophil Chemotaxis and Shear-stress Studies: Chung et al. used these membranes to achieve shear-free chemotaxis of neutrophils allowing the separation of mechanical and biochemical factors for influencing neutrophil migration [124]. This study demonstrated the ability to develop a mechanically robust microfluidic platform around silicon nanomembranes, and the ability of the membranes to withstand higher levels of shear stress.

Scalable Manufacturing: Further advancement in silicon fabrication processes were responsible for the manufacturing of large sheets of *glass-like*

membrane, also known as 'lift-off' membranes. Carter et al. were able to show the biocompatibility of these new class of materials, and also demonstrated the advantages of ultrathin materials in coculture through confocal imaging [73]. Thus, the silicon nanomembrane technology has found applications in studying barrier tissues and has been instrumental in addressing fundamental questions surrounding endothelial biology. In the next section, we discuss the active research projects that involve the fabrication of microsystems using silicon nanomembranes that are specifically used to study the permeability of blood-brain barrier (BBB) *in vitro* for different applications.

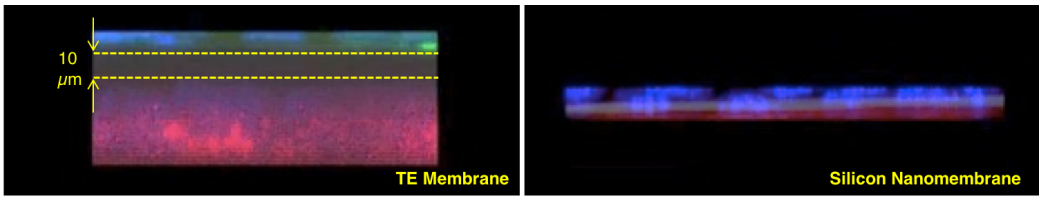

Figure 1.3: Confocal Imaging on Silicon Nanomembranes: Representative confocal images of two different cell types grown on the apical and basal side of a polymer track etched (TE) membrane (left), and silicon nanomembrane (right). Image Courtesy: Dr. Barrett Nehilla, McGrath Lab unpublished data.

1.6 *In vitro* Blood-Brain Barrier (BBB) Models

The brain and central nervous system (CNS) are two of the most important and sensitive organs of the human body with significantly different defense mechanisms than other tissues. The blood-brain barrier (BBB) is fundamentally constituted of 3 three main barriers: brain endothelial cells in the parenchymal vessels, the choroid plexus, also known as the blood-cerebrospinal fluid (CSF) barrier, and the arachnoid epithelial lining beneath the dura matter [126]. However, since the brain endothelium presents the largest surface area of all the three barriers, it plays a key role in monitoring the trafficking of substances and cells across the brain. Henceforth, BBB will be used to refer this barrier only. The BBB is composed of four main elements: 1) microvascular endothelial cells forming the inner lining of the blood vessels, 2) pericytes, 3) basement membrane secreted by endothelial cells and pericytes and, 4) end-feet projections of astrocytes, glial cells, and neurons that encapsulate the exterior of the blood vessels [127]. Like the ECs of peripheral circulations, brain ECs also exhibit multiple modes of physical barrier, as discussed above, such as endothelial glycocalyx, tight junctions, basal lamina etc. However, unlike other ECs where the formation of intercellular junctions renders effective pore size of $\sim$3 nm [19], tight junctions in brain ECs form a pore size of only 0.4 nm [128]. This exceptionally tight barrier provides significant impedance to otherwise passively

diffusing molecules, and a significant amount of molecular trafficking happens through transcellular pathways via absorptive- and receptor-mediated transcytosis (AMT/RMT) [129].

Breaching of the BBB is responsible for various debilitating neurodegenerative diseases including multiple sclerosis, Alzheimer's, Parkinson's, amyotrophic lateral sclerosis (ALS) etc. [128]. Because of the critical role played by BBB in maintaining homeostasis, a variety of *in vivo* and *in vitro* models have been developed to understand drug-delivery mechanisms, immune cell trafficking, and other pathophysiological events that affect brain occurring during different diseases. One focus of the work in this thesis is to advance the existing *in vitro* platforms for BBB research. This has been achieved by the development of two platforms with similar design and structures - first, to facilitate and image immune cell activation during inflammatory conditions and second, to observe the transport (or lack thereof) of nanoparticles across BBB under normal conditions. The following two sections discuss these studies briefly.

1.6.1 *In Vitro* Models to Study Immune Cell Activation

Inflammatory diseases such as multiple sclerosis (MS) are characterized by the excessive trafficking of T-cells across the BBB. Hence, therapeutic strategies against MS have been focused on developing inhibitory molecules to reduce the trafficking of T-cells across the BBB [130]. Unfortunately, the inhibition of T-cell activation leads to immunosuppression, giving rise to col-

lateral disorders such as progressive multifocal leukoencephalopathy (PML), which is strictly observed in human species due to the activation of the dormant JC virus [131]. Due to the inability to study these side-effects effectively in animal models, numerous anti-inflammatory therapies have failed in human clinical trials despite positive results in animal models [132]. Thus, there is a gap between human therapy and animal model testing that needs to be bridged for successful preclinical studies that essentially demand robust *in vitro* studies focusing on cells and tissues derived from human origin. Towards this end, Cecchelli and colleagues developed an *in vitro* model that uses umbilical cord blood-derived $CD34^+$ hematopoietic stem cells in conjunction with bovine pericytes. When $CD34^+$ cells were cocultured with the pericytes, they observed the differentiation of $CD34^+$ cells and the expression of brain endothelial markers with enhanced tight junctions, elevated TEER values, and reduced macromolecular permeability [133]. The authors, therefore, named these cells brain-like endothelial cells (BLECs). Further studies also demonstrated the application of BLECs to study the interaction of immune cells with human BBB [134], making them an ideal candidate for *in vitro* studies of BBB.

Despite the obvious advantages of these stem cell derived BBB cell cultures, the potential of these cells has not been realized due to the lack of equally competent engineering platforms to advance this *in vitro* model. Most of the studies with BLECs were executed using the commercial transwell inserts under static conditions. As discussed earlier, while these platforms

offer convenience, they suffer from poor imaging, lack of shear-conditioned endothelium, and also demand *macro*-fluidic volumes for studies. The last aspect is critical for studies that use cerebrospinal fluid (CSF) because CSF can be obtained only in trace amounts. Furthermore, it has been shown that physiological levels of shear stress are essential for the efficient diapedesis of T-cells (similar to the neutrophil diapedesis) [135]. Thus, there has been an unmet need to develop flow-systems featuring BLECs for T-cell studies under dynamic conditions that allow for live-imaging of activated T-cells transmigrating across BBB to enhance our knowledge of MS pathology. To address this issue, we employed silicon nanomembrane technology to engineer microfluidic systems to recreate acute inflammation *in vitro*, and observe the interactions of T-cells with BLECs under these conditions. Using the modified versions of the microvessel mimetic (MVM) platform developed for neutrophil studies, we were able to 1) grow and characterize BLECs on silicon nanomembranes, 2) achieve equally reduced permeability values as observed with the original BLEC studies [133] but on silicon nanomembranes, 3) facilitate T-cell chemotaxis on TNF-α activated BLECs under shear conditions, and 4) observe and quantify various steps involved in the emigration cascade. Further details are elaborated in Chapter 4.

1.6.2 *In Vitro* Models to Study Nanoparticle Translocation Across BBB

Due to the unique structural properties of the BBB, drug-delivery mechanisms to the central nervous systems differ fundamentally from those that are effective in other tissues in the body. One of the most widely used strategies to achieve drug delivery in the brain is by the use of nanoparticles (NPs). In the past, multiple studies have tried to develop size- and charge-based modifications of NPs to enable their permeation across BBB [136, 137]. Nanoparticles need to be functionalized with different molecules to make them amenable for endocytosis and absorption across brain endothelial cells [138, 139]. Despite the advancements in polymer science that enable these delivery options, the underlying mechanisms that promote the transport of nanoparticles remain to be completely understood and need further study [Hudecz and Khire et al., Manuscript under review]. This understanding is crucial for more targeted and efficacious drug delivery across BBB. Along with the efficacy of NP delivery, an equally important question that needs to be addressed is the safety and (non-)toxicity of the translocated NPs. We believe that the ability to detect the translocated NPs will be a significant advancement in addressing this question. These experiments demand a robust *in vitro* platform that can support the growth of BBB and provide a spatiotemporal map of NPs as they are translocating across the BBB. To achieve this, high-resolution optical microscopy can be employed to detect and locate the position of the NPs in real-time. Unfortunately, the

commercially available polymer systems, in addition to creating large separations between ECs and cocultured cells because of their 10 μm thickness, are also auto-fluorescent, making high resolution imaging more difficult.

Silicon nanomembranes carry the potential to provide physiologically relevant thinness during coculturing (Figure 1.3), thus, allowing for more representative transports of NPs across BBB *in vitro*. However, the existing microsystems that use silicon nanomembranes require long working distances for optical imaging, and this also limits the ability to use high-resolution confocal imaging, which requires short working distances. The work presented in this thesis aims to address this concern. We have successfully built a microfluidic system that is used for coculturing human cerebral microvascular endothelial cells (hCMEC/D3) and normal human astrocytes (NHA) in close proximity of each other. This coculture model demonstrated lower permeability than their counterparts in the transwell system. Another unique feature of this system is its exceptionally low working distance of only 50 microns to perform high-resolution 3D imaging of 100 nm (in diameter) carboxylated polystyrene NPs as they translocate through the BBB. Not only were we able to confirm their (obvious) inability to cross the BBB as observed by their entrapment in the endothelial layer, but we were also able to capture rare events where NPs were able to actually cross the BBB. This ability to study the translocation of the BBB under live conditions will be beneficial in designing NPs with characteristics to make them more accessible to the CNS. Further details are elaborated in Chapter 5.

1.7 Thesis Overview

Chapter 2 describes the mathematical modeling of the electrical behavior of the microsystem featuring silicon nanomembranes that are used for TEER measurement. This work lays down the foundation of methods and principles used for TEER measurement, and provides an experimentally-verified algorithm to analyze and interpret TEER values from custom *in vitro* systems. Chapter 3 describes the microvessel mimetic (MVM) platform to model and study acute inflammation, its effects on endothelial cells and neutrophil activation, and highlights the beneficial effects of regulating subendothelial migration of neutrophils in reducing endothelial permeability. This chapter elaborates, in depth, the engineering aspects and nuances of the MVM platform-construction and operation, and serves as a basis for the work presented thereafter. Chapters 4 and 5 demonstrate the utility of this MVM platform for BBB studies, particularly to image live events of T-cell migration and NP translocation across the BBB respectively. Finally Chapter 6 concludes the work, presents the overall summary of the project, including its achievements and potential shortcomings, and provides insights on future work in expanding the MVM platform for advanced biomedical applications.

Chapter 2

Finite Element Modeling to Analyze TEER Values Across Silicon Nanomembranes[†]

2.1 Abstract

Silicon nanomembranes are ultrathin, highly permeable, optically transparent and biocompatible substrates for the construction of barrier tissue models. Trans-epithelial/endothelial electrical resistance (TEER) is often used as a non-invasive, sensitive and quantitative technique to assess barrier function. The current study characterizes the electrical behavior of 'Transwell®' devices featuring silicon nanomembranes by measuring the TEER. In conventional practice with commercial Transwell® systems, raw resistance values are multiplied by the area of the membrane supporting cell growth to normalize TEER measurements. We demonstrate that under most circumstances this multiplication does not 'normalize' TEER values as is assumed, and that

[†]Reprinted by permission from RightsLink Permissions Springer Nature Customer Service Centre GmbH: Springer Biomedical Microdevices, [77], Copyright 2018

the assumption is far worse if applied to nanomembrane chips with a limited active area. To compare the TEER values from nanomembrane devices to those obtained from conventional polymer track-etched (TE) membranes, we develop finite element models (FEM) of the electrical behavior of the two membrane systems. Using the FEM and parallel cell-culture experiments on both types of membranes, we successfully model the evolution of resistance values during the growth of endothelial monolayers. Further, by exploring the relationship between the models we develop a 'correction' function, which when applied to nanomembrane TEER, maps to experiments on conventional TE membranes. In summary, our work advances the utility of silicon nanomembranes as substrates for barrier tissue models by developing an interpretation of TEER values, and a generalizable method for the comparison of TEER values between alternative devices and membranes.

2.2 Introduction

There is a need for cell culture systems that faithfully mimic the physiological response of human tissues. These systems aim to overcome enormous inefficiencies in the drug discovery pipeline [140] by developing platforms that have higher throughput than existing animal models, and are more reliable predictors of human tissue behaviors [59]. There are now dozens of examples of microphysiological systems (MPS) or 'tissue chips' that use artificial membranes to pattern cells as barriers between apical and basal

compartments of the device [71, 97, 101, 103, 107, 141]. Such designs allow investigators to create mimetic devices that can be used to understand the role of barrier tissues in diseases and to study the permeation of pharmacological drugs to underlying tissue. Despite the ubiquity of membranes in MPS devices, relatively little attention has been paid to the role that membrane properties play in the tissue models. In principle, the permeability, pore size, thickness, stiffness, and surface chemistry of an artificial membrane can each affect the accuracy of a physiological mimic. The need for optically transparent membranes that enable imaging assays complicates the situation. The most popular forms of artificial membrane in MPS systems have been track-etched polycarbonate (TE-PC) or polyethylene terephthalate (TE-PET) membranes. These membranes are available stand-alone and also are the component of the commercial 'Transwell® inserts' (hereafter simply referred as 'transwell' or 'transwell inserts') that have been used for decades in biomedical research. The membranes are much thicker (∼10 um) than physiological barriers and perform poorly in microscopy because of light scattering by pores. 'Transparent' versions of these membranes feature a dramatic reduction in porosity ($< 1\%$) with low pores:cell ratio and thickness more than 10 microns [107].

Our laboratories have pioneered the development of ultrathin silicon-based membranes for a variety of applications including cell culture [68, 71–73, 109, 141, 142]. The thickness of these 'nanomembranes' is between 15 nm and 400 nm with porosities as high as 30%. Their thinness makes these

nanomembranes far better mimics of native basement membranes (100 nm thickness *in vivo*) [24, 26] than TE membranes. Also, these nanomembranes exhibit a permeability to small molecules that is indistinguishable from free diffusion [111, 112]. Silicon nanomembranes also have glass-like optical qualities enabling superior imaging, and the silicon platform enables facile and robust bonding to silicone/polydimethylsiloxane (PDMS) materials using oxygen-plasma and UV-ozone treatments that is difficult to achieve using the chemically inert TE-PET/TE-PC membranes. Thus, silicon nanomembranes are a superior choice to TE membranes for the construction of barrier tissue models *in vitro*.

This report focuses broadly on the assumptions, conventions and sources of errors involved during the interpretation of TEER values from customized microfluidic systems for studying barrier properties, and more specifically on one of the challenges involved in the use of silicon nanomembranes to study barrier function. We present a brief background on *in vivo* methods for measuring vascular permeability from which the conventions used for *in vitro* measurements originate. Using Finite Element Analysis (FEA), we then develop electrical models of 'transwell' systems employing silicon nanomembranes and conventional TE membranes. The modeling results demonstrate that the limited active (permeable) areas of silicon nanomembranes add significant baseline electrical resistance even though the membranes themselves add negligible resistance. Analyzing the TEER values from parallel cell-culture experiments of brain endothelial cells (bEnd.3), we illustrate how

the FEA models relate nanomembrane-TEER values to values from TE-membranes. This conversion is needed because the abundant literature from traditional device-membrane formats have resulted in rubrics that are often used to interpret barrier function. Using the model conversion we show that bEnd.3 barrier values are comparable when grown on silicon nanomembranes vs. TE membranes, despite large differences in the raw resistance values.

2.3 *In vivo* Characterization of Endothelial Permeability: Standards and Conventions

The conventions for reporting TEER values in cell culture studies originate in classic experiments on blood vessels in the brain of live frogs [143, 144]. *In vivo* electrical impedance measurements of the frog blood-brain-barrier is a gold standard in the field of (cerebral) vascular biology [143]. In these experiments, two pairs of electrodes are introduced in the isolated superficial brain capillary of the live animal, one pair for current injection and other for recording the changes in electric potential. The current pulse travels through the solution (blood) within the capillary, while simultaneously leaking through the porous capillary wall. This geometry (Figure 2.1) is analyzed using traditional cable theory [145].

Briefly, according to cable theory, the signal decay follows a simple exponential assuming the ionic permeability is constant along the measured

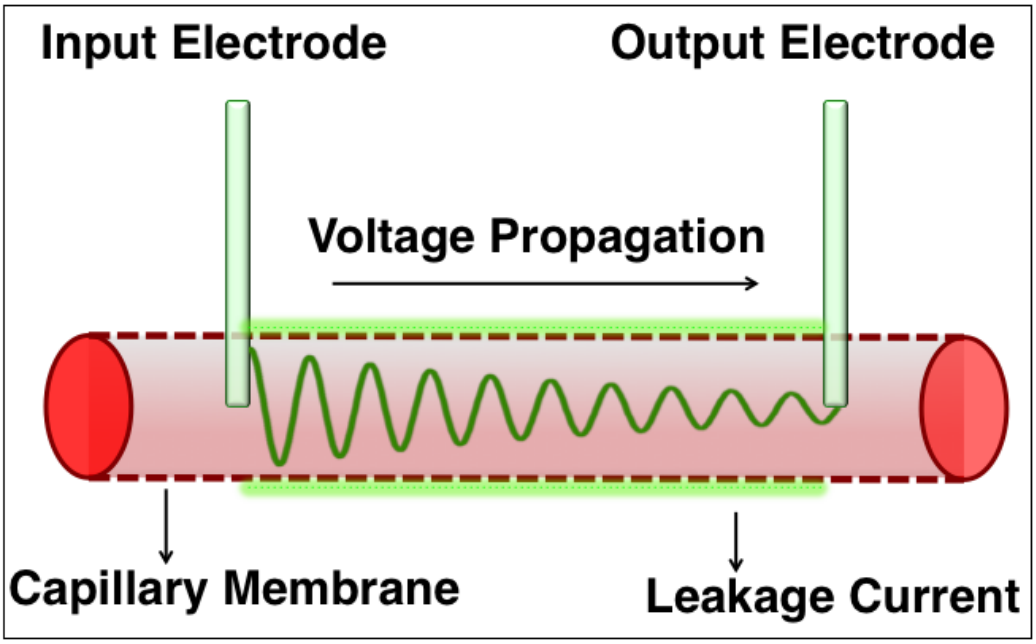

Figure 2.1: *In vivo* measurement of capillary resistance: The voltage drop across the two electrodes can be used to understand the ionic permeability of the blood vessel. The magnitude of signal lost is proportional to the area of the membrane between the electrodes, the electrical conductivity of the membrane bilayer, and the electrical resistivity of blood. For the sake of visual clarity, only one set of electrodes has been shown.

vessel:

$$V(x) = V(0)e^{(-x/\lambda)} \tag{2.1}$$

where x is the distance from the source electrode along the axis of the capillary, and λ is the length constant that described how rapidly the potential decays. The membrane resistance R_m is related to the internal resistance of the capillary r_i through the length constant according to:

$$R_m = r_i \cdot \lambda^2 \cdot 2\pi a \tag{2.2}$$

where a is the radius of the capillary [143, 145]. r_i is determined by dividing the resistivity of the blood by the capillary cross-section area (hence Ω/cm). Thus R_m is reported in $\Omega \cdot cm^2$ (and not *just* Ω). This is appropriate since the loss of ionic species occurs *over* the surface of a capillary-wall and not *at* a singular location.

In vitro measurements of cellular barrier properties also employ 4-probe electrodes for the measurement of electrical resistance. Typically a low frequency, low amplitude alternating current, I, is applied across the cell-membrane barrier, and the corresponding potential drop, V, is recorded. The resistance, R, is calculated using Ohm's law: $R = V/I$, where root mean square (RMS) values are used for V and I. However, since transwell inserts are commercially available in different sizes with membrane area ranging from 0.33 cm^2 to 4.7 cm^2, the resistance values are 'normalized' by multiplying

the resistance with the effective membrane area, thus reporting final TEER in $\Omega \cdot cm^2$. This normalization gives transwell TEER measurements the same units as *in vivo* measurements of vascular membrane resistance, even though the two experimental set-ups use different operating principles. Thus, the use of electrical resistance values from living frog brain capillaries (or other similar *in vivo* studies) as a gold standard for tissue culture measurements on endothelial cells is questionable. The practice of normalizing tissue culture resistance values with the membrane area enables comparisons between measurements in different sized transwell systems only if the current density remains uniform across the entire device geometry as required for the straightforward application of Ohm's law. We illustrate that this assumption is not true for most transwell set-ups because of non-uniform current distribution across the membrane. Furthermore, this assumption is clearly violated for silicon nanomembranes, which have a limited active membrane area near the center of an impermeable chip. Naive 'normalization' by multiplying resistance with area results in erroneous TEER values, and make it impossible to compare barrier function between different systems. Therefore, we have developed a mapping or 'correction' function that allows for the conversion of TEER values obtained from silicon nanomembranes' systems to the commonly reported values for commercial transwell systems. In this way, TEER data acquired with nanomembranes can be related to the rich literature on *in vitro* barrier function that has been built almost exclusively using commercial transwells.

2.4 Materials and Methods

2.4.1 Fabrication of Silicon Nanomembranes and Transwell Assembly

Porous nanocrystalline silicon (pnc-Si) samples were fabricated as described previously [109] with the nanoporous membranes only 30 nm thick. Photolithography masks constrained the free-standing membrane area to comprise two 2 x 0.1 mm rectangular slits. The pore size is ∼15 nm with 5% porosity. Before assembling transwells, the pnc-Si samples were thermally treated at 1000°C for 5 minutes in a Surface Science Integration Rapid Thermal Processing (RTP) system (El Mirage, AZ). The RTP treatment significantly delays the biodegradation rate of pnc-Si [71]. Pnc-Si samples were secured in custom polypropylene housings (Harbec Plastics, Inc., Ontario, NY) with a biocompatible O-ring to form pnc-Si transwells [141]. The pnc-Si transwells were autoclaved before use. It is important to note that while the entire cross-sectional area is available for cell growth, only the free standing area is permeable.

2.4.2 Effects of Membrane Geometry on Baseline TEER Values

Commercially available transwell inserts of different sizes (6-, 12-, and 24-well) featuring TE membranes were used for this study. Additionally, different active area geometries were engineered on the 12-well transwell by using

wide annular silicone gaskets to cover the membrane and expose different percentages of the TE membrane in the center for permeation. In this way, we were able to simulate the situation with nanomembranes. The transwells were submerged in 1x cell medium per recommended volumes, and resistance was measured using the STX2 'chopstick' electrodes connected to EVOM Epithelial VoltOhmeter [World Precision Instruments (WPI) Inc., Sarasota, FL]. Four transwells were tested for each configuration, and 3 measurements per transwell corresponding to 3 different access-locations in the transwell.

2.4.3 Cell Culture

Cell culture studies were performed with the mouse brain endothelial cell line 'bEnd.3' (ATCC, Manassas, VA). The bEnd.3 cells (passages 8-17) were grown in DMEM media with 1% penicillin/streptomycin, 1X non-essential amino acids and 10% FBS. The bEnd.3 cells were seeded at 50000 cells/cm^2 and grown on the bottom surface of transwells. All the cell cultures were maintained in an humidified incubator at 37°C with 5% CO_2.

2.4.4 Evolution of TEER Values in Cell Culture

Barrier function of cell monolayers was assessed by measuring the electrical resistance across the transwell membranes. An EVOM Epithelial Voltohmeter connected to an EndOhm-6 (also referred as 'EndOhm') culture cup (WPI Inc., Sarasota, FL) was used for these studies. The EndOhm chamber gen-

erates a more uniform electric field as compared to the STX2 'chopstick' electrodes, and measures more accurate TEER values. Day 0 measurements were acquired before seeding cells to obtain baseline values for each transwell device, and then the TEER was measured every 2-3 days thereafter.

2.4.5 COMSOL Simulations

All the experimental TEER measurements of barrier function were performed using an EndOhm cup for 24-well insert. The entire geometry of the EndOhm cup assembled with both commercial transwells and custom designed transwells was modeled in COMSOL Multiphysics (hereafter referred as 'COMSOL') using suitable 2D axiosymmetric and 3D models [Figure 2.2]. A transwell insert consisted of a permeable membrane (TE or pnc-Si) with cells growing either on the top or bottom of the membrane, and the entire volume was filled with conducting cell medium. The conductivity (K) of the cell medium was 1.5 S/m as measured experimentally using conductivity measurement probes. The superposition principle allowed us to estimate the conductivity of the TE membrane by suitably multiplying its porosity with the cell medium conductivity; thus a 0.5% porosity membrane will be modeled as a layer with conductivity equivalent to 0.005*1.5 = 0.0075 S/m. For the pnc-Si membrane, the inactive silicon substrate is a bad conductor (K=0), while the 30 nm thin freestanding porous membrane offers negligible background impedance (K= K_{medium} = 1.5 S/m)[119].

The cell growth was modeled using a biphasic growth curve: initial phase of exponential cell growth (Eq. 2.3) followed by a stabilizing growth due to contact inhibition (Eq. 2.4) [146].

$$\frac{dN}{dt} = rN \tag{2.3}$$

$$\frac{dN}{dt} = rN\left(1 - \frac{N}{N_{max}}\right) \tag{2.4}$$

Initial cell seeding density was 50000 cells/cm^2. Endothelial cells were assumed to have a total surface area of 1000 μm^2 [147]. Thus, the total area occupied by cells was 5x10^7 μm^2 or 0.5 cm^2, and the initial fraction of area occupied by cells was 0.50 or 50%. The cells were simulated to grow without any inhibition until they reach 90% confluence, after which their growth slowed due to contact-inhibition [146]. The final termination density was >97% (represented by 'N_{max}' in Eq. 4). Since the experiments spanned for 14 days, the growth curve was modeled from day zero to day 14, with day zero being the time of initial cell seeding, and the density at day 14 set to be the termination density.

The electrical characteristics of the growing cell monolayer were modeled from the growth curve in accordance with the superposition principle. The cell monolayer was modeled as a 10 micron thick conducting sheet above the membrane. This layer was assigned a spatially uniform conductivity value that varied with the density of cell confluence. This model is consistent with

an assumption that cells are perfect insulators and all ionic transport essentially occurs through the gaps (junctions) between cells. This assumption (of non-conducting cells) is valid, because at low frequency AC, capacitive impedance offered by the lipid bilayer is significantly higher than the junctional resistance [100], channeling the electric current through the 'path of least resistance'. Thus, a 20% confluent monolayer rendered a conductivity value of 80% of the bulk media (i.e. K_{cell} = 0.8*K_{medium} = 0.8*1.5 = 1.2 S/m) and, as the cell monolayer grew more confluent, the assigned conductivity of the cell monolayer proportionately decreased and the transmembrane resistance increased.

To reduce the computational complexity of the simulations, time-independent DC simulations were performed. This approximation is valid since the experimental apparatus uses only a very-low frequency (12.5 Hz) AC current. AC prevents the electric corrosion of the silver-silver chloride electrodes used in the EndOhm apparatus. Since the electric simulations are independent of this electrochemical phenomenon, DC current provides a simplified alternative without compromising the accuracy of the simulation output. COMSOL model was validated by comparing experimentally obtained TEER values from transwells filled with solutions of known conductivity to the FEA simulations with same transwell geometry and identical conductivity solutions. Transwells with 6.5 mm diameter TE membrane (24-well configuration) were used for these studies. The transwells were immersed in the cell media of different dilutions and TEER was measured (n=3). Regular cell media has a

conductivity of ∼1.5 S/m, and 2x and 4x dilutions yielded lower conductivity values.

2.5 Results

2.5.1 Effects of Membrane Geometry on Resistance: The Fallacy of Resistance Normalization

TEER measurements are very sensitive to the dimensions and the geometry and type of the membrane, to its housing, and to the configuration of electrodes [85, 102, 103, 106]. We illustrate this dependance by using transwell inserts of increasing membrane area: 24-, 12-, and 6-well plate transwells. Experiments were done without cellular monolayers to avoid any cell-induced variability. Recommended volumes of cell culture medium were introduced in the transwells and their bottom compartments, and TEER was measured using STX2 chopstick electrodes. The unequal length of chopstick electrodes in apical and basal compartments ensure that the electric field lines bend around the housing, and can 'accommodate' a larger media volume in case of bigger transwells. Thus, STX2 electrodes are useful since they can be used with any size of transwell inserts, unlike EndOhm chambers that are designed for a particular transwell size. The use of the popular chopstick electrodes (rather than the EndOhm chamber), also increases the non-uniformity of field lines for the purposes of this illustration (data now shown). In Figure 2.2, the dashed red curve represents TEER measurements taken with commercial

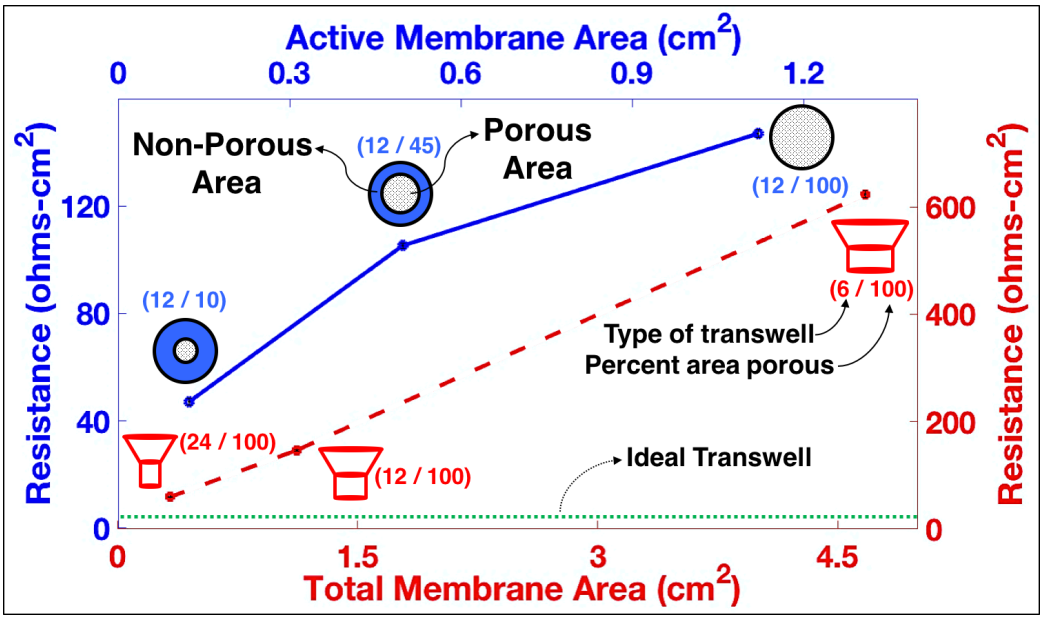

Figure 2.2: Effect of Membrane Geometry on TEER Values: The graph depicts different transwell configurations used and their TEER values. For e.g., (12,45) indicates a 12-well transwell insert with only 45% area exposed in the center for permeation. Error bars (very small) indicate standard error of mean.

transwells. As the area of the membrane increases, the product of resistance and the respective membrane area also increases. These resistance values represent 'background' resistances during an actual cell-culture experiment, and typically are subtracted from experimentally measured values to yield the resistance offered by cells only. This background subtraction, however, does not correct for the non-linearities involved in TEER acquisition. Next, in order to simulate the limited active area seen with silicon nanomembrane chips, we used impermeable silicone gaskets to seal the annular regions of

the membrane in the TE-transwell inserts. The annular shape exposed only a fraction of the TE membrane for permeation, and the covered regions were impermeable to ionic transport, mimicking the case for silicon nanomembranes. Even for these 'modified' transwells, the product of resistance and respective membrane area increases with exposed area, but non-linearly in this case, as represented by the solid blue curve in Figure 2.2. The dotted green line at the bottom of the plot represents an expected (ideal) outcome of normalizing the decreased resistance values with increasing membrane area. The results for both conventional and modified transwells can be understood as follows. As the size of the transwell increases, the average path taken by the charge-carrying species from the transmitting electrodes to the receiving electrodes also increases in a non-linear fashion. The geometry of the system is too complex to analytically deduce the changes in path length and verify the increase in resistance values theoretically. The resistance does not decrease with increased cross-sectional area as might be expected for a cable, and the product of resistance and area increases at larger membrane sizes. While the details of this example are particular to the chopstick electrode configuration, it illustrates the need for caution when comparing TEER values between systems even if they are 'normalized' for different areas.

2.5.2 Development and Validation of a FEA Model

Since the geometry of the transwell units are too complicated to be analyzed using analytical methods, we employed finite element analysis (FEA)

models to study and characterize the electrical behavior of these systems. We used COMSOL for modeling the transwell geometry and FEA. Since our model excludes any time- or frequency-variant component, time-independent simulations were performed to yield the resistance values. This approach is computationally efficient, and also valid because the experimental measurements were obtained at a very low frequency of 12.5 Hz. The FEA model simulations used 10 μA as an input parameter, and the resultant voltage drop was used to yield the resistance values. The FEA model is shown in the Figure 2.3, and results of the validation are shown in Figure 2.4. For all three values of conductivity, the resistance values from the COMSOL simulations matched closely with the ones obtained experimentally.

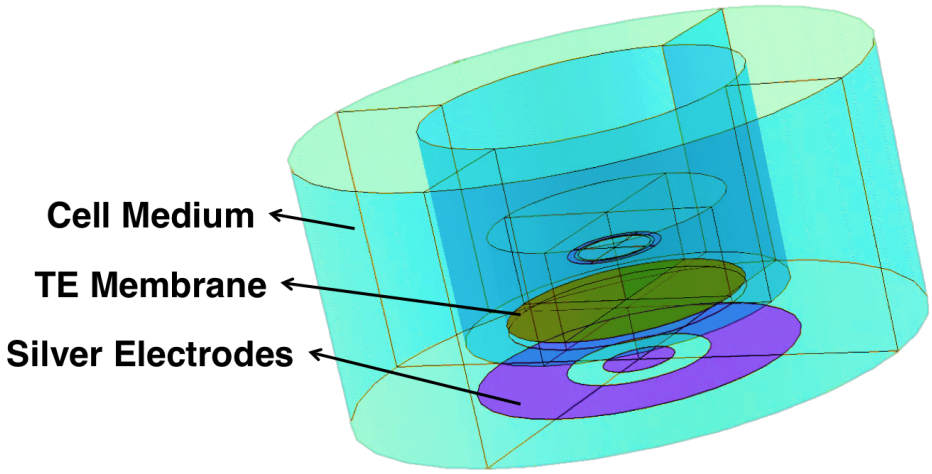

Figure 2.3: COMSOL model of EndOhm chamber: EndOhm chamber with a TE membrane transwell insert inside.

Having validated the model with TE membranes, we then compared the

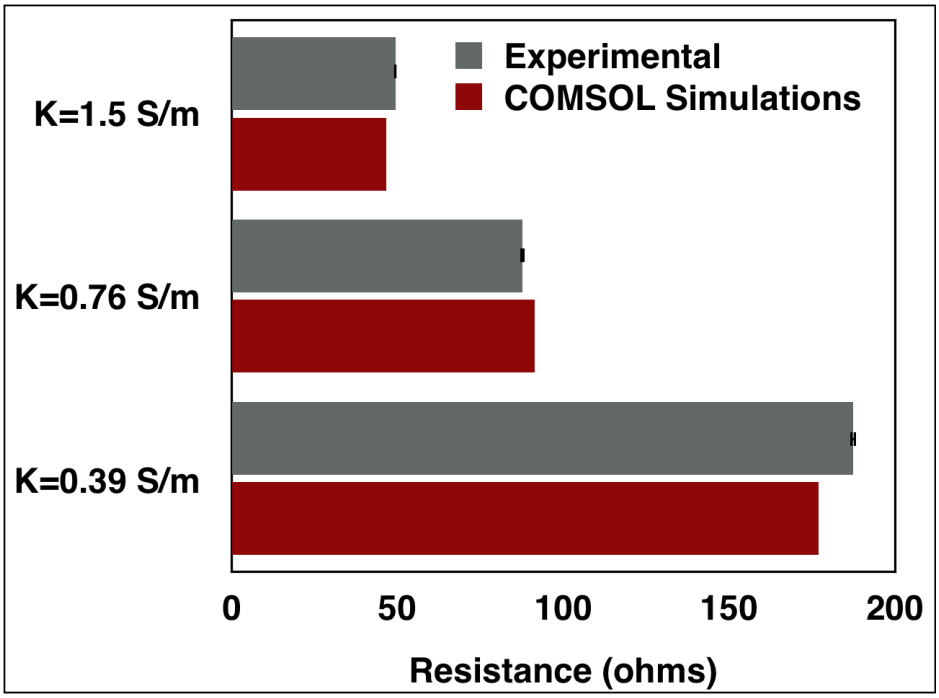

Figure 2.4: Validation of COMSOL Model: TEER values from experiments compared with simulation results. Cell culture medium of known conductivity was used. Error bars (very small) show standard error of mean [n=3].

electrical behavior of TE membranes and nanomembranes under identical input conditions. The nanomembranes also had a total area of ∼0.33 cm^2 like TE membranes, but were only permeable through two 2 mm by 0.1 mm wide slots in the center of the chip. Thus, the total active area available for ionic transport was only 0.4 mm^2 in the nanomembrane simulations. Simulation results show that the TE membrane experiences nearly uniform electric field lines that pass orthogonally through the membrane in the EndOhm system (Figure 2.5). This quasi-uniform electrical behavior likely explains the reliability of the EndOhm compared to the STX2 (chopstick) electrodes. By contrast, a simulated nanomembrane-insert resulted in bent field lines that are concentrated at the porous membrane 'windows' (Figure 2.6). The additional path length caused by the field line focusing increases the baseline system resistance. Under otherwise identical conditions, simulations predicted a baseline resistance for inserts with 2-slot nanomembranes ∼10.8 times higher than the ones with uniform TE membrane.

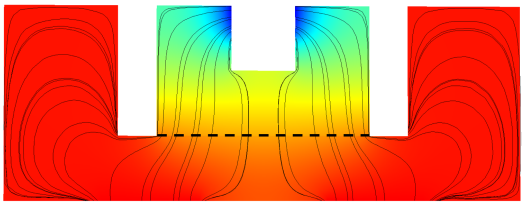

Figure 2.5: Electric field lines for track-etched membranes: Simulated electric field lines in the cross-section of EndOhm system for transwell inserts with TE membranes. The dashed line represents the position of the TE membrane within the system.

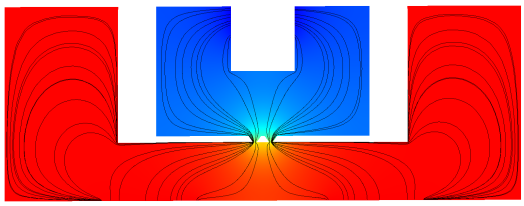

Figure 2.6: Electric field lines for silicon nanomembranes: Simulated electric field lines in the cross-section of EndOhm system for transwell inserts with 2-slot silicon nanomembranes. The two constricted regions at the similar position in the system represents the active area of silicon nanomembrane. The 'squeezing' of electric field lines in the nanomembrane leads to a 10-12X higher baseline resistance as predicted by the COMSOL model.

2.5.3 Modeling Cell Growth

To explore how changes in field line behavior translate to TEER values in barrier studies, we cultured brain endothelial (bEnd.3) cells on 2-slot nanomembrane substrates both *in vitro* or *in silico*. Changes in TEER values reflected the growth and maturation of the culture, with resistance values eventually achieving a plateau upon cell confluence. We modeled cell growth kinetics in COMSOL using a contact inhibited logistic growth curve previously developed in our lab [146]. In the electrical model, cell growth was simulated as a layer above the membrane that increases in resistivity over time. Since the COMSOL data simulates the same cell-growth phenomena on two different membrane systems, we can use the predictions from each system to convert TEER values from one system to the other. In this way TEER values obtained on nanomembranes in a microdevice can be 'corrected' to enable comparisons to TEER values obtained by others on TE membranes

in transwell devices.

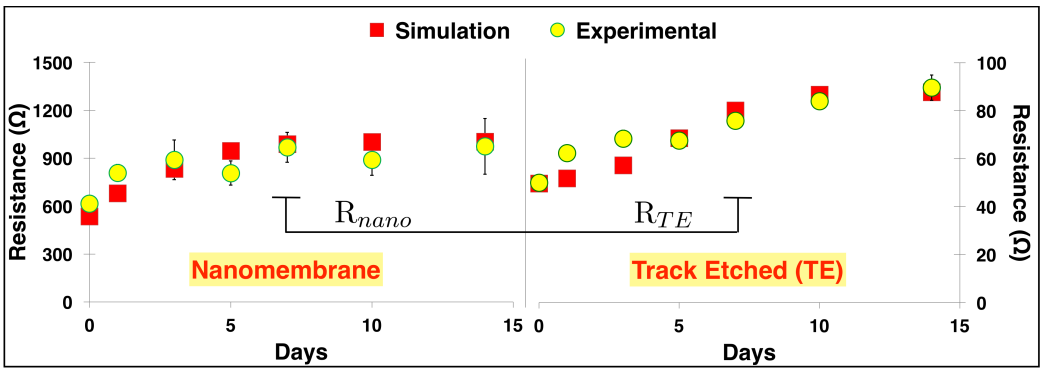

Figure 2.7: Comparison of experimental and simulated TEER values in different membrane-systems: Experimental (yellow circles) vs simulation (red squares) results demonstrating the increase in TEER during bEnd.3 cell growth on silicon nanomembrane and on TE membranes. Note the difference in the magnitude of the measured resistances, although both experimental curves follow a similar trend. Error bars represent standard error of mean [n=3-5]. The ratio of simulated resistances (R_{nano} : R_{TE}) is calculated by dividing the resistance from nanomembrane on a given day (for e.g. day 7, as shown in the figure) to the resistance obtained from TE membrane on the same day (i.e. day 7 in this case). This ratio is used to create a mapping function between the two systems (refer Figure 2.8 and section 4.4)

Brain endothelial (bEnd.3) cells were cultured in the transwells fitted with either silicon nanomembranes or with polymer TE membranes. Baseline resistance values were measured in both the systems before initial cell seeding. In COMSOL simulations, cell-growth was represented by the changes in the conductivity of the cell layer, K_{cell}, which was calculated from the degree of confluence, c, according to: $K_{cell} = (1\text{-}c)*K_{medium}$, where K_{medium} is the bulk media conductivity, and $0 < c < 1$. This effectively assumes the growing cell layer is a superposition of insulators (cells) and resistors (media between

the cells) with the degree of confluence equal to the ratio of cell- occupied area to the total area. This superposition principle is valid because cell membranes act as insulating capacitors at low frequency AC [100], and the electric current essentially flows through paracellular gaps. We assume that a perfect monolayer (100% confluent) is not achievable since this would give an open circuit and therefore we must use the maximum confluence value as a free parameter in each model fit. With this addition to the EndOhm model developed and validated earlier, we accurately predicted the increases in TEER values on the both membrane systems (Figure 2.7; RMS errors of 7% for TE membranes and 9% for silicon membranes). The terminal TEER values obtained here ($\sim$13 Ω-cm^2) are much lower than the published values for blood brain barrier (BBB) ($>$100 Ω-cm^2) [108], but this difference is not due to the geometry or the nature of the membrane used for culturing brain endothelial cells, since the corrected values on both TE and nanomembranes are identical. Instead we note that, BBB typically needs the growth of brain endothelial cells under physiological levels of shear stress ($>$10 dynes/cm^2), and needs to be cocultured with astrocytes and pericytes for enhanced barrier properties [108]. This has motivated us to develop a more comprehensive nanomembrane microsystem for vascular mimetics, which we will introduce in forthcoming chapters.

2.5.4 Mapping Function

To obtain a mapping function between the two membranes we used 'number of days in culture' as an implicit parameter in a plot of TEER values for silicon and TE membranes (Figure 2.7). The results show a local nonlinearity that can be best understood from a plot of the ratio of simulated resistance values for the nanomembrane to the TE membrane (Figure 2.8). Here, we see that the ratio (R_{nano} : R_{TE}) is initially $\sim$11 and returns to a similar value once both monolayers become confluent. The intermediate increase in the ratio is likely due to the fact that the cells are growing at slightly different rates on the two materials. We have previously shown that endothelial cells grow slightly faster on nanomembranes compared to polymeric substrates (0.0296 divisions/cell-hour for silicon membranes vs 0.0223 divisions/cell-hour for polymer substrates) [71]. The more rapid achievement of a TEER plateau value on nanomembranes (3-5 days) compared to TE membranes (5-7 days) is consistent with this earlier finding. Thus, we do not believe that the different dynamics during the logistic growth phase are due to the electrical behavior of the two membranes. However, once the cells have reached confluence, both systems act as a series of resistors, where the only difference is attributed to the membrane geometry (Figure 2.10). Hence, the mapping, or the correction function, is simply a line (Figure 2.8 dashed line), whose ordinate (Y) intercept is equal to the ratio of the plateau resistances of the two systems. Because this ratio is a function of the membrane geometry and electrode positioning, a different configuration of these

variables would require a new FEA simulation to obtain a new ratio. In this case, the ratio is 11.4 and hence, if one wishes to report 2-slot nanomembrane TEER values as equivalent TEER values on a commercial 24 well TE insert, one would first divide the nanomembrane value by 11.4 and then multiply by the area of a 24 well insert (0.33 cm^2), to obtain the conventional transwell value in ohms-cm^2. Once the conversion is completed, background subtraction needs to be performed to yield cellular resistances only. Figure 2.9 compares the corrected resistance values (using the mapping function) for cell growth on nanomembrane to those on TE membranes. The two curves match very closely, with a RMS error of $\sim$8%.

2.6 Discussion

Intact barrier tissues are important for homeostasis and normal functioning of all the organs in our body including skin, lungs, gastrointestinal (GI) tract, kidney, retina and brain [148]. Damage or loss of integrity of these barrier properties can be responsible for multiple degenerative and fatal disorders. Loss of intact blood-brain-barrier (BBB) due to excessive infiltration of immune cells in the brain is responsible for disorders such as multiple sclerosis [149]. Systemic inflammatory conditions like septic shock disrupts microvascular barrier function leading to excessive fluid loss and increased patient mortality [64, 150]. Disruption of barrier tissues in lungs can lead to increased extravasation of neutrophils in bronchial spaces causing chronic

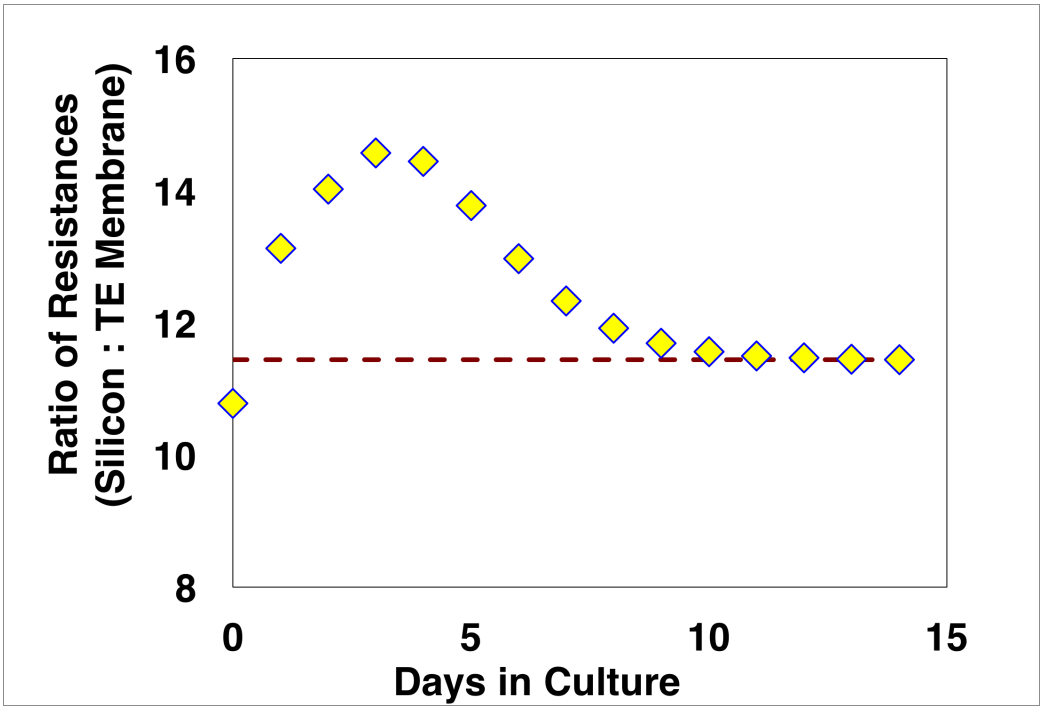

Figure 2.8: Ratio of simulated resistance in different membrane-systems: The ratio of resistances (Nano:TE) obtained from COMSOL simulation for the two membranes. Note that the ratio is dynamic during the intermediate phases of growth due to different growth rates on different substrates, but plateaus as the cells reach confluence. The plateauing value of ratio (11.4 in this case) reflects the difference in the geometry of the two systems, and can be used to convert TEER values from nanomembrane to TE membranes equivalents.

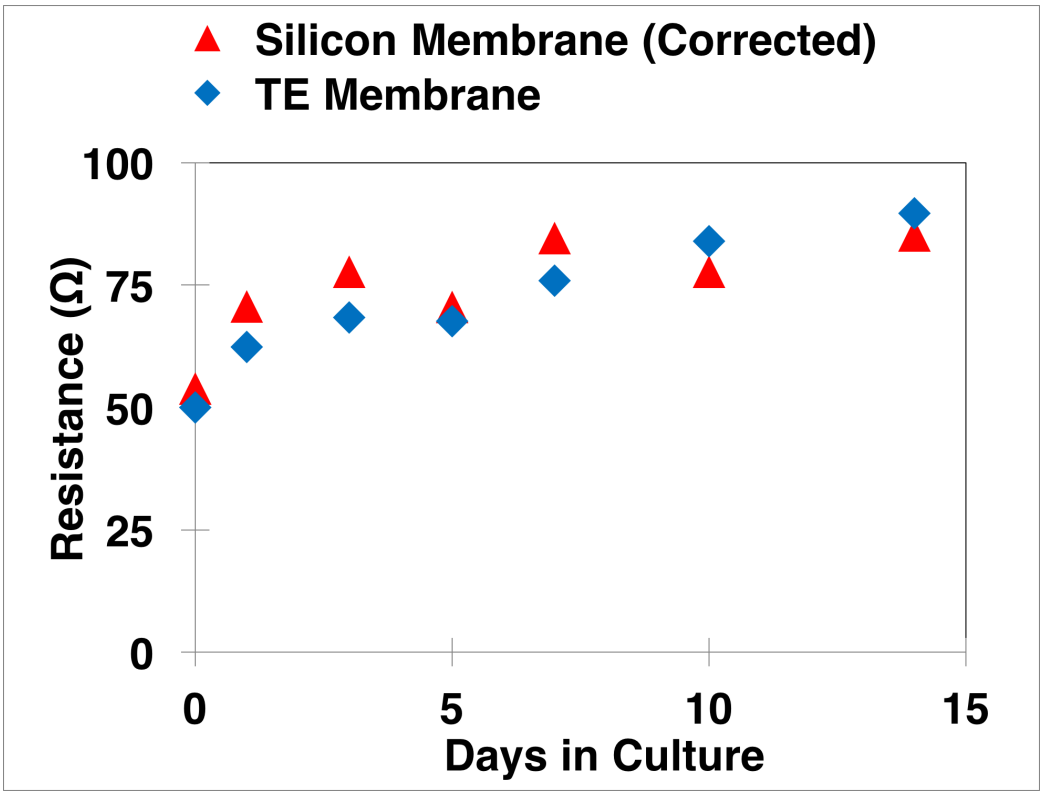

Figure 2.9: Overlapping of the mapped data across different membrane-systems: Resistance values obtained from silicon membrane are corrected by dividing with 11.4 to yield the corrected values, which match well with the values from TE membranes. Error bars not indicated for visual clarity.

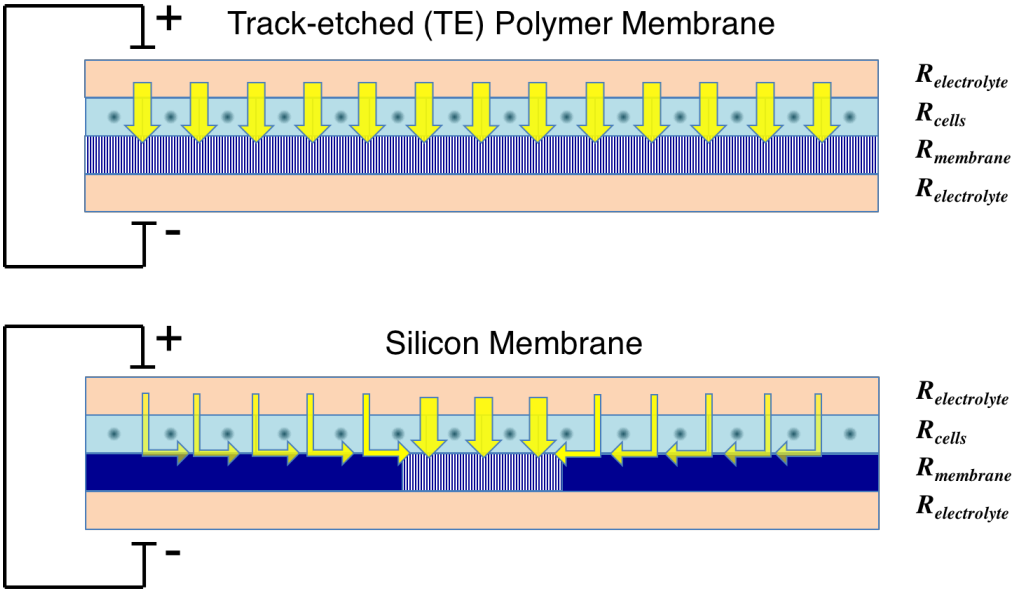

Figure 2.10: Difference in electric field lines in confluent culture in different membrane-systems: The schematic demonstrates the spatial distribution and intensity of the electric field through the confluent monolayer of cells on different systems. The effective path length and the cross sectional area approach a constant value for the systems as cells reach confluence, and the resistances can be linked together through a simple multiplicative constant.

obstructive pulmonary disorder (COPD) [151]. Thus, it is extremely important to understand the organ- and tissue-specific physiology of the barrier tissues for a more targeted clinical intervention [148]. Development of *in vitro* platforms that can accurately capture the pathophysiology of the barrier tissues will be an important step towards the discovery, development, and delivery of therapeutic drugs [152]. Towards this end, development of micro-physiological systems (MPS) serve as a promising platform to model and study human pathological conditions [140].

A variety of MPS are used to model different organ specific tissue barriers including the brain [107, 108, 153], GI tract [154], lung [155], microvessel [88, 98] etc. Most of these *in vitro* models of barrier tissues employ a porous membrane for coculture of relevant cell types. Commercially available systems featuring track etched (TE) membranes suffer significant limitations including 1) *aphysiological* barrier thicknesses ($\sim$10 microns), 2) poor phase imaging quality and autofluorescence, 3) low porosity (pore:cell ratios $<$1) and permeability, and 4) challenges with microsystem integration. In contrast, silicon nanomembranes developed over the last decade are extremely thin, highly permeable, offer superior imaging characteristics, and are manufacturable at large scales [109, 142]. The permeability of membranes used for coculturing plays an important role in the differentiation of growing cells to mimic *in vivo* functions [72, 76]. The ultrathin nature of silicon nanomembranes make them ideal for proximal coculture applications and for modeling barrier tissues *in vitro* [71, 73]. In the past, we have demonstrated the ad-

vantages of using silicon nanomembranes over commercially available TE membranes for a variety of biological applications including vasculogenesis [141], stem cell differentiation [72], shear-free chemotaxis of leukocytes [124] and hemodialysis [116]. The nanometer thickness renders negligible diffusive resistances to small molecules [119] - a characteristic that should enhance paracrine signaling in cocultures [73]. The advantages that nanomembranes have for studying cell barriers, including multi-cellular layers, motivate the present analysis so that TEER measurements can be reliably understood and interpreted for cell layers grown using nanomembrane platforms.

Electrical methods of characterizing tissue permeability have been used for over 60 years in different animal models. These methods provide better temporal resolution over chemical methods because they depend on the instantaneous mobilities of the ionic species across the barrier structure instead of much slower diffusion of the macromolecular fluorescent markers. The pioneering work on using electrical measurements to assess tissue barrier function was published by Hans Ussing in the 1950's in the course of his studies on transport properties of frog epithelium. Subsequently, using slightly different principles, Crone and colleagues, in the early 1980s, successfully measured the ionic conductances in the BBB of a live frog, establishing the gold standard for TEER values in brain microvasculature [143, 144]. Presently, hanging bucket transwell systems, inspired from the Boyden chambers, are the most popular systems used for barrier studies because of their ease of use, and are routinely used in combination with STX2 'chopstick' electrodes for

TEER measurement [WPI Inc., Sarasota, FL]. Unfortunately, this method of TEER measurement is subject to artifactual differences in measured values because of differences in the size of the transwells that are used, and the precise placement of the electrodes. To compare the TEER values obtained from the *in vitro* setup (in Ω) to the *in vivo* values (in Ω-cm^2), and the desire to standardize measurements across different *in vitro* systems required that the resistance be multiplied with the membrane area supporting the cells in the transwell. While this convention was widely adopted for decades, it is clearly flawed as highlighted in our work. A simple experiment presented in Figure 2.2 illustrates that the product of resistance and the membrane area increases monotonically with area - a clear sign that the multiplication does not constitute a proper normalization of the measurements. Our attempts to apply these same corrections to silicon nanomembranes with very small active areas revealed even more problematic discrepancies with this approach. Confronted with this paradox, we sought a computational model to help us rationalize the differences between the two systems.

The past decade witnessed the growth of a variety of microfluidic systems that enabled different research groups to develop and customize devices to meet their specific research requirements [97, 98, 101–103, 105, 107, 108, 156]. As these microsystems have become more sophisticated, relatively little attention has been paid to the underlying assumptions in permeability measurements. While the *in vitro* systems typically fail to match the physiological complexity of the *in vivo* environment, making a proper comparison

between any two systems is typically not as simple as multiplying resistance by membrane area[106]. Research groups developing microsystems for barrier models have taken different approaches for the interpretation of TEER values. One recent study designed their microsystem to match the shape of the commercially available 6.5 mm wide transwell insert [101]. The rationale behind this approach is to obtain similar TEER values as observed in the commercial system, which will allow the researchers to directly multiply the resistance values with the membrane area, and make it easy to compare them against the published TEER values in the literature. Although sound, this obviously limits the design and applications of the microsystem. Another study developed a mapping function for their system to interpret the raw resistance values using finite element analysis [102]. Our work provides a general modeling approach, which can be easily developed, verified, and applied to interpret the resistance values from *any* customized microsystem. The scope of these analytical models is to make a fair comparison between different *in vitro* models only. *In vivo* measurement systems differ significantly from these *in vitro* systems and developing a sound analytical framework to compare with *in vivo* techniques is beyond the scope of this Chapter. FEA modeling of microsystems not only allows the user to understand the electric behavior, but also reveals opportunities to optimize for more sensitive and reliable TEER measurements. For instance, current efforts in our lab are focused on developing microsystems with integrated patterned electrodes, and the FEA modeling is able to predict the raw resistance values observed

experimentally.

The key to linking an understanding of electrical behavior in a microsystem to that expected in a commercial Transwell system is an accurate FEA model of both systems. In the last few years, several studies have employed FEA tools to understand the electrical behavior of cells in their microsystem [99, 100, 157]. Our own analysis demonstrated the utility of the FEA model in multiple ways. First, we were able to accurately simulate the electrical behavior in the EndOhm system in the absence of the cells in COMSOL Multiphysics by using media of different conductivity values (Figure 2.4) as seen elsewhere [101]. The close match between the experiment and simulation also established the validity of using simpler time-independent DC simulations to model low frequency AC experiments. Next, we modeled a growing cellular layer using a modified logistic growth curve [146] to model the evolution of TEER values with time. Interestingly, we have shown that endothelial cells grow faster on silicon nanomembranes compared the polymer substrates [71] and a similar phenomenon can be observed here with a faster rise of our TEER data (Figure 2.9). TEER values eventually stabilize at a plateau in both systems (4-5 days on silicon nanomembranes; >one week on TE membranes) (Figure 2.7). Assuming the cells achieve the same resistant monolayer on both systems, the ratio of the plateau values is the transfer function between the two systems that can be used to relate TEER values as a measure of barrier function. The final ratio of resistances differs slightly from the initial ratio (Figure 2.8) indicating that the cell layer slightly affects

the field lines through the membrane. Using the percentage confluence as the only floating parameter, we were able to predict the end-point TEER values with less than 10% RMS error.

2.7 Conclusion

We have successfully employed the COMSOL model to understand the electrical response of the transwell inserts with different membrane geometries. This development is important to the application of nanomembranes for the creation of barrier models where their optical transparency and ultrathin nature have advantages over conventional systems. The model provided the necessary correction function to convert the resistance value from silicon nanomembrane transwell microsystem to the conventional TE membrane inserts enabling reliable comparisons between the two datasets. Although these results are specific to 2-slot silicon nanomembranes, the modeling approach can be easily extended to different membrane geometries and device configurations. The development of a mapping function provides an unique and reliable algorithm to interpret and compare the TEER values across different platforms.

Acknowledgements

Authors would like to thank Dr. Henry Chung and Tucker Bergin for their help in COMSOL modeling and Thomas Andolsek in obtaining the TEER data for validation experiments. They also acknowledge the support of Dr. Allison Elder (Department of Environmental Medicine, University of Rochester) during the early days of this project.

Chapter 3

Vascular Microphysiological System to Study Neutrophil-Endothelial Interactions

3.1 Introduction

Neutrophils are the first responders in the innate immune response [158]. Upon infection, 'policing' neutrophils exit the circulation through post-capillary venules and follow gradients of soluble chemoattractants until they reach the site of infection [32]. The typical leukocyte adhesion cascade consists of the sequential steps of capture, rolling, activation, arrest, spreading, crawling, and diapedesis [31] as shown in Figure 3.1. Each of these steps is facilitated by a specific set of receptors expressed on both the leukocyte surface and the endothelial luminal surface. The coordinated cellular and molecular interactions between activated leukocytes and endothelium are essential for a regulated inflammatory response. The loss of regulated trafficking of neutrophils and other leukocytes from the vasculature is a hallmark of various acute and chronic inflammatory diseases. In sepsis, there is dele-

terious accumulation of neutrophils in extravascular tissues [159]. Chronic diseases like chronic obstructive pulmonary disorder (COPD) are characterized by enhanced neutrophil-endothelial interactions in bronchial circulation leading to a massive infiltration of neutrophils into the lungs [151]. Neutrophilic inflammation is also responsible for many other pathologies such as acute respiratory distress syndrome (ARDS), ulcerative colitis, acute phases of rheumatoid arthritis, autoimmune vasculitis [160] etc. The prolonged presence and accumulation of neutrophils at the site of tissue injury may result in the irreversible loss of tissue function leading to organ dysfunction. Thus, it is essential to enhance our understanding of the mechanisms of leukocyte transmigration across vascular barriers during acute inflammation and to use this understanding to develop therapies that prevent neutrophilic infiltration in specific disease models.

Neutrophil-induced Endothelial Permeability *

One of the classic symptoms of an acute inflammation is edema formation, or the leakage of vascular fluids in the extravascular spaces. Endothelial cells (ECs) tightly regulate the passage of fluid, macromolecules and cells between the blood and these interstitial tissue spaces [161]. Neutrophil-endothelial interactions can increase endothelial permeability in multiple ways. First, neutrophils secrete four different types of granules during their respiratory burst (hence the term 'granulocytes') that alter endothelial permeability [15]

*See Chapter 1 for a more detailed discussion

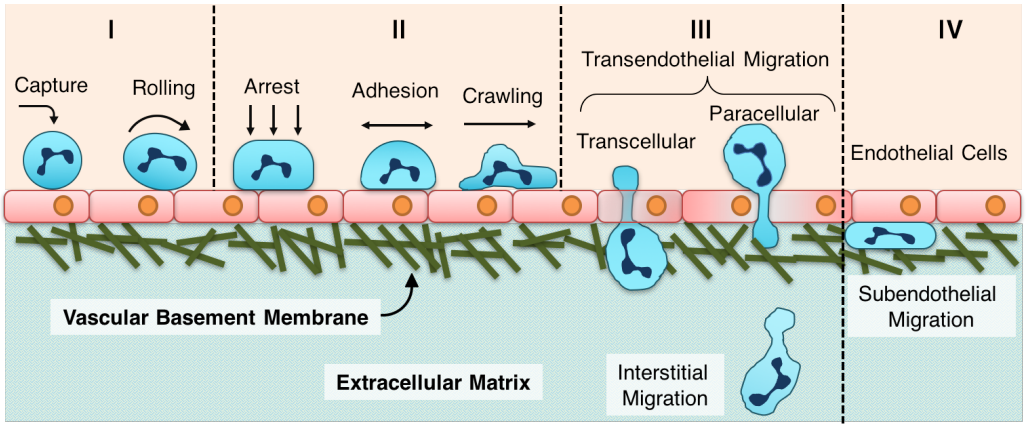

Figure 3.1: Leukocyte Adhesion Cascade: Multiple steps involved in leukocyte adhesion cascade can be broadly categorized into four main phases. Phase 1 involves the capturing and rolling of cells and constitute the first step in the cascade responsible for increasing endothelial permeability [56, 57]. Phase 2 typically involves integrin mediated arrest and crawling on the luminal surfaces of endothelial cells and also promotes endothelial permeability [50, 56]. Phase 3 consists of transendothelial migration, either through or across endothelial cell body, and is suspected to further promote the leakage of vascular fluid [37, 49]. Final steps in phase 4 highlight subendothelial migration on secreted basement membrane followed with interstitial migration into deep tissue.

(Table 3.1). The physical interactions between neutrophils and endothelial surface molecules during rolling and adhesion events are responsible for cytoskeletal rearrangements that alter the junctional integrity of endothelial cells [15, 49, 56, 57]. Transmigration events through paracellular and transcellular routes are also thought to lead to an increase in the vascular permeability *in vivo* [37]. Activated neutrophils also secrete reactive oxygen species, which have been shown to alter endothelial permeability in the past [52]. In the current study, we aim to understand the impact of neutrophil transmigra-

Table 3.1: Neutrophilic Granules: Granules released by neutrophils during respiratory burst [15].

Granules	Composition	Function
Primary (azurophilic)	Elastase, myeloperoxidase, cathepsins, defensins	Cytotoxic and bactericidal activity
Secondary (specific)	Collagenase, chemotactic receptors, adhesion receptors	Neutrophil phagocytosis
Tertiary	Metalloproteinase, Gelatinase	Degradation of basement membrane
Secretory	Plasma proteins, integrins, complement receptor	Neutrophil adhesion

tion events on endothelial permeability, specifically resolving the importance of subendothelial migration. We define 'permeability' as the permeability to the ionic species and macromolecules in the nanometer size range specifically occurring through the paracellular route, but not necessarily governed by the ability of endothelial cells to allow neutrophil invasion.

Strategies to Mitigate Neutrophil-induced Permeability

During diapedesis, the surface receptors of activated neutrophils engage with their corresponding ligands on ECs. As each step in the extravasation cascade has been associated with increased endothelial permeability [15], therapeutic blocking of these surface receptors can potentially reduce neutrophil mediated damage during inflammation. Since $\beta 2$ integrins are primarily responsible for luminal migration [31] and early activation of neutrophils, one possible strategy can be the inhibition of these integrins. However, due to their constitutive expression on neutrophils and the eminent role played by

integrin signaling in neutrophil activation, blanket inhibition of $\beta 2$ integrins is often deleterious to the host immune response and is not considered as a viable therapy against hyperinflammation [162]. Neutrophils employ $\beta 1$ integrins to transit the basement membrane [45] potentially probing for preferred sites of egress, and to vacate the subendothelial space [47]. Lerman and colleagues recently demonstrated that pharmacological blocking of $\alpha 3\beta 1$ integrins, but not $\beta 2$ integrins, improved survival rates in a mouse model of sepsis [38]. Consistent with the greater abundance of ligands for $(\alpha 3)\beta 1$ integrins in the BM, the authors also found that pharmacologically blocking these integrins prevented (septic) neutrophils from breaching the BM layer. How this incomplete extravasation of neutrophils might improve survival is not fully known, but one compelling hypothesis is that arresting neutrophils in the subendothelial spaces can reduce the neutrophil-induced edema, while the disruption of BM facilitated by neutrophil migration contributes to enhanced vascular permeability. Neutrophil-induced edema is known to cause ischemia and organ failure in conditions with capillary malperfusion, thus supporting the idea that neutrophil-induced permeability and mortality are interrelated [163]. In the current study, thus, we aim to address the question: *how does the BM migration of neutrophils affect the overall permeability, and what are the molecular mechanisms involved in regulating this migration-induced permeability changes?*

Need for an *in vitro* Platform

To be able to address the above question, it was necessary to engineer an *in vitro* model that allows different biochemical and cellular assays while simultaneously measuring the changes in endothelial barrier properties. While many *in vivo* animal models have been historically used to delineate different events occurring in the microvasculature that lead to neutrophil activation and extravasation, the reliability of these animal models has been challenged in recent years due the inherent discrepancies in the human and animal pathophysiologies [59]. On the other hand, while *in vitro* models offer a reductionist approach and provide a platform to work with human tissues, they invariably lack the structural and functional complexities of the *in vivo* vessels that may be key to understanding pathophysiology. Thus there remains an unmet need to engineer physiologically relevant *in vitro* platforms to provide a better readout of human pathology. To be useful for drug discovery studies, these devices also need to facilitate high throughput studies, be mass producible, affordable, and enable the metrology used in conventional physiological assays, namely barrier function measurements and optical microscopy. An *in vitro* platform integrated with multiple metrological tools will allow us to study different nuances of neutrophil activation and associated changes in endothelial permeability during regulated inflammatory conditions, providing foundational knowledge for the development and testing of new therapeutic approaches.

Considerations of an Ideal *in vitro* Platform and the Choice of Cell Substrate

Requirements: We propose that the ideal microvessel mimetic platform for the study of neutrophil transmigration would have the following characteristics: 1) The platform should recreate physiological microenvironments (3D culture, shear stress, porous substrate with compatible stiffness, proximity to extracellular matrix (ECM)) for the growth of human endothelial monolayers with high barrier properties; 2) The platform should contain luminal and abluminal compartments with facile (micro)fluidic access. This will allow the control and measurement of soluble factors in each compartment and also enable the 3D chemotaxis of neutrophils across the vascular barrier; 3) The platform should allow for non-invasive, real-time and sensitive measurements of endothelial permeability; and 4) The platform should be transparent to enable live phase-contrast imaging of neutrophil migration and high quality fluorescent imaging unhindered by the autofluorescence and opacity typical of many polymer membranes.

Rationale: The presence of a porous substrate renders a three dimensional growth environment for cells and allows for basal communication with soluble factors. The significance of a permeable membrane for physiologically relevant growth has been studied by our group and also by others [68, 72, 73, 76, 77]. Furthermore, biological tissues are softer than glass or plastic substrates typically used for cell culturing applications. Compliant

substrates promote enhanced cell-cell cohesive interactions and are known to improve barrier properties *in vitro* [69]. Similarly, shear stress is known to elevate barrier properties of endothelial cells *in vitro* [164], and the ability to grow them under shear is important for a physiological mimetic device [156]. While many coculture platforms are commercially available, most of them do not permit shear-conditioned growth needed for barrier maturation. Electrical methods of measuring permeability provide a real-time readout of the transient changes in monolayer barrier function, while the tracer-diffusion methods have the potential to distinguish between para- and transcellular modes of transport. Thus, an ideal *in vitro* platform should allow the implementation of both electrical and tracer assays. Finally, optical imaging is key for biological assays, especially to study neutrophil migration. Activated neutrophils turn from phase bright to phase dark upon transendothelial migration [165], and the ability to perform live phase imaging is essential to improve the utility of a microvessel mimetic device.

In vitro Permeability Measurement

To investigate the influence of leukocyte extravasation on endothelial barrier properties, it is essential to understand and improve the existing *in vitro* models of permeability measurement. There are many examples of *in vitro* vascular barrier models in the research literature and several tools are now available commercially [97, 98, 105, 107, 108]. Most of these existing systems, however, have important shortcomings for the study of leukocyte transmi-

gration across the vascular barrier. The popular commercial Transwells® and other membrane inserts are simple devices that suspend a semipermeable polymer based track-etched (TE) membrane in the middle of a culture dish. Cells are grown on the membrane surface and manually positioned 'chopstick' (STX2) electrodes are used to measure the transendothelial electrical resistance (TEER) as a measure of barrier function (World Precision Instruments, Sarasota, FL). These assays are highly sensitive to handling errors and are known to overestimate the electrical resistances [85]. Furthermore, these static culture devices do not allow shear-stress enhancement of endothelial barrier function [153, 164]. The TE membranes often limit imaging capability and preclude phase imaging. Indeed, a majority of the vascular barrier models in the literature have used TE membranes, which explains the lack of phase images in these publications. Sophisticated impedance spectroscopy instruments for TEER measurement (ECIS) are being adapted to shear flow (Applied BioPhysics Inc.). However, these devices do not use membranes at all and instead grow cells directly on impermeable and optically translucent gold electrodes. Thus, ECIS systems are not amenable to the construction of the two-compartment culture system required for 3D chemotaxis. Another commercial platform cellZscope provides a bicompartmental system to record impedance measurement, but support only static growth (nanoAnalytics GmbH, Germany), and requires dedicated instrumentation for measurement and analysis. Thus, an integrated platform to facilitate shear-conditioned endothelial growth in a bicompartmental system and si-

multaneous live imaging needs to be engineered for advanced *in vitro* studies.

In this chapter, we describe the development of a novel microvessel mimetic (MVM) platform that can image transmigration (phase and fluorescence) in a two-compartment system, while applying apical shear, and measuring electrical resistance and impedance. In addition to these key elements, the new platform introduces innovations such as the inclusion of a type 1 collagen gel (ECM component) in the abluminal compartment and the use of an ultrathin, transparent, and highly permeable silicon nanomembrane. With the capacity to simultaneously monitor neutrophil transmigration in a 3D culture environment and changes in cellular permeability, our vascular mimetic is ideally suited to address the impact of basement membrane migration by activated neutrophils in altering endothelial barrier properties.

3.2 Materials and Methods

The entire assembly and operation of the MVM consists of different fabrication, design and assembly steps. The process is multifold with parallel engineering and biological assays. The summary of this process is listed in the flowchart as shown in Figure 3.2, and elaborated in detail in the sections below.

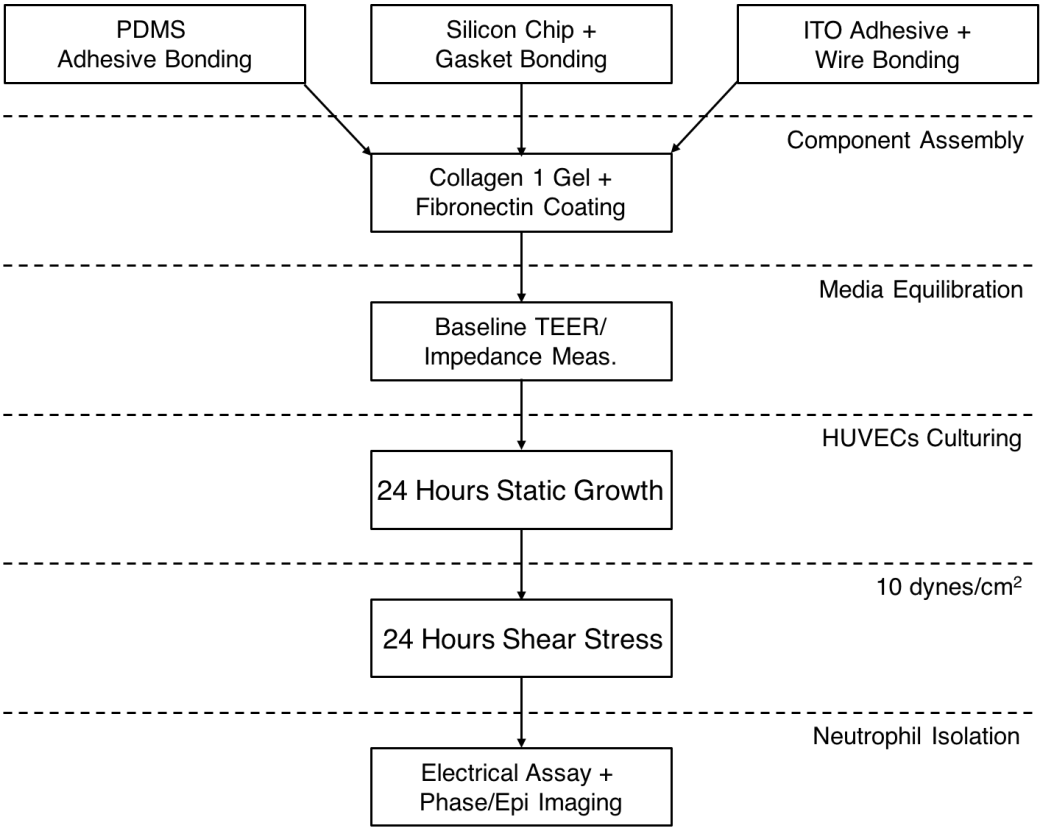

Figure 3.2: Assembly and Operation Flowchart: A representative flowchart showing different steps involved in MVM assembly and operation

3.2.1 Manufacturing of Microporous Silicon Nanomembranes

Silicon dioxide (SiO_2) membranes used in this study were purchased from SimPore Inc. (Henrietta, Rochester NY), and were manufactured according to protocols described elsewhere [72]. Briefly 300 nm of SiO_2 was deposited on double-side polished 6 inch wafers using plasma enhanced chemical vapor deposition (PECVD). Wafers were patterned on the backside with a mask to yield 5.4 x 5.4 mm^2 chips with 2 x 0.7 mm^2 windows after through-etching of the wafer. The oxide membrane was front-side patterned with an ASML PAS 5500/200 i-line stepper to create 3.0 micron holes with a center-to-center spacing equal to 20 microns, thus rendering $\sim$5% porosity to SiO_2 membranes. Reactive ion etching was used to etch the oxide film using Drytek 482 Quad Etcher. The wafer was through-etched from the backside using ethylenediamine pyrocatechol (EDP) in a custom fabricated one-sided heated etch cell as discussed in [109]. The etched wafer was broken into individual membrane 'chips' and analyzed using electron microscopy to verify pore dimensions and spacing.

3.2.2 Microvessel Mimetic (MVM) Platform Fabrication

The microfluidic platform features a SiO_2 membrane and consists of different fluidic, mechanical and electronic components. The device consists of two main compartments: luminal ('top' or 'apical') and abluminal ('bottom'

or 'basal') chambers separated by the nanomembrane. Figure 3.3 represents the 2D schematic of the device, and Figure 3.4 shows the intricate features of the various structural components used in the device assembly. The silicon nanomembrane is sandwiched between different silicone layers obtained from Specialty Silicone Fabricators (California, US) and precision-cut to specified dimensions using a Silhouette Cameo craft cutter (Lindon, Utah). The dimensions of the different layers are as shown in Table 3.2. These dimensions have been carefully optimized to yield flow profiles in the cell culture channels that would recreate physiological shear stress.

Table 3.2: Gasket Dimensions: Dimensions of the total and active area of the gaskets and electrode layers

Layer	Thickness	Total Area	Active area
PDMS Block	5 mm	20x10 mm^2	N/A
Adhesive Tape	130 microns	20x10 mm^2	N/A
Top & Bottom ITO	100 microns	24x16 mm^2	N/A
Top & Bottom Channel	130 microns	20x10 mm^2	17 mm^2& 28 mm^2
Top & Bottom Gel Layer	100 microns	20x10 mm^2	4x1.8 mm^2
Space (Membrane) Layer	300 microns	20x10 mm^2	5.6x5.6 mm^2
Nanomembrane chip	300 microns	5.4x5.4 mm^2	2x0.7 mm^2

The top and bottom channels are used for introducing cells and media in the respective channels, while the top and bottom gel layers contain polymerized collagen gels. The membrane layer matches the thickness of the silicon membrane chip (300 μm-substrate thickness), and is used as a spacer layer separating top and bottom chambers. The top and bottom indium tin oxide (ITO) layers serve as conducting electrode layers for tetrapolar TEER measurements. The inlet and outlet holes in all the gaskets and electrode

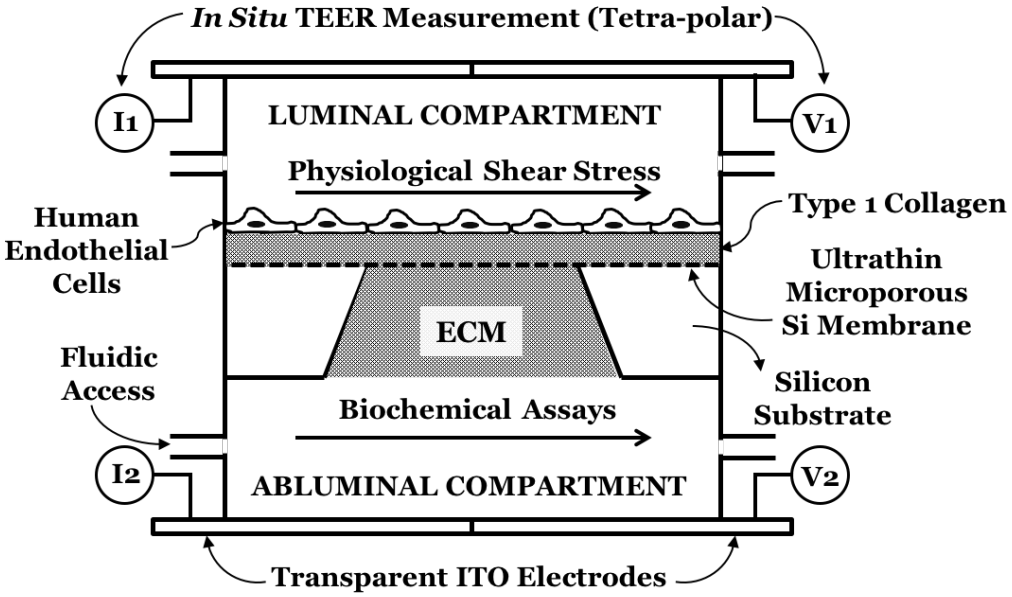

Figure 3.3: Device Schematic: A schematic indicating different elements of the MVM namely silicon nanomembrane, endothelial cells and collagen gels, indium tin oxide (ITO) electrodes and flow channels.

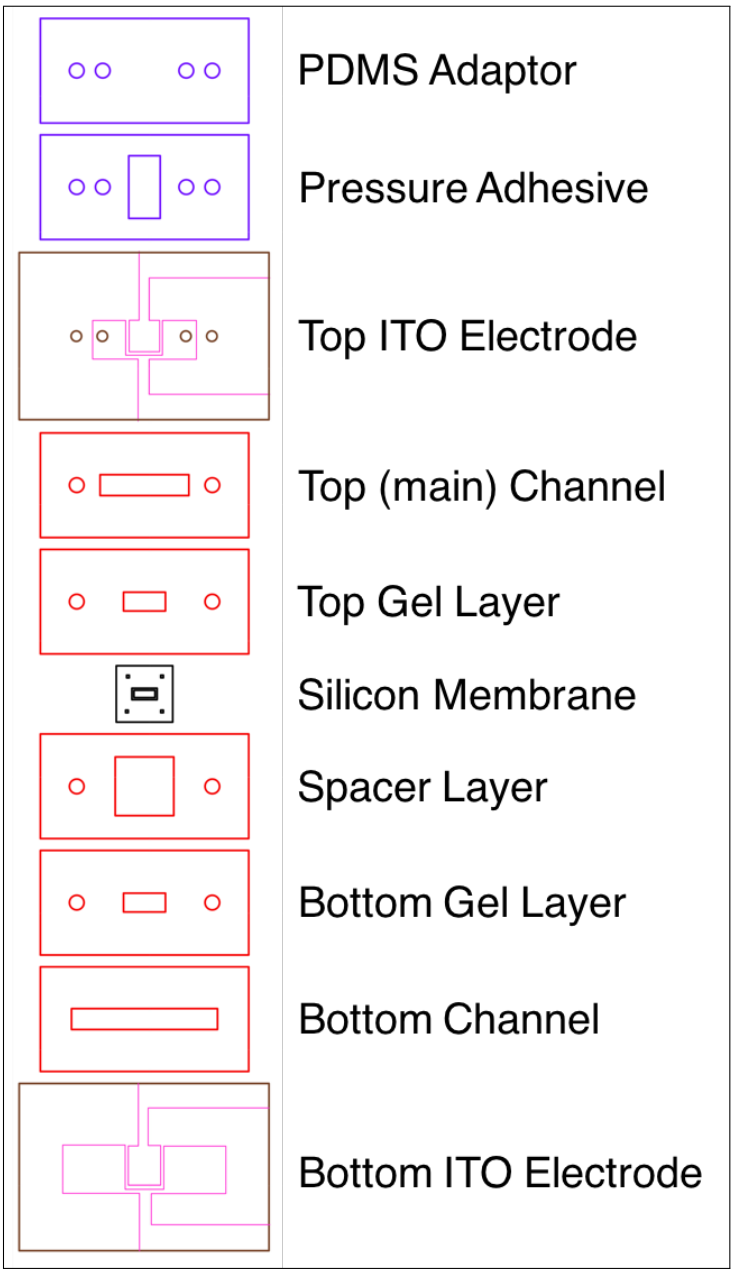

Figure 3.4: Designs for Precision Cutting: 2D patterning of the different silicone gaskets, PDMS and electrode layers achieved by using a precision craft-cutter.

layers are positioned to facilitate fluid access to top and bottom chambers independently and without mixing. Figure 3.5 shows the 3D exploded view of the device, while Figure 3.6 is an actual image of the assembled device.

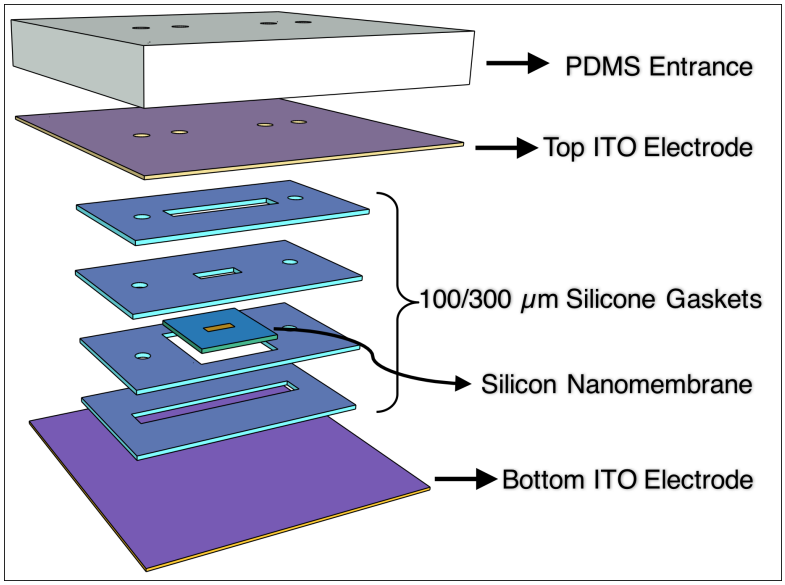

Figure 3.5: 3D CAD Model: A 3D exploded view of the different gasket and electronic components as rendered using Google SketchUp. The scorings on the ITO films are not indicated for visual clarity. Also, not shown are the connecting wires to interface with TEER acquisition system and the tubings and other peripheral flow accessories.

The assembly of the different layers is achieved using standard microfabrication techniques. The gasket-chip and gasket-gasket interfaces are assembled by exposing the to-be-bonded surfaces to UV-Ozone (Novascan, Iowa, US) for 10 mins and then curing the bonded layers at 70°C for 1 hour. The resulting bond is permanent. The adhesive layer consists of double-sided tape 468MP purchased from 3M (Minnesota, USA) and patterned using the

same craft-cutter. For bonding tape to silicone gasket and to ITO sheet, only the gasket layer is exposed to UV-Ozone and is immediately brought in contact with the tape, and then cured as described above. ITO sheet (PF-65IN) is commercially purchased from Delta Technologies (Colorado, USA) and consists of 200 nm of In_2O_3/Au/Ag film thermally deposited on $\sim$100 micron thick polyethylene terephthalate (PET) substrate with a resistivity of 10 Ω/sq. and visible transmittance of $>$78%. Silver wires of 250 μm diameter (A-M Systems, Carlsborg, WA) are bonded to ITO films using silver epoxy (8331S, MG Systems, Surrey, B.C., Canada) and cured at 70°C overnight to achieve high conductance wire bonding. The wire-to-electrode conductance is confirmed using a digital multimeter.

The electrode design has been carefully optimized to generate uniform electric field inside the cell culture chamber for sensitive TEER measurements. The ITO film on PET substrate acts as a polarizable electrode when in contact with electrolytic solution. 4-probe measurements are better than 2-probe ones because they don't include the contact impedances, which are typically large for semiconductor films such as ITO. Since only 2 film-substrates are used to create 4 electrodes, each film is scored using the craft-cutter to physically separate the ITO films on each side of the insulate, thus creating two separate electrodes on a single planar sheet of ITO. This scoring is sufficient for electrical insulation as verified using electron microscopy. The 'current' electrodes typically have a larger surface area than the 'voltage' electrodes to create uniform electric fields and the small sizes

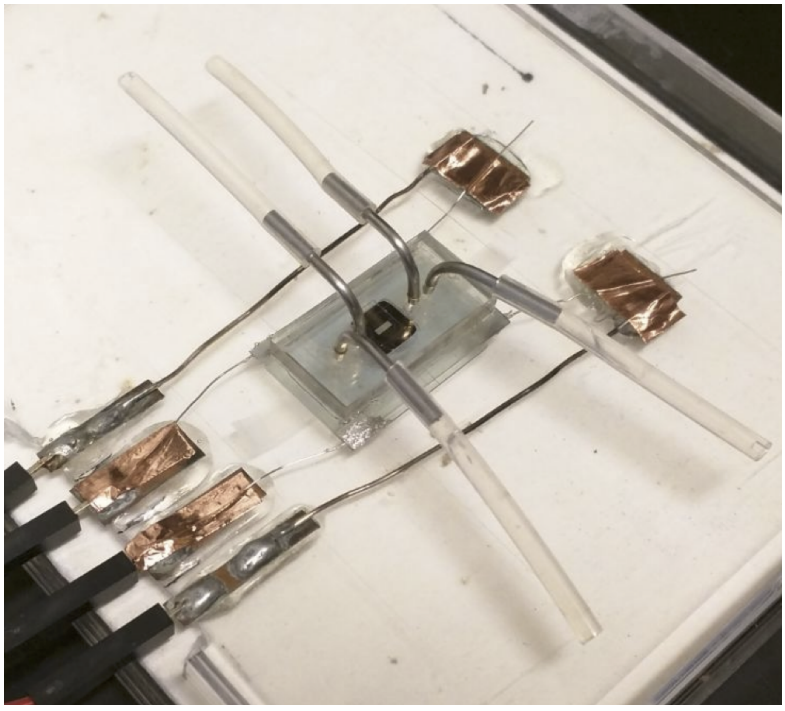

Figure 3.6: Assembled Device: An actual picture of the assembled device featuring the silicon nanomembrane, and highlighting the wire-connections for TEER measurement and flow tubings for cell and media perfusion.

of the voltage-sensing electrodes is advantageous to prevent stray potentials, thus improving the sensitivity of the measurement. Figure 3.7 shows a scored electrode substrate with 2 insulated current- and voltage-sensing electrodes.

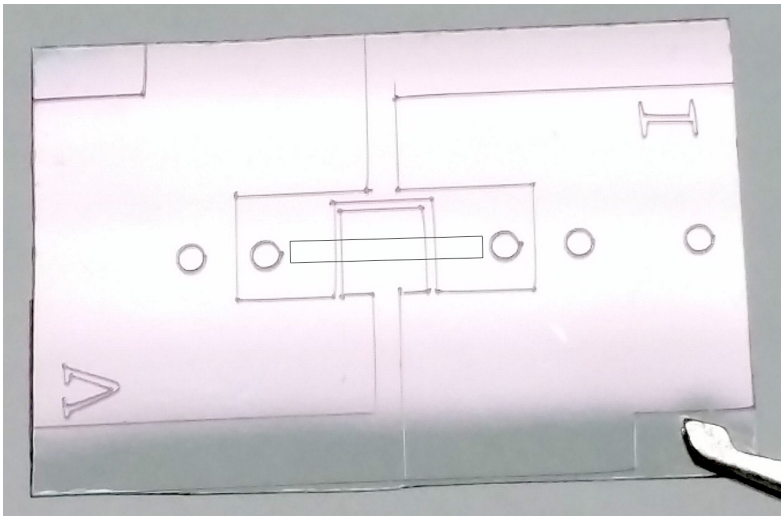

Figure 3.7: Indium Tin Oxide Electrode: An actual picture of the ITO electrode representing thin (200 nm) film of ITO (purple) deposited on thick PET substrate. The demarcation between 'I' and 'V' areas is achieved using precise surface scoring to create two insulated electrodes.

3.2.3 Flow Circuit Optimization

To remove the pulsatile nature of the flow profile generated by the peristaltic pump, a fluidic capacitor was installed downstream of the pump. The capacitor consists of small chamber of liquid (cell culture media) tightly sealed in a container with inlet and outlets connected to air tight tubings. The container has roughly half of its volume occupied by the liquid, and remainder

is air. Due to the compressibility of the air, it is able to absorb the pressure undulations created by the peristaltic pump. The principle of the capacitor operation is schematized in Figure 3.8. The fluidic capacitor is characterized using pressure sensors (LabSmith Inc., Livermore, CA) connected to the flow circuit. The amplitude of pressure oscillations was reduced by 2 orders of magnitude (see Figure 3.11).

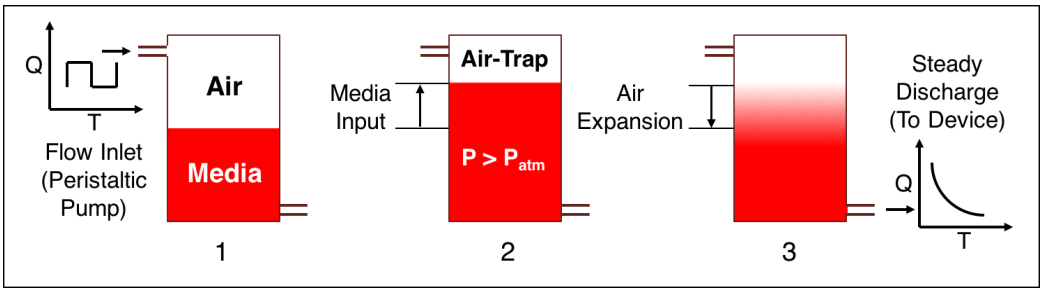

Figure 3.8: Fluidic Capacitor: A schematic demonstrating the operation of the fluidic capacitor developed to dampen the pulsatile nature of the peristaltic pump. The input liquid (cell culture media) waveform traps the air inside the chamber with every rotation of the pump. During the refractory period, the compressed air slowly expands, and causes the liquid to escape from the bottom outlet connected to the device. Since this discharge depends on the pressure difference between inside and outside the capacitor, this discharge is continuous and not discrete. The flow rate of discharge is directly proportional to the input flow-rate, as well as the ratio of air:liquid inside the capacitor.

3.2.4 Cell Culture Protocols

Pooled human umbilical vein endothelial cells (HUVECs) and MCDB-131 Complete Medium were obtained from VEC Technologies (Rensselaer, NY).

The silicon nanomembranes were first coated with rat tail collagen 1 gel (Enzo Life Sciences, Farmingdale, NY) at a density of 2 mg/ml. Collagen 1 was polymerized using the manufacturer's protocol inside the 100 μm Gel Layer (Table 3.2). After gel formation, the surface is further treated with 1/6 mg/ml of human plasma fibronectin (BD Biosciences) for one hour at room temperature. After the coating process, the devices are filled with MCDB-131 media for 1-2 hours for equilibrium prior to cell seeding. Confluent monolayers of HUVECs were trypsinized from tissue culture flasks and seeded inside the devices (top chamber) at the density of $\sim$40,000 cells/cm^2. Cells were allowed to grow under static conditions for $\sim$24 hours and then subjected to shear stress of 10 dynes/cm^2 for another 24 hours before any biochemical assay. While the apical media was perfused continuously, the basal media was changed regularly to avoid any evaporation and replenish the nutrients. The entire flow circuit, including peristaltic pump, media/nutrient reservoir, fluidic capacitor and the MVM device was placed inside the incubator to maintain gaseous environment and temperature conditions suitable for endothelial cell growth.

3.2.5 Neutrophil Assays

Human blood was collected from antecubital veins of healthy non-smoking individuals in heparin-coated tubes. The blood was gently suspended atop 1-step polymorph solution (Accurate Chemical, Westbury, NY) and spun at 500 RCF (Relative Centrifugal Force) for 30 minutes. After the spin, the

buffy layer was gently isolated from the remaining layers and washed with Hank's Balanced Salt Solution (HBSS) buffer (composition: 1x HBSS without cations + 10mM HEPES + 5mg/ml BSA). The washing steps were to remove the polymorph solution from neutrophils. After 2 washes with HBSS solution at 200 RCF, red blood cells (RBC) were lysed by first exposing the mixture to hypotonic solution (3 parts of 1/6x PBS) for 60 seconds followed with hypertonic solution (1 part of 4x PBS) to normalize the osmolarity. After washing, the supernatant containing dead RBC population was discarded and the pelleted neutrophils were again washed with HBSS solution and suspended in the final volume of 1 ml. The isolation procedure is finished in less than 2 hours, and the neutrophil assays are further conducted for another 3-4 hours to ensure normal neutrophil functionality. For chemotaxis assays, the neutrophils are suspended in MCDB-131 medium (to assimilate with the endothelial cells' media) at the density of 10 million/ml and added in the apical chamber. Chemotaxis is mediated by 10 nM formyl methionine-leucyl-phenylalanine (fMLP) (Sigma Aldrich) suspended in MCDB-131 and added in the basal chamber. Before the introduction of fMLP, a phase image is obtained for counting neutrophils added in the apical chamber. For chemotaxis experiments, the chambers are either kept inside the incubator, or on a heated stage over microscope for optical imaging. Neutrophil migration-blocking is achieved using Anti CD29 (β1) monoclonal antibody, strain P5D2 (Biolegend, San Diego, CA). Anti CD29 is added at concentration of 1 μg per million neutrophils suspended in a volume of 100 μl.

3.2.6 TEER and Impedance Measurement

The transendothelial electrical resistance (TEER) measurements were achieved using EVOM Voltohmmeter (WPI Inc., Sarasota, FL). The TEER measurement requires a tetrapolar electrical output from the MVM device, as indicated in Figure 3.6. The silver wires are connected to EVOM Voltohmmeter using custom-designed breadboard circuits. The circuits and the devices are placed in the incubator, while the EVOM Voltohmmeter is placed outside using connecting cables. TEER measurement is performed at 12.5 Hz using a low amplitude square-wave AC current (10 μA), and the corresponding potential drop is internally recorded to yield the final resistance in ohms as displayed on the Voltohmmeter. The EVOM Voltohmmeter also has an analog output, and is connected to Agilent Digital Multimeter 34401a (Keysight, Santa Rosa, CA) using coaxial cables. The multimeter is further operated using its software installed on Windows PC. Thus, ultimately, the TEER data acquisition is fully automated and the temporal evolution of electrical resistance can be recorded digitally on computer for further analysis and interpretations.

The MVM platform is also compatible with electrochemical impedance spectroscopy measurements, and is used for assays that demand high temporal sensitivity. The fabrication of the electrodes is slightly simplified for impedance measurements as compared to TEER measurement. While TEER measurement relies on tetrapolar output, impedance measurement requires

only two electrodes - one on either side of the membrane. The device assembly is identical except the ITO electrodes are not patterned but instead used as planar sheets. The bipolar output is connected to custom-designed breadboard circuit, which is further connected to VersaSTAT Potentiostat Galvanostat (Princeton Applied Research, Oak Ridge, TN) to conduct frequency sweep. The VersaSTAT instrument is controlled using its corresponding software installed on Windows PC. The frequency sweep is performed from 10 Hz to 10^6 Hz with a sampling frequency of 10 points per decade with Data Quality (DQ) set to 3 (number of measurements averaged) for measurements with transient phenomenon, or 50 points per decade and DQ set to 5 for time-insensitive measurements. While the higher DQ improves the robustness of the data acquisition, it also adds up the total time of the sweep, and can reduce the ability to capture time-sensitive changes. The impedance data at 12.5 Hz and 1000 Hz is analyzed in MATLAB^{TM} using custom-written programs for further analysis.

3.2.7 Macromolecular Permeability Characterization Assays

Macromolecular permeability was determined by monitoring the diffusion of 10 kDa ($<$ 3 nm) dextran conjugated with fluorescein isothiocyanate (FITC-dextran, TCI, VWR). Briefly, the apical chamber of the device was perfused with 1mg/ml of FITC-dextran pre-warmed to 37°C. The FITC-dextran solution is allowed to diffuse through the endothelial monolayer and is ob-

served in the basal chamber at a location adjacent to, but not directly under the membrane window to avoid any out-of-focus fluorescence. Image acquisition is performed using a Nikon camera controlled by a custom-written MATLAB^{TM} program to obtain one image per minute for 20-30 minutes. Images are acquired at 100 ms exposure and gain of 2. The image processing is performed using MATLAB^{TM} scripts to understand the temporal evolution of fluorescence in the basal compartment under different test conditions. The setup for this experiment is illustrated in Figure 3.9.

3.2.8 Electron Microscopy

Samples were fixed with 25 μL of media containing 2.5% glutaraldehyde for 10 minutes. They were then carefully extracted from the device and transferred to 50% ethanol in a six well plate. The samples were dehydrated in sequential ethanol steps (10% increase per step) to 100% ethanol. To prepare for electron microscopy, the samples were then dried using a Tousimis Samdri®-PVT-3D (Tousimis, Rockville, MD, USA) critical point dryer and then sputter-coated with 10 nm of gold in a Denton PVD (Denton Vacuum, Moorestown, NJ, USA) sputter coater. Samples were then imaged in a Zeiss Auriga (Carl Zeiss Microscopy GmbH, Jena, Germany) field emission scanning electron microscope with a 10 kV accelerating voltage.

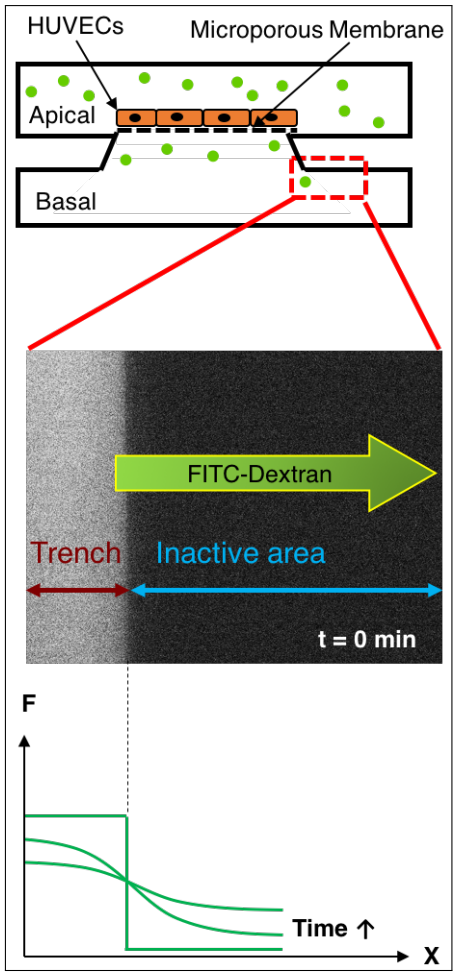

Figure 3.9: FITC-Dextran Permeability Assay: A schematic showing the setup for monitoring the diffusion of FITC-dextran in the basal chamber over time. The focal plane is always fixed on the basal side of the silicon nanomembrane, and a small section of the 'trench' (silicon substrate) is included in the imaging region of interest (ROI) to serve as a fiducial marker for imaging consistency. The top panel shows the setup, while the middle panel is a representative image as observed under the microscope. Since the trench is right under the active area of membrane, the fluorescence intensity is higher than the inactive area due to the proximity to the source of epifluorescence. The green arrow indicates the direction of diffusion. Bottom panel is a set of empirical curves highlighting the gain in intensity in the inactive region due to the diffusion of FITC-dextran through endothelial monolayers.

3.2.9 Finite Element Analysis in COMSOL Multiphysics®

To delineate the electrical characteristics of the TEER measurement systems and to understand the electrical behavior of the endothelial monolayers grown in the MVM device, we used COMSOL Multiphysics® (hereafter referred to as 'COMSOL') simulations to perform finite element analysis (FEA). The basic construction of the model has been adapted from the previous work in McGrath Lab [77], and as elaborated in Chapter 2. Briefly, the entire device is modeled in COMSOL using the actual device dimensions. The active area of microporous membrane has been modeled as 100% conductive element due to its negligible electrical resistance [77, 119], whereas the bulk silicon substrate has been assigned zero conductivity. The cell monolayer is modeled as 10 μm thick layer, with its conductance determined as: $K_{cell} = K_{medium} \times (1\text{-}c)$, where c is the degree of confluence defined as the ratio of cell occupied area to the total area available for cell growth at any given time point. Thus $0 \leq c \leq 1$. The cell growth is assumed to be contact inhibited and has been verified previously in our lab [77, 146]. Single frequency direct current (DC) simulations were performed to estimate the evolution of TEER with the growth of the cell monolayer in the apical (top) chamber.

3.3 Results

The microvessel mimetic (MVM) device serves as a physiological representation of the human blood vessel to study acute inflammatory responses *in*

vitro. The device was first characterized for physiological responses of endothelial cells in the absence of any inflammatory stimulus or neutrophil migration. Following this validation, neutrophil assays were performed, first under normal conditions and later in the presence of $\beta 1$ integrin-inhibition. These later assays were designed to address the effects of neutrophil migration on endothelial permeability using both electrical and tracer diffusion methods.

3.3.1 MVM Device Assembly and Flow Characterization

Shear Stress Generation

One of the most important characteristics of our MVM system over the majority of the cell culture platforms is the ability to grow endothelial cells under flow. A major limitation of 'transwell' inserts, is the inability to expose cells to shear stress. Post-capillary venules, which are the site of neutrophil diapedesis, typically experience 10-15 dynes/cm^2 of shear stress [166]. To achieve this, we developed a closed loop flow circuit to expose ECs to shear stress for 24 hours after their static growth for 24 hours. The flow setup is as shown in Figure 3.10. The nutrient reservoir consists of MCDB-131 complete medium needed for proper growth of ECs. This reservoir is also exposed to an incubator environment via 0.22 μm filter to allow gas exchange without compromising sterility of the media. The reservoir is connected to

a peristaltic pump to flow the media at a rate of ∼0.52 ml/min to generate the shear stress of 10 dynes/cm^2. The rotational velocity of the peristaltic pump depends on the type of tubing used and has been characterized for the desired flow rates. The flow rate and shear stress are tied by the Equation 3.1:

$$\tau = 6\mu Q/(wh^2) \tag{3.1}$$

where μ is the viscosity of the fluid, Q is the volumetric flow rate, w and h are the width and the height of the rectangular channel respectively.

Pulsation Dampening using a Fluidic Capacitor

Since the peristaltic pump relies on the motion of the rotations of the motor, the flow output is pulsatile and not continuous in nature. Microvessels are resistance vessels and experience continuous flow devoid of any pulsations [167]. To dampen the pulsations in our device, the output of the pump is connected to a fluidic capacitor. The capacitor is structurally similar to a reservoir except for being hermetically sealed. This concept is described in Figure 3.8. The compressibility of the trapped air inside the capacitor allows for absorbing the pressure oscillations, and renders a 'smooth' discharge during the refractory period of the peristaltic pump. The capacitor performance is characterized as shown in Figure 3.11, where blue curve represents noisy signal (flow pattern) upstream of the capacitor, while the red curve is the

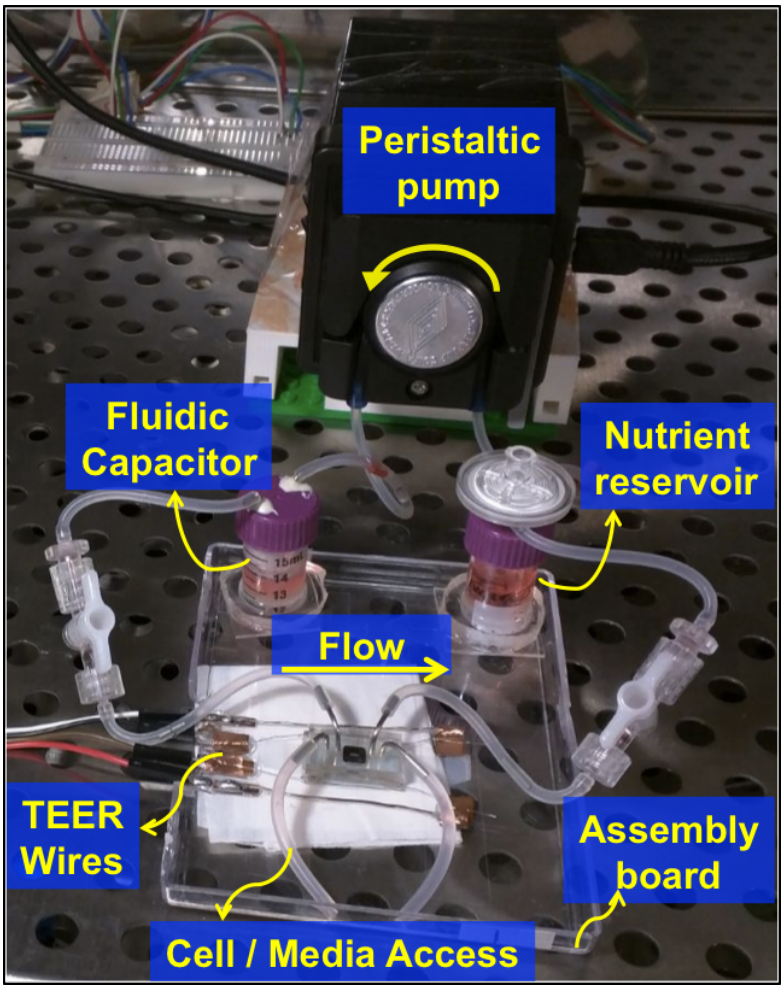

Figure 3.10: Flow Setup: Picture of the flow setup highlighting different components of the system. The nutrient reservoir hosts the media to feed the cells, and is exposed to incubator environment for gas exchange. The peristaltic pump delivers the media from the reservoir to the fluidic capacitor, which removes the pulsatile nature of the flow and renders a continuous discharge. It also acts as a bubble trap and feeds media to the apical side of the device. The other outlet of the apical side of the device is connected to the reservoir thus completing the flow circuit. The basal side of the device is exposed to open atmosphere to allow for further gas exchange. The TEER wires are connected to a breadboard circuit (not shown), which is further connected to EVOM Voltohmmeter for TEER measurements placed outside the incubator.

'smoothened' signal downstream of the capacitor and upstream of the actual device.

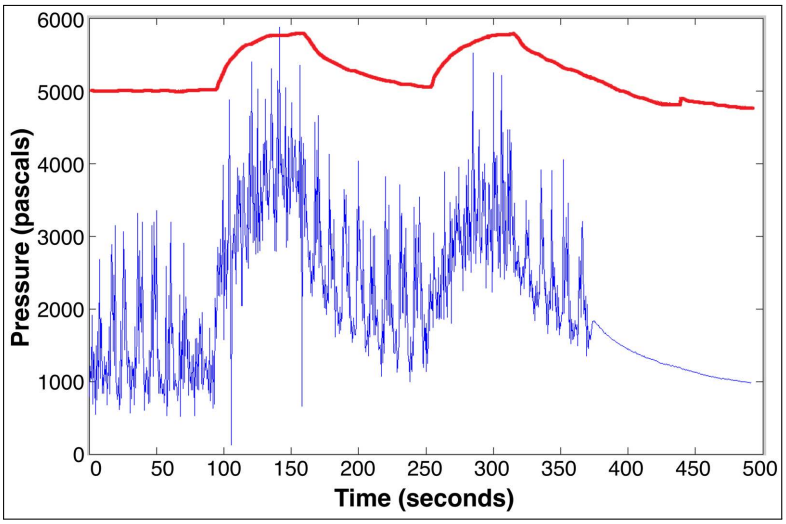

Figure 3.11: Pulsation Dampening: Pressure fluctuations are measured using pressure sensor connected before (blue noisy signal) and after (smooth red curves) the capacitor. The flow rate of the pump is rapidly changed from low (0.1 ml/min) to high (4 ml/min) settings that cause a sudden jump in pressure around 90 seconds. After the sudden rise, the flow rate is reduced to low setting and this cycle is repeated few times. Note the higher fluctuations in the 'before' signal (blue curve) with pressure amplitudes exceeding 1000 pascals. The 'after' signal (red curve) almost completely eliminates the fluctuations with the amplitude less than 50 pascals. The red curve has been plotted with an offset for visual clarity.

Shear Stress Verification

To empirically verify whether the shear stress generated within the apical chamber achieves the desired flow rates, we used particle tracking to deduce the volumetric flow rate. FITC-conjugated particles (1μm) were introduced

in the flow circuit in the absence of any endothelial cell culture, and were imaged at the flow rate of ∼40 μl/min to produce 1 dynes/cm^2 shear stress at the apical surface. Image processing in MATLAB^{TM} revealed the velocity of the particles, and shear stress was then calculated using Equation 3.2.

$$\tau_{wall} = 4\mu * v_{max}/h \tag{3.2}$$

where μ is viscosity, v_{max} is the maximum velocity, which is observed at the center of the flow channel, and h is the height of the channel. Figure 3.12 demonstrates agreement between the observed and theoretically calculated shear stress, thus verifying the accuracy of the peristaltic pump under use.

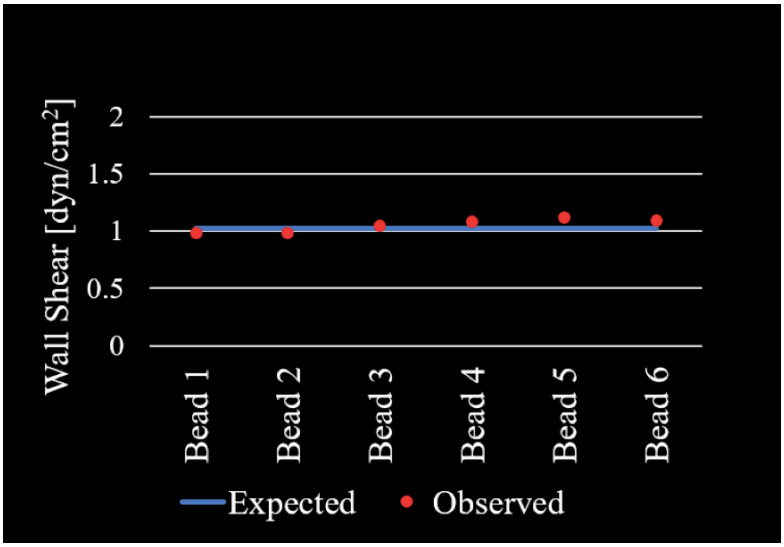

Figure 3.12: Flow Verification: 1 micron beads were imaged as they flow atop the membrane inside the device. Time-lapse imaging yielded velocities for 5 such beads that was used to estimate the shear stress.

3.3.2 Flow-conditioned Cell Culture

Endothelial cells are grown under static condition for first 24 hours atop collagen gel coated with human plasma fibronectin. This static culture allows the cells to achieve confluency before the induction of flow. The flow-induced shear stress then remodels the cell morphology and aligns the cell bodies in the direction of the flow. Figure 3.13a shows the phase images of endothelial cells grown under static condition for 24 hours. The same cell culture exposed to 10 dynes/cm^2 of shear stress realigns in the direction of flow as observed in Figure 3.13b.

Necessity of Luminal Collagen Gel

A key element of cell adhesion under shear stress is the strong interaction of the cell monolayer with the substrate. Both adhesive and cohesive forces play roles in maintaining cell-substrate interactions in the presence of high shear forces [69]. Although the silicon nanomembrane has native surface charge due to its resemblance to glass, the porous nature of the membrane makes it insufficient for the cells to adhere on the membrane surface. In the past, Gaborski and colleagues have found that microporous substrates provide discontinuous regions for cell attachment and can have negative effects on the ability of the cells to form strong focal adhesion complexes [68, 74]. In our own experience, we observe significant cell detachment within 2 hours when cells are grown directly on membrane with 3 μm pores (Figure 3.14b). Salminen et al. have developed dual scale micro-nanoporous membranes to

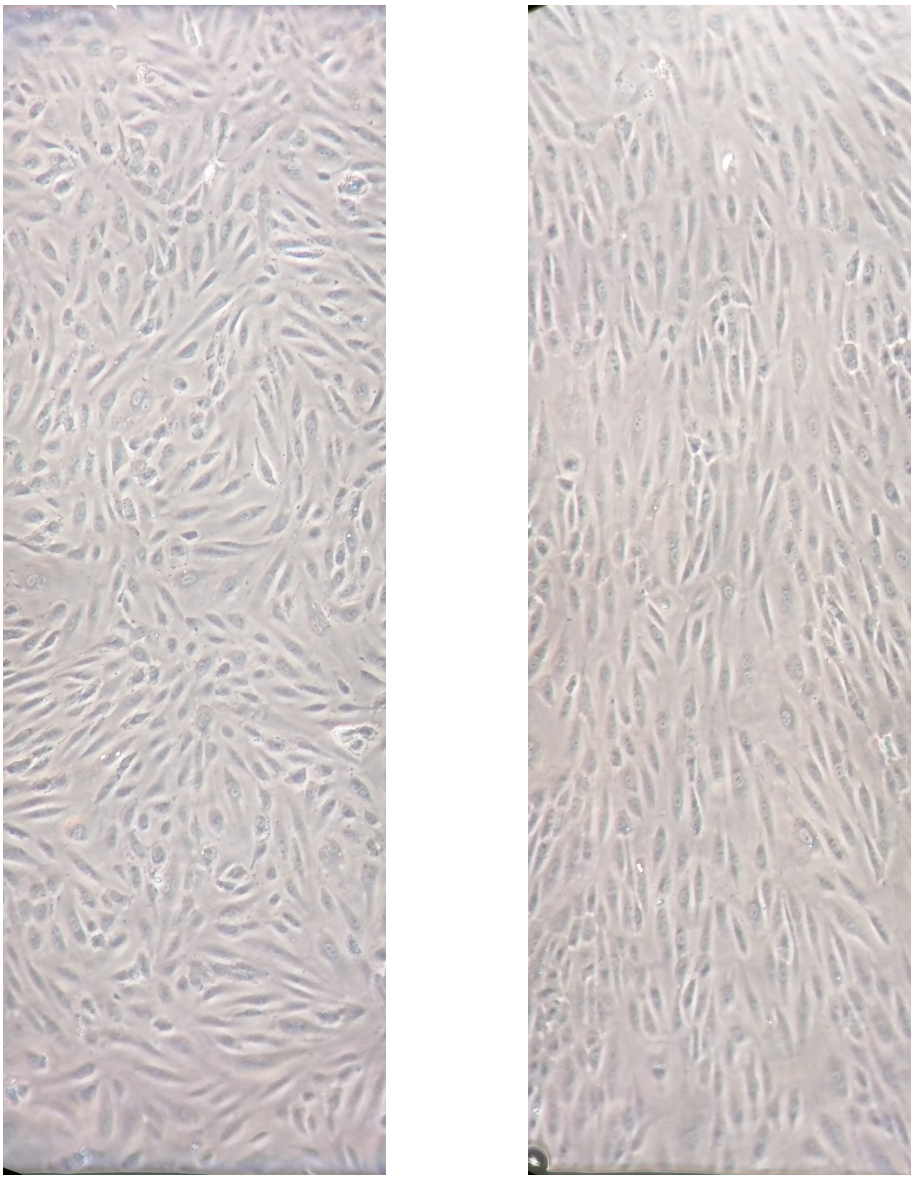

(a) **(b)**

Figure 3.13: Effect of Shear Stress on Endothelial Cells: Endothelial cells after 24 hours of static growth in MVM (a) are exposed to 10 dynes/cm^2 shear stress for another 24 hours (b). Notice the changes in the alignment of the cells along the long axis (flow direction).

avoid this cell loss, but it is a complex approach that requires sophisticated microfabrication tools [Salminen et al., Manuscript in review, SMALL]. To address cell loss in our device, we incorporated thin 100 micron layer of type 1 collagen atop the silicon membrane. This gel layer helps in creating a thin separation between the membrane and the endothelial monolayer and essentially provides a continuous substrate for enhanced cell adhesion that prevents any noticeable cell loss without affecting the quality of optical imaging.

The presence of the luminal collagen gel also renders a compliant surface for the growth of endothelial cells. The elastic moduli of acellular collagen gel is in the range of few kilopascals [168], and is more representative of the gels surrounding capillaries *in vivo* [67], as compared to silicon dioxide nanomembranes (whose moduli is in MPa range). Thus, in addition to enhanced cell attachment, the 100 micron thick type 1 collagen gel allows for more physiological growth of endothelial cells.

Alignment of Endothelial Cells

To further characterize the alignment of endothelial cells under shear on collagen gel-coated nanomembranes, we developed image processing algorithms to characterize the orientation of endothelial cells under flow. The algorithm thresholds the greyscale images and identifies the long and the short axis of the binarized cell bodies. These perpendicular axes define the orientation of the cells with respect to the X axis (short axis) and Y axis (flow direction).

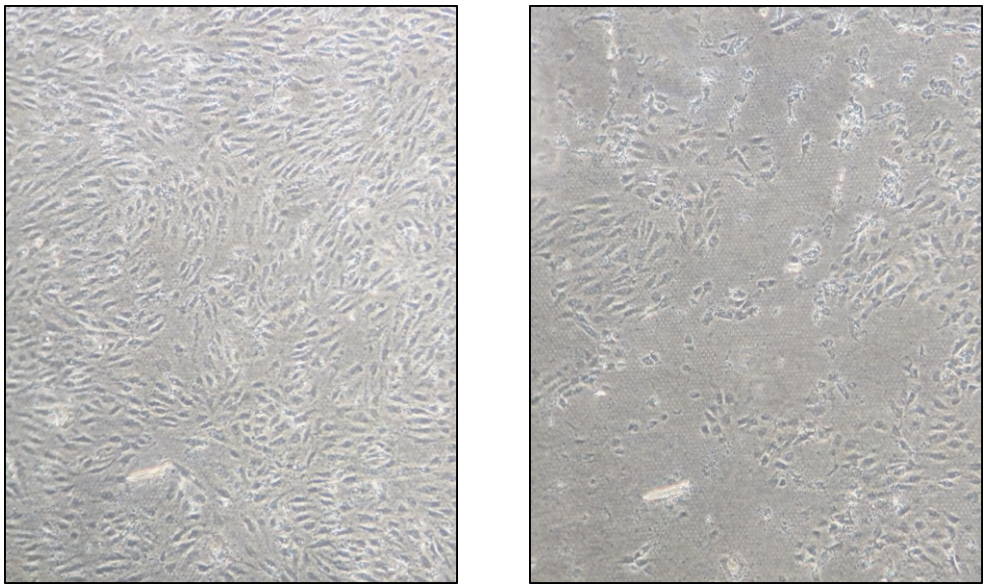

(a) **(b)**

Figure 3.14: Detachment of Endothelial Cells: Endothelial cells exposed to shear stress detach within 2 hours of shear stress exposure in the absence of collagen gel underneath cell surface.

The population-averaged orientation metric along with an intermediate image analysis step is shown in Figure 3.15. Note that this characterization is done using live phase images, eliminating the necessity of fixing the cells to stain for cortical actin and illustrating the simplicity of microscopy-based assays in physical characterization in the MVM platform.

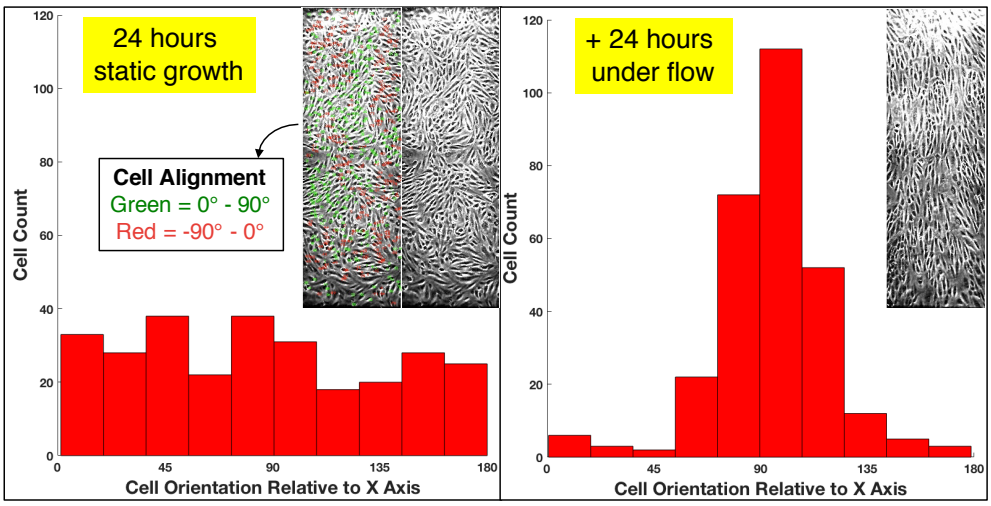

Figure 3.15: Alignment Characterization: Image analysis of the cells grown under shear to quantify the alignment of the HUVECs in the direction of the flow. Note the changes in histogram distribution before and after the flow. The red/green marked cells in the inset of left panel highlight an intermediate processing step to quantify the angular orientation of the cells to generate the histogram.

3.3.3 TEER Results

To characterize the barrier properties of the endothelial monolayer, the MVM device is equipped with biocompatible indium tin oxide (ITO) electrodes as

shown in Figure 3.7. There are multiple advantages of using ITO over conventional electrode materials used in the past. ITO is a thin film deposited on either polymer or glass substrate and, hence, is two dimensional in nature. Having 2D electrodes is beneficial to create more uniform electric fields and current densities, unlike the probe-based 'chopstick' electrodes used in commercially available TEER measurement instruments. Furthermore, these commercial instruments use silver-silver chloride electrodes, which may have cytotoxicity issues. For this reason, devices with silver electrodes are not continuously kept in contact with the biological media. Thus, the biophysical and electrochemical equilibrium established in the cell culture device gets potentially disturbed during each measurement due to the insertion of electrodes. For impedance spectroscopy, thin film gold and platinum electrodes are used in the commercial instruments such as ECIS systems (Applied Biophysics, Troy, NY). However, these materials are translucent, stiff, and do not allow bi-compartmental design of the devices for 3D assays. While a few studies have been published in the past that incorporate transparent thin film electrodes in a 3D design, they rely on polymer membranes for cell culturing, which greatly suffer from inferior phase imaging [108], and/or low permeabilities [107]. Thus, the MVM system we present features an enhanced TEER measurement system that addresses the limitations of the existing systems.

Figure 3.16 shows the evolution of electrical resistance over a period of $\sim$2 days under static or dynamic conditions. The red curve highlights the increment in the resistance as the cells proliferate under static conditions.

Continued growth under static conditions leads to a stabilization of the resistance, and TEER doesn't increase any further as indicated by the blue curve. This implies that ECs have reached confluence within the first 24 hours, and do not increase their barrier properties any further. However, if the cells are subjected to shear stress after reaching confluence, they do realign as demonstrated in Figure 3.13b. Along with this alignment, shear stress also contributes to tighter junction maturation and further increases the TEER to almost twice of the static cultures (brown curve). Subsequent treatment with thrombin (a barrier disrupting agent) immediately attacks the junctional integrity of ECs causing a sudden fall in the TEER values (black dashed line). The ability to measure these temporal changes in real-time is a useful feature of the MVM platform to characterize endothelial growth.

One important feature of this result is as indicated in the inset of Figure 3.16 that shows 2 panels of images with cells before and after shear. Despite the integration of multiple fluidic and electrical components in the miniaturized geometry of the device, the ability to perform live phase imaging (without any fluorescent staining) is unaffected. To our knowledge, this is the first demonstration of a dual chambered microphysiological system with a highly permeable substrate that is capable of performing live cell imaging and TEER measurements simultaneously.

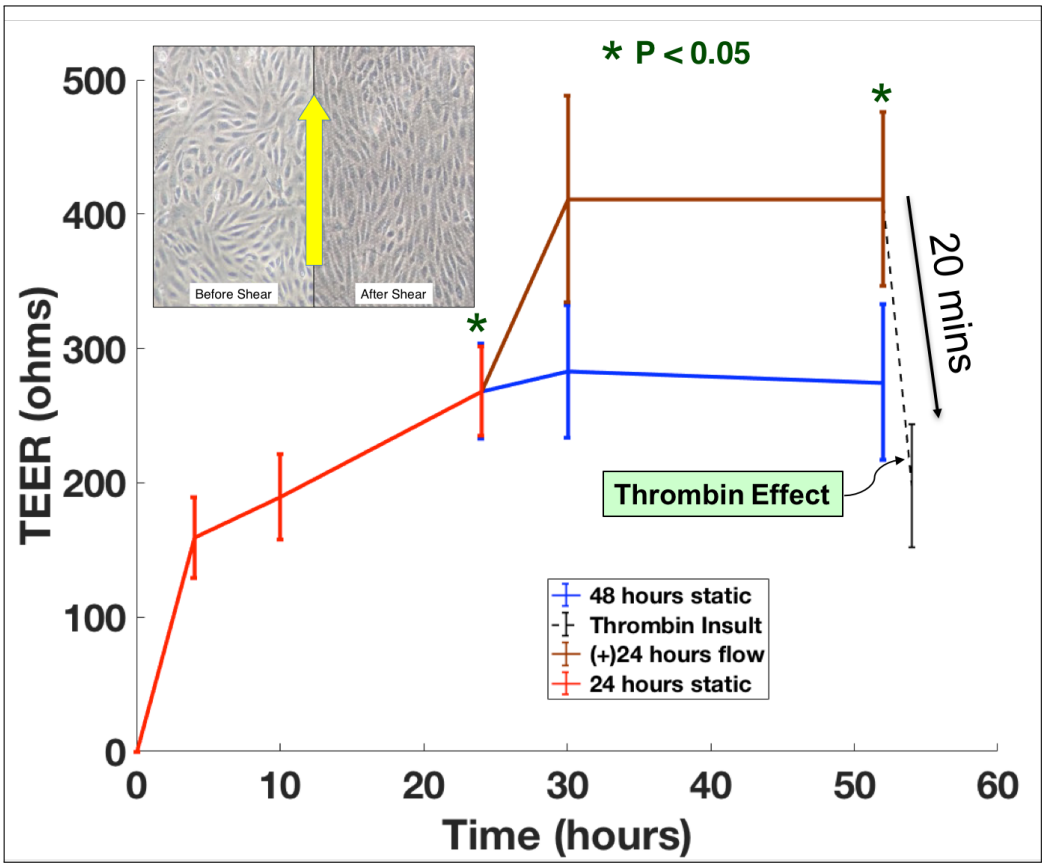

Figure 3.16: TEER vs Endothelial Growth: TEER measurement was performed over 48-52 hours post cell seeding in the MVM. TEER rises during first 24 hours (red curve), after which it remains stable in the absence of shear (blue curve), or increases to an elevated level in the presence of shear (brown curve). The addition of thrombin immediately causes the TEER to decay below 50% of its maximum value in less than half hour (black dashed line). Error bars represent standard error of mean with at least n=5. Inset shows the retainment of the imaging clarity in spite of the presence of fluidic and electronic accessories around the cell culturing area.

3.3.4 Mathematical Analysis of TEER Values

The TEER data presented in Figure 3.16 reports electrical resistance in ohms instead of more widely used ohms-cm^2 to report TEER values. In Chapter 2, we established the rationale behind the existing convention of reporting TEER in ohms-cm^2, the implicit assumptions in use, and the potential fallacy of these assumptions in custom microsystems [77]. We also suggested an alternative way of reporting TEER values using raw resistances, and the results of finite element analysis to convert resistances between systems having different geometries. Only such a careful analysis of TEER data can ensure that the values are not *blindly* compared across different systems, with erroneous over/underestimation of resistance values interpreted as properties of the barrier model. In this spirit, we modeled our existing MVM platform in COMSOL Multiphysics. The results of these simulations are as shown in Figure 3.17. The X axis represents the confluency level of the cells grown in the device, while the Y axis represents the net increase in the raw resistance values as reported in ohms. The evolution of the TEER values can be roughly explained by a biphasic behavior of cell growth as indicated by pink and green colors. During the initial stages of cell growth, the cells proliferate and occupy increasing amounts of porous membrane area, thus effectively decreasing the path of electric current through the barrier. However, in the absence of complete confluence and loose junction formations, ionic permeability does not change significantly and the rise in the TEER is modest. When the cells are beyond 98-99% confluent, cell growth slows down, most

likely due to contact inhibition [146]. At this stage, we suspect that increased cell-cell contact will lead to tighter junction maturation, causing the resistance to rise rapidly despite absence of apparent cell growth. The red dashed circle in the 'green' phase approximately marks the lower and upper limits of the TEER values obtained experimentally in our platform in the absence and presence of shear stress respectively. It needs to be noted that since 100% confluence is a theoretical singularity that yields infinite resistance in our model, the match between the experimental and theoretical values is bound to be over a broad range of values, as seen in Figure 3.17. This non-linear and biphasic increase of TEER over time/cell-confluence has also been observed in previous studies [102]. Furthermore, the COMSOL model also allowed us to analyze the electrical field behavior, as indicated by the non-uniform and 'bent' field lines shown in Figure 3.18. The impact of these nonlinear field lines is resultant in the non ohmic behavior of the microsystem, which makes it erroneous to report the TEER values in ohms-cm^2 (See Chapter 2 for more details).

3.3.5 Impedance Spectroscopy in MVM Platform

Our MVM platform can also be adopted to perform electrochemical impedance spectroscopy. Impedance spectroscopy involves measuring the impedance values of the biological sample over a wide frequency range, and has multiple benefits over single-frequency TEER measurements. Biological cells and tissues demonstrate a strong dependance on the alternating current (AC)

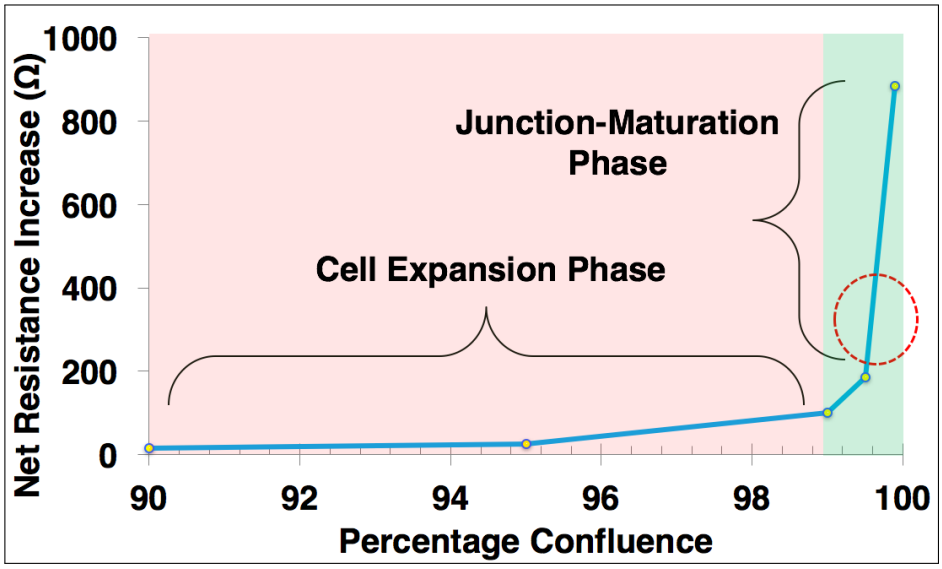

Figure 3.17: TEER Prediction in COMSOL Multiphysics: Non-linear nature of TEER progression inside the MVM device as simulated using COMSOL Multiphysics. TEER changes are subtler until the cells are 98-99% confluent, beyond which the resistance rises rapidly. The red dashed circle in that region represents the range of the values as observed experimentally and shown in Figure 3.16.

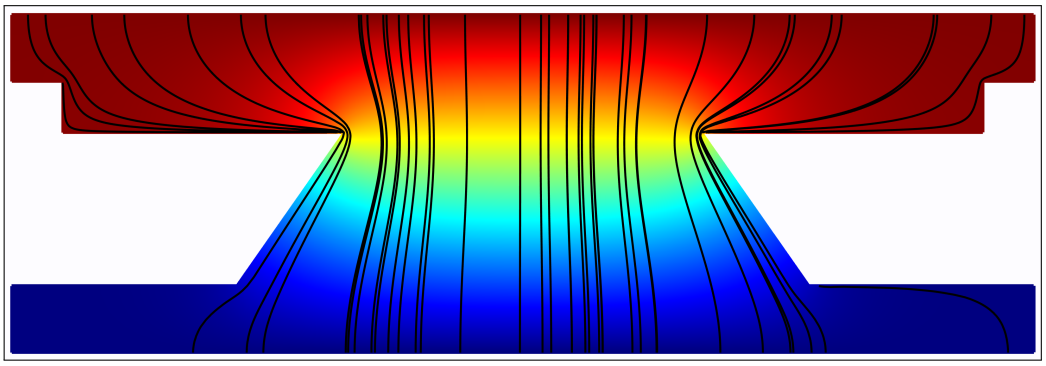

Figure 3.18: Electric Fieldlines in the MVM: 2D view of a FEA model of the MVM demonstrating the electric fieldlines, as simulated in COMSOL Multiphysics®. Notice the non-uniformity of the fieldlines, and bending around the corners generating overestimated resistance values.

and the frequency used for recording the impedance. Cell-cell junctions form tight barriers and provide resistive impedance to the ionic species. Cell membrane consists of lipid bilayers that acts as a thin insulator separating electrolytic media (cytoplasm and extracellular media), thus providing capacitive impedance in the presence of alternating current. Thus, the cell monolayer acts as a RC circuit and can be simplified for analysis using the schematic provided in Figure 3.19.

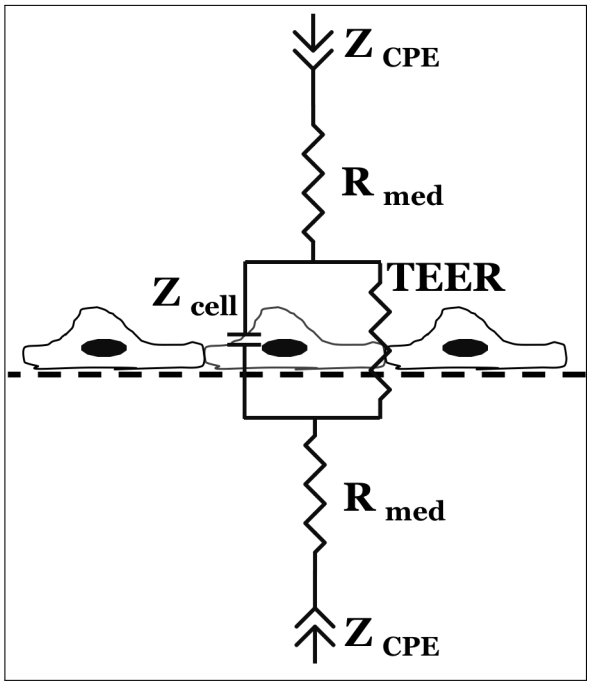

Figure 3.19: Equivalent Circuit for Impedance Analysis: Equivalent circuit representing the different biological and electrochemical components contributing to the total impedance as measured using impedance analyzer. Z_{CPE} is the impedance of the ITO-media interface that acts as a constant phase element (CPE). Z_{cell} is the capacitive impedance offered by the cell lipid bilayer while R_{med} is the resistance offered by the cell media.

Capacitive impedance varies inversely with applied frequency, while resistance has a constant magnitude. Due to the parallel nature of the RC circuit, at low frequencies, the current chooses the resistive path of transport, and at higher frequencies, it chooses the capacitive path. Thus, low frequency impedance values capture the intercellular resistance and is used for TEER measurement, whereas high frequency values capture cell occupancy or area-coverage, and is used to determine the confluency of the monolayer. This dual behavior of the cell monolayer makes impedance spectroscopy a useful tool to characterize biological growth. Figure 3.20 captures the impedance scans in the MVM before cell seeding and after 2 days of HUVEC culture.

For our experiments, we analyzed impedance at both 12.5 Hz (as measured by EVOM Voltohmmeter), and also at 1000 Hz. We observed similar trends for all the experimental conditions at both the frequencies, but the signal to noise ratio was better for 1000 Hz experiments (data not shown). Thus, for all the subsequent experimental conditions, impedance data were analyzed at the frequency of 1000 Hz.

3.3.6 Neutrophil Diapedesis in MVM Platform

Neutrophil activation is the hallmark of acute inflammation and is involved in various vascular pathologies. In this work, we aim to understand the impact of neutrophil migration through the subendothelial basement membrane (BM). Towards this end, we first developed 3D chemotaxis assays to allow for neutrophil extravasation from the apical to basal chambers in the presence of

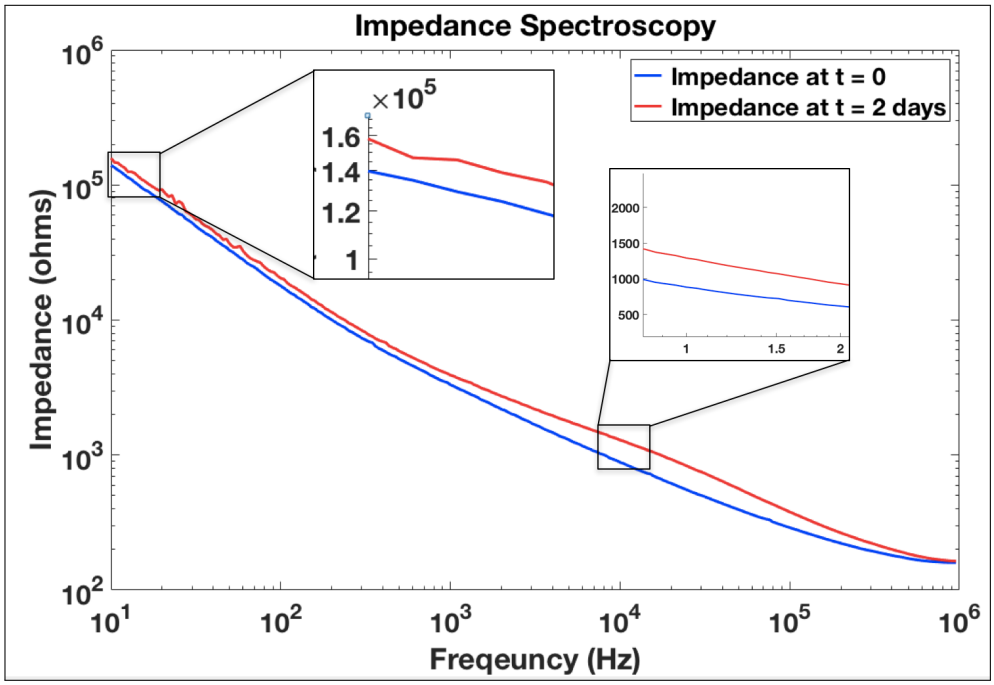

Figure 3.20: Growth Characterization Using Impedance Analysis: Representative impedance scans before seeding HUVECs (blue curve), and 2 days after seeding (24 hours static + 24 hours flow, red curve). Insets show the elevated values of net impedance over the period of 2 days, with different amounts of increments over different ranges of frequency.

chemotactic cues. Fresh isolated human neutrophils were added in the apical chamber consisting of endothelial cells, and 10 nM fMLP was added in the basal chamber. fMLP is a small bacterial tri-peptide known to cause potent neutrophil activation, and is widely used for neutrophil chemotaxis. Figure 3.21 illustrates the schematic of the device modified to study 3D neutrophil chemotaxis.

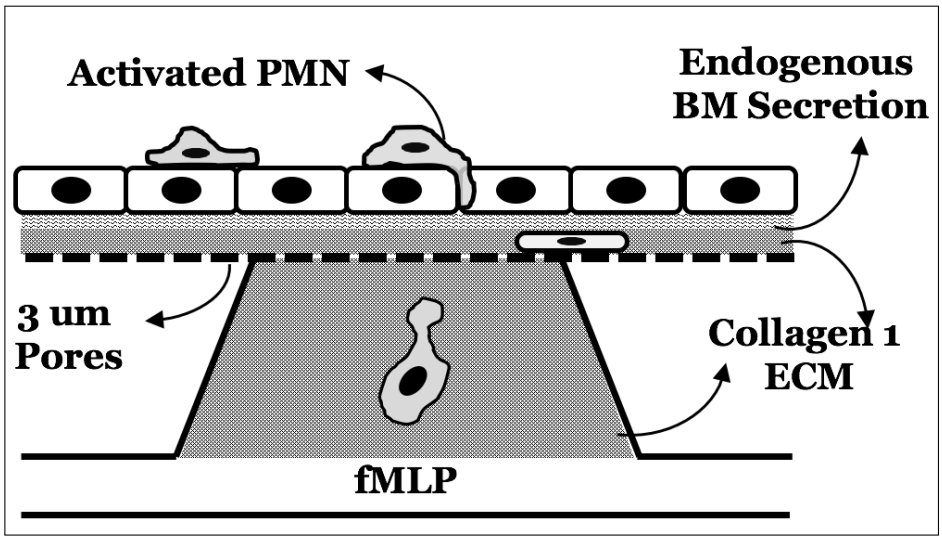

Figure 3.21: Neutrophil Migration Schematic: 2D Schematic of the MVM setup used to facilitate and study neutrophil chemotaxis under the influence of fMLP. Neutrophils exit the luminal side, egress through the endothelial monolayer and the secreted basement membrane and finally through the thick collagen gel (ECM).

While the 100 micron thin collagen layer above the membrane helps in enhancing endothelial cell attachment to the substrate, the presence of a much thicker (600 micron) collagen gel in the basal compartment mimics the extracellular matrix (ECM) and serves as a 'deep tissue' for neutrophil migration.

This is also valid because type 1 collagen is the most abundant ECM protein. fMLP diffuses rapidly through the porous ECM layer creating a soluble gradient of chemoattractant, causing neutrophil activation and migration towards the basal chamber. The ability to visualize this process is feasible because neutrophils undergo an obvious phase change from bright to dark upon transendothelial migration indicating their departure from the luminal compartment. Figure 3.22 shows the process of transendothelial migration as observed using live phase imaging.

In Figure 3.22, Panel a points to a phase-bright neutrophil at an endothelial cell border. Panels b and c show the changes in the phase of a neutrophil undergoing transendothelial migration at the junction between two endothelial cells. Panels d and e point to the gap created by neutrophil 'squeezing' (blue arrows). Panels e and f show a fully transmigrated neutrophil in phase dark undergoing subendothelial migration In Panel f, we see the closing of the apparent gap, marking the completion of the transmigration process. These temporal snapshots of a live migration process are essential to understand the behavior of egressing leukocytes and can have further implications to advance the state-of-the-art knowledge of different disease models [Mossu et al., Manuscript in press, JCBFM; refer Chapter 4 for further discussion]. We further suspect that this creation of a physical gap might be instrumental in altering the endothelial permeability to a measurable extent. Although this process was transient, one can appreciate cumulative neutrophil migration events may sum up to a significant leakage of ionic species across the barrier

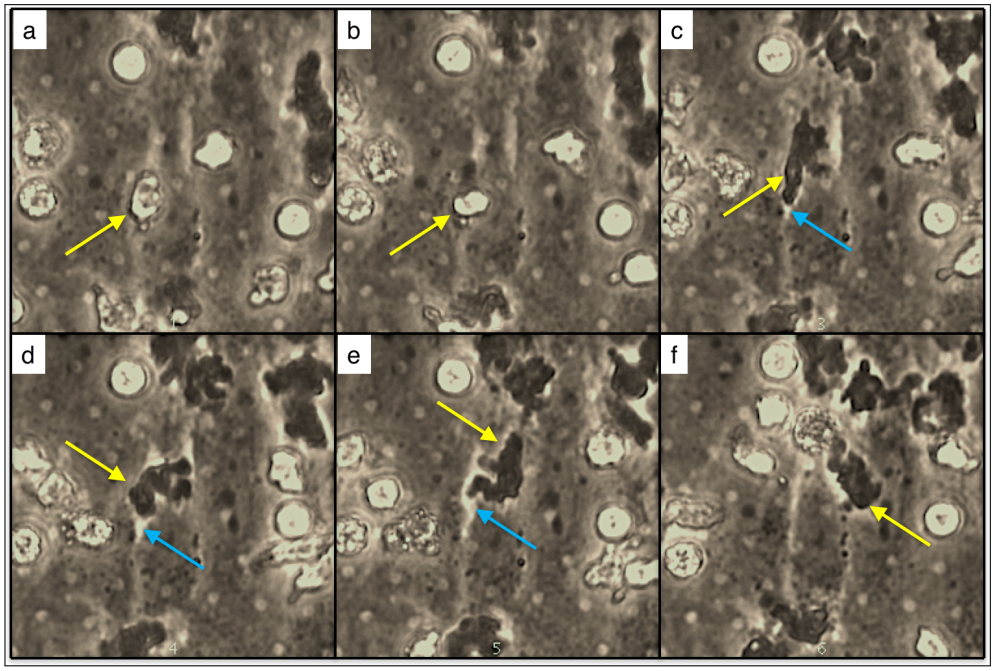

Figure 3.22: Neutrophil Transendothelial Migration: Neutrophil transendothelial migration can be observed from phase change of neutrophils from bright to dark. Yellow arrows in all the 6 panels represent a neutrophil undergoing transmigration, while the blue arrows in panels c, d, and e point to the gap created within the endothelial monolayer as neutrophil egresses between the adjacent endothelial cells. The 'gap' is observed by bright exposure between endothelial cells and is suspected to be seen due to transient contractions of the endothelial cell membrane at the spots affected by neutrophil transmigration. The field of view also demonstrates many other neutrophils in phase bright or phase dark, indicating that neutrophils migrate at different rates.

that can impact the net electrical resistance.

3.3.7 Electron Microscopy to Image Neutrophil Transmigration

To further investigate the detailed nuances of neutrophil migration, samples were imaged under scanning electron microscopy. Sample preparation for electron microscopy is described in the Methods' section. Figure 3.23 is a representative image that captured an activated neutrophil transmigrating through the endothelial junction. Note the tight barrier established by endothelial cells. The apparent gaps in the monolayer (green arrows, also discussed above) expose the underlying collagen gel, which is also shown in Figure 3.24. The collagen gel is a crosslinked structure with a dense mesh providing tortuous paths for molecular diffusion and cellular migration. The concentration of 2 mg/ml collagen gel leads to mesh formation with openings of $\sim$3 microns [169], which is ideal for neutrophil migration. Electron microscopy allows us to analyze subcellular events at higher resolution and magnification, which is not possible using optical microscopy. Figure 3.25 further elucidates various biological and physical elements of the MVM and the interplay between them.

The collagen gel atop the silicon nanomembrane can be 'lifted' above the supporting scaffold after careful desiccation procedures. The peeled-off collagen gel also allows us to image the porous membrane, which is not directly accessible otherwise. HUVECs seeded on the collagen gel can be

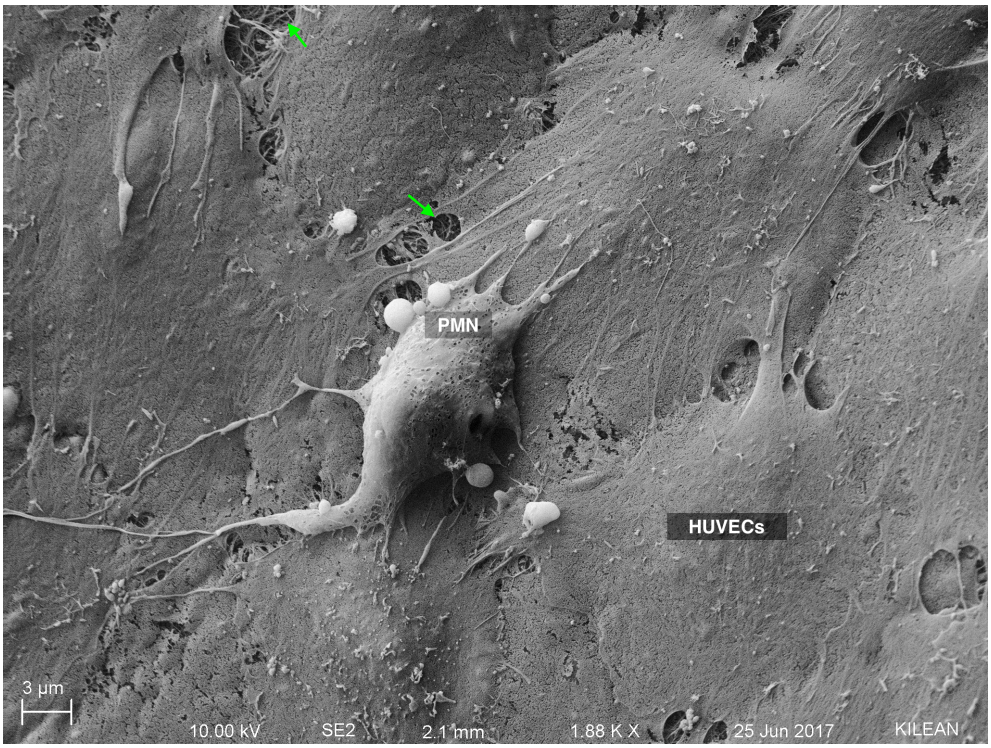

Figure 3.23: Scanning Electron Microscopy (SEM): SEM image capturing a activated neutrophil (labeled as polymorphonuclear granulocyte (PMN)) attempting to transmigrate through a confluent endothelial monolayer seeded atop type 1 collagen gel, as exposed at few locations labeled by green arrows.

observed to be neatly aligned in the direction of the flow (long axis of the channel) in Figure 3.25. The black inset indicates a neutrophil escaping the top gel and heading towards the microporous membrane for further egress, whereas the yellow inset shows neutrophils in already advanced stages of transmembrane migration. The co-localization of neutrophils with pores in the membrane indicate this behavior. The capability of an *in vitro* platform to provide this rich physiological information with relatively easy sample

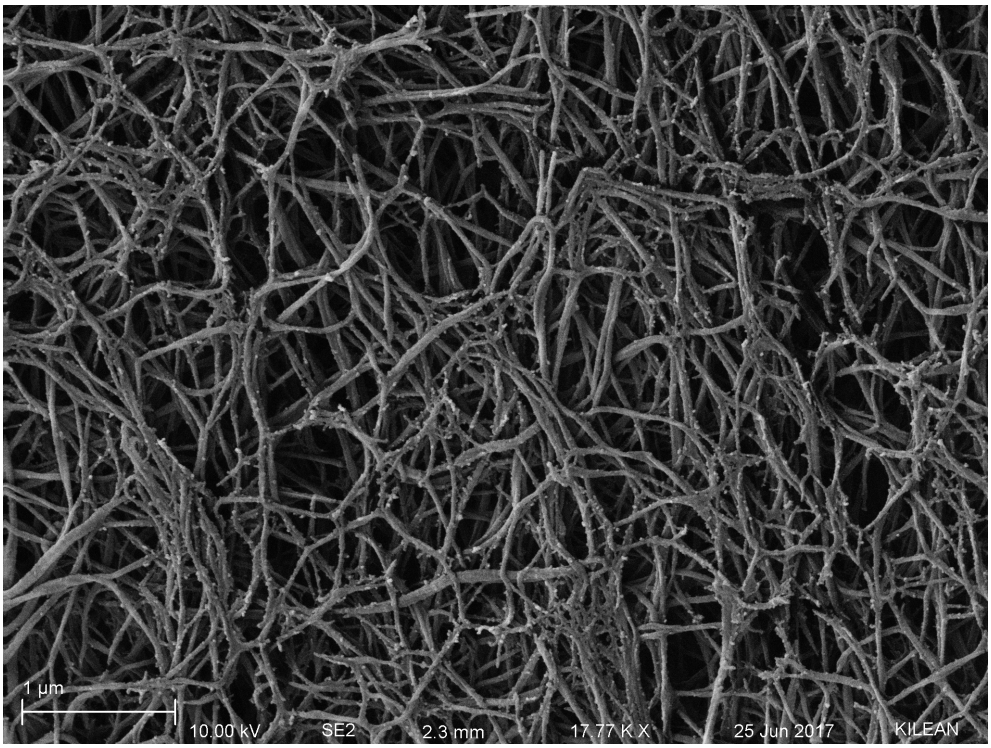

Figure 3.24: Collagen Gel under SEM: SEM image of polymerized collagen 1 gel. Note the crosslinked mesh-like morphology presenting a tortuous and *apparently* steric path for neutrophil migration.

preparation demonstrates the added benefit of the MVM platform.

3.3.8 Influence of Blocking Neutrophil Basement Membrane Migration

Neutrophils need to cross the endothelial basement membrane (BM) to be able to invade the interstitial matrix during chemotaxis. Neutrophil migration on BM is integrin dependent and relies on their ability to recognize the

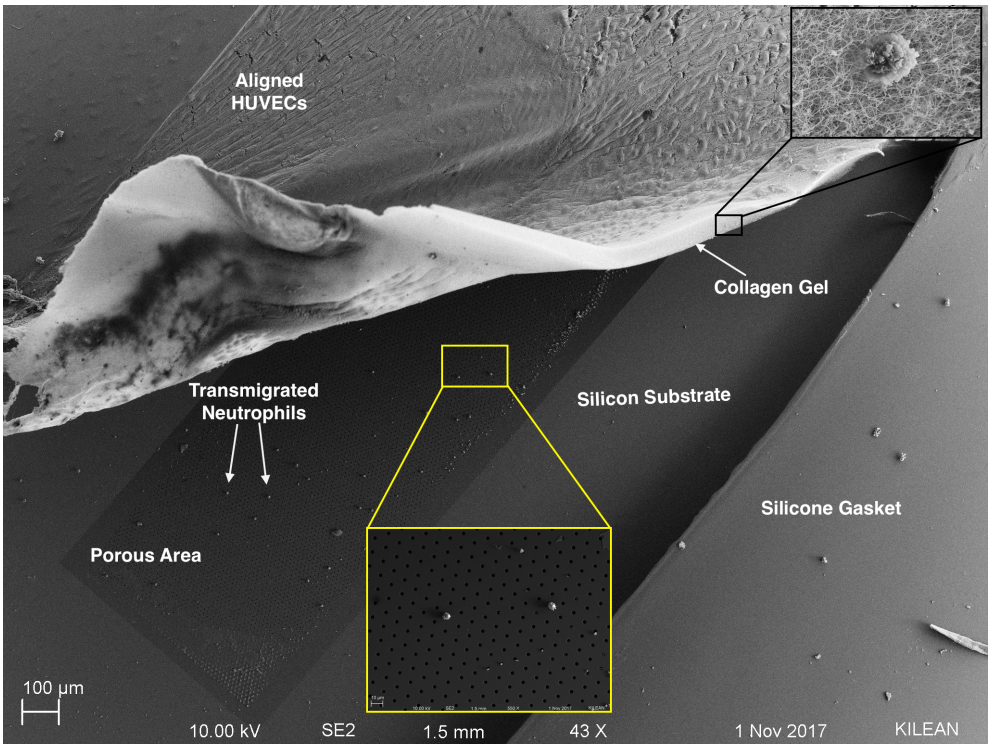

Figure 3.25: 3D Migration of Neutrophils under SEM: SEM image highlighting different components of the MVM platform fixed while under operation. Black inset: A single neutrophil embedded in the collagen gel as it is invading through the gel layer and proceeding towards the microporous membrane for further egress. Yellow inset: neutrophils already transmigrated through endothelial and collagen layers are co-localized with the pores in the membrane, about to egress to the basal side towards the fMLP source.

ligands present in the BM available for migration. $\beta 1$ integrins recognize a wide variety of BM ligands as listed in Table 3.3.

Table 3.3: ECM Ligands of $\beta 1$ Integrins: Different integrins on neutrophil surface recognizing major ECM proteins

ECM Protein	**Alpha subunits pairing with $\beta 1$ subunit**
Fibronectin	$\alpha_2, \alpha_3, \alpha_4, \alpha_5, \alpha_8, \alpha_{10}, \alpha_{11}, \alpha_v$
Collagen	$\alpha_1, \alpha_2, \alpha 10, \alpha_{11}$
Laminin	$\alpha_1, \alpha_2, \alpha_6, \alpha_7$
VCAM-1	α_4, α_9
Fibrinogen	α_5
Vitronectin	α_v

Also known as CD29, the $\beta 1$ subunit pairs with different α subunits to form different integrin moieties capable of recognizing BM and ECM proteins. Due to their ability to recognize and bind to a large number of BM proteins, we decided to study the effects of blocking $\beta 1$ integrins on neutrophil surface using pan-$\beta 1$ blocking antibody. Similar blocking approaches were also used by Nash and colleagues in inhibiting BM migration of neutrophils [44, 47]. Neutrophils express $\beta 2$ (CD18) integrins constitutively, whereas the expression of $\beta 1$ integrins depends on the activation status of the neutrophil and involves upstream activation of other signaling pathways [170]. Hence, to enhance the inhibition capabilities of the blocking antibody, neutrophils were incubated with anti-CD29 blocking antibody while undergoing fMLP chemotaxis. fMLP activation is presumed to increase the expression of $\beta 1$ integrins on the surface, and in the presence of the blocking antibody, they

will be inactivated. Neutrophils added in the apical chamber were imaged prior to fMLP addition, and after introducing fMLP they were allowed to migrate for 3 hours. After the 3 hours, neutrophils in the same field of view, but present in the basal chamber, were imaged. The count of neutrophils in the basal chamber at the 3 hour time point was divided by the count of neutrophils in the apical region at initial time point to yield the percentage migration of the neutrophils. Representative images used for this analysis are shown in Figure 3.26.

The data obtained after image analysis can be quantified as shown in Figure 3.27. The error bars represent the standard error of the mean, thus demonstrating a statistically significant difference in the number of neutrophils migrated across the basement membrane over the course of 3 hours with and without blocking $\beta 1$ integrins.

To further ensure that the blocking antibody does not alter the endothelial attachment to its native basement membrane, similar blocking experiments were performed in the absence of neutrophils but for shorter duration. TEER measurements were obtained upon the addition of $\beta 1$ blocking antibody within 30-45 minutes. During this time course, the endothelial cells did not demonstrate any noticeable morphological changes indicating the intact attachment of the HUVECs to their basal lamina. After blocking treatments, the cells were treated with thrombin as a positive control, which caused severe disruption of the barrier properties and decay in TEER signal, as summarized in Figure 3.28. The contrast with this positive control strongly suggests that

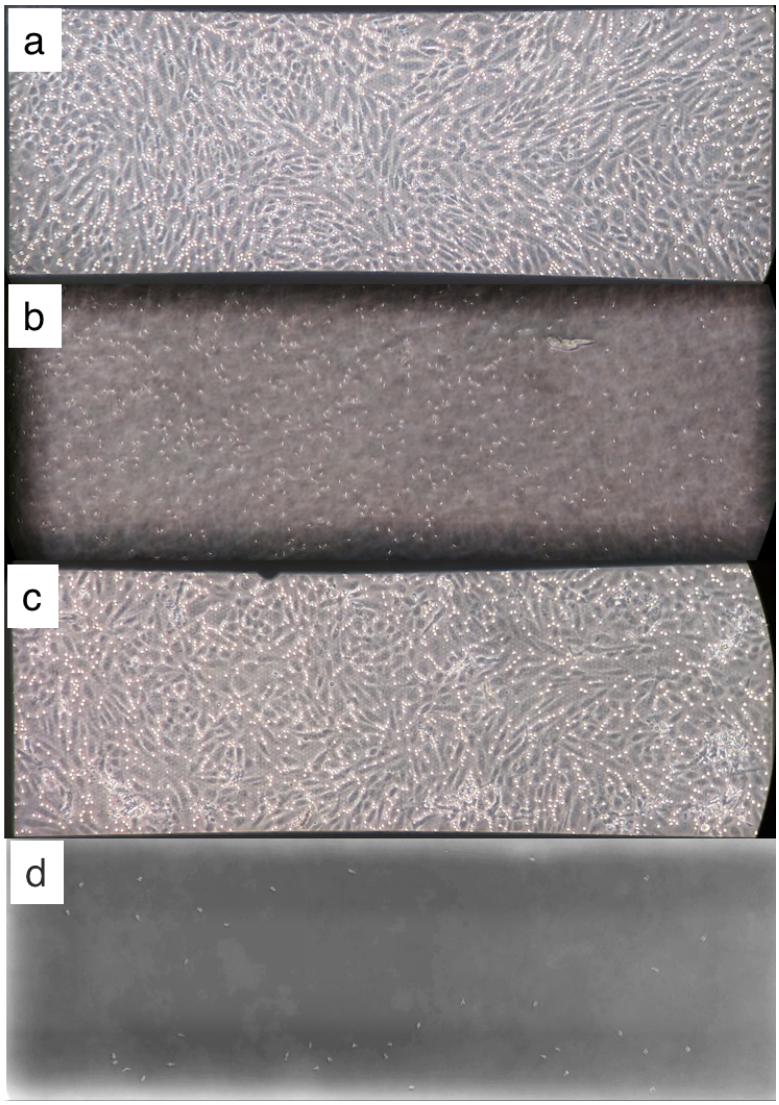

Figure 3.26: Blocking Neutrophil Migration: (a) and (c) are the live phase images of neutrophils seeded on endothelial cultures without and with blocking antibody respectively, as viewed in the apical compartment. (b) and (d) are the corresponding images of neutrophils without and with blocking antibody respectively, as imaged in the basal chamber after 3 hours of migration. (d) has been imaged in the absence of a phase ring to avoid any optical interference from the endothelial cells and improve the imaging-contrast for the neutrophils in the basal chamber.

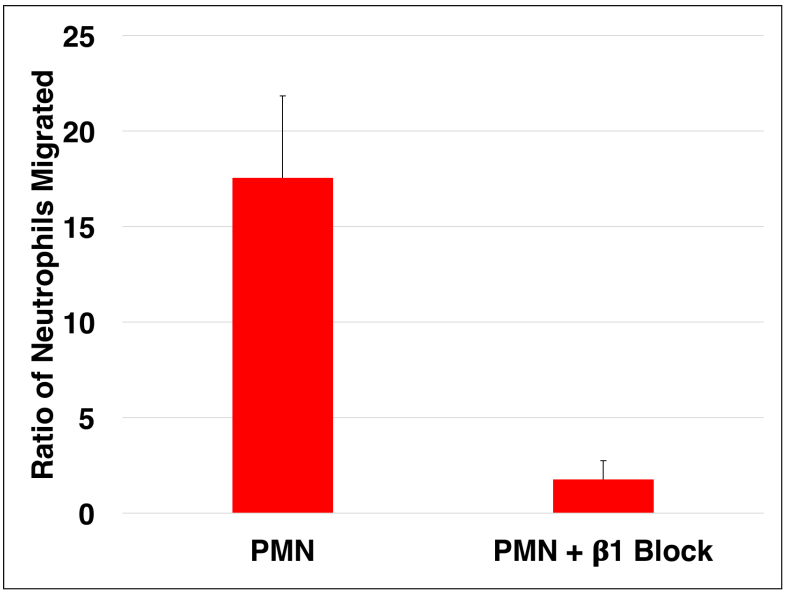

Figure 3.27: Effects of $\beta 1$ Blocking on Neutrophil Migration: Cell counts from the basal and apical images in Figure 3.26 revealed that the migration of neutrophils under the influence of $\beta 1$ blocking antibody is significantly reduced by almost a order of magnitude. n=3 for both conditions.

anti-CD29 antibody has no effect on the baseline endothelial barrier function.

3.3.9 Neutrophil Migration - Impedance Analysis

We used impedance spectroscopy to understand the impact of neutrophil trans- and subendothelial migration on barrier properties. The baseline characterization of the impedance spectroscopy was performed as shown in Figure 3.20. After 48 hours of endothelial culturing, neutrophils were added in the apical chamber either with or without blocking antibody as described above.

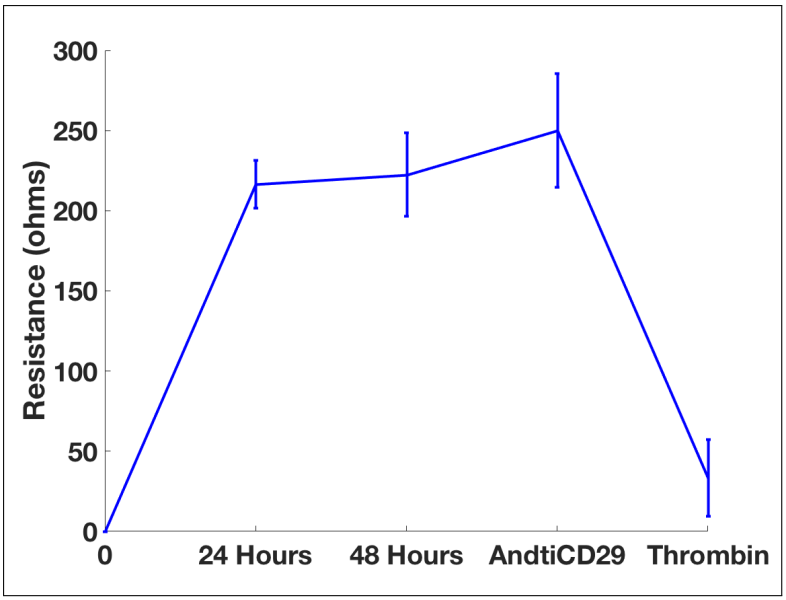

Figure 3.28: Effects of $\beta 1$ Blocking on HUVECs Alone: Presence of $\beta 1$ integrin blocking antibody ("AntiCD29" antibody) does not significantly affect the native endothelial barrier properties as observed by TEER measurement. The blocking antibody was immediately added after the 48 hour measurement, and thrombin was added after the antibody samples were washed away. The time-axis is expanded for visual clarity of the events.

An impedance scan was started to yield an entire frequency sweep per minute for a total of 20-30 minutes per device. The data obtained was median-filtered (using manually adjusted window sizes) for noise removal and fit using exponential decay. The impedance signals upon neutrophil migration in the presence or absence of antibody are shown in Figure 3.29. Impedance scans are normalized to their initial time points to yield a common starting point for appropriate comparisons. While the decay in the impedance values is about $\sim 22\%$ for control neutrophils, it is only $\sim 12\%$ for antibody-treated

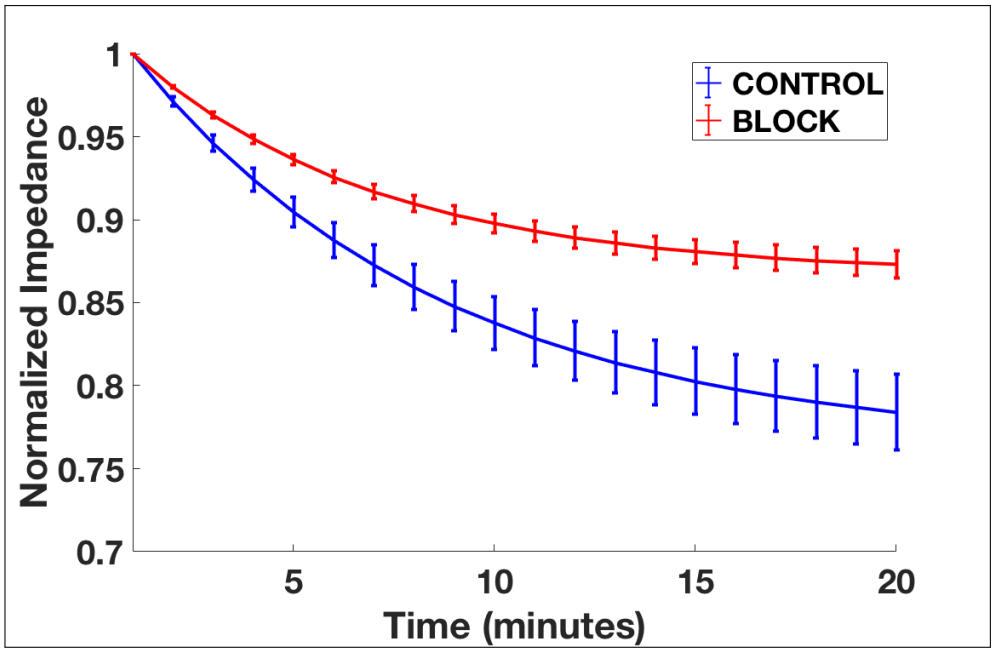

Figure 3.29: Impedance Analysis During Neutrophil Migration: Differential decay in the net impedance during neutrophil migration with (red curve) and without (blue curve) the blocking of $\beta 1$ integrins on neutrophil surface. Impedance values for each individual scan is normalized to its initial value before averaging, to yield a common starting point for comparison. n=3 for each test condition. Error bars represent standard error of the means.

neutrophils, demonstrating significant protective effect of blocking $\beta 1$ integrins against decreased barrier function. This also indicates that breaching the basement membrane makes a significant contribution to the overall increase in endothelial permeability.

3.3.10 Neutrophil Migration - Dextran Permeability

To investigate the effects of neutrophil transmigration on macromolecular permeability, we implemented tracer diffusion assays using 10 kDa FITC-dextran (size $<$ 3 nm). Fluorescent dextran was introduced in the apical chamber with neutrophils with or without the blocking antibody. Using precise focusing and optimized image acquisition parameters, the basal side of the membrane was imaged to observe the changes in the intensity of fluorescence signal over periods of 20-30 minutes (Figure 3.9). This recovery was analyzed for neutrophil migration events without and with the blocking antibody present in the solution. The results are summarized in Figure 3.30. All the experiments start at a very similar baseline indicating the high reproducibility of our imaging assay. While the increase in the basal fluorescent signal is 3-4x in 20 minutes for untreated neutrophils, the corresponding increase is significantly lower for neutrophils in the presence of β1 blocking antibody. This result confirms that there are reduced permeability changes associated with neutrophil egress when the BM migration of neutrophils is reduced by blocking treatments.

Finally, we repeated the electron microscopy experiments after permeability measurements to ensure the short-term blocking effects of antibody ($<$30 minutes). After the fluorescence data was acquired, we prepared the samples for SEM imaging as described in Materials and Methods Section, and allowed it desiccate for $\sim$10 days. This allowed us to 'peel back' the top collagen layer (as illustrated in Figure 3.25). The representative image

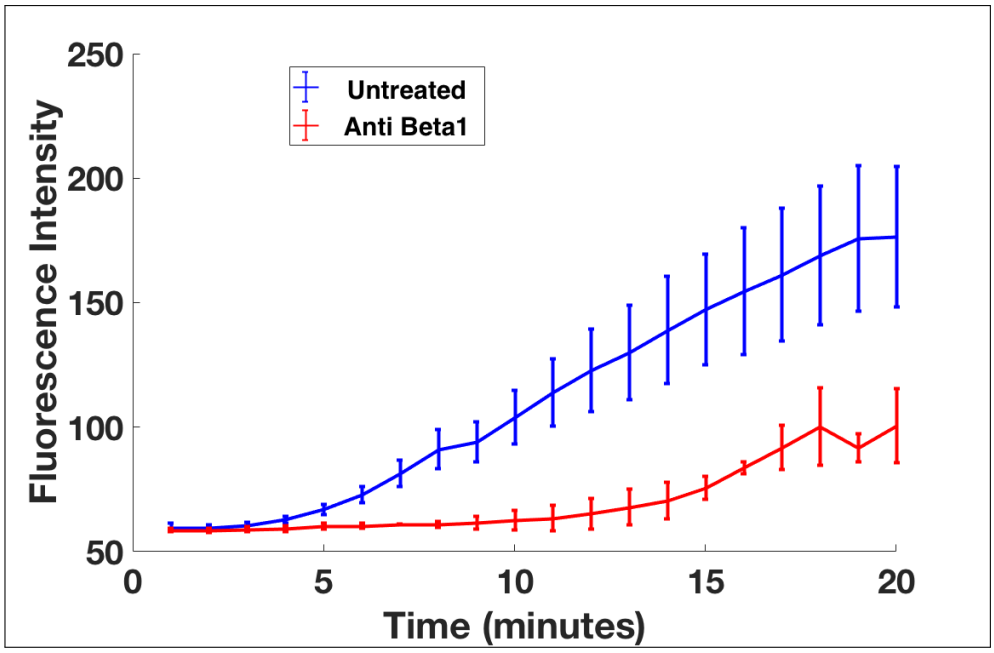

Figure 3.30: Fluorescence Analysis During Neutrophil Migration: Using the setup as shown in Figure 3.9, diffusion of 10 kDa FITC-dextran is observed by measuring the raw fluorescent intensity plotted on Y axis. The increase in fluorescent intensity is different in the case of control neutrophils (blue curve) and $\beta 1$ integrin-blocked neutrophils (red curve). n=5 for control condition, n=2 for blocking condition. Error bars represent standard error of the means.

is shown in Figure 3.31. We did not find any neutrophil population that had egressed beyond the collagen layer, thus, validating the inhibitory effects of the antibody treatment.

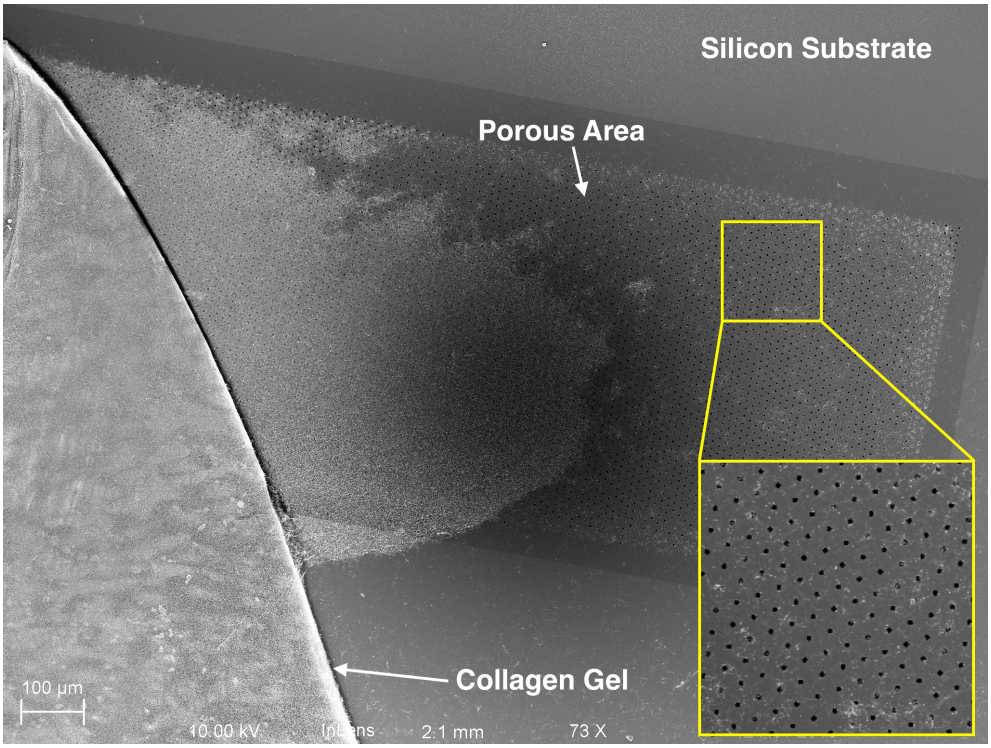

Figure 3.31: 3D Migration of $\beta 1$ integrin-blocked Neutrophils under SEM: The luminal collagen gel is peeled back to image the neutrophil population that has migrated beyond the basement membrane of endothelial monolayer. The yellow inset shows the zoomed-in portion of the membrane indicating the absence of neutrophils, which have egressed beyond the collagen gel. The entire membrane-area was thoroughly scanned to identify any neutrophils present on the porous membrane.

3.4 Discussion

Microvessels consist of arterioles, capillaries, and venules. They are responsible for oxygen and nutrient exchange and play a crucial role in maintaining and restoring homeostasis. Endothelial cells, which line the inner lumen of the vascular beds, are responsible for creating a physical barrier between the blood and the extravascular tissues. The integrity of the endothelial barrier, is thus, extremely important for regulating vascular tone, and maintaining a *healthy* trafficking of proteins, micromolecules, nutrients, and cells of different origins across the vessel walls. Compromised endothelial barriers are the cause of numerous disease pathologies, and are often responsible for severe morbidity and mortality in local and systemic inflammatory disorders. Thus, the proper mechanistic understanding of endothelial permeability under normal physiological conditions, and their subsequent disruption during pathological events may be the key to improving survival outcomes in clinical settings.

Current *in vitro* Systems

Over the last decade, multiple microfluidic platforms and devices have been published in the literature or made available commercially to study microvessel pathophysiology *in vitro*. Broadly speaking, these devices fall into two main categories: 1) membrane-free platforms developed using microfabrication procedures and/or tissue engineering based approaches using patterned

hydrogels or other biomaterials, and 2) microsystems with a membrane for monoculture and/or coculture applications with and/or without fluid shear stress. The membrane-free systems rely on ECM gels to form and demarcate two compartments. This makes these devices unsuitable for shear stress application because they rely on the stiffness of the polymerized gel to contain the flow. Also these platforms usually require fluorescent staining for confocal imaging. Microsystems incorporating an artificial membrane aim to solve these issues but are limited by the choice of the membrane - track-etched (TE) and PDMS membranes. These membranes are thick, have low permeability and suffer from poor optical imaging. Overcoming these limitations of existing technologies in recreating the physiological microenvironment while preserving metrological readouts have been the motivation behind this work.

Silicon Nanomembranes and MVM Platform

The work presented here aims to develop a unique multi-functional platform to investigate the effects of leukocyte activation on endothelial permeability *in vitro*. The platform developed and used for this study features silicon nanomembrane technology that has found applications in diverse areas of biomedical sciences for basic, applied, and translational research [109, 142]. The nanomembrane technology has revolutionary potential for bioseparations due to its ability to filter closely related biomolecules on the basis of size, shape, and charge in a precise and regulated manner. The current work further pushes the application of the silicon nanomembrane technology for cell

culturing, and successfully creates an *in vitro* model of blood-tissue barrier for diagnostic and preclinical therapeutic research.

Apart from its clear benefits in terms of imaging, porosity, and thinness, these membranes are compatible with standard microfabrication processes that essentially revolve around silicon and other semiconductor-based nanomaterials. These standardized microfabrication techniques also allow for mass-manufacturability, with each 6 inch silicon wafer producing around 400 membrane 'chips', reducing the per device cost of manufacturing. The focus of the current study is to build a microsystem around silicon nanomembranes to exploit their advantages and create physiologically relevant *in vitro* models of the blood-tissue barrier. The MVM platform reported here is an advanced version, and addresses different shortcomings of the earlier published iterations [Salminen et al., Manuscript in review, SMALL; Mossu et al., Manuscript in press, JCBFM]. This device, for the first time, incorporates the ability to monitor intact endothelial permeability, with minimum intervention and allowing for live cell-imaging. The following sections further elaborate the key features of the MVM devices and potential applications for future research.

Incorporating ECM in MVM Platform

The ECs in our MVM are grown on thin 100 micron collagen gel atop silicon nanomembrane. The top collagen gel not only improves cell-substrate adhesion, but also provides physiological compliance for the growth and dif-

ferentiation of ECs. The presence of a biomaterial with tunable stiffness is an added advantage that can be probed for mechanobiological studies. For instance, it is possible to study substrate stiffening that happens in aging vessels prone to atherosclerosis and its potential impact on barrier function. The thicker collagen gel present beneath the silicon membrane mimics the deep tissue and can allow for 3D migration of leukocytes. The ability to introduce collagen underneath the silicon substrate is enabled by the etching procedure used to make silicon nanomembranes. This gel can be modified in its concentration and composition independently of the top gel, and can be optimized for different biological assays. For example, instead of introducing neutrophils in the luminal chamber, the neutrophils can be premixed in the collagen gel, and can be forced to chemotax to the apical chamber by introducing chemoattractants in the top chamber. This configuration will, thus, mimic 'reverse diapedesis', which can be difficult to facilitate and observe otherwise. ECM plays a very important role in inflammation [22], and the ability to alter the biochemical properties of this layer, thus, greatly improves the physiological relevance of the MVM platform.

Electronics and Fluidics in MVM Platform

Another important characteristic of this platform is the embedded electronics that enable TEER measurement. Electrical methods allow for faster and non-invasive measurements of endothelial permeability. Unlike the popular 'chopstick' electrode and other similar electrode setups, the indium tin

oxide (ITO) electrodes have been carefully patterned to render uniform electric fields and accurately measure electric potentials across the device. The sensing and reference electrodes are placed above and below the porous membrane that hosts the endothelial cells. This eliminates the measurement of stray signals and contact impedances that can cause significant overestimation of TEER values. Also, the system validation using finite element analysis (Figure 3.18) helps in better understanding and characterizing the electrical behavior of the system, which is often overlooked in the literature.

Shear-conditioning improves the TEER values as we observed in our own studies (Figure 3.16). The resistance values for long-term static growth are $\sim$ 250 ohms and remains fairly constant for over 24 hours. The absence of any significant rise in TEER indicates the confluency of the cell monolayer. Application of shear, however, elevates this terminal value up to $\sim$ 420 ohms. These terminal values fall in the *junction-maturation* phase shown in the Figure 3.17 that is observed when cells are around 99% confluent. The COMSOL model is, thus, able to capture the effects of cell growth on endothelial barrier observed experimentally. This result is significant because it highlights the importance of a healthy and confluent monolayer in maintaining the vascular barrier. The ability to model these *in vivo* phenomena *in vitro* using mathematical simulations presents a synergistic approach to study biological events.

The extended application of this electrical measurement system is further established by performing impedance spectroscopy as shown in Figure

3.20. There are two major platforms commercially available to understand the impedance spectra of endothelial/epithelial monolayers: ECIS (Applied Biophysics) and cellZScope (nanoAnalytics GmbH). While the ECIS system is multifunctional and can provide very sensitive readouts to understand cell-cell barriers, cell-substrate gaps, and cell-substrate coverage, the major limitation of this platform is the growth of the cells on a flat gold substrate, essentially eliminating coculture or 3D migration experiments. The cellZScope platform allows impedance measurement in a 'transwell' format and facilitates 3D assays and coculture, but is limited to static assays only. The MVM platform provides for both flow, and impedance measurements, and allows easy integration with the commercially available spectroscopy instruments for measurements.

The flow system designed to perfuse cell media and induce shear stress is another advancement of the current platform. While a majority of the commercial microfluidic systems grow cells under static conditions, the few studies that actually implement shear stress suffered from low shear levels probably due to the complications involved in implementing the system [107]. Our flow setup is capable of providing physiological shear levels and allows for easy media replacement that makes long-term growth possible. Furthermore, the design of the top and the bottom chambers allow for facile flow introduction in both the chambers independently and simultaneously without fluid leakage. This may be helpful for coculture applications, especially, if the second cell type also requires fluid perfusion.

Neutrophil Migration Studies in MVM Platform

Neutrophil induced endothelial permeability is complex, with both physical and biochemical factors contributing significantly to altered endothelial barrier properties [52]. Multiple steps are involved in facilitating neutrophil diapedesis through the blood lumen into the extravascular space, and each of these events are known to affect endothelial permeability [15]. While most of the knowledge about neutrophil migration has been derived from *in vivo* animal models, there is no consensus about the contribution of neutrophil transmigration to endothelial permeability due to the confounding influence of multiple factors on the same [refer Chapter 1 for a more elaborate discussion on this topic]. One of the earliest *in vitro* studies was published by Silverstein and colleagues in 1980s in which it was concluded that neutrophil migration through endothelial monolayers does not cause any change in TEER values [62]. In order to observe any noticeable change in the TEER values, the authors found that the neutrophil:EC ratio needs to be higher than 25:1. Since this influential study, many other investigators have examined the effects of neutrophil transmigration on endothelial barrier properties *in vitro* [49, 50, 171, 172] and concluded otherwise. In our own studies, we found that neutrophil transendothelial migration is responsible for a reduction in the net electrical impedance as observed in Figure 3.29. At the (neutrophil) seeding density of 10 million/ml, the neutrophil:EC ratio in the MVM device was around 1.5:1, assuming the 1000 μm^2 as average size

of endothelial cells [147]. The phase images of the transmigration process shown in Figure 3.22 highlight the *gap* formed between adjacent endothelial cells. These gaps, cumulatively formed over the entire monolayer, may be responsible for transient but finite changes in ionic permeability. Thus the simultaneous optical and electrical readouts are useful in shedding light on a hitherto controversial question.

Furthermore, the inhibitory effects of blocking antibody can be verified using phase imaging (Figure 3.26). The effects of blocking $\beta 1$ integrins demonstrate the advantages of using the MVM platform for exploring unknown effects of neutrophil subendothelial migration. The reduced count of extravasated neutrophils in the basal chamber by blocking $\beta 1$ integrins (Figure 3.27) is consistent with the findings of Lerman and colleagues, who found neutrophil arrest in the subendothelial layer upon inhibiting $\alpha 3\beta 1$ integrin *in vivo* [38]. We measured the changes in electrical impedance and the transport of macromolecules with and without the presence of $\beta 1$-blocking antibody. Electrical analysis clearly demonstrated a reduced depression in the impedance values when neutrophils were incubated with the blocking antibody (Figure 3.29). Teleologically, this finding suggests that neutrophils arrested in the subendothelial layer might provide a negative feedback for the luminal neutrophils discouraging them from further extravasation. Such reduced migration might reduce changes in permeability. Alternatively, the inability of the neutrophils to invade the interstitial space might be responsible for the sustainment of the barrier properties at the subendothelial layer

("dam effect"). Both these possibilities favor a reduced inflammatory response, which might further explain the improved survival of the mice treated with anti-$\alpha 3\beta 1$ peptide [38]. The ability to investigate these inhibitory mechanisms by optical imaging and simultaneous electrical measurements is a clear advantage for future preclinical studies.

An unique feature of this system is the possibility of activating neutrophils *without* their complete migration. In the past, this has been achieved by using agonists such as phorbol myristate acetate (PMA), which causes neutrophil activation without migration [173]. In this study, authors used PMA treatment to understand the contribution of cell migration in increasing permeability. In the MVM platform, this can be achieved by using a nanoporous membrane instead of a microporous membrane. The nanometer-sized pores will allow the fMLP-induced neutrophil activation, but will physically prohibit the neutrophils from vacating the subendothelial space and will render the interstitial matrix 'intact'. It would be interesting to test if this *physical* inhibition also contributes to less decay in impedance as compared to control condition (as observed in Figure 3.29).

Macromolecular Transport in MVM Platform

Finally, the imaging setup described in Figure 3.9 demonstrates an innovative approach to record macromolecular permeability with a high temporal resolution. Typical protocols for estimating dextran permeability are end-point assays and employ plate readers for fluorescence spectroscopy. It requires

fraction collection and, thus, estimates the permeability *ex situ*. For the first time, we have optimized a live-cell imaging setup that can allow for continuous measurement of fluorescent tracers diffusing across the endothelial barrier *in vitro*. We used this setup to corroborate our findings about the effects of blocking $\beta 1$ integrins on neutrophil-induced increases in endothelial permeability. The increase in fluorescence signal from FITC-Dextran was almost doubled in the absence of any blocking treatment (Figure 3.30) indicating that the breach of BM enhances the transport of macromolecules and plasma proteins.

Pulse-chase experiments with tracer molecules of different sizes and color spectra can be coupled in a time-lapse imaging mode to understand multiple aspects of endothelial permeability simultaneously. For example, Figure 3.22 highlighted that neutrophils create a physical gap in the monolayer while transmigrating. Using a dextran ladder of increasing molecular weights (and sizes) and observing the trends in recovery over time, it is possible to estimate the size resolution of these gaps, which is very difficult using existing methods of imaging. The recovery analysis can also provide insights into the kinetics of molecular transport based on real-time data sampling. Overall, the live-imaging of dextran-diffusion creates the possibility to execute multiple exciting experiments, and should be advantageous in addressing numerous biological questions in future studies.

3.5 Conclusion

In summary, we have successfully engineered a microfluidic system that facilitates long-term shear-conditioned growth of ECs on permeable and transparent substrates and allows for measuring the changes in ionic and macromolecular permeability in the presence of an inflammatory stimulus. The variety of simultaneous readouts obtained from the MVM platform makes it the most metrologically rich example of an *in vitro* microvessel mimetic to date. Using this system, we were able to identify the contribution of trans- and subendothelial migration of neutrophils in altering endothelial barrier function.

Chapter 4

A Silicon Nanomembrane-based *in vitro* Platform to Visualize Immune Cell Trafficking across the Human Blood Brain Barrier[†]

4.1 Abstract

Background

In vitro devices that mimic vascular tissue are becoming increasingly sophisticated tools for understanding microvascular physiology and as drug discovery platforms. Despite these advances, current *in vitro* systems are not suited to

[†]This chapter is adapted from a manuscript accepted in the Journal of Cerebral Blood Flow & Metabolism. I am the second author of this manuscript and was responsible for data curation, formal analysis, investigation, methodology and writing the original draft. The work presented in this chapter is a collaborative research between the labs of James McGrath (University of Rochester) and Britta Engelhardt (University of Bern, CH). The microfluidic platform that is central to the studies in this paper was designed, developed, and optimized by me. Because all the experiments and gathered data directly involve the application of this platform, the entire study has been presented in this chapter.

the study the multi-step extravasation of rare patient derived T-cells across the human cerebral vascular barrier (CVB) under physiological flow. The primary deficiencies of existing systems relate to the challenges of live cell imaging of T-cell /endothelial interactions on permeable substrates and the need to study these interactions in the presence of physiological flow.

Results

Here we use nanoporous silicon nitride (NPN), an ultrathin (∼50 nm) highly permeable membrane with abundant ∼40 nm pores, to create a vascular mimetic that overcomes these limitations. The sub-optical dimension of NPN pores results in glass-like imaging, and supports endothelial cell adhesion under physiological levels of shear stress. These properties, and the high permeability of NPN, make it an ideal membrane for the creation of a dual-chamber flow cell and microvascular mimetic. Here we show that cord blood $CD34^+$ hematopoietic stem cell derived endothelial cells differentiate into an *in vitro* model of the human blood-brain barrier (BBB). Importantly, pericytes-conditioned media can replace pericytes in the basal chamber of the device to eliminate the confounding effects of cocultures on imaging. With these outstanding optical and physical properties, we demonstrate the utility of our platform by introducing human T-cells under physiological flow and documenting the sequential multi-step T-cell extravasation across the BBB (arrest, intraluminal crawling, probing, diapedesis) using live cell imaging.

Conclusions

We call our nanomembrane-enabled platform the "μSiM-CVB" with "μ" highlighting the small ($\sim$ 20 μL) volumes required in the transcellular compartments and "Si" denoting the use of a silicon-based membrane. The μSiM-CVB is the first *in vitro* human BBB model to enable live and high quality imaging of human T-cell interactions with an *in vitro* model of the human BBB under physiological flow, addressing an unmet need in the research community. Because the μSiM-CVB is also suitable for potentially patient-derived (e.g. iPSC) *in vitro* models of the human BBB and is a highly manufacturable device platform, we anticipate that it will become a valuable tool for the study of extravasation across the BBB by both rare patient-derived immune and metastatic cancer cells.

4.2 Introduction

The endothelial blood-brain barrier (BBB) in central nervous system (CNS) parenchymal microvessels protects the CNS from the constantly changing milieu in the blood stream. In addition to strictly controlling the movement of molecules across its interfaces it also rules the entry of immune cells and immune mediators into the CNS [174]. Under physiological conditions, immune cell entry into the CNS is very low. In contrast, in CNS inflammatory diseases such as multiple sclerosis (MS) high numbers of immune cells infiltrate the CNS, where they cause inflammation, BBB dysfunction and

demyelination [175]. Immune cell trafficking across the BBB is thus a critical hallmark of MS [130] and has been extensively studied in experimental autoimmune encephalomyelitis (EAE), an animal model for multiple sclerosis [176]. *In vitro* and *in vivo* live cell imaging studies in rodents suffering from EAE have provided evidence that T-cell migration across the BBB is a multi-step process, where T-cells start to roll on the endothelial surface and after their arrest, crawl against the direction of the blood flow to sites permissive of T-cell diapedesis across the BBB (summarized in [174]). α-4 integrins on the T-cells were identified to mediate their arrest to the BBB in the absence or presence of autoimmune neuroinflammation in rodent EAE models, and antibodies blocking α-4 integrins were shown in a variety of EAE models to inhibit the development of clinical symptoms [174]. These findings were successfully translated into the clinic, where the humanized monoclonal anti-α-4 integrin antibody natalizumab is used for the treatment of MS [130]. Unfortunately, natalizumab comes with the unforeseen and rare side effect of progressive multifocal leukoencephalopathy (PML), which is caused by infection of human oligodendrocytes with the John Cunningham (JC) virus and can thus not be modeled in animals. Furthermore, a number of anti-inflammatory treatments that were highly effective in EAE, have failed in MS trials [132], underscoring that the autoimmune pathogenesis underlying MS and its treatments cannot be modeled in their entire complexity in available animal models. Therefore, there is an unmet need for detailed functional studies employing human disease-relevant tissues and cells. This

includes the necessity for human models of the BBB allowing the study of migration by disease-relevant immune cell subsets across the cellular barrier as a critical step in MS pathogenesis.

Most well-characterized BBB culture models are based on primary brain endothelial cells or brain endothelial cell lines from animal origin (bovine, porcine and murine) [177–179]. Although elegant human *in vitro* BBB models employing primary human brain endothelial cells have been established [180], their availabilities are limited to few laboratories with privileged access to human brain tissue. Thus, human brain endothelial cell lines like the hCMEC/D3 have been established and widely used as *in vitro* models of the human BBB [181, 182]. Although hCMEC/D3 retain morphological and functional characteristics of human brain endothelium, they fail to establish barrier characteristics resembling their tightness observed in BBB *in vivo* [183]. This limits the suitability of hCMEC/D3 for pharmacological, toxicological and functional assays on the human BBB with *in vivo* predictability.

Recently, stem cell sources have demonstrated substantial advantage over other brain endothelial cells sources for BBB modeling given their human origin, stability, scalability, self-renewal and potential to generate syngeneic cellular components of the neurovascular unit [184, 185]. We have recently employed cord blood $CD34^+$ hematopoietic stem cells to differentiate endothelial cells (ECs) [133]. By coculturing $CD34^+$ -derived ECs with bovine pericytes we were able to differentiate those ECs into brain-like endothelial cells (BLECs) providing a valuable *in vitro* model for the human BBB

[133]. Growing BLECs on conventional cell culture filter inserts in coculture with pericytes, we and others used both small molecule diffusion and transendothelial electrical resistance [133, 186] to establish that BLECs form tight barriers. With their excellent barrier function and robust expression of BBB signature molecules in combination with large-scale availability, BLECs are an ideal culture platform to study the interaction of human immune cells with the human BBB *in vitro* [134].

Live cell imaging and phase microscopy on coverglass substrates, are well-established as the means of monitoring immune cell migration across endothelial monolayers *in vitro* under static and flow conditions [187–190]. Following its arrest on the endothelial monolayer, an immune cell rapidly changes from a phase-bright roundish shape that can easily be distinguished from the endothelial monolayer, to a polarized cell that first spreads atop of the endothelial monolayer and then crawls along the endothelium, and then finally to a phase-dark cell as it migrates beneath the endothelial monolayer [191–194]. Similarly, live fluorescence imaging has been used to reveal the dynamics of immune cells and adhesion receptors [195] during their interaction with endothelial monolayers and to eventually distinguish between paracellular and transcellular routes of diapedesis [193, 196, 197]. Because glass coverslips are impermeable, they cannot support the establishment of a valid BBB model, which requires cross talk between brain microvascular endothelial cells in a luminal compartment and perivascular cells such as pericytes or astrocytes or CNS derived factors in an abluminal compartment [198, 199].

Microscopic imaging in conventional membrane inserts is severely hampered by the fact that the polymer track-etched (TE) membranes used in these devices are largely opaque to transmitted light and degrade fluorescence signals [73]. Even the routine monitoring of endothelial monolayers during cell culture growth is impaired by the incompatibility of TE membranes with phase contrast microscopy. The optical quality of these systems does therefore not suffice to delineate immune cell interaction with the BBB *in vitro*.

Another critical feature of an *in vitro* model for the study of the interaction of immune cells with the BBB is the ability to maintain fluid flow during the interaction of the immune cells with the endothelial monolayer maintaining its BBB characteristics. The inability to introduce any flow in the apical and basal compartments of two chamber systems employing filter inserts limits their application to assays performed under static conditions (no shear forces). Although static BBB models have provided provisional answers to questions regarding the molecular mechanism of immune cell trafficking across the BBB [134, 179, 200], the physiological representation of immune cell trafficking across the BBB clearly requires the presence of flow [135, 179, 194, 201]. Several studies convincingly demonstrated that physiological shear forces influence each phase of the multi-step process including the arrest and crawling of T-cells on the endothelium, and the cellular pathway of diapedesis across the endothelial monolayer [135, 179, 201].

Here we report on the development of a novel *in vitro* platform, the μSiM-CVB, for the study of the interaction of human T-cells with human *in vitro*

models of the BBB. An enabling component of this platform is ultrathin nanoporous silicon nitride (NPN), a 50 nm thick 'nanomembrane' with a high density (10^{10} cm^{-2}; 20% porosity) of ∼40 nm pores [111, 142]. The thinness and high porosity of NPN result in a luminal/abluminal divider with extraordinary small molecule permeably [109, 111] and the sub-optical pore sizes of NPN provide requisite imaging and cell-adhesion properties that cannot be achieved by any membrane alternative. The stiffness of the inorganic NPN membranes maintains image stability during the introduction of flow, which is prerequisite to study T-cell - BBB interactions by live cell imaging. We here establish that CD34$^+$ stem cell derived ECs differentiate into BLECs when cultured on NPN with pericyte condition media supplied basolaterally, eliminating the need for coculture with pericytes. This is a second key innovation of our platform because it removes the confounding effects of subluminal cell cultures on imaging at the endothelial monolayer. Finally, we demonstrate the utility of the μSiM-CVB by capturing each step of the multi-step T-cell migration across the BBB using live cell imaging under physiological flow. We expect the μSiM-CVB to become a valued *in vitro* platform for studying the dynamics of extravasation by immune cells in the brain. More broadly, we propose that our NPN-enabled flow cell allows the creation of superior vascular mimetics for the study of live cell trafficking in other vascular phenomena such as inflammation, sepsis, and cancer metastasis.

4.3 Results

4.3.1 Commercial Supports are Not Suitable for Live-cell Imaging of the Human *in vitro* BBB Under Physiological Flow

We have previously developed a custom-made flow chamber that allowed us to observe the interaction of immune cells with an *in vitro* model of the mouse BBB established from primary mouse brain microvascular endothelial cells (pMBMECs) by live cell imaging [187]. As pMBMECs do not require coculture conditions to establish BBB characteristics, they can be grown in petri dishes with polymer coverslip bottoms, e.g. μ-dish 35mm (ibidi) allowing for high imaging quality. A custom made flow chamber can, in this case, be tightly mounted over the pMBMEC monolayers using a magnetic system [187]. For experimental conditions requiring coculture of pMBMECs, e.g. with astrocytes, prior to live cell imaging of immune cell interaction with pMBMECs under flow, we have successfully adapted the flow chamber setup such that it allows for insertion of pMBMEC monolayers grown on commercially available filter membranes [202]. Although this adaptation came with a reduction in imaging quality of the pMBMEC monolayer, the multi-step immune cell interaction with the pMBMEC monolayer could be investigated [202].

In the present study, we therefore employed our established methodology to transfer our novel human *in vitro* model of the BBB established

from $CD34^+$-derived endothelial cells (EC) [133] to the established custom-made flow chamber device [187]. In order to perform the $CD34^+$-derived EC/pericyte cocultures necessary to establish the BBB, we first tested several commercially available inserts. We first used the Millicell standing inserts with a PTFE membrane to grow the $CD34^+$-derived ECs. To this end $3.5x10^5$ $CD34^+$-derived ECs were seeded on the Matrigel^{TM} coated membrane and the coculture with pericytes was started as described before [133]. Unfortunately, we could not show the BBB maturation on these filters because $CD34^+$-derived ECs did not form confluent monolayers. To improve adhesive characteristics of the Millicell PTFE filters, we tested coating with different extracellular matrix proteins and combinations thereof including Matrigel^{TM}, laminins, collagens and fibronectin. None of these coatings provided attachment of the endothelial monolayers suitable to perform flow assays, as EC readily detached upon the application of flow.

We therefore systematically tested adhesion and growth of $CD34^+$-derived EC on additional 6 commercially available filter systems to test their optical properties and their compatibility with the cell growth: Millicell polycarbonate, the Millicell mixed cellulose esters, Corning polycarbonate, Corning PTFE with collagen coating, Corning PET and Greiner PET (Table 4.1). Although these filters all allowed for the growth of $CD34^+$-derived EC into confluent monolayers as confirmed by immunofluorescence staining of the fixed BLECs, the Millicell membranes (polycarbonate and mixed cellulose esters) and the Corning polycarbonate membrane were not optically trans-

parent to allow us to judge the confluency of the live cell monolayer. The other three filter inserts (Corning PTFE with collagen coating, Corning PET and Greiner PET) were used to perform the flow assays. After the coculture procedure, the filters had to be cut out of their frame and inserted into our custom-made flow chamber [187] by placing the filter on an ibidi dish with the flow chamber mounted on top. Cutting out the filters beared the risk of mechanical rupture of the endothelial monolayer. Also, the live cell imaging studies performed with this setup had a very low imaging quality and were not of sufficient quality for a thorough evaluation of T-cell/BBB interactions. In the assay with the Corning pre-coated PTFE filters, we were able to see the shapes of the T-cells but it was impossible to clearly visualize the BLECs. On the PET filters from Corning and Greiner we were again not able to clearly see the BLECs and the background was too high to evaluate the behavior of the T-cells even though they were visible. Thus, we concluded that we could not adapt our existing flow chamber for the study of T-cell/BLEC interactions under flow.

A review of experimental microfluidic culture devices described in the literature also suggests that these would not provide ready solutions to our needs. Most generally, these systems are not amenable to live cell observations of T-cell/BLEC interactions due to the lack of membrane transparency [203, 204], and/or due to the fact that the endothelial cells are not grown in a single horizontal plane but vertically [205] or on the luminal surface of tubings [206–208]. Moreover, some of these systems employ large amounts

Table 4.1: Inserts Tested: Different inserts of varying material-properties and obtained from different sources were tested for their optical performance.

'Insert' Description	**Experiments Performed**	**Limitations of 'Insert'**
6 well standing inserts, low wall, 0.4 μm pore size, PTFE Millipore (PICM0RG50), Sevelen, Switzerland (Enzmann et al. 2013)	Cell growth on coated filter Membranes: Matrigel, laminin, gelatin and rat tail collagen *in vitro* flow assay [n=4]	BLECs do not adhere on this filters
6 well standing inserts, high wall, 0.4 μm pore size, polycarbonate Millipore (PIHP03050), Sevelen, Switzerland	Cell growth & Light Microscopy [n=1]	Filter membrane is not transparent
6 well standing inserts high wall 0.4 μm pore size mixed cellulose esters Millipore (PIHA033050), Sevelen, Switzerland	Cell growth & Light Microscopy [n=1]	Filter membrane is not transparent
6 well hanging inserts, 0.4 μm pore size, polycarbonate Corning Incorporated (3412), NY, USA	Cell growth & Light Microscopy [n=1]	Filter membrane is not transparent
6 well hanging inserts, 0.4 μm pore size, PTFE coated Corning Incorporated (3491), NY, USA	Cell growth & Light Microscopy & *in vitro* flow assay [n=4]	Filter membrane is not sufficiently transparent
6 well hanging inserts, 0.4 μm pore size, PET Corning Incorporated (3450), NY, USA	Cell growth & Light Microscopy & *in vitro* flow assay [n=1]	Filter membrane is not sufficiently transparent
6 well hanging inserts, 1 μm pore size, PET Greiner (657610), Huber & Co. Ag Reinach Switzerland	Cell growth & Light Microscopy & *in vitro* flow assay [n=4]	Filter membrane is not sufficiently transparent

of fluid volume to maintain flow over time [203, 204, 209], which would limit our ability to study the interaction of a limited number of patient derived T-cell subsets with BLECs.

4.3.2 $CD34^+$-derived ECs adhere and grow on nanoporous silicon nitride membranes

We found that $CD34^+$-derived ECs efficiently adhered to and built a confluent monolayer on Matrigel^{TM}-coated nanoporous silicon nitride (NPN) and that NPN provided glass-like clarity of monolayers in phase microscopy (Figure 4.1). NPN is a recently developed ultrathin silicon membrane technology [142] and the third generation of ultrathin porous 'nanomembranes' we have developed using silicon manufacturing techniques [72, 109]. NPN membranes are 50 nm thick with ∼20 % porosity and a narrow distribution of pores centered around 40 nm. NPN is far more mechanically and chemically robust than our original porous nanocrystalline silicon membranes [142], and unlike microporous SiO_2 membranes [72, 73], the nanoscale pores of NPN are invisible to light microscopy. Importantly, we have found that NPN supports vascular endothelial cell adhesion under physiological shear stress, while microporous SiO_2 membranes do not (Figure 4.2). While the reasons for poor cell adhesion to SiO_2 nanomembranes are not yet clear, it may be related to the fact that micron-scale pores disrupt the normal architecture of basement membranes [74].

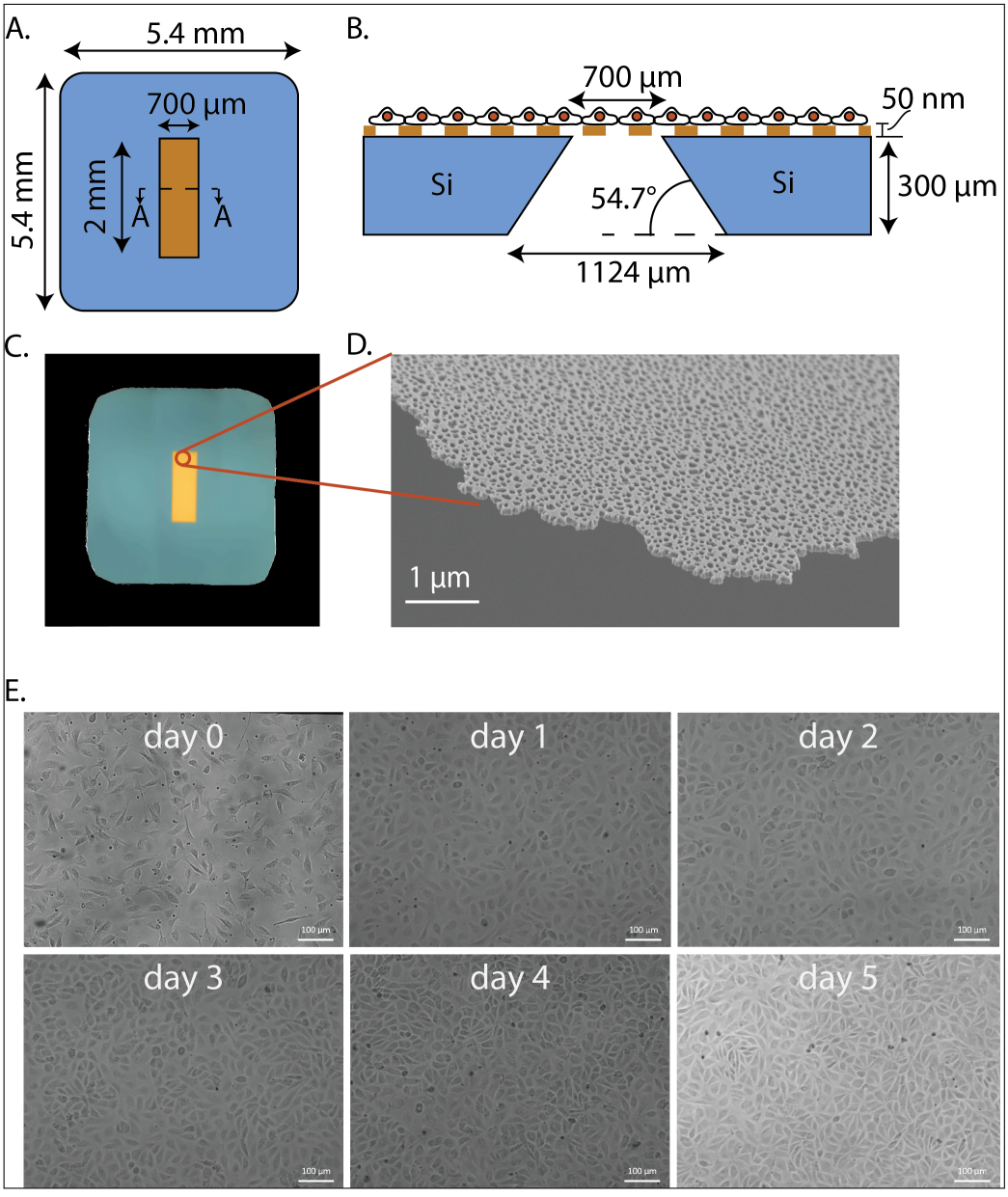

Figure 4.1: Caption Next Page

Figure 4.1: $CD34^+$-derived ECs grow to confluent monolayers on the nanoporous silicon nitride membrane: (A) Schematic of the nanoporous silicon nitride membrane used for the cell culture experiments. The free-standing membrane region is a 2 mm × 0.7 mm window in the center of a 5.4 mm x 5.4 mm membrane 'chip'. (B) The cross-sectional (A-A) schematic of the membrane. The bulk substrate consists of 300 microns of crystalline silicon, which is etched at the center to remove the bulk leaving a free standing 50 nm thin silicon nitride membrane. The manufacturing of these membranes was described before [142]. (C) Optical micrograph of the membrane chip. (D) Scanning electron micrograph of the porous membrane demonstrating the ultrathin nature and porous structure of the silicon nitride membrane ($>$ 20% porosity in this example). (E) Phase contrast pictures of $CD34^+$-derived ECs adhering and growing to confluent monolayers on the NPN membranes from day 0 until day 5 after plating. The $CD34^+$ ECs adhere on the NPN membrane after 1 to 2 hours and start to grow to form a confluent monolayer between 1 and 2 days of culture. Cellular density increases until day 5. Scale bar, 100 microns.

4.3.3 Pericyte coculture can be replaced by pericyte-conditioned medium to induce BBB characteristics in $CD34^+$-derived ECs

Coculture of $CD34^+$-derived ECs with pericytes has been shown to be essential for induction of BBB characteristics [210]. This procedure involves changes in gene expression of Wnt signaling, tight junctions and transporters that occur over 6 days of coculture [210]. In theory, coculture of ECs and pericytes could be accommodated by designing a two-chamber microfluidic device with the EC grown on the silicon membrane in the upper compartment and the pericytes in the lower compartment. The major disadvantage of this set up would be that *in vitro* live cell imaging of the BBB under flow employs inverted microscopy, which positions the pericyte cul-

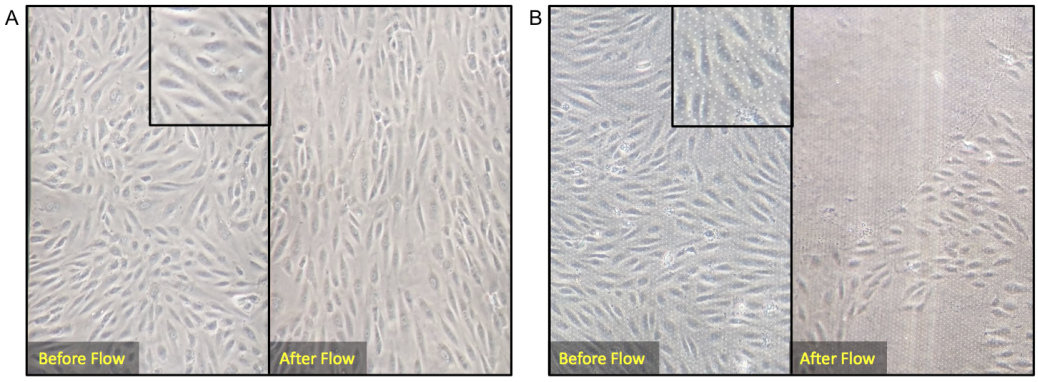

Figure 4.2: Endothelial cell adhesion under shear stress: (A) Human umbilical vein endothelial cells (HUVECs) are grown on nanoporous silicon nitride (NPN) for 24 hours under static condition (left panel), and were later exposed to ∼9-10 dynes/cm^2 of shear stress of fluid flow for another 24 hours (right panel). Inset represents a zoomed in image of the cell monolayer without any noticeable pore distribution on the membrane substrate. (B) HUVECs were grown under similar static conditions on 3 micron pores silicon dioxide membrane (left panel) followed with identical shear stress exposure. Notice the visible presence of 3 micron pores during phase imaging as observed in the inset (magnified view). Within 2 hours of shear introduction, there is over 60% cell loss from the membrane substrate as shown in the right panel. Various surface coating techniques were implemented to improve the cell adhesion on the microporous substrates. Extracellular matrix (ECM) proteins such as fibronectin, collagen 1, as well as basement membrane mimetic compositions (Geltrex^{TM}, Corning, NY) were tested. Aminopropyl triethoxy silane (APTES) - 4% in acetone and 100% - were also used to modify the surface properties to enhance cell adhesion under shear stress. None of the coating methods prevented cell detachment from the microporous substrate under shear stress and the substrate was decellularized in few hours post-flow, as represented in the right panel.

ture between the microscope objective and the EC monolayer potentially impairing the imaging quality of the EC monolayer. We therefore asked if the pericyte-coculture could be replaced by administrating the conditioned medium of the pericyte cultures. To this end, we cocultured $CD34^+$-derived ECs with or without pericytes in the original Transwell filter coculture setup for 5 days as positive and negative control, respectively. In parallel, $CD34^+$-derived ECs plated on additional matrigel coated Transwell filter inserts were co-incubated with pericyte-conditioned medium (PCM) from the abluminal (lower compartment) or luminal (upper compartment) side (Figure 4.3A,B) and subsequently replaced on a daily basis by alternating between 24h and 48h. In order to obtain the PCM, 2.25×10^4/well pericytes were seeded into 24-well Costar plates one day prior to seeding the $CD34^+$-derived ECs. After the adhesion of the $CD34^+$-derived ECs on the Matrigel coated Transwell filter inserts, the 24 hours PCM was collected from the pericyte cultures and administered to the luminal or abluminal side of the $CD34^+$-derived ECs (Figure 4.3A,B) and subsequently replaced on a daily basis by alternating between 24h and 48h PCM to ensure an optimal concentration of the pericyte-derived factors (Figure 4.3B). After 5 days of culturing the $CD34^+$-derived ECs under the different conditions, their barrier characteristics were compared side-by-side by testing the permeability of the EC monolayers for the small molecular weight tracer lucifer yellow (LY) (Figure 4.3C). In accordance to our previous findings the monoculture of $CD34^+$-derived ECs did not establish a diffusion barrier for LY (Pe LY = $2.04 \pm 0.19 \times 10^{-3}$

cm/min), while the coculture with pericytes established brain-like endothelial cells (BLECs) with tight barrier characteristics as shown by the significantly reduced clearance of LY across the EC monolayer (Pe LY = 0.52 ± 0.08 $\times 10^{-3}$ cm/min; Figure 4.3C). PCM applied from the abluminal side of the $CD34^+$-derived EC monolayer induced barrier characteristics comparable to those induced by the pericyte-coculture (Pe LY = 0.55 ± 0.06 $\times$ 10^{-3} cm/min; Figure 4.3C). Interestingly, applying PCM from the luminal side failed to induce comparable barrier characteristics, which underscores that our *in vitro* model of the BBB appropriately mimics the *in vivo* situation with pericytes embedded in the endothelial basement membrane at the abluminal side of the brain microvascular endothelial cells.

Following the permeability assay, the EC monolayers were stained for the transmembrane adherens and tight junction proteins VE-cadherin and claudin-5, respectively and the junctional scaffolding protein ZO-1 to address the junctional integrity and maturation. The staining revealed that PCM when applied from the abluminal side induced a junctional architecture in $CD34^+$-derived ECs comparable to that induced by coculture with bovine pericytes [210]. Specifically, the pericyte coculture or the abluminally administered PCM induced a continuous and more jagged staining of the junctional and scaffolding proteins VE-Cadherin and ZO-1 compared to the monoculture and PCM luminal conditions (Figure 4.3D). Moreover, junctional claudin-5 immunostaining was enhanced in BLECs under conditions of pericytes coculture and in the abluminally administered PCM conditions

(Figure 4.3D) when compared to controls. In addition, the F-actin staining revealed an absence of stress fibers underscoring the quiescent nature of the ECs monolayers (Figure 4.3D). Overall, these results confirmed that $CD34^+$-derived ECs are polarized and that the barrier-inducing signals provided by the pericytes have to be provided from the abluminal side to induce BBB characteristics like junctional maturation and low permeability to small molecules. Taken together, these results show that differentiation of $CD34^+$-derived ECs into BLECs does not rely on true coculture with pericytes; it can equally well be achieved by applying PCM to the abluminal side.

4.3.4 $CD34^+$-derived ECs establish BBB characteristics when grown on NPN membranes

In a next step, we asked if PCM induced barrier characteristics in $CD34^+$-derived ECs also occurred when the cells were grown on NPN membranes. The silicon chip platform of nanomembranes makes it easy to create customized, tightly bonded microfluidic devices using layer-by-layer assembly and ozone based activation of silicone/PDMS layers [124]. Thus, for these purposes, we fabricated a "Transwell®mimetic", in which a NPN membrane simply divides an upper and lower compartment in static culture (Figure 4.4A). The membrane compartment of this device is open for media and reagent application from the top and promotes easy gas exchange for maintaining physiological pH within the media. The basal compartment can be easily accessed from fluid ports on the top of the device and is separated from

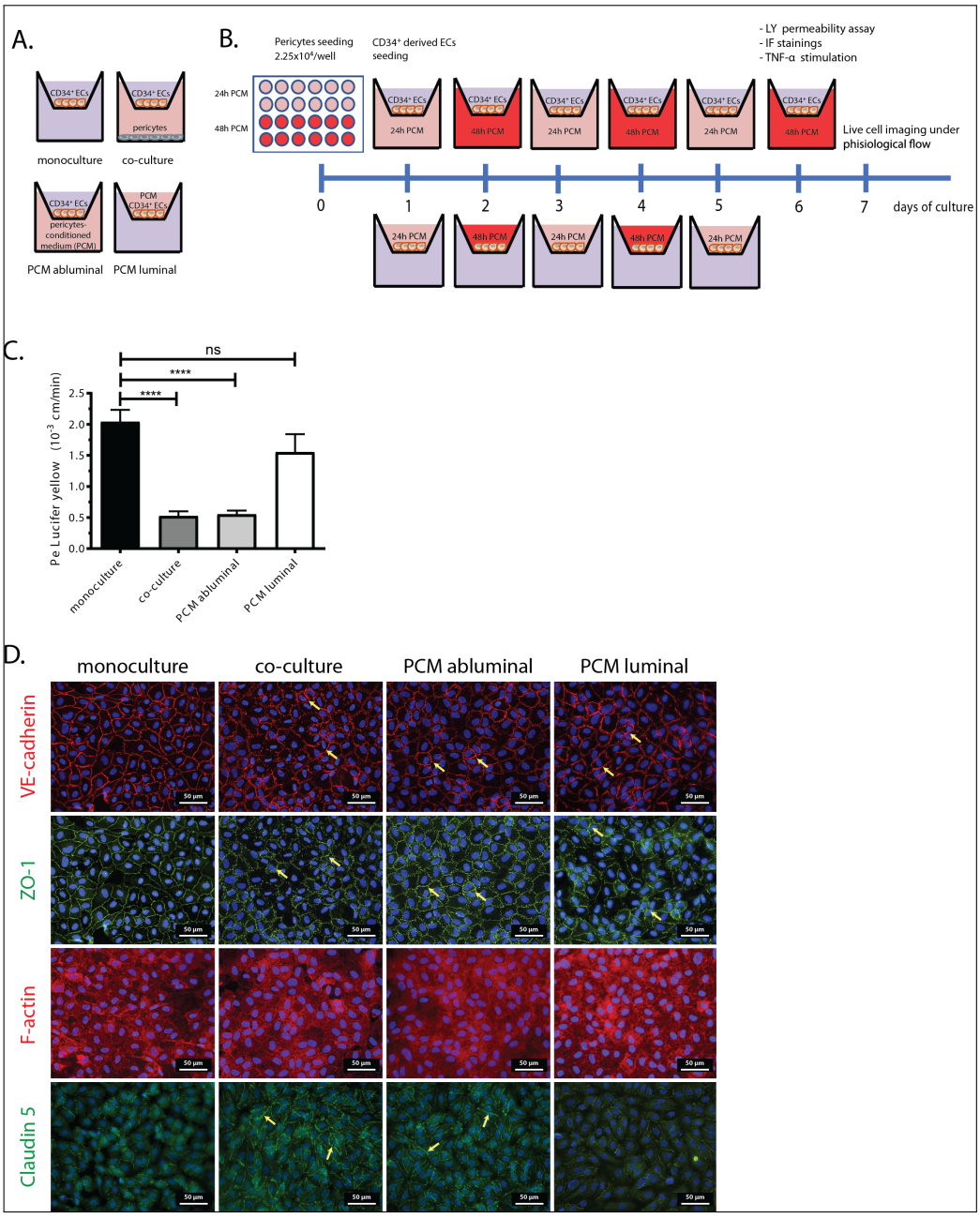

Figure 4.3: Caption Next Page

Figure 4.3: Induction of BBB characteristics in $CD34^+$ ECs by pericyte-conditioned medium: (A) Scheme of the different culture conditions used to test the BBB induction (B) Timeline of experimental procedures: scheme of the PCM production and luminal or abluminal administration to the $CD34^+$-derived ECs followed by Lucifer Yellow (LY) permeability assay, immunofluorescence stainings and live cell imaging under physiological flow. (C) Lucifer Yellow (LY) permeability assay: the permeability was measured across monocultures of $CD34^+$-derived ECs (monoculture), $CD34^+$-derived ECs cocultured with pericytes (coculture), or pericyte-conditioned medium at the abluminal (PCM abluminal) or luminal (PCM luminal) side. Bars show means ± S.E.M of n = 3 independent experiments performed at least in duplicate for each condition. Statistical analysis: one-way ANOVA followed by Dunnett's multiple comparison test **** $p < 0.0001$. (D) Immunofluorescence stainings for the junctional proteins VE-cadherin (red), ZO-1 (green), claudin-5 (green) and for F-actin (red) in $CD34^+$-derived ECs grown in monoculture, in coculture with pericytes or with PCM administered at the abluminal or luminal side are shown. The pictures show a more jagged VE-cadherin and ZO-1 fluorescent staining in the coculture and PCM conditions (arrows). The claudin-5 staining is also more important and continuous in the coculture and PCM abluminal conditions (arrows). Scale bar, 50 μm.

the membrane compartment with the NPN membrane providing the sole area for exchange of factors between compartments. The entire device can be autoclaved and the volume requirements in the upper and lower compartments are only 50 μL and 20 μL respectively. In order to induce barrier characteristics in $CD34^+$-derived ECs, we followed the same culture procedure as depicted in Figure 4.3B. $CD34^+$-derived ECs (1×10^5 cells/mL) were seeded on the Matrigel coated NPN membrane and grown in the absence or presence of PCM applied in the basal compartment (Figure 4.4B). $CD34^+$-derived ECs were cultured for 5 days replacing the PCM in the basal compartment every 24 hours while alternating the 24h and 48h PCM. Barrier characteristics were tested after 5 days of culture by performing a LY permeability assay (Figure 4.4B). The paracellular permeability value across the endothelial monolayers was evaluated as described in details in Material & Methods and the PSe was divided by a cell growing area (0.014 cm^2), in order to generate the endothelial Pe in cm/min. The permeability assay revealed that $CD34^+$-derived ECs grown on NPN membranes in monocultures did not establish a tight barrier with permeability coefficients Pe LY = 1.82 $\pm$ 0.18 x10^{-3} cm/min. In contrast in the presence of abluminal PCM, $CD34^+$-derived ECs grown on NPN membranes established BLEC characteristics with a permeability coefficient Pe LY= 0.39 $\pm$ 0.07 $\times$ 10^{-3} cm/min (Figure 4.4A,B), which is comparable to the LY paracellular permeability of BLECs grown on Transwell filter inserts (Figure 4.3A). Thus, NPN membranes are suitable for the induction of BBB properties by PCM in $CD34^+$-derived ECs. BLEC properties were further

confirmed by labeling the junctional localization of VE-cadherin, claudin-5 and ZO-1 in BLECs grown on NPN membranes in the presence of abluminal PCM (Figure 4.4C).

Next, we investigated cell surface expression of adhesion molecules known to mediate T-cell interaction with the BBB on BLECs grown on the NPN membranes. We found constitutive cell surface expression of the adhesion molecule ICAM-2, constitutively expressed in human endothelial cells [211] and to a lesser degree for ICAM-1 but not of VCAM-1 on BLECs (Figure 4.4D). To mimic an inflammatory environment, BLECs were stimulated with tumor necrosis factor alpha (TNF-α) activating the pleiotropic nuclear factor-κB (NF-κB) [212]. Accordingly, BLECs showed an up-regulation of ICAM-1 and VCAM-1 after stimulation with TNF-α (10 ng/mL) for 16 h, as demonstrated in our previous work [134]. Moreover, the TNF-α stimulation was inducing the formation of F-actin stress fibers as revealed by the immunofluorescence staining (Figure 4.4D). Taken together, these results show that our human *in vitro* BBB model is functionally reproduced on our customized silicon nanomembrane system and suitable to investigate the role of the signature molecules involved in the T-cell trafficking.

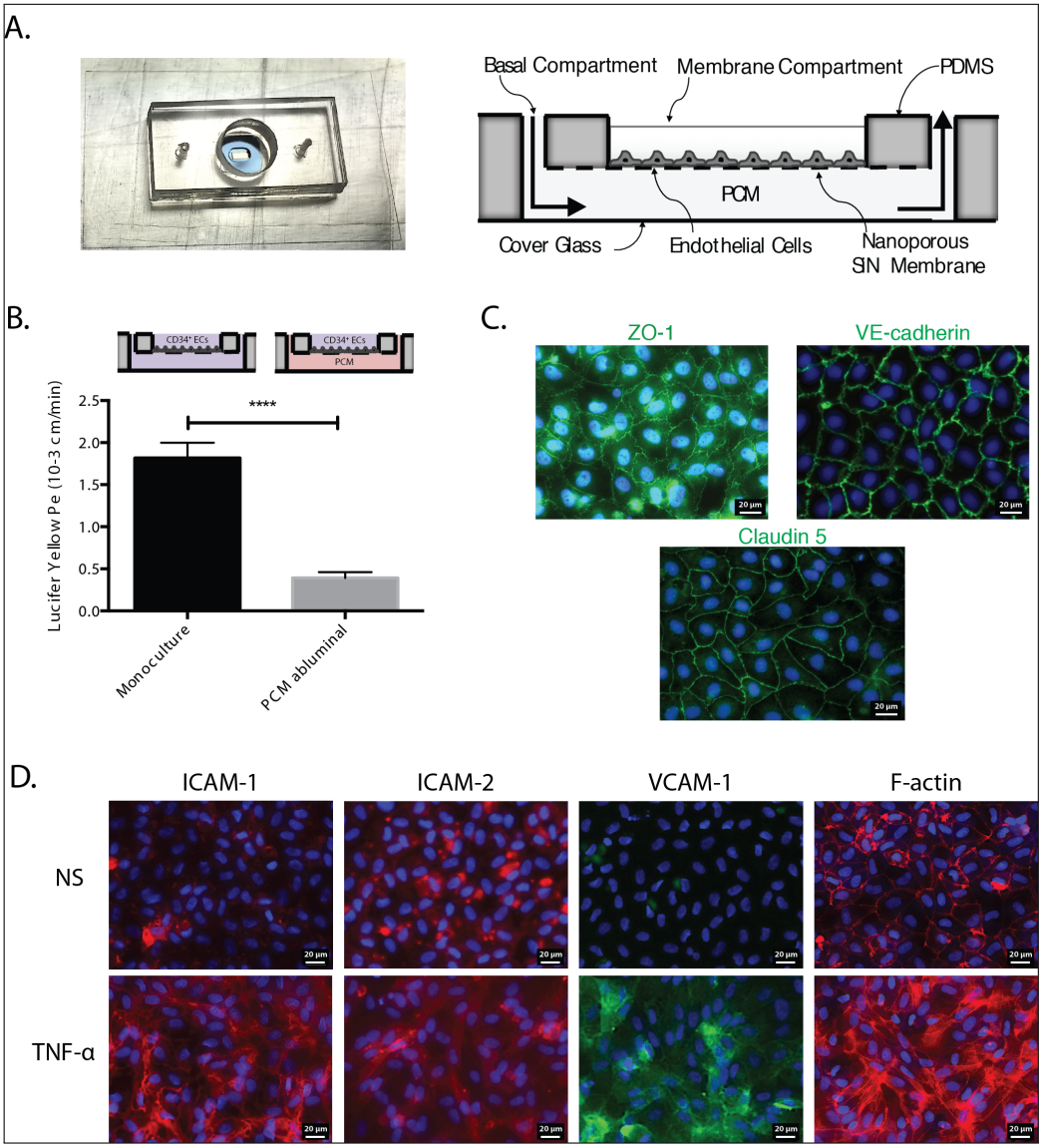

Figure 4.4: Caption Next Page

Figure 4.4: CD34$^+$-derived ECs grown on nanoporous silicon nitride membranes establish BLECs characteristics: (A) Design of a "Transwell mimetic" device developed to culture CD34$^+$-derived ECs in the membrane compartment of the NPN membrane, in close proximity to the pericyte-conditioned medium (PCM) in the basal compartment. The device is constructed from poly dimethyl siloxane (PDMS) and silicone gaskets sandwiched together using UV-ozone bonding. Note the transparent nature of the whole device in general, and specifically of the silicon membrane used to supporT-cell growth. The schematic is shown on the right (drawn not to scale). Molecular tracers can be added to the membrane compartment and collected from the basal compartment for fluorometric analysis. (B) The permeability Lucifer Yellow (PeLY) was measured across monolayers of CD34$^+$-derived ECs grown alone (monoculture) and CD34$^+$-derived ECs cultured in the presence of PCM in the abluminal compartment. The values show mean ± SEM of 11 customized devices for the CD34$^+$-derived ECs mono-cultures and 12 devices for the CD34$^+$-ECs cultured in the presence of abluminal PCM. Statistical analysis: Student's t-test **** $p < 0.0001$. (C) Immunofluorescence staining on BLECs, induced by pericyte-conditioned medium in the basal compartment, for the junctional markers ZO-1 (green), VE-cadherin (green), and claudin-5 (green). Each staining is representative of 2 independent experiment performed on 2 distinct devices, Scale bar, 20 μm. (D) Immunofluorescence staining for ICAM-1 and ICAM-2 (red), VCAM-1 (green), and F-actin (red) on BLECs unstimulated (NS) or stimulated with TNF-α for 16h. Each staining is representative of 2 independent experiment performed on 2 distinct devices. Scale bar, 20 μm.

4.3.5 Establishment of a small scale human *in vitro* BBB model under flow: Introduction of the μSiM-CVB flow system

Using the same layer-by-layer fabrication produced used for open Transwell® mimetics, we constructed a closed, two-chamber flow device, which we refer to as "μSiM-CVB flow system" (Figure 4.5A). This new device is composed of several 300 μm thick silicone layers that create the compartments necessary for the apical growth of the $CD34^+$-derived ECs and the abluminal application of PCM. The top of the μSiM-CVB flow system is sealed by a layer of gas-permeable and transparent PDMS with fluid access ports to both the top and bottom compartments of the device. The $CD34^+$-derived ECs are seeded on the silicon nanomembrane via the top channel that also serves as the flow channel, while the bottom channel is strictly accessed by pipettes. In addition, reservoirs have been added to the top PDMS block of the device at both ends of each channel. This allows the addition of excess culture medium (200 μL per channel) to prevent evaporation during prolonged cell culture (Figure 4.5A). In order to grow the BLECs monolayer, $CD34^+$-derived ECs are seeded in the top channel on the silicon nanomembrane (1.4 mm^2) at a concentration of 1×10^6 cells/mL. Then, the induction of BLECs is achieved by the daily and alternating administration of 24h and 48h PCM for 6 days, as established in the "Transwell mimetic" system. To apply flow on the BLEC monolayer, both ends of the top channels are connected with transparent PVC tubing (dia = 1 mm) with the help of 18 gauge straight needles. The

inlet tubing is then connected to a 3-way tap linked to 2 reservoirs respectively containing the Th1 cell suspension and migration assay medium, and the outlet tubing was connected to a programmable pump that is pulling medium over the BLEC monolayer to create a controlled laminar flow.

With this device and scheme, it was possible to superfuse the Th1 cells over the BLEC monolayer and directly image the T-cells in phase contrast with a transmitted light inverted microscope (Axio Observer Z1, Zeiss) equipped with a temperature-controlled chamber (37 °C), and to observe the multi-step T-cell migration across the BBB under physiological flow *in vitro* (scheme in Figure 4.5C). To perform the flow experiment, first the Th1 cells were infused in the top channel for 4 min at a low flow rate of 0.1 dyne/cm^2 to allow the first contact with the BLECs (accumulation phase). Then the migration assay medium only was infused and the flow rate was increased to 1.5 dyne/cm^2 to reach a physiological shear for 30 min (shear phase). In order to see if we could image the BLECs at high resolution and keep the focus on the cells for the duration of the flow experiment, a temporal snapshot of the BLECs taken from a video recorded with a 10x magnification was made, showing the first and last frame of an area where T-cells did not attach to the BLECs monolayer (Figure 4.5D). In order to mimic conditions of the BBB under inflammatory or non-inflammatory conditions, BLECs were pretreated or not with TNF-α after 5 days of culture with the PCM, when the BBB characteristics (permeability, expression of tight junction molecules) were established (Figure 4.4B,C), 16h before starting the flow experiment

recorded with a 10x objective (EC Plan-Neofluar 10X/0.30 Ph1). First, we found that the resolution was sufficient to perfectly distinguish each endothelial cell in phase contrast images. Then, we could observe that treatment of BLECs with TNF-α induced a more elongated shape of the BLECs (Figure 4.5D), which is in accordance with the induction of F-actin stress fibers as observed with the immunofluorescence staining (Figure 4.4D). When starting to apply flow (0 min) the NPN membrane's stiffness kept it perfectly in focus (34 min 55 sec) and allowed us to continuously image the BLEC monolayer under physiological flow in the same focal plane. In addition, we ensured that the monolayer stayed perfectly intact and in focus under physiological flow for a time period of at least 30 minutes, which is a prerequisite for following the T-cell-BLECs interactions over time.

4.3.6 Live cell imaging of the interaction of human T-cells with BLECs under physiological flow

In the final step, we employed the μSiM-CVB to study the interaction of human T-cells with the human BBB under physiological flow. To infuse T-cells on the BLECs monolayer, we aspirated human Th1 cells from a reservoir via an inlet tubing over the BLEC monolayer for 4 minutes with a flow rate of 0.1 dyne/cm^2 (accumulation phase). After this accumulation phase the flow rate was increased to a physiological flow rate of 1.5 dyne/cm^2 for 30 min (shear phase) allowing the study of post-arrest T-cell behavior on the BLECs monolayer under physiological flow by live cell imaging.

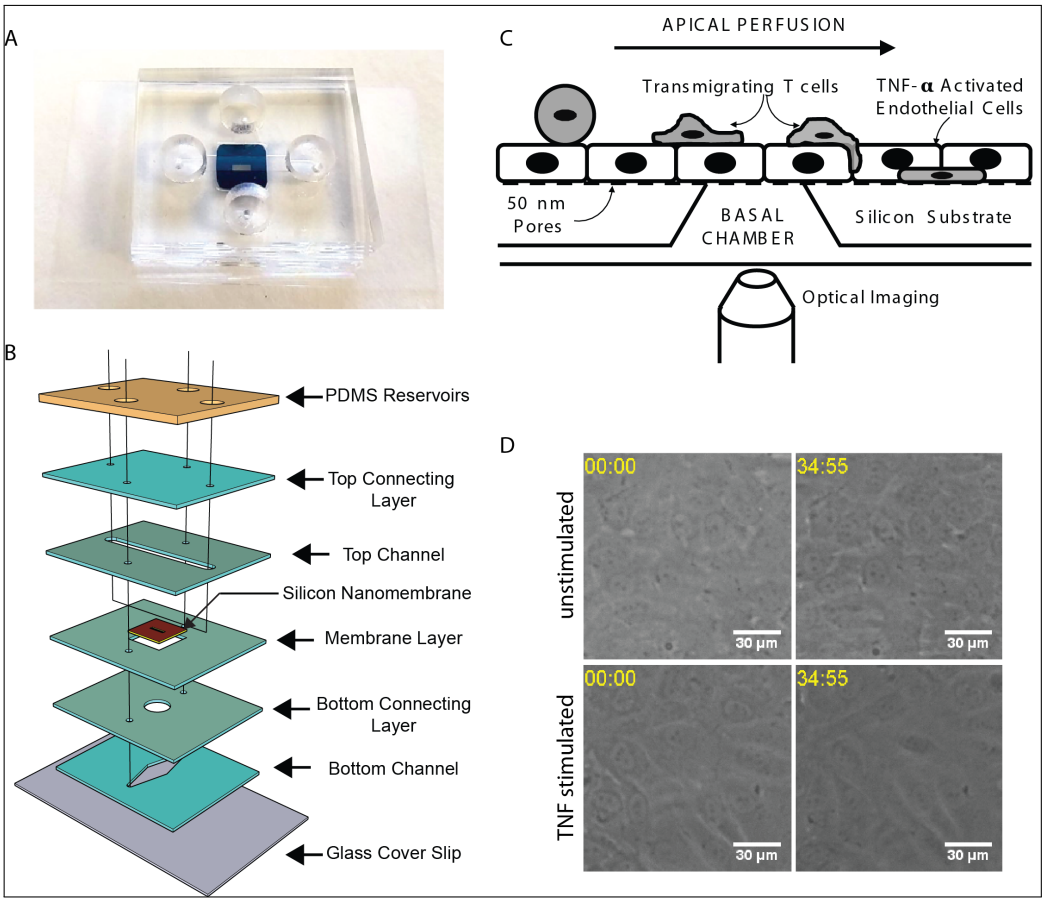

Figure 4.5: Caption Next Page

Figure 4.5: Assembly of the μSiM-CVB flow system: (A) Photograph of the assembled μSiM-CVB flow system. Note the optical transparency of the assembled device components (PDMS, silicone gaskets and silicon membrane). (B) Exploded view of the μSiM-CVB flow system. The supporting layer of the device is a thin number 1.5 glass cover slip. All the silicone layers (blue/green/teal) are 300 μm thick. 'Top' and 'Bottom' channel allows the perfused media to run through the respective layers, while the 'Top Connecting Layer' and 'Bottom Connecting Layer' demarcate the top and bottom compartments respectively, and prohibit the media from leaking outside. The 'Membrane Layer' provides a framework for supporting the membrane, and is also 300 microns. The topmost layer is PDMS reservoirs, which hold the media and act as storage units. They are exposed to the outside environment in the incubator to allow for gas exchange. Similarly, all the other device components- PDMS, and the silicone gaskets are all gas-permeable and sterile. The entire device is autoclavable for sterilization. During flow set-up, the 18 gauge needles fitted with silicone tubings are inserted in the 4 holes in the Top Connecting Layer, and form a liquid-tight connection. (C) Schematic of the settings allowing the live cell imaging of the T-cells-BLECs interactions under flow. T-cells are perfused on the apical (top) side of the device, which transmigrate through the endothelial cells and crawl in the subendothelial layer above the nanoporous membrane. The pores in the silicon membrane are too small ($\sim$50 nm) to allow crawling into the basal (bottom) compartment of the device. The working distance of the device (distance between microscope objective and T-cells) is 1.180 mm. (D) A temporal snapshot illustrating the level of resolution as well as the stability of the focus under flow has been made with several frames taken from two videos recorded with a 10x magnification (EC Plan-Neofluar 10X/0.30 Ph1). The $CD34^+$-ECs were cultured in the top channel of the flow chamber with the pericyte-conditioned medium in the bottom channel for 6 days and the $CD34^+$-ECs were stimulated or not with TNF (10 ng/mL) 16h before starting to record the videos. Th1 cells are allowed to accumulate on the BLECs monolayer at a low flow rate of 0.1 dyne/cm^2 for 4 min from the first frame after the first Th1 cells appear in the field of view, then the flow rate was set to 1.5 dyne/cm^2 for 30 min (shear phase). The pictures are showing areas without any T-cells interacting with the BLECs to illustrate the imaging clarity and the stability of the focus from the start (00min) to the end (34min55s) of the recording session under flow. Scale = 30 μm.

In order to illustrate how we could observe various types of T-cell/BLEC interactions with high resolution, we generated temporal snapshots from a video recorded with a 20x magnification where BLECs were stimulated with TNF-α (Figure 4.6A). In addition, we also recorded videos with a 10x magnification of T-cell-BLEC interactions where BLECs were stimulated or not with TNF-α. These 10x magnifications videos allowed us to have a statistical comparison of the T-cell behavior on the BLEC monolayers in unstimulated and TNF-α stimulated conditions (Figure 4.6B), since a higher number of T-cells could be tracked compared to higher magnification videos, at the cost of a lower resolution. To analyze the respective T-cell behavior on the BLECs monolayers in a quantitative manner, we performed a visual frame-by-frame offline analysis of the time-lapse videos. To this end, each T-cell was categorized into a specific behavioral group. Under both, unstimulated and TNF-α stimulated conditions, the majority of T-cells were found to polarize upon arrest and to migrate across the BLEC monolayer with or without prior crawling on the BLECs. These were categorized under "diapedesis" (Figure 4.6A). T-cells that crawled on the surface of the BLECs for the entire observation time were categorized as "crawling" (Figure 4.6A). One additional behavior observed was T-cells that remained stationary without displacing beyond a distance exceeding their own diameter and presenting dynamic cellular protrusions and thus "probing" the BLEC monolayer (Figure 4.6A). Also, a certain number of T-cells were found to quickly "detach" from the BLECs monolayer when the flow rate increased at the beginning

of the shear phase. In general, we observed a higher number of T-cells arresting on the TNF-α stimulated BLECs versus the non-stimulated BLECs monolayers resulting in an increased number of T-cells interacting with the TNF-α stimulated BLECs in each T-cell behavioral category (Figure 4.6B). Overall, the TNF-α stimulation favored T-cell-BLECs interactions without modulating their behavior among categories. This observation is in accordance with the upregulated cell surface expression of ICAM-1 and VCAM-1 previously shown (Figure 4.4D), suggesting that upon TNF-α stimulation, the upregulation of adhesion molecules could explain the significantly higher number of Th1 cells found to arrest on BLECs under physiological flow, $\sim$4 min after starting to infuse T-cells and just after the accumulation phase (Figure 4.6B). Taken together, our novel μSiM-CVB flow system allows for detailed observation of the multi-step T-cell extravasation across a human model of the BBB at a very small scale suitable for employing rare patient derived immune cells.

4.4 Discussion

The development of an *in vitro* platform to study the migration of immune cells across the BBB in the context of human CNS disorders has provided many challenges. We began addressing these challenges by first establishing a novel human *in vitro* model of the BBB from human ECs derived from cord blood $CD34^+$ hematopoietic stem cells [133]. We demonstrated that when

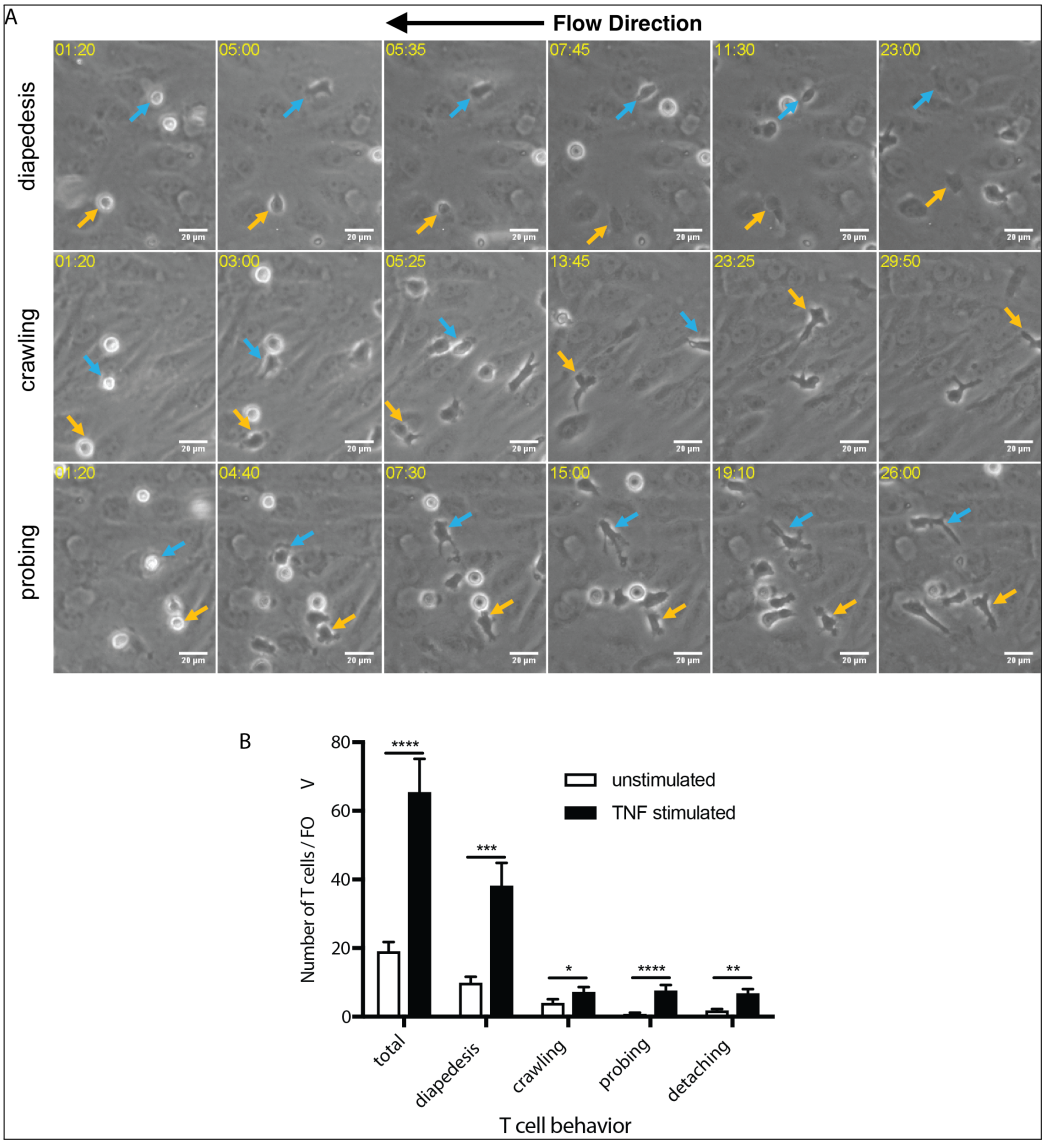

Figure 4.6: Caption Next Page

Figure 4.6: *In vitro* live cell imaging of the T-cell-BBB interactions under flow: (A) Temporal snapshots illustrating the different T-cell-BLECs interactions extracted from a video recorded with a 20x magnification (LD Plan-Neofluar 20X/0.4 Korr Ph2). The $CD34^+$ ECs were cultured in the top channel with the PCM in the bottom channel for 6 days and the $CD34^+$ ECs were stimulated with 10 ng/mL TNF-α 16h before recording the video. Th1 cells are allowed to accumulate on the BLECs monolayer at a low flow rate of 0.1 dyne/cm^2 for 4 min from the first frame after the first Th1 cells appear in the field of view, then the flow rate was set to 1.5 dyne/cm^2 for 30 min (shear phase). Each row is showing a specific behavior of the Th1 cells with the BLECs with the example of 2 differenT-cells highlighted with a blue and a yellow arrow. The first row illustrates the diapedesis event where T-cells start to arrest (1min20s) and then polarize and firmly adhere (5min) to the BLECs. Then the T-cells start to transmigrate through the BLECs monolayer (5min35s) and take more (23min, blue arrow) or less (7min45s, yellow arrow) time to complete diapedesis. T-cells are trapped in the subendothelial spaces and can still be followed and identified by their darker gray shape in comparison of the BLECs monolayer (23min). The second row illustrates the crawling event where T-cells first arrest (1min20s) and then polarize and firmly adhere (3min) to the BLECs. Then the T-cells start to form a leading edge with a lot of small protrusions (5min25s, blue arrow and 13min45s, yellow arrow) and actively move on the BLECs against the direction of the flow until they even disappear from the field of view (13min45s, blue arrow and 29min50s, yellow arrow). The third row illustrates the probing event where T-cells first arrest (1min20s) and then polarize and firmly adhere (4min40s) to the BLECs. Then, the T-cells remained stationary without displacing beyond a distance exceeding their own diameter and presenting the ability to greatly modulate their shape, sending a lot of dynamic cellular protrusions around them (from 7min30s to 26min). Scale=20 μm. (B) Analysis of the arrest and post-arrest T-cell interactions with NS and TNF-α stimulated BLECs in the field of view of the videos recorded with a 10x magnification under physiological flow (1.5 dyne/cm^2) for 30 min. T-cells remaining arrested to the BLECs monolayer where quantified (total) at the end of the accumulation phase (0.1 dyne/cm^2 for 4 min from the time the first T-cells appear in the field of view). Then post-arrest T-cell behavior on the BLECs was analyzed; each T-cell were categorized as follows: diapedesis, crawling, probing and detaching. Values are means $\pm$ SEM, n=10 for each condition. Statistical analysis: t-test * $p < 0.05$, ** $p < 0.01$, *** $p < 0.001$, **** $p < 0.0001$.

cocultured with pericytes, $CD34^+$ EC differentiate into brain-like endothelial cells (BLECs) establishing low permeability barriers and mature tight junctions. Due to the general availability of cord blood stem cells, BLECs can be widely adopted to study molecular mechanisms in pathologies implicating the BBB such as neurodegenerative or neuroinflammatory disorders (e.g. Alzheimer's disease, multiple sclerosis), stroke and traumatic brain injury, infectious processes and inflammatory pain.

While we have previously used BLECs to study immune cell extravasation and cancer metastatic cells across the BBB in static culture conditions [134, 186, 213], the application of physiological flow is needed for more physiological observations. Physiological flow has been shown to have a significant impact on T-cell diapedesis across vascular monolayers *in vitro* [179, 201]. The visualization of the multi-step immune cell extravasation across the vascular wall requires a testing platform compatible with transmitted light microscopy, preferably phase contrast. The desire for flow and live-cell imaging has compelled us and others to use flow chambers with endothelial cells cultured on glass coverslips, as the track-etched membranes used in traditional two-chamber filter devices are notoriously bad for imaging under transmitted light [73]. This choice, however, introduces new complications as non-permeable substrates are not physiological and are thought to compromise the polarization of barrier cells due to the lack of basal transport [214]. In addition, these flow chambers are not suitable for *in vitro* BBB models that rely on the continuous and polarized cross-talk of the brain endothelial cells

with cellular or acellular elements of the neurovascular unit, such as pericytes or astrocytes and CNS derived factors, respectively [215, 216]. Here, we provide new and compelling evidence of the need for a dual compartment for maintaining barrier characteristics in our human *in vitro* BBB model: the addition of pericyte conditioned media (PCM) to the basal, but not to the apical compartment, was sufficient for the induction of tight BLEC barriers (Figure 4.3A). Thus, $CD34^+$ ECs monocultures on non-permeable glass or tissue culture plastic would not mimic the human BBB *in vitro*, even in conditioned media. Our observations identify the challenges for developing a device platform suitable to study the migration of human immune cells across human *in vitro* models for the BBB: The device must: 1) provide for high quality live cell imaging, 2) be sufficiently small to allow for investigation of rare patient derived immune cells or BBB models, 3) enable physiological flow over the endothelial monolayer, 4) include two compartments to deliver an abluminal signal inducing the BLEC phenotype and 5) be separated by a highly permeable yet sufficiently rigid membrane that flow does not shift the image focus.

The previous decade has witnessed the emergence of customized microsystems for 'organ-on-chip' models or 'microphysiological systems' (MPS)[152]. While a number of these efforts have focused on BBB [203–207], only Walter and colleagues [107] addressed the need for membrane transparency. Their solution was to employ 'transparent' track etched membranes that have 100 fold fewer pores than conventional materials (10^6 pores/cm^2 vs 10^8

pores/cm^2) and are more than twice as thick (23 μm vs 6-10 μm). While these membrane modifications diminish the confounding influence of pores on light transmission and enabled the team to acquire clear phase images of monolayers, they also dramatically reduce the diffusive permeability of the membranes by more than two orders of magnitude. Indeed, we calculated the small molecule permeability of the low porosity TE membranes used by Walter et al. to be 10^{-5} cm/s, a value lower than some of the permeabilities we report here for luciferase yellow (LY) transport across BLEC monolayers. Thus, these low porosity TE membranes can be rate limiting for small molecule transport if used in a two chambers system. This would mask the properties of monolayers in barrier measurements and may prohibit induction of BBB characteristics in endothelial monolayers grown on these membranes because of the hindrance of small molecule diffusion to and from the basal side of cells.

We addressed the need for optical transparency by building the first *in vitro* barrier models featuring nanoporous silicon nitride (NPN) [142]. NPN is a durable and highly manufacturable 'silicon nanomembrane', a family of ultrathin free-standing porous membranes produced by silicon microfabrication methods [72, 109, 217]. NPN membranes are 50 nm thick NPN with ∼40 nm pores and a density of 10^{10} pores/cm^2 [142]. The small molecule diffusive permeability of these membranes is a remarkable ∼0.1 cm/s [218], a value so high that is indistinguishable from free diffusion through water in practical assays [111]. In other words, small molecule diffusion across a nanomembrane

occurs as if the membrane is not even there, even as it provides a physical divide to define the compartments of a two-chamber system. For our purposes, two key features make NPN superior to the microporous SiO_2 nanomembranes previously used to visualize direct HUVEC/ADSC cocultures [72]: 1) The sub-optical pore sizes of NPN give a feature-free background for high quality visualizing immune cell/endothelial interactions; 2) Endothelial cell adhesion to NPN is excellent even under high levels of shear stress that readily strips endothelial cells from microporous SiO_2 (Figure 4.2).

NPN membranes are produced on 6" silicon wafers containing hundreds of 5.4 mm x 5.4 mm 'chips'. An individual chip features the membrane suspended across a central window (2 mm x 0.7 mm) etched into 300 μm thick silicon platform (Figure 4.1A) that is used for membrane handling and bonding. This chip format makes easy to both design and build custom microfluidic devices in the laboratory using layer-by-layer assembly (Figure 4.5A) [124]). While the "Transwell® mimetic" and the μSiM-CVB flow system devices used here were all hand built, we have recently translated the layer-by-layer manufacturing to a commercial fabrication with greater than 95% device yield (McGrath lab, unpublished results).

Our objective in the present project was not to build a three-dimensional *in vitro* model of the human BBB including all cellular and acellular elements of the neurovascular unit. Rather our study addressed an unmet need in the CVB research community for the transfer of a well characterized model of the human BBB into an *in vitro* platform allowing to study the migration of

human immune cells across the human BBB under physiological flow by live cell imaging. High fidelity, high-throughput manufacturing at both the chip and device levels are key to our goal of making the μSiM-CVB system widely available to this community. Furthermore the volumes of the basal channels in both the "Transwell mimetic" and the μSiM-CVB flow system, and the apical channel in the μSiM-CVB flow system of the device are less than 20 μL. This feature will eventually allow the use of small samples of body fluids or cells obtained from patients for personalized medicine. Even for *in vitro* mouse models, microfluidic volumes of these devices are beneficial, since the volume of body fluids of mice are equally small. For example, a metabolic profile analysis is difficult to achieve unless the working sample volumes are on the same order as the volumes in the body.

In our present study, NPN membranes were superior to any commercially available membrane systems with respect to their optical characteristics and most critically by providing the adhesive properties that allowed maintenance of a BLEC monolayer under physiological flow. Indeed, the $CD34^+$ ECs grew perfectly on the NPN membrane reaching confluency 24h after seeding and building a dense monolayer after 6 days of culture. Because the silicon platform enables the facile construction of dual compartment culture devices, we readily adapted the coculture based human *in vitro* BBB model requiring coculture of $CD34^+$ ECs with pericytes [133]. Successful replacement of the pericyte coculture with pericyte-conditioned medium (PCM) supplied from the basal compartment further advanced the human *in vitro* BBB model for

in vitro live cell imaging. Basal application of PCM allowed for differentiation the $CD34^+$ ECs in BLECs monolayer with low permeability to small molecular tracers and BBB like morphology as visualized by the junctional localization of VE-cadherin, claudin-5 and ZO-1 and the establishment of a cortical F-actin ring.

The next step, which was to apply flow in our μSiM-CVB flow system, took full advantage of the properties of the NPN material that help distinguish it from all commercial membrane materials. While its thinness gives it a superior transparency and makes it excellent for live cell imaging, the ceramic-like membrane is sufficiently stiff that it remains in focus with the onset of flow. Indeed, in our present study we found that applying shear forces up to 1.5 dynes/cm^2 in the apical compartment of our novel device did lose focus in more than 30 minutes of continuous recording. Optical imaging quality of the T-cell interactions observed on the BLECs monolayer using the novel μSiM-CVB flow system were indistinguishable from those previously recorded when studying T-cell interaction with endothelial monolayer grown on glass [193, 194, 219]. The observations of T-cell arrest, crawling on, and diapedesis across the BLECs monolayer under physiological flow as well as the observed influence of the inflammatory status of the BLEC on these interactions, validates the μSiM-CVB as an *in vitro* BBB platform.

By applying our previously established stem cell derived *in vitro* model of the human BBB to a nanomembrane-based microfluidic device with key physical and optical characteristics, we have established the μSiM-CVB as an

important new tool allowing for study of barrier functions of the human BBB. While we developed the platform using BLECs, including the replacement of coculture with PCM in the basal compartment, the devices are likely compatible with alternative and potentially patient derived BBB models, such as those established from iPSC derived [184, 220]. The manufacturability of both our membranes and devices, will help us disseminate this tool to the CVB community to study the process of extravasation by immune cells, and potentially metastatic cancer cells, with the human BBB under physiological flow *in vitro*. Additionally, the small volume requirements of the μSiM-CVB platform can support studies with rare patient-derived samples in personalized medicine. Overall, we expect the μSiM-CVB platform to open new opportunities to define novel therapeutic targets for neurological disorders ranging from neuroinflammation and neurodegeneration to tumor metastasis and for adaptation to investigate other cellular barriers.

4.5 Methods

4.5.1 Device Fabrication

The key feature of the engineered devices used in the cell culture applications presented here is the nanoporous silicon nitride (NPN) membranes, also referred to as silicon nanomembranes. The details of the fabrication of these membranes are provided elsewhere [142]. The membranes are commer-

cially available at SiMPore Inc., West Henrietta, NY. These membranes are manufactured on 300 micron silicon substrates with a resulting freestanding permeable film that is 50 nm thick with a pore aspect ratio of 1:1 (i.e., average pore diameter is also 50 nm). The overall dimension of the silicon membrane 'chips' is 5.4 x 5.4 mm^2. The permeable area or membrane 'window' of the chip is 2 mm x 0.7 mm.

The microfluidic device used for static and dynamic assays consist of 2 compartments: apical and basal, separated by the permeable membrane chip in between. The apical and basal fluidic compartments or channels are composed of transparent silicone gaskets (300 microns thick) commercially available from Specialty Silicone Fabricators, CA. The different layers of the devices are shown in Figures 4.4 and 4.5 representing the devices for static and flow configurations respectively. The channels and the silicon chip are covalently bonded to each other via surface functionalization of the silicon atoms in each layer. Briefly, both the bonding surfaces are exposed to UV-Ozone environment for 10-15 minutes, followed by thermal curing at 70°C for 2 hours. The fluidic access ports for these devices are provided by a thick slab of poly dimethylsiloxane (PDMS) (Sylgard 184, Dow Corning). Flow devices have 4 access ports: 2 for the apical chamber and 2 for the basal chamber, while "Transwell mimetics" only have access ports for the basal chamber. These ports are made by simply punching holes in the PDMS block using a 18 gauge needle. Media reservoirs are added to support T-cell culture in both types of devices. In the "Transwell mimetic" this is a single reservoir

immediate above the membrane while the flow devices have a media reservoir on the top of all the 4 access ports. The reservoirs are made out of PDMS blocks as well with wider punched holes, and bonded to the intermediate PDMS blocks via UV-Ozone exposure. The PDMS blocks and the bottom glass substrates are also bonded to the gaskets-chip-gaskets' assembly using similar UV-Ozone chemistry.

4.5.2 Isolation and differentiation of $CD34^+$ cells from human umbilical cord blood

The isolation of $CD34^+$ cells required the collection of human umbilical cord blood (UCB) from infants. Parents signed an informed consent form in compliance with French legislation. The protocol was approved by the French Ministry of Higher Education and Research (CODECOH Number DC2011-1321) and all experiments were carried out in accordance with the approved protocol. $CD34^+$ cells were isolated from human umbilical cord blood (UCB) according to a protocol previously reported [221]. Then, $CD34^+$ cells isolated from the UCB were differentiated in ECM basal medium (ScienCell) supplemented with 20% (v/v) fetal bovine serum (FBS; Life Technologies) and 50 ng/mL of VEGF165 (PeproTech Inc.), on 1% (w/v) gelatin-coated 24 well plates ($2x10^5$ cells/well). After 15-20 days ECs are seen in the culture dish. For each experiment, the cells were expanded in 0.2% (w/v) gelatin-coated 100 mm Petri dishes (Corning) in ECM basal medium supplemented with 5% FBS, 1% endothelial cell growth supplement (ECGS; ScienCell) and 50

μg/mL gentamycin (Biochrom AG).

4.5.3 Induction of BBB characteristic in CD34$^+$-derived endothelial cells

Induction of BBB like characteristics in CD34$^+$-derived endothelial cells was achieved by coculture with bovine pericytes as described before [133]. In brief, pericytes were initially seeded on 100-mm gelatin-coated petri dishes (Corning) and cultured in Dulbecco's Modified Eagle's Medium (DMEM) (Life Technologies) supplemented with 20% (v/v) FBS (Life Technologies), 2 mM L-glutamine, 50 μg/mL gentamycin. Upon reaching confluency pericytes (2.25x10^4/well) were seeded into 24-well plates (Costar). On the following day, CD34$^+$-derived ECs grown on gelatin-coated 100 mm petri dishes in ECM (Sciencell) were trypsinized and seeded (4x10^4/filter insert) onto Matrigel-coated (Corning, 354230) Transwell filter inserts (Costar cat number 3495) and placed above the pericyte cultures. At the end of this culture procedures the CD34$^+$-derived ECs will acquire the features of brain like endothelial cells (BLECs) as revealed by the expression of BBB marker and functional properties revealed by LY permeability assay evaluated from 2 to 20 days of coculture [133].

4.5.4 Endothelial Permeability (Pe) Measurements

Endothelial permeability was investigated by measuring the clearance of Lucifer yellow (LY; 20 nM; Life technologies) across the BLECs monolayer exactly as described before [133, 194, 210, 222]. In brief, prior to experiments, LY (MW 457.3 g/mol) was diluted in assay medium (DMEM (Gibco, Paisley, UK), 5% FCS (Gibco, Paisley, UK), 25 mM Hepes (Gibco, Paisley, UK), 2% l-glutamine Gibco, Paisley, UK) as previously published in [133] and 100 μl of the LY solution (20 nM) was added to the upper side of the filter inserts, which were subsequently placed into wells containing 600 μl of assay medium. The plate was incubated at 37°C and the inserts were transferred into wells containing fresh assay medium every 10 min, avoiding long exposure to light and room temperature. 200 μl samples from all lower compartments were transferred to a 96-well plate. For the "Transwell mimetic" system, the membrane compartment was filled with 50 μL of a LY solution (20 nM), and in the basal compartment with 20 μL of permeability assay medium. After 60 min incubation, the assay medium was collected from the basal compartment and the fluorescence was evaluated with the TECAN reader infinite M1000 PRO. A standard dilution curve (20-0.05 μM) and empty filters or "Transwell mimetic" were used to obtain the reference permeability of the empty filter inserts. The permeability coefficient was calculated as follows: the slope of the average tracer volume cleared was plotted versus time in order to obtain the linear regression designated as PSt. The slope of the tracer clearance curve of the coated empty filters was indicated as PSf. The permeability

surface area product of the endothelial cell monolayer (PSe) was calculated from PSt and PSf: 1/PSe = 1/PSt - 1/PSf. The PSe was divided by the filter surface area, in order to generate the epithelial Pe in cm/min. The fluorescence detection was performed using the Tecan Infinite M1000 device and the Tecan i-control software (Tecan Trading AG, Minnerdorf, Switzerland).

4.5.5 Stimulation of BLECs with the pro-inflammatory cytokine TNF-α

To mimic neuroinflammatory conditions, human brain like endothelial cells (BLECs) were stimulated with human recombinant tumor necrosis factor-α (TNF-α, 210-TA, R&D Systems, Inc.) at a concentration of 10 ng/ml for 16 to 20h prior to performing experiments.

4.5.6 Immunofluorescence staining of BLECs

For staining in the Transwell filter inserts, BLECs were fixed in 1% (w/v) formaldehyde diluted in calcium and magnesium-free phosphate- buffered saline (PBS) for 10 min at room temperature (RT) and permeabilized with Triton X-100 (0.1% (w/v) in PBS) for 10 min at RT. After three rinses with PBS, the filter membranes were carefully cut out with a scalpel and blocked for 30 min with skimmed milk 5% (w/v) in PBS. BLEC monolayers were incubated for 1h at RT with primary antibody against zonula occludens-1 at 5 μg/mL (ZO-1, Thermo Fisher Scientific, 617300) or VE-Cadherin at 7.5

μg/mL (ref. sc-9989; Santa Cruz). For the staining of claudin-5, BLECs were fixed in methanol at -20°C for 30s before a permeabilization step of 20 min at RT in Triton X-100 0.3% in PBS, followed by a blocking step of 20 min at RT in in skimmed milk 5% in PBS. Next BLECs were incubated with primary antibody against claudin-5 at 2.5 μg/mL (Invitrogen, 381700) diluted in skimmed milk 5% (w/v) in PBS. After three washes in PBS, cells were incubated with secondary antibody for 30 min at RT with goat anti rabbit/Alexa Fluor 488 at 5 μg/mL (life technologies, 11034) for ZO-1 and claudin-5 and goat anti mouse-Cy3 at 7.5 μg/mL (Jackson ImmunoResearch, 115-166-06) for VE-Cadherin. After Triton permeabilization, staining of F-actin was obtained with rhodamine-labeled phalloidin (Invitrogen, R415) 1:50 in PBS for 1h at RT. Nuclei were stained using DAPI at 1 μg/mL. Each filter was mounted on a glass slide under a rounded coverslip, using a drop of Mowiol (Sigma-Aldrich) containing 1,4-diazabicyclo [2.2.2] octane (Sigma-Aldrich) as an antiquenching agent.

For BLECs staining on NPN membranes live cells were incubated with 10 μg/ml of anti-ICAM-1 (R&D system), ICAM-2 (Fitzgerald), or VCAM-1 (Clone 51-10C9, cat 551146) antibody for 20 min at 37°C in the culture medium. After a washing step with PBS, BLECs were fixed with 1% PFA in PBS and permeabilized with Triton X-100 (0.1% (w/v) in PBS) for 10 min at RT. For ICAM-1 and ICAM-2 staining, cells were incubated with the secondary antibody donkey anti-mouse-Cy3 (Jackson ImmunoResearch, 715-165-151). For F-Actin staining, after Triton permeabilization, cells were

incubated with rhodamine- labeled phalloidin (Invitrogen, R415) 1:50 in PBS for 1h at RT. Nuclei were stained with DAPI at 1 μg/mL. For the staining of ZO-1 and VE-Cadherin, after incubation with primary antibody, BLECs were washed in PBS and incubated with secondary antibodies, goat anti-rabbit-Alexa Fluor 488 and goat anti mouse-Alexa Fluor 488, respectively, for 30 min at RT. For the claudin-5 staining, the same protocol as for BLECs staining on Transwell filters was applied. Stained samples were analyzed with a fluorescence microscope (Axio Observer, Zeiss) and pictures were acquired at the day of the staining and processed with the ZEN software.

4.5.7 Human peripheral blood T-cells

Human $CD4^+CD45RO^+$ T helper 1 (Th1) cells were obtained by fluorescence activated cell sorting from the peripheral blood of healthy donors according to their specific expression pattern of chemokine receptors ($CXCR3^+$, $CCR4^{neg}$ $CCR6^{neg}$) exactly as previously described [223, 224]. Th1 cells were cultured in the presence of interleukin-2 (IL-2, 500U/ml) for a total of 20 days. At the day of the experiment dead cells were removed by a Ficoll gradient (780g, 20 min, 20°C) and Th1 cells were resuspended in migration assay medium (DMEM without phenol red, Hepes 25 mM, Fetal Bovine Serum 5%, L-glutamine 4mM) at $1x10^6$ cells/mL.

4.5.8 *In vitro* live cell imaging

BLECs were grown to confluency in ECM basal medium supplemented with 5% FBS, 1% endothelial cell growth supplement (ECGS; ScienCell) and 50 μg/mL gentamycin (Biochrom AG) for 6 days as described before and stimulated or not 16 h to 20 h prior to the assay with TNF-α at 10 ng/mL (R&D System, 210-TA). The flow experiment settings consisted of an open reservoir containing migration assay medium only and another one containing the T-cell suspension both connected with an inlet transparent PVC tubing (dia = 1 mm, Semadeni, ref 1336) to the flow chamber by a 3-way tap allowing to alternatively infuse T-cells or migration assay medium without stopping or disturbing the laminar flow. The inlet and outlet tubing were connected to the flow chamber with an 18 gauge straight needle with the tap open to avoid any increased pressure in the chamber. Flow was applied by connecting the outlet tubing to a syringe automatically drawn up by a precision pump (Harvard Apparatus, Holliston, MA, USA). The flow rate was calculated as described in [187]. Briefly, the shear stress was calculated according to the formula: $\tau = (3 \text{ x } \mu \text{ x } Q)/(2 \text{ x } a^2 \text{ x } b)$ with τ = shear stress (dyne/cm^2), μ (coefficient of viscosity) = 0.0083 dyne x sec/cm^2 (migration assay medium), Q (volumetric flow rate) = variable controlled by the pump in cm^3/sec, a (half height of the chamber) = 0.015 cm, b (width of chamber) = 0.2 cm. To allow for the accumulation of sufficient Th1 cells on the BLECs monolayer, Th1 cells were first infused with a flow rate of 0.1 dyne/cm^2 for 4 min (accumulation phase). After the accumulation phase, the tap is switched to

infuse migration assay medium only and the flow rate was increased to 1.5 dyne/cm^2 thus mimicking a physiological laminar flow condition for 30 min (shear phase). T-cell interaction with the BLECs was recorded for 30 min in time lapse mode (1 picture/5 s) with 10x (EC Plan-Neofluar 10X/0.30 Ph1) or 20x (LD Plan-Neofluar 20X/0.4 Korr Ph2) objectives with a field of view (FOV) respectively of 0.645 μm x 0.645 μm and 0.323 μm x 0.323 μm using an inverted research microscope (Axio observer Z1, Zeiss) equipped with a camera (Zeiss Axiocam MRm) and the ZEN-blue software. The microscopic equipment used for the *in vitro* live cell imaging has been described in depth before [187]. Video editing was performed with the software "Adobe After Effect" allowing to export the image sequences as videos running at 30 frames/s as well as to edit the videos to show the different T-cell behavior with the BLECs. Fiji software was used to classify the T-cell behavioral categories observed on the BLECs under physiological flow (diapedesis, crawling, probing and detaching).

4.5.9 Statistical Analysis

Data are shown as the mean ± S.E.M. Statistical significance was assessed by Student's t-test or one-way ANOVA followed by Dunett's post hoc test. For multiple comparison p-values are indicated in the corresponding figures (**** $p < 0.0001$). Statistical analyses comprising calculation of degrees of freedom were done using GraphPad Prism 6 software (Graphpad software, La Jolla, CA, USA).

4.5.10 Ethics approval and consent to participate

The isolation of $CD34^+$ cells required the collection of human umbilical cord blood (UCB) from infants. Parents signed an informed consent form in compliance with French legislation. The protocol was approved by the French Ministry of Higher Education and Research (CODECOH Number DC2011-1321).

Funding and Acknowledgements

This study was funded by the Swiss National Science Foundation (CRSII3_154483, Sinergia UnmetMS) to BE and FS, the Swiss Multiple Sclerosis Society to AM and the Germaine de Stael PHC program to FG and BE. JLM and TK were supported by NIH R01 HL125265. We gratefully acknowledge Thomas Andolsek for the initial phase of device manufacturing, and the support of the Microscopy Imaging Center of the University of Bern.

4.6 Author's Contribution

Britta Engelhardt: Conceptualization; Resources; Supervision; Funding acquisition; Project administration; Writing-review and editing.

Adrien Mossu: Data curation; Formal analysis; Investigation; Methodology; Writing-original draft.

Maria Rosito: Data curation; Formal analysis; Investigation; Methodology;

Writing-original draft.

Tejas Khire: Data curation; Formal analysis; Investigation; Methodology; Writing-original draft.

Hung Chung: Data curation; Methodology.

Hideaki Nishihara: Data curation; Formal analysis; Investigation; Methodology.

Isabelle Gruber: Data curation; Formal analysis; Investigation; Methodology.

Emma Luke: Methodology.

Lucie Dehouck and Federica Sallusto: Resources; Methodology.

Fabien Gosselet: Resources; Methodology; Writing-review and editing.

James McGrath: Conceptualization; Supervision; Funding acquisition; Project administration; Writing-review and editing.

Chapter 5

Porous Silicon Nitride Membranes for *in situ* Optical Analysis of Translocation of Nanoparticles across the Blood-Brain Barrier[†]

5.1 Abstract

Despite the increased expectations of leveraging nanomaterials to enhance therapeutic delivery to the central nervous system, methods to directly study the transportation of nanoparticles (NPs) across the blood-brain barrier (BBB) remain relatively undeveloped. *In vitro* BBB models have been used for decades to study mechanisms of cerebrovascular transportation. The

[†]This chapter is adapted from and is a condensed version of a manuscript in preparation. I am the second author of this manuscript and was responsible for data curation, analysis, troubleshooting, and writing the original draft. The work presented in this chapter is a collaborative research between the labs of James McGrath (University of Rochester) and Kenneth Dawson (University College Dublin, IE). The microfluidic platform that is central to the studies in this paper was designed, developed, and optimized by me. Only the results directly obtained from this platform and that are relevant to the main theme of this thesis have been presented in this chapter.

most common BBB model is based on cocultures on track-etched thick semi-permeable membrane (e.g. Transwell® systems), which does not allow physical interactions between the cocultures, nor high-resolution imaging analysis due to light scattering. In this study, an ultrathin silicon nitride (SiN) membrane (0.5 μm pore size, 20% porosity, 400 nm thickness) supported by a cell culture device was used to refine an established human BBB coculture model by growing human brain endothelial cells and primary astrocytes on opposite sides of the membrane. Our data have confirmed that the human brain endothelial cells form tight junctions on the SiN membrane when grown in physiological proximity to astrocytes, with enhanced barrier properties in comparison to Transwell® devices. Furthermore, the enhanced optical properties of SiN membrane render the devices compatible with *in situ* live and fixed high-resolution imaging, which allows us to directly study the translocation of nanoparticles (NPs) across the barrier using confocal microscopy. The results reveal not only significant NP accumulation in lysosomes in the endothelial cell barrier but also rare events of NP translocation, which are not possible with conventional thick and opaque membrane supports. These translocated NPs are comprised of less than 0.04% NPs of all the NPs detected, highlighting the sensitivity of the imaging-based approach, and the value of ultrathin silicon membranes as a platform for evaluating the NPs passage through the BBB.

5.2 Introduction

Nanoparticles- (NPs) based drug delivery approaches enable the transport of therapeutic molecules in the central nervous system, and numerous studies have been published in the past that modify the NP surface chemistry for an efficient uptake and transport across the BBB [136–139]. To enhance our knowledge of the mechanisms that makes this uptake possible, it is valuable to visualize translocation under live conditions across the human BBB *in vitro*. Existing platforms such as Transwell® systems (hereafter referred to as transwell or transwell inserts) offer poor imaging quality, non-physiological thickness under coculturing conditions, and are not suitable for high-resolution confocal microscopy due to large working distances. In this study, we report, for the first time, the NP transcytosis analysis using an *in vitro* BBB coculture model based on a cell culture device prototype using ultrathin (400 nm thick), highly porous (20% porosity) SiN membrane with pores of 0.5 μm diameter. Immortalized human brain capillary endothelial hCMEC/D3 cells [225] and primary human NHA astrocytes are grown in juxtaposition on the opposite side of the SiN membrane. In comparison to an equivalent transwell model, the optical visualization by transmitted light and fluorescence of both endothelial cells and astrocytes was significantly enhanced in the SiN membrane model. In addition, the SiN model demonstrated an elevated improved barrier compared to transwells in a permeability assay. Results confirm that the hCMEC/D3 cells express claudin-5 tight junction protein, form a con-

fluent monolayer, and Normal Human Astrocytes (NHA) express astrocytic marker glial fibrillary acidic protein (GFAP) on collagen/fibronectin coated SiN membranes. Furthermore, we employ high-resolution three-dimensional (3D) live-cell imaging to analyze NP translocation across the barrier *in situ*. While the overwhelming majority of carboxylated polystyrene (PS-COOH) NPs (100 nm in size) become trapped in the endothelial cells, this platform allows us to identify several rare (less than 0.04% of NPs detected) translocation events of NPs across the intact barrier. Given the challenges of designing NPs that can successfully deliver drugs into the CNS, these results suggest that the nanomembrane platform will be useful for identifying and amplifying those characteristics of NPs that successfully translocate the BBB.

5.3 Results and Discussion

5.3.1 Coculture Device Prototype for *In Vitro* BBB Model

The coculture device used for this study has the design resembling to the ones described in Chapters 3 and 4. The main difference lies in the type of nanomembrane used for this study - 0.5 micron pore and 400 nm thick. Materials used for fabrication and the assembly procedure is described in previous chapters. Figure 5.1 represents the schematic of the device used for the current work. 500 nm pore size will allow NP to pass through the membranes, but will prevent any events of cell migration.

Next, we sought to examine the barrier property of the SiN membrane-based BBB coculture. In a functional BBB, endothelial cells express tight junctions, adherens junction proteins, and junctional adhesion molecules, such as claudins, occludins, and zonula occludens, to form a tight physical barrier that only allows small water-soluble compounds to pass [226]. To analyze the formation of cell adhesion by endothelial cells in the BBB coculture, cells were directly fixed, stained with anti-claudin-5 tight junction protein antibody, and imaged in the SiN membrane device (Figure 5.1A). Glial fibrillary acidic protein (GFAP) that is exclusively expressed in astrocytes was immunostained to identify the astrocytes (Figure 5.1B). By labeling the cells with their distinctive markers, the two adjacent layers of cells became clear (Figure 5.1C). Our data showed that claudin-5 tight junction protein was uniformly abundant in cells that were lacking GFAP expression (i.e. hCMEC/D3 cells). The high expression of claudin-5 tight junction protein suggests the formation of a tight and functional barrier that has very low permeability. To confirm this, we estimated the paracellular permeability of fluorescently labeled 4 kDa FITC-dextran ($\sim$1.5 nm). The paracellular permeability of the BBB coculture formed on the SiN membrane is 1.51 $\pm$ 0.50*10^{-6} cm/sec, much smaller (3.5-9.2 times smaller) than the permeability of hCMEC/D3 monoculture models [225, 227, 228] and approximately 3.3 times smaller than the permeability of the equivalent BBB coculture grown on Transwell insert (4.93 $\pm$ 0.10*10^{-6} cm/sec) (Table 5.1). To form a tighter barrier, astrocytes release various signaling molecules that stim-

ulate the differentiation of endothelial cells [229]. Our data suggests that the ultrathin permeable SiN membrane significantly promote such cell-cell communications in comparison to commercial transwell inserts with polymer membranes, resulting in better barrier properties for the BBB model.

Table 5.1: Paracellular Permeability of 4 kDa FITC-dextran: Enhanced barrier properties of BBB

Permeability (x10^{-6} cm/s	**Membrane Specifications**	**BBB Model**)
1.51 ± 0.50	Silicon Nitride, 0.5 μm	hCMEC/D3 + NHA
4.93 ± 0.10	Polyester, 0.4 μm	hCMEC/D3 + NHA
5.42	Polycarbonate, 3 μm	hCMEC/D3 [225]
13.8 ± 0.5	Polythelene Terephthalate, 0.4 μm	hCMEC/D3 [227]
8.83 ± 0.33	Polythelene Terephthalate, 0.4 μm	hCMEC/D3 [227]
12.0 ± 1.17	Not indicated	hCMEC/D3 [228]

5.3.2 Nanoparticle Transport in the BBB Model

Commercial fluorescently labeled 100 nm PS-COOH NPs were chosen to study transport across the SiN membrane-based *in vitro* BBB model. The apical side of the *in vitro* BBB coculture model was exposed with PS-COOH NPs (100 μg/mL in cell culture medium supplemented with 10% fetal bovine serum) for 10 minutes followed by removal of the NPs in excess and further culturing for up to 48 h (chase time). First, we determined the optimal magnification for high-resolution fluorescence imaging for tracking NPs. Our studies have shown that a 60x oil objective gave the best quality of imag-

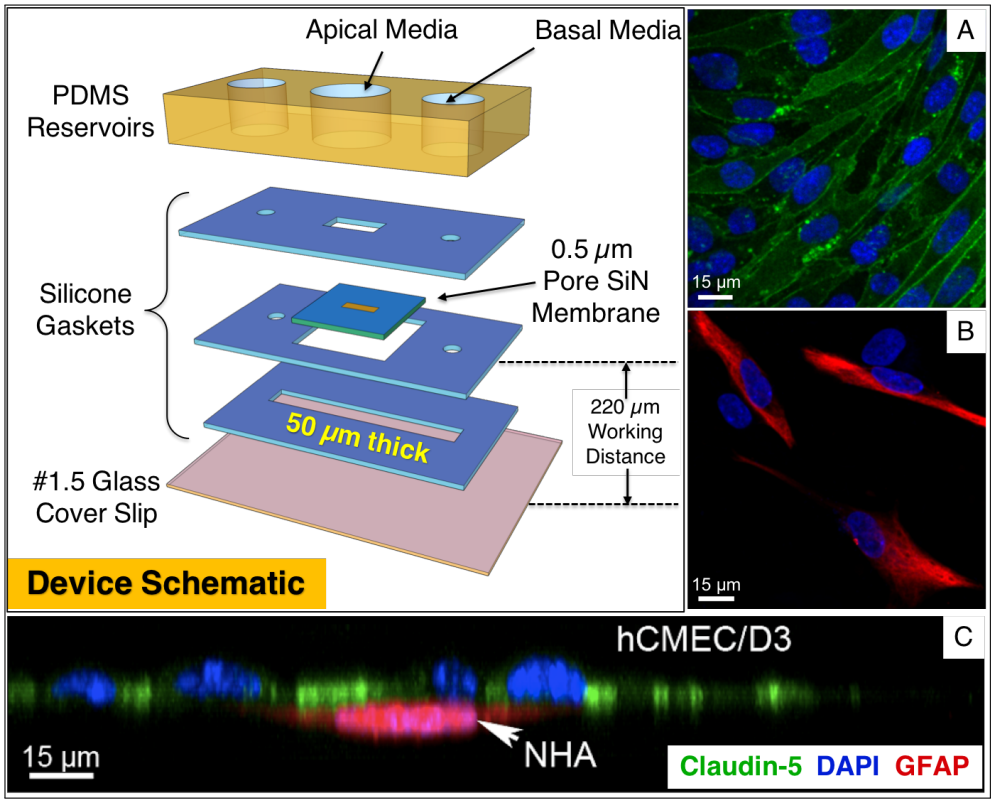

Figure 5.1: Schematic and Expression of BBB Markers *In Vitro*. The device consisted mainly of two components: the silicone-based housing that hosts the membrane chip and the membrane chip itself. The central well of the top PDMS reservoir hosts the media for long-term endothelial cell-culture. The two peripheral smaller wells are connected to the bottom channel where the astrocytes were grown and provide the additional media volume. Including the glass substrate, the total working distance is ∼220 microns. Immunocytochemical analysis of the SiN membrane-based BBB coculture model. (A-B) Expression of tight junction protein claudin-5 (green) in hCMEC/D3 cells and astrocytic marker GFAP (red) in NHA cells. (C) The y-z cross-sectional view of the coculture model showing the distinctive two layers of cells. The nuclei were stained by DAPI (blue). Image acquisition: 40x oil objective. Scale bars: 15 μm.

ing, as any higher magnification and/or shorter working distance resulted in images out of focus. To outline the two layers of cells in the coculture, the acidic organelles of both endothelial cells and astrocytes were fluorescently labelled (LysoTracker^{TM} Deep Red). Due to the distinctively different nature of the cell types, the lysosomes in astrocytes exhibited much stronger staining, allowing clear identification of the two layers (Figure 5.2). By scanning the entire apical and basal compartments (including the bottom cover glass located 50 μm from the membrane), we found that virtually all NPs were retained at the endothelial barrier (Figure 5.2A). In contrast, when the endothelial layer was not fully confluent, NPs were observed in both apical and basal compartments including a significant population in astrocytes (Figure 5.2B).

Finally, we sought to challenge the sensitivity of high-resolution fluorescence imaging using the SiN membrane-based BBB model for detection of rare translocation events. Using the aforementioned NP exposure conditions, we scanned the entire apical and basal compartments at different chase time points. Combining 4 independent experiments (i.e. two for 24 h and two for 48 h), more than 10,000 NPs were identified using a built-in spot algorithm of Imaris. Only four NPs were found on the basolateral side, one of which is shown in Figure 5.2C. Figure 5.2D is a representative 3D image showing the ability to image thousands of particles while scanning to identify the rarity of translocation events. Previous studies have shown that translocation of NPs across the BBB is rare for a wide range of NP size [230, 231]. To some

extent, the larger sized NPs have been suggested to exhibit a lower efficiency to translocate the BBB (e.g. 100 nm PS-COOH in comparison to 40 nm PS-COOH [231]). Hence, the infrequency of 100 nm PS-COOH NP translocation events observed in this study underscores the exceptional sensitivity of our system. In addition, it is puzzling that these rare events occurred even 24 - 48 h after the NP exposure. In this time frame, most NPs have been accumulated in lysosomes in the endothelial cells. Such lysosomal accumulation of 100 nm PS-COOH NPs in the endothelial of has been shown to trigger a set of paracrine signaling between the endothelial cells and the underlying astrocytes, including down-regulation of pro-inflammatory cytokines and up-regulation of growth hormones [232]. It has been widely acknowledged that cell-cell communication between endothelium and astrocytes can modulate the permeability of the BBB [229, 233]. Clearly, there is a need to further understand how NPs can impact the barrier cells, and how the resulting signaling between the barrier cells and astrocytes can in turn influence NP transcytosis. By capturing very rare and localized translocation events, high resolution nanomembrane-based imaging provides an important new tool for this endeavor.

5.4 Conclusion

While imaging-based analysis, such as point scanning or spinning disk confocal microscopy and total internal refection fluorescence microscopy can

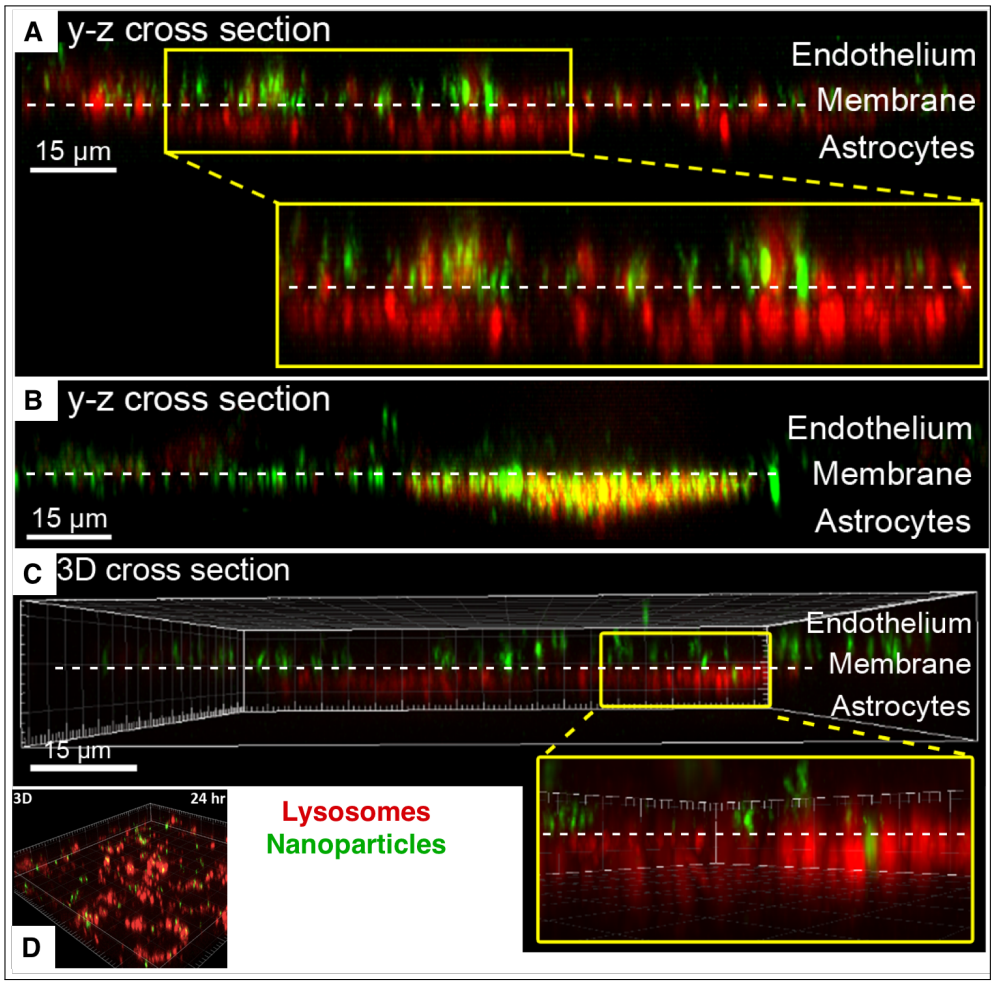

Figure 5.2: Caption Next Page

Figure 5.2: Nanoparticle Translocation Across BBB: Subcellular location of 100 nm PS-COOH NPs 24 hours post-exposure. (A) Representative y-z cross-sectional view of the intact coculture model showing that no NPs (green) were found inside the astrocytes (red) or in the basal compartment. (B) Representative y-z compressed cross-sectional view of a coculture model with sub-confluent endothelial cell barrier showing that significant number of NPs (green) accumulated inside astrocytes where they co-localized with or located closed to (yellow) the lysosomes (red) 24 hours post-exposure. The fluorescence intensity of lysosomal staining in astrocyte was much stronger than in endothelial cells (both labeled by LysoTracker^{TM} Deep Red lysosomal dye), therefore, endothelial cells are not visible in the reconstructed 3D image. (C) Rare case of translocation of NPs across an intact BBB coculture was observed 24 hours after a 10 min NP exposure. (D) A representative 3D isometric view of the scanning region showing the location of NPs 24 hours post exposure.

provide evidence of translocation [231], these studies ideally demand permeable substrates that support a valid BBB model with the cell types of the neural vascular unit. Imaging on permeable substrates, however, presents a different set of challenges, which are addressed here by the use of SiN nanomembranes. Here we presented an *in vitro* BBB coculture model based on an ultrathin and transparent SiN membrane device that was specifically designed for high-resolution imaging purposes. Both hCMEC/D3 endothelial cells and NHA astrocytes preserved their morphology and phenotype on the collagen/fibronectin pre-treated membrane and presented enhanced barrier properties in comparison with the transwell model, presumably because of better cell-cell communication. One of the clear advantages of this model is that it is compatible with both *in situ* fixed-cell and live-cell high-

resolution imaging that enable monitoring of different cellular and spatiotemporal events, including rare events of NP translocation across the BBB. By using 100 nm PS-COOH NPs as a model delivery system, we have illustrated that a high degree of lysosomal co-localization of NPs in the endothelial layer. We were also able to quantify that less than 0.04% of all NPs in four long term (24+ hours) experiments actually crossed the barrier. This result is a testament to the sensitivity of nanomembrane-enabled high-resolution imaging in detecting rare NP translocations. Given that most CNS-targeted NPs are captured by the BBB, our platform may be the key to improving the design of NPs by amplifying those characteristics that produce a modest translocation until therapeutic doses can be achieved.

5.5 Materials and Methods

5.5.1 Nanomembrane Fabrication

Silicon nitride membranes were purchased from SiMPore Inc. (West Henrietta, NY), and manufactured as described elsewhere [141]. The membrane dimensions were 5.4x5.4 mm^2, with an active (porous) area of 2.0x0.7 mm^2, pore size of 0.5 μm, and thickness of 400 nm.

5.5.2 Device Assembly

The devices used for the *in vitro* BBB studies were assembled using the processes described in Chapters 3 and 4 according to the design shown in Figure 5.1.

5.5.3 Routine Cell Culturing

Immortalized human brain capillary endothelial hCMEC/D3 cells (provided by P.O. Couraud, INSERM, France) were used between passages 28 and 35. For routine cell culture, cells were seeded in collagen-coated flask (Corning Collagen I flasks or rat tail type I collagen (Sigma Aldrich) pre-coated flasks from Greiner Bio-One GmbH) and supplemented with EBM-2 basal medium containing vascular endothelial growth factor (VEGF), insulin-like growth factor-1 (IL-1), epidermal growth factor (EGF), basic fibroblast growth factor (bFGF), ascorbic acid, gentamicin sulfate/amphotericin B (GA-1000), hydrocortisone (all from Lonza Biosciences) and 2.5% fetal bovine serum (FBS) (Gibco). For functionality assays and other experiments, all cultureware were coated with rat tail type I collagen (Sigma Aldrich) at a concentration of 100 μg/ml or with the mixture of 100 μg/ml rat tail type I collagen and 50 μg/ml bovine plasma fibronectin (Thermo Fisher Scientific) (collagen/fibronectin) and incubated for 1 hour at 37°C; the cells were supplemented with growth factor depleted EBM-2 medium containing bFGF, hydrocortisone, GA-1000 (all from Lonza Biosciences), 2% FBS (Gibco), and 10 mM HEPES (Sigma

Aldrich), referred as assay medium. Clonetics™ Normal Human Astrocytes (NHA) (Lonza Biosciences) were used between passage 1 and 6. For routine cell culture, cells were seeded in Nunclon™ Delta treated flasks (Thermo Scientific Nunc™ Cell Culture Treated EasYFlasks™) and supplemented with ABM basal medium containing rhEGF, insulin, L-Glutamine, ascorbic acid, GA-1000 (all from Lonza Biosciences), and 3% FBS (Gibco), referred as astrocyte medium. Cells were cultured in an incubator at 37°C with 5% CO_2/95% air and saturated humidity. Cell culture medium was changed every 2 days, and assay medium twice weekly.

5.5.4 BBB Cocultures on Transwell Inserts

Twenty thousand hCMEC/D3 cells were seeded on the upper side of collagen pre-coated polyester Transwell® inserts (12-well format, 1.12 cm^2, 0.4 μm pore size, 4x10^6 pores/cm^2, i.e. approximately 0.5%, porosity, Corning #3460) and maintained in assay medium (0.5 mL of assay medium in the apical compartment and 1.5 mL of assay medium in the basolateral compartment) at 37°C with 5% CO_2/95% air and saturated humidity. The medium was changed twice a week. Ten thousand unstained or pre-labelled NHA cells (in 150 μL astrocyte medium) were seeded on the bottom side of the flipped membrane inserts on day 5 or 6. After 1.5-2 hours of incubation at 37°C, the membrane inserts were flipped back to the original orientation and fresh assay medium was added to both apical and basolateral compartments. The

experiments were conducted 7 days post transwell seeding of hCMEC/D3 cells.

5.5.5 BBB Coculture on SiN-based Devices

Prior to cell seeding, the SiN membrane devices were sterilized and both sides of the membrane were coated with collagen/fibronectin. The top reservoir was seeded with 10,500 hCMEC/D3 cells and the bottom reservoir was filled with assay medium. The device was then placed inside a 6 mm cell culture dish (Greiner Bio-One GmbH) with sterile MilliQ water wetted Kimcare wipes (Kimberly Clark) and kept in an incubator at 37°C with 5% CO_2/95% air and saturated humidity. The cells were grown under static condition and the assay medium (100 μl medium/top reservoir) was replaced 2-3 hours after plating the cells and every second day afterwards. Unstained or pre-stained NHA cell suspension (12 μl of 300,000-400,000 cells/ml cell suspension) was seeded to the bottom reservoir on day 4 (or once hCMEC/D3 cells reached confluency). After the two loading channels were filled with astrocyte medium, the device was covered with parafilm and was flipped upside down to allow settlement of astrocytes onto the bottom side of the membrane. After 1.5-2 hours of incubation at 37°C, the device was flipped back to its original orientation and fresh astrocyte medium (approximately 25 μl) was added to the two 5 mm reservoirs to allow long-term cell culture. On the next day, the astrocyte medium was replaced with assay medium. Due to the small volume (2.4 μl) of the bottom reservoir, the medium was replaced

every day in the lower channel. The BBB model was used for experiments 5-7 days after plating the hCMEC/D3 cells.

5.5.6 Immunocytochemistry

Endothelial cells and astrocytes were cultured on the opposite side of the Transwell or SiN membrane devices in the above described way. On the day of the experiment, the cells were washed with pre-heated medium and were fixed with 4% paraformaldehyde (Sigma-Aldrich) for 20 min at room temperature (RT), washed three times with phosphate buffer saline (PBS) (Sigma-Aldrich), permeabilized with 1 x saponin (Life Technologies) for 10 min, and blocked in 1% bovine serum albumin (BSA) (Sigma Aldrich) (in 0.05% PBS-Tween 20 (Sigma Aldrich) (PBS-T)) for 30 min. Cells were then incubated for 2 hours at RT or overnight at 4°C with relevant primary antibody (Ab) (mouse monoclonal Ab to claudin-5 [4C3C2] (35-2500) (Invitrogen, Thermo Fisher Scientific); 2.5 μg/ml concentration in 1% BSA-PBS-T, rabbit monoclonal [EP672Y] (ab33922) or polyclonal (ab7260) Ab to glial fibrillary acidic protein (GFAP) (Abcam); 2 μg/ml concentration in 1% BSA-PBS-T). After that the cells were washed three times with PBS and incubated with Alexa Fluor® 488 or Alexa Fluor® 546 -mouse or anti-rabbit IgG secondary Ab (Invitrogen, Thermo Fisher Scientific) (the concentration of secondary Ab was half of the primary Ab) for 1 hour in dark at RT, followed by rinsing three times with PBS. In addition, the nuclei of both hCMEC/D3 NHA cells were stained with 4',6-diamidino-2-phenylindole (DAPI) (1 μg/ml concentration

in PBS) (Sigma Aldrich). In case of transwell coculture, the polyester membrane was excised using scalpel and scissors from the plastic insert and was mounted on a glass coverslip using MOWIOL (Polysciences, Inc.). The cells were observed and photographed using a spinning-disk confocal microscopy system consisting of a CSU22 spinning-disk unit (Yokogawa Electric Corporation, Japan) and an Andor iXon3 897 EMCCD camera (Andor, UK), mounted on an inverted fully motorized Nikon Ti microscope body (Nikon Instruments, US). The raw images were processed using Imaris imaging software version 7.4.2 (Bitplane AG, Switzerland).

5.5.7 Paracellular Permeability Assays

In order to determine the barrier tightness of *in vitro* BBB coculture model, paracellular permeability of fluorescein isothiocyanate (FITC) labelled 4 kDa dextran (Sigma Aldrich) was measured. The paracellular permeability was calculated as described by Czupalla et al. [234].

5.5.8 Nanoparticle Characterization

FluoSpheres^{TM} carboxylate-modified polystyrene (PS-COOH) (YG: $\lambda_{ex/em}$ = 505/515 nm, Red: $\lambda_{ex/em}$ = 580/605 nm) (Life Technologies, Thermo Fisher Scientific) with 100 nm nominal size was used as model NPs. The size distribution was determined in PBS and cell culture medium supplemented with 10% FBS by dynamic light scattering using a Malvern Zetasizer 3000HSa

(Malvern Instruments Ltd., UK) under experimental conditions (100 μg/ml NP concentration, at 37°C). The effective surface charge (zeta potential) of the NPs (100 μg/ml NP concentration, at 37°C) was also measured using a Malvern Zetasizer 3000HSa. The results are the average of minimum three separate runs, the errors represent the standard deviation over measurement and indicates the reproducibility of the measurement.

5.5.9 Subcellular Localization and Translocation Studies on NPs in SiN-based Devices

The *in vitro* BBB coculture model on SiN membrane was cultured as described above using unstained or CellTracker™ Green CMFDA (CTG) prelabelled NHA cells. PS-COOH NPs (FluoSpheres™ Carboxylate-Modified Microspheres, 0.1 μm, red (580/605) or yellow/green (505/515) fluorescent, 2% solids) were dispersed in assay medium supplemented with 10% FBS at 37°C prior to cellular exposure. Endothelial cells on the apical side of the SiN membrane were exposed to NP dispersions at 100 μg/ml concentration. After 10 or 15 min NP exposure, the medium was removed, and the samples were washed three times with NP-free assay medium supplemented with 10% FBS and finally 100 μl fresh assay medium was added to the cells. The devices were kept at 37°C until imaging. Prior to imaging, the acidic organelles of the cells were stained with 100 nM LysoTracker™ Deep Red for 1 hr and the cell membrane was labelled with 0.5 mg/ml CellMask™ Green for 15 min and washed three times with cell culture medium (the dye was only

added to and washed away from the apical side). Three-dimensional images ('z-stacks') were obtained up to 48 hours (2, 4, 8, 24, and 48 hours time points, imaging for up to 1 hour/time point) by using a spinning-disk confocal microscopy system consisting of a CSU22 spinning-disk unit (Yokogawa Electric Corporation, Japan) and an Andor iXon3 897 EMCCD camera (Andor, UK), mounted on an inverted fully motorized Nikon Ti microscope body (Nikon Instruments, US) and Plan Apo VC 60x/1.40 (WD = 0.13 mm) oil immersion objective (Nikon). The following excitation laser lines and emission filters were used: CTG, CellMask™ Green, Yellow/Green PS-COOH NP: λ_{ex} = 488 nm, λ_{em} = 505/530 nm band pass filter, LysoTracker™ Deep Red and Red PS-COOH NPs: λ_{ex} = 560 nm, λ_{em} = 610 nm long pass filter. Images were acquired using Andor iQ software and processed using Imaris imaging software version 7.4.2 (Bitplane AG, Switzerland). The lysosomal co-localization of NPs was determined using ImarisColoc using Mander's overlap coefficient and manual thresholding.

Acknowledgements

This work was supported by EU FP7 Marie-Curie Initial Training Network PathChooser (PITN-GA-2013-608373), the Science Foundation Ireland (SFI) Starting Investigator Researcher Grant (Agreement No. 15/SIRG/3423), and EuroNanoMed III (Grant No. 16/ENM- ERA/3457). **JLM and TK were supported by NIH R01 HL125265**. The authors acknowledge the Con-

way Imaging Core Facility and the imaging facilities at the School of Biology, UCD. P.O. Couraud, I. A. Romero, and B. Weksler are also acknowledged for providing endothelial hCMEC/D3 cells.

Chapter 6

Summary

Microvessel physiology is an important aspect of the circulatory system, and plays an eminent role in maintaining and restoring homeostasis. Microvessel permeability is essential for an adequate inflammatory response and wound-healing, but chronically elevated vascular permeability is associated with morbidity in many acute and chronic diseases. The ability to study microvessel barrier properties *in vitro* is, therefore, crucial to enhance our understanding of vascular disorders and develop improved therapeutic strategies. The main focus of this thesis has been to develop *in vitro* platforms that can simulate the pathophysiology of microvessels in general to study the increase in permeability during acute inflammatory responses and investigate potential mechanisms to ameliorate blood-tissue barrier pathology. To this end, we employed advanced silicon nanomembrane technology to engineer a microvessel mimetic (MVM) platform that can support the physiological growth of endothelial cells (ECs) under shear conditions and in the close proximity of the extracellular matrix (ECM). This platform was used primarily to observe

neutrophil chemotaxis and image their 3D migration through endothelial and subendothelial layers in the presence of inflammatory stimuli. This platform was equipped with multiple metrology tools to monitor the permeability of endothelial cells in real-time. The broad capabilities of this platform also enabled its application to study blood-brain barrier (BBB). The MVM platform was modified for two different *in vitro* BBB models to image and study T-cell migration and nanoparticle (NP) translocations across the BBB.

Chapter 2 describes the existing methods used to monitor ionic permeability across endothelial junctions by measuring trans endothelial electrical resistance (TEER). It highlights the assumptions and potential sources of errors in the conventional models used to interpret TEER values, and also illustrates how the normalization procedures produce further erroneous resistance values for silicon nanomembranes. The mathematical analysis presented in this chapter is important for the microfluidics community working on developing customized tissue-barrier models. The sophistication in the design of microsystems with different membrane geometries, arrangements of the endothelial monolayer and TEER electrodes can make the conventional methods of resistance calculation (Ohm's law) inaccurate. Hence, a deeper mathematical understanding of the physics governing resistance measurement is required. The finite element analysis and the corresponding development of a 'mapping function' presented in Chapter 2 is a universal approach and can be used to interpret the TEER values in their raw form to allow for correct normalization. The mathematical simulation also has

the capability to model cell growth kinetics and can predict the non-linear dependance of TEER evolution with cell growth. This result is further useful in resolving the advanced stages of cell growth such as contact-inhibited growth. Finally, the COMSOL model developed in Chapter 2 to interpret resistance values can be also adapted to analyze impedance values and provide a foundation for impedance spectroscopy studies (as elaborated in the Chapter 3).

Chapter 3 describes the development of the MVM platform for the studies of neutrophil-endothelial interactions and associated increase in endothelial permeability. The work presented in this chapter is novel in many aspects. First, the MVM platform allowed for the growth of endothelial cells (ECs) under physiological shear stress on a compliant, porous, and permeable substrate without compromising the ability to employ live-cell phase microscopy. This is difficult to achieve using commercially available platforms. We also characterized the flow profile applied to ECs, the subsequent alignment of the cells in the direction of flow, and established the advantage of using collagen gels as a suitable substrate for the growth of ECs. Next, the TEER data confirmed the benefit of shear stress in elevating the barrier properties of the monolayer. It demonstrated the temporal sensitivity in capturing the transient effects of barrier-altering agents (thrombin, for instance) on electrical resistance and endothelial permeability. After the physiological characterization, we induced neutrophil chemotaxis in the presence of a bacterial chemoattractant. We were able to image neutrophil lu-

minal and transendothelial migration without any fluorescent labeling under live conditions. Electron microscopy shed further light on the subendothelial accumulation of neutrophils undergoing chemotaxis. Furthermore, we were able to assess the changes in endothelial permeability using impedance spectroscopy and fluorescence microscopy during the process of neutrophil migration. These assays allowed us to parse the contribution of neutrophil subendothelial migration with and without blocking $\beta 1$ integrins responsible for their migration on basement membrane. The decay in impedance in the absence of the blocking antibody confirmed that neutrophil trans- and subendothelial migration *does* reduce the junctional integrity of the endothelial cells, and that this loss of junctional integrity can be reduced by the blocking of $\beta 1$ integrins present on neutrophil surface. This result is important as it demonstrates the benefit of alleviating the rise in permeability by blocking neutrophils at the subendothelial layers, and lays down the path for the further investigation to use this blocking approach as a therapeutic strategy. Finally, the microscopy imaging-assay to monitor the diffusion of fluorescent dextran across endothelial layer is an advancement over the existing assays to measure tracer permeability. The existing protocols fail to provide a high temporal resolution in capturing the diffusion of tracers and the assay developed in Chapter 3 addresses this issue enabling us to observe the diffusion of tracer molecules using standard epifluorescence illumination.

This platform can be used for a variety of studies involving neutrophil migration and its impact on permeability. While all the neutrophil studies

have been performed in the absence of shear stress, the obvious extension of this work is to repeat under low levels of shear to recreate *in vivo* condition. Next, the membranes used in all the studies presented in Chapter 3 have 3 μm pores to allow neutrophil passage. While this allows for physical passage, an interesting future direction will be to test the effects of chemical activation of neutrophils in the absence of physical migration by using membranes with submicron pores. Silicon nanomembranes with 100 nm pore size will facilitate fMLP diffusion and stimulate neutrophil transendothelial migration. However, the neutrophils will be trapped below the endothelial cells and won't be able to invade the ECM gel present below the membrane. This will essentially mimic the case of chemical blockade of neutrophils achieved using β1-blocking antibody, but without the signaling inhibition. It will allow us to answer the question: "*Is the physical migration of neutrophils through the basement membrane into the ECM necessary for the rise in overall permeability, or is the associated biochemical activation sufficient to damage endothelial barrier function?*". Another potential study feasible in the MVM platform will involve phase imaging. Figure 3.22 in Chapter 3 highlights the physical gaps created in the endothelial monolayer during neutrophil transmigration. These gaps may potentially explain the drop in impedance and rise in fluorescence as observed in Figures 3.29 and 3.30. While fMLP insult activates the neutrophil directly, an interesting question that arises is whether these gaps are also formed in the presence of an agent directly influencing ECs like TNF-α, and if the corresponding gap-formation also contributes to

similar changes in barrier properties or not. Finally, the use of multiple devices connected in series in the same flow circuit can enable us to study the transformation of a local inflammatory response to a systemic one. Figure 6.1 illustrates the scheme to perform such studies.

Chapters 4 and 5 use modified versions of the MVM platform for BBB studies. Chapter 4 presents a novel approach to induce BBB like characteristics from umbilical cord derived stem cells in the presence of pericyte-conditioned media (PCM). This work is unique in several ways. First, the brain-like endothelial cells (BLECs) used in those studies demonstrate low permeability values consistent with the properties of the BBB *in vivo*. The ability to achieve these tight barrier properties merely by the introduction of PCM, and not pericytes themselves, saves time, effort, and reagents required for coculturing pericytes along with BLECs. Furthermore, the absence of a second cell layer improved the imaging quality significantly. The microfluidic nature of these devices is also ideal to work with cerebrospinal fluids from animal models, which are obtained only in small amounts. In this chapter, we present quantitative results of studies of healthy T-cell migration under (low) physiological shear levels present during T-cell diapedesis. In future work, we plan to use rare subsets of T-cells derived from the blood samples of patients suffering from multiple sclerosis (MS). These quantitative studies will be useful in identifying the surface receptors contributing to the leukocyte migration and be instrumental in testing new blocking strategies to prevent T-cell migration across the BBB. This platform can also serve

as a testing bed for investigational new drugs (INDs) in preclinical studies. Drug discovery aspects such as dose-dependancy, mode of delivery, changes in T-cell-ECs interactions and collateral effects on the host endothelium can be potentially studied in this *in vitro* configuration.

In Chapter 5, we exploit the advantages of the silicon nanomembranes to achieve high resolution microscopy imaging to observe NP translocation across the BBB. NP-based drug delivery across the BBB is not well understood, and the ability to visualize the NPs in real-time will be important for developing NP-based drug delivery strategies. In our studies to date, we were able to confirm the expression of tight junctions and astrocyte markers in endothelial-astrocyte cocultures. We determined that 100 nm NPs were retained on in the apical layer of the BBB. Only a very small subset of NPs (0.04%) managed to pass through endothelial junctions and accumulate in the basal chamber. These rare events, although unexpected, can shed light on potential 'bypass' mechanisms employed by NPs to translocate through the BBB. Further investigation of such modes of transport will be valuable in developing targeted NP-based drug delivery approaches to the central nervous system.

In summary, the development of a microvessel mimetic (MVM) platform has enabled us to study acute inflammation and, in particular, the effects that activated neutrophils have on the endothelium and endothelial permeability. This microsystem presents unique capabilities to make diverse measurements and visual observations simultaneously. It has the potential for

studying vascular disorders, leukocyte-induced vascular damage, drug delivery, BBB physiology, as well as physiological functions and abnormalities in other barrier tissues. The diversity of silicon nanomembranes and the ability to integrate them into a variety of microfluidic configurations is an invaluable asset in pursuing answers to many questions about fundamental cell physiology, disease pathology and therapeutic approaches.

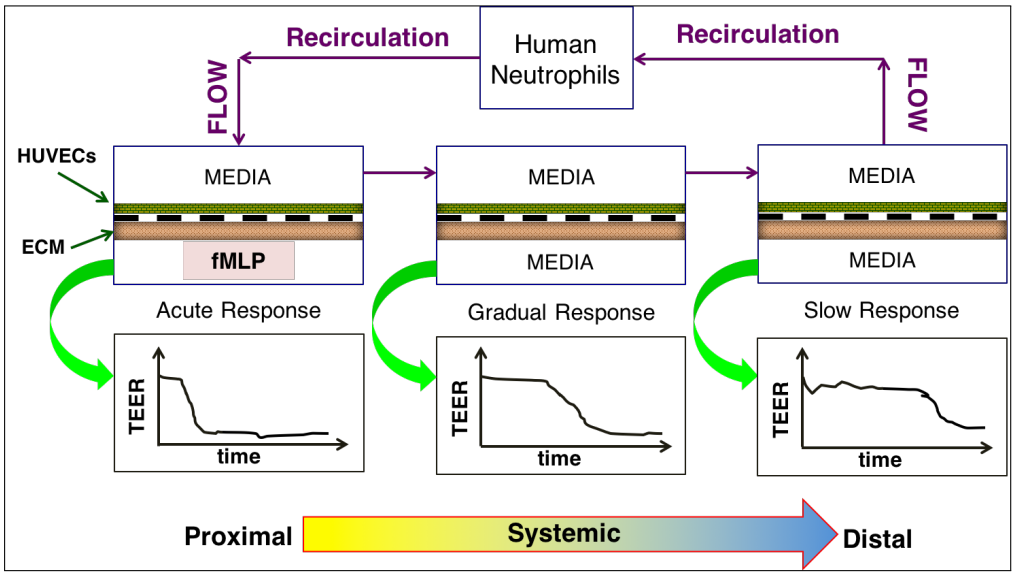

Figure 6.1: Systemic Inflammation *In Vitro*: A schematic showing three MVM devices connected in series in a single flow circuit, with each device featuring ECs and ECM on either side of the silicon nanomembrane. The three devices will be connected to a common reservoir with human neutrophils, and the device proximal to neutrophils will be basolaterally stimulated with fMLP, and the remaining two devices won't have any basal chemoattractant. TEER will be monitored in all three devices simultaneously. We hypothesize that the device with fMLP present in it will first demonstrate changes in TEER. Simultaneously, the activated neutrophils will activate ECs that will secrete endogenous chemokines (such as TNF-α) that will circulate to other devices. The distant devices will then experience endothelial activation that will promote neutrophil migration on their endothelium as well. These advanced reactions will facilitate changes in TEER, although to a different extent and with slower kinetics. We hypothesize that, eventually, the ECs in all three devices will get activated (as reflected by the changes in their resistance/permeability) and thus the 'local' bacterial infection can cause the activation of distant vascular beds making the inflammatory response 'systemic'.

Bibliography

[1] A Scott, KM Khan, JL Cook, and V Duronio. What is "inflammation"? are we ready to move beyond celsus? British journal of sports medicine, 38(3):248–249, 2004.

[2] D Neil Granger and Elena Senchenkova. Inflammation and the microcirculation. In Colloquium series on integrated systems physiology: from molecule to function, volume 2, pages 1–87. Morgan & Claypool Life Sciences, 2010.

[3] Neville A. Punchard, Cliff J. Whelan, and Ian Adcock. The journal of inflammation. Journal of Inflammation, 1(1):1, Sep 2004. ISSN 1476-9255. doi: 10.1186/1476-9255-1-1. URL https://doi.org/10.1186/1476-9255-1-1.

[4] Linda Mayer and Rashid Bhikha. The challenging response of physis to inflammation. 2013.

[5] Jeremy D Pearson. How early studies of inflammation led to our current views on the roles of vascular adhesion molecules. In Vascular Adhesion Molecules and Inflammation, pages 1–10. Springer, 1999.

[6] Julius Arnold. Ueber diapedesis. Archiv für pathologische Anatomie und Physiologie und für klinische Medicin, 58(2):203–230, 1873.

[7] Fong W Lam, Rolando E Rumbaut, and Alan R Burns. Mechanisms of neutrophil migration. In The Neutrophils: New Outlook for Old Cells, pages 129–188. World Scientific, 2013.

[8] M Rocha e Silva. A brief survey of the history of inflammation. Agents and actions, 8(1-2):45–49, 1978.

[9] Jordan S Pober. Physiology and pathobiology of microvascular endothelium. In Microcirculation, pages 37–55. Elsevier, 2008.

[10] Vidula Vachharajani and D Neil Granger. Adipose tissue: a motor for the inflammation associated with obesity. IUBMB life, 61(4):424–430, 2009.

[11] Sussan Nourshargh, Peter L Hordijk, and Michael Sixt. Breaching multiple barriers: leukocyte motility through venular walls and the interstitium. Nature reviews Molecular cell biology, 11(5): 366–378, 2010. ISSN 1471-0072.

[12] H. Stanley Bennett, John H. Luft, and James C. Hampton. Morphological classifications of vertebrate blood capillaries. American Journal of Physiology-Legacy Content, 196(2):381–390, Jan 1959. ISSN 0002-9513. doi: 10.1152/ajplegacy.1959.196.2.381. URL http://dx.doi.org/10.1152/ajplegacy.1959.196.2.381.

[13] AR Pries and WM Kuebler. Normal endothelium. In The Vascular Endothelium I, pages 1–40. Springer, 2006.

[14] M Simionescu and F Antohe. Functional ultrastructure of the vascular endothelium: changes in various pathologies. In The Vascular Endothelium I, pages 41–69. Springer, 2006.

[15] Matthew R DiStasi and Klaus Ley. Opening the flood-gates: how neutrophil-endothelial interactions regulate permeability. Trends in immunology, 30(11):547–556, 2009. ISSN 1471-4906.

[16] Hemant Sarin. Physiologic upper limits of pore size of different blood capillary types and another perspective on the dual pore theory of microvascular permeability. Journal of angiogenesis research, 2(1):14, 2010.

[17] Sheldon Weinbaum, John M Tarbell, and Edward R Damiano. The structure and function of the endothelial glycocalyx layer. Annu. Rev. Biomed. Eng., 9:121–167, 2007.

[18] Graham Marsh. Molecular accessibility: microvilli and the endothelial glycocalyx. PhD thesis, University of Rochester, 2015.

[19] Dolly Mehta and Asrar B Malik. Signaling mechanisms regulating endothelial permeability. Physiological reviews, 86(1):279–367, 2006.

[20] Emily Vandenbroucke, Dolly Mehta, Richard Minshall, and Asrar B Malik. Regulation of endothelial junctional permeability. Annals of the new York Academy of Sciences, 1123(1):134–145, 2008.

[21] Alan SL Yu. Paracellular transport as a strategy for energy conservation by multicellular organisms? Tissue barriers, 5(2):2509–2518, 2017.

[22] Lydia Sorokin. The impact of the extracellular matrix on inflammation. Nature Reviews Immunology, 10(10):712–723, 2010. ISSN 1474-1733.

[23] Raghu Kalluri. Basement membranes: structure, assembly and role in tumour angiogenesis. Nature Reviews Cancer, 3(6):422–433, 2003. ISSN 1474-175X.

[24] Laura C Kelley, Lauren L Lohmer, Elliott J Hagedorn, and David R Sherwood. Traversing the basement membrane in vivo: a diversity of strategies. J Cell Biol, 204(3):291–302, 2014. ISSN 0021-9525.

[25] R Grant Rowe and Stephen J Weiss. Breaching the basement membrane: who, when and how? Trends in cell biology, 18(11):560–574, 2008.

[26] Kandice Tanner. Regulation of the basement membrane by epithelia generated forces. Physical biology, 9(6):065003, 2012. ISSN 1478-3975.

[27] CATHERINE A Partridge, JOHN J Jeffrey, and ASRAR B Malik. A 96-kda gelatinase induced by tnf-alpha contributes to increased microvascular endothelial permeability. American Journal of Physiology-Lung Cellular and Molecular Physiology, 265(5):L438–L447, 1993.

[28] Yelena V Lerman and Minsoo Kim. Neutrophil migration under normal and sepsis conditions. Cardiovascular & Haematological Disorders-Drug Targets (Formerly Current Drug Targets-Cardiovascular & Hematological Disorders), 15(1):19–28, 2015.

[29] Elzbieta Kolaczkowska and Paul Kubes. Neutrophil recruitment and function in health and inflammation. Nature Reviews Immunology, 13(3):159, 2013.

[30] Yu Chen and Wolfgang G Junger. Measurement of oxidative burst in neutrophils. In Leucocytes, pages 115–124. Springer, 2012.

[31] Klaus Ley, Carlo Laudanna, Myron I Cybulsky, and Sussan Nourshargh. Getting to the site of inflammation: the leukocyte adhesion cascade updated. Nature Reviews Immunology, 7(9):678, 2007.

[32] Wolfgang Weninger, Maté Biro, and Rohit Jain. Leukocyte migration in the interstitial space of non-lymphoid organs. Nature Reviews Immunology, 14(4):232–246, 2014. ISSN 1474-1733.

[33] Dietmar Vestweber. How leukocytes cross the vascular endothelium. Nature Reviews Immunology, 15(11):692, 2015.

[34] Mia Phillipson and Paul Kubes. The neutrophil in vascular inflammation. NATURE MEDICINE, 17(11):1381, 2011.

[35] Thomas R Gaborski, Alfred Clark, Richard E Waugh, and James L McGrath. Membrane mobility of $\beta 2$ integrins and rolling associated adhesion molecules in resting neutrophils. Biophysical journal, 95(10):4934–4947, 2008.

[36] Bryan Heit, Pina Colarusso, and Paul Kubes. Fundamentally different roles for lfa-1, mac-1 and $\alpha 4$-integrin in neutrophil chemotaxis. Journal of cell science, 118(22):5205–5220, 2005.

[37] Mia Phillipson, Jaswinder Kaur, Pina Colarusso, Christie M Ballantyne, and Paul Kubes. Endothelial domes encapsulate adherent neutrophils and minimize increases in vascular permeability in paracellular and transcellular emigration. PLoS One, 3(2):e1649, 2008. ISSN 1932-6203.

[38] Yelena V Lerman, Kihong Lim, Young-Min Hyun, Kathleen L Falkner, Hongmei Yang, Anthony P Pietropaoli, Arnoud Sonnenberg, Pranita P Sarangi, and Minsoo Kim. Sepsis lethality via exacerbated tissue infiltration and tlr-induced cytokine production by neutrophils is integrin $\alpha 3\beta 1$-dependent. Blood, 124(24):3515–3523, 2014. ISSN 0006-4971.

[39] MS Tonetti, MA Imboden, and NP Lang. Neutrophil migration into the gingival sulcus is associated with transepithelial gradients of interleukin-8 and icam-1. Journal of periodontology, 69(10):1139, 1998.

[40] Alan R Burns, David C Walker, Evelyn S Brown, Lisa T Thurmon, Robert A Bowden, Charles R Keese, Scott I Simon, Mark L Entman, and C Wayne Smith. Neutrophil transendothelial migration is independent of tight junctions and occurs preferentially at tricellular corners. The Journal of Immunology, 159(6):2893–2903, 1997. ISSN 0022-1767.

[41] Shijun Wang, Mathieu-Benoit Voisin, Karen Y Larbi, John Dangerfield, Christoph Scheiermann, Maxine Tran, Patrick H Maxwell, Lydia Sorokin, and Sussan Nourshargh. Venular basement membranes contain specific matrix protein low expression regions that act as exit points for emigrating neutrophils. Journal of Experimental Medicine, 203(6):1519–1532, 2006.

[42] Mathieu-Benoît Voisin, Doris Pröbstl, and Sussan Nourshargh. Venular basement membranes ubiquitously express matrix protein low-expression regions: characterization in multiple tissues and remodeling during inflammation. The American journal of pathology, 176(1):482–495, 2010. ISSN 0002-9440.

[43] Jian Song, Xueli Zhang, Konrad Buscher, Ying Wang, Huiyu Wang, Jacopo Di Russo, Lixia Li, Stefan Lütke-Enking, Alexander Zarbock, Anika Stadtmann, et al. Endothelial basement membrane laminin 511 contributes to endothelial junctional tightness and thereby inhibits leukocyte transmigration. Cell Reports, 18(5):1256–1269, 2017.

[44] Victoria J. Burton, Lynn M. Butler, Helen M. McGettrick, Phil C. Stone, Hannah C. Jeffery, Caroline O. Savage, G. Ed Rainger, and Gerard B. Nash. Delay of migrating leukocytes by the basement membrane deposited by endothelial cells in long-term culture. Experimental Cell Research, 317(3):276–292, 2011. ISSN 0014-4827. doi: http://doi.org/10.1016/j.yexcr.2010.10.022. URL `http://www.sciencedirect.com/science/article/pii/S001448271000488X`.

[45] Joachim Werr, Xun Xie, Per Hedqvist, Erkki Ruoslahti, and Lennart Lindbom. Îš1 integrins are critically involved in neutrophil locomotion in extravascular tissue in vivo. Journal of Experimental Medicine, 187(12):2091–2096, 1998. ISSN 0022-1007.

[46] Pranita P Sarangi, Young-Min Hyun, Yelena V Lerman, Anthony P Pietropaoli, and Minsoo Kim. Role of Îš1 integrin in tissue homing of neutrophils during sepsis. Shock (Augusta, Ga.), 38(3):281, 2012.

[47] Ding Luo, Helen M McGettrick, Phil C Stone, George E Rainger, and Gerard B Nash. The roles of integrins in function of human neutrophils after their migration through endothelium into interstitial matrix. PloS one, 10(2):e0118593, 2015. ISSN 1932-6203.

[48] Robert Pick, Doris Brechtefeld, and Barbara Walzog. Intraluminal crawling versus interstitial neutrophil migration during inflammation. Molecular immunology, 55(1):70–75, 2013.

[49] N Gautam, P Hedqvist, and L Lindbom. Kinetics of leukocyte induced changes in endothelial barrier function. British journal of pharmacology, 125(5):1109–1114, 1998. ISSN 1476-5381.

[50] Narinder Gautam, A Maria Olofsson, Heiko Herwald, Lars F Iversen, Evy Lundgren-Åkerlund, Per Hedqvist, Karl-E Arfors, Hans Flodgaard, and Lennart Lindbom. Heparin-binding protein (hbp/cap37): a missing link in neutrophil-evoked alteration of vascular permeability. Nature medicine, 7(10):1123–1127, 2001.

[51] SANNA Rosengren, A MARIA Olofsson, ULRICH H von Andrian, E Lundgren-Akerlund, and KARL-E Arfors. Leukotriene b4-induced neutrophil-mediated endothelial leakage in vitro and in vivo. Journal of Applied Physiology, 71(4):1322–1330, 1991.

[52] Lennart Lindbom. Regulation of vascular permeability by neutrophils in acute inflammation. In The Neutrophil, volume 83, pages 146–166. Karger Publishers, 2003.

[53] Elizabeth D Fox, Daithi S Heffernan, William G Cioffi, and Jonathan S Reichner. Neutrophils from critically ill septic patients mediate profound loss of endothelial barrier integrity. Critical care, 17 (5):R226, 2013. ISSN 1364-8535.

[54] Pingnian He. Leucocyte/endothelium interactions and microvessel permeability: coupled or uncoupled? Cardiovascular research, 87(2):281–290, 2010.

[55] Ellinor Kenne. Leukocyte recruitment and control of vascular permeability in acute inflammation. Institutionen för fysiologi och farmakologi/Department of Physiology and Pharmacology, 2010.

[56] Ronen Sumagin, Julia M Kuebel, and Ingrid H Sarelius. Leukocyte rolling and adhesion both contribute to regulation of microvascular permeability to albumin via ligation of icam-1. American Journal of Physiology-Cell Physiology, 301(4):C804–C813, 2011. ISSN 0363-6143.

[57] Ingrid H Sarelius and Angela J Glading. Control of vascular permeability by adhesion molecules. Tissue barriers, 3(1-2):e985954, 2015. ISSN 2168-8370.

[58] John Greenwood, David J Begley, and Malcolm B Segal. New concepts of a blood-brain barrier. Springer, 1995.

[59] Junhee Seok, H Shaw Warren, Alex G Cuenca, Michael N Mindrinos, Henry V Baker, Weihong Xu, Daniel R Richards, Grace P McDonald-Smith, Hong Gao, and Laura Hennessy. Genomic responses in mouse models poorly mimic human inflammatory diseases. Proceedings of the National Academy of Sciences, 110(9):3507–3512, 2013. ISSN 0027-8424.

[60] Jon A Buras, Bernhard Holzmann, and Michail Sitkovsky. Model organisms: animal models of sepsis: setting the stage. Nature reviews Drug discovery, 4(10):854, 2005.

[61] STEVEN M Albelda, PHYLLIS M Sampson, FREDERICK R Haselton, JM McNiff, SN Mueller, SK Williams, AP Fishman, and EM Levine. Permeability characteristics of cultured endothelial cell monolayers. Journal of Applied Physiology, 64(1):308–322, 1988. ISSN 8750-7587.

[62] Ada J Huang, Martha B Furie, Susan C Nicholson, Jorge Fischbarg, Larry S Liebovitch, and Samuel C Silverstein. Effects of human neutrophil chemotaxis across human endothelial cell monolayers on the permeability of these monolayers to ions and macromolecules. Journal of cellular physiology, 135(3):355–366, 1988.

[63] Kihong Lim, Ronen Sumagin, and Young-Min Hyun. Extravasating neutrophil-derived microparticles preserve vascular barrier function in inflamed tissue. Immune network, 13(3):102–106, 2013.

[64] Angela Acheampong and Jean-Louis Vincent. A positive fluid balance is an independent prognostic factor in patients with sepsis. Critical care, 19(1):251, 2015.

[65] William Moy Stratton Russell, Rex Leonard Burch, and Charles Westley Hume. The principles of humane experimental technique, volume 238. Methuen London, 1959.

[66] Edmond WK Young and Craig A Simmons. Macro-and microscale fluid flow systems for endothelial cell biology. Lab on a Chip, 10(2):143–160, 2010.

[67] Koshala Sarveswaran, Volker Kurz, Zhuxin Dong, T Tanaka, S Penny, and Gregory Timp. Synthetic capillaries to control microscopic blood flow. Scientific reports, 6:21885, 2016.

[68] Stephanie M Casillo, Ana P Peredo, Spencer J Perry, Henry H Chung, and Thomas R Gaborski. Membrane pore spacing can modulate endothelial cell–substrate and cell–cell interactions. ACS Biomaterials Science And Engineering, 2017. ISSN 2373-9878.

[69] Julie C Kohn, Dennis W Zhou, François Bordeleau, Allen L Zhou, Brooke N Mason, Michael J Mitchell, Michael R King, and Cynthia A Reinhart-King. Cooperative effects of matrix stiffness and fluid shear stress on endothelial cell behavior. Biophysical journal, 108(3):471–478, 2015. ISSN 0006-3495.

[70] John Huynh, Nozomi Nishimura, Kuldeepsinh Rana, John M Peloquin, Joseph P Califano, Christine R Montague, Michael R King, Chris B Schaffer, and Cynthia A Reinhart-King. Age-related intimal stiffening enhances endothelial permeability and leukocyte transmigration. Science translational medicine, 3(112):112ra122–112ra122, 2011.

[71] Anant Akash Agrawal, BJ Nehilla, KV Reisig, TR Gaborski, DZ Fang, CC Striemer, PM Fauchet, and JL McGrath. Porous nanocrystalline silicon membranes as highly permeable and molecularly thin substrates for cell culture. Biomaterials, 31(20):5408–5417, 2010. ISSN 0142-9612.

[72] Andrea R Mazzocchi, Alan J Man, Jon-Paul S DesOrmeaux, and Thomas R Gaborski. Porous membranes promote endothelial differentiation of adipose-derived stem cells and perivascular interactions. Cellular and Molecular Bioengineering, 7(3):369–378, 2014. ISSN 1865-5025.

[73] Robert N Carter, Stephanie M Casillo, Andrea R Mazzocchi, Jon-Paul S DesOrmeaux, James A Roussie, and Thomas R Gaborski. Ultrathin transparent membranes for cellular barrier and co-culture models. Biofabrication, 9(1):015019, 2017. ISSN 1758-5090.

[74] Henry H Chung, Stephanie M Casillo, Spencer J Perry, and Thomas R Gaborski. Porous substrates promote endothelial migration at the expense of fibronectin fibrillogenesis. ACS biomaterials science & engineering, 4(1):222–230, 2017.

[75] Henry H Chung, Marcela Mireles, Bradley J Kwarta, and Thomas R Gaborski. Use of porous membranes in tissue barrier and co-culture models. Lab on a Chip, 2018.

[76] Seungmi Ryu, Jin Yoo, Yeongseon Jang, Jin Han, Seung Jung Yu, Jooyeon Park, Seon Yeop Jung, Kyung Hyun Ahn, Sung Gap Im, and Kookheon Char. Nanothin coculture membranes with tunable pore architecture and thermoresponsive functionality for transfer-printable stem cell-derived cardiac sheets. ACS nano, 9(10):10186–10202, 2015. ISSN 1936-0851.

[77] Tejas S Khire, Barrett J Nehilla, Jirachai Getpreecharsawas, Maria E Gracheva, Richard E Waugh, and James L McGrath. Finite element modeling to analyze teer values across silicon nanomembranes. Biomedical microdevices, 20(1):11, 2018.

[78] Carlos O Lizama and Ann C Zovein. Polarizing pathways: balancing endothelial polarity, permeability, and lumen formation. Experimental cell research, 319(9):1247, 2013.

[79] Yi-Shuan J Li, Jason H Haga, and Shu Chien. Molecular basis of the effects of shear stress on vascular endothelial cells. Journal of biomechanics, 38(10):1949–1971, 2005.

[80] John T Flaherty, Joseph E Pierce, Victor J Ferrans, Dali J Patel, W Kirk Tucker, and Donald L Fry. Endothelial nuclear patterns in the canine arterial tree with particular reference to hemodynamic events. Circulation research, 30(1):23–33, 1972.

[81] John M Tarbell. Shear stress and the endothelial transport barrier. Cardiovascular research, 87(2): 320–330, 2010.

[82] Olga C Colgan, Gail Ferguson, Nora T Collins, Ronan P Murphy, Gerardeane Meade, Paul A Cahill, and Philip M Cummins. Regulation of bovine brain microvascular endothelial tight junction assembly and barrier function by laminar shear stress. American Journal of Physiology-Heart and Circulatory Physiology, 292(6):H3190–H3197, 2007.

[83] Sabrena Noria, Douglas B Cowan, Avrum I Gotlieb, and B Lowell Langille. Transient and steady-state effects of shear stress on endothelial cell adherens junctions. Circulation research, 85(6): 504–514, 1999.

[84] Jeng-Jiann Chiu and Shu Chien. Effects of disturbed flow on vascular endothelium: pathophysiological basis and clinical perspectives. Physiological reviews, 91(1):327–387, 2011.

[85] Kathrin Benson, Sandra Cramer, and Hans-Joachim Galla. Impedance-based cell monitoring: barrier properties and beyond. Fluids and Barriers of the CNS, 10(1):5, 2013. ISSN 2045-8118.

[86] Iris Bischoff, Michael C Hornburger, Bettina A Mayer, Andrea Beyerle, Joachim Wegener, and Robert Fürst. Pitfalls in assessing microvascular endothelial barrier function: impedance-based devices versus the classic macromolecular tracer assay. Scientific reports, 6:23671, 2016.

[87] Seunggyu Kim, Wanho Kim, Seongjin Lim, and Jessie S Jeon. Vasculature-on-a-chip for in vitro disease models. Bioengineering, 4(1):8, 2017.

[88] Max I Bogorad, Jackson DeStefano, Johan Karlsson, Andrew D Wong, Sharon Gerecht, and Peter C Searson. in vitro microvessel models. Lab on a Chip, 15(22):4242–4255, 2015.

[89] Cara F Buchanan, Elizabeth E Voigt, Christopher S Szot, Joseph W Freeman, Pavlos P Vlachos, and Marissa Nichole Rylander. Three-dimensional microfluidic collagen hydrogels for investigating flow-mediated tumor-endothelial signaling and vascular organization. Tissue Engineering Part C: Methods, 20(1):64–75, 2013.

[90] Robert G Mannino, David R Myers, Byungwook Ahn, Yichen Wang, Margo Rollins, Hope Gole, Angela S Lin, Robert E Guldberg, Don P Giddens, Lucas H Timmins, et al. Do-it-yourself in vitro vasculature that recapitulates in vivo geometries for investigating endothelial-blood cell interactions. Scientific reports, 5:12401, 2015.

[91] Jordan S Miller, Kelly R Stevens, Michael T Yang, Brendon M Baker, Duc-Huy T Nguyen, Daniel M Cohen, Esteban Toro, Alice A Chen, Peter A Galie, Xiang Yu, et al. Rapid casting of patterned vascular networks for perfusable engineered three-dimensional tissues. Nature materials, 11(9):768, 2012.

[92] Ying Zheng, Junmei Chen, Michael Craven, Nak Won Choi, Samuel Totorica, Anthony Diaz-Santana, Pouneh Kermani, Barbara Hempstead, Claudia Fischbach-Teschl, José A López, et al. In vitro microvessels for the study of angiogenesis and thrombosis. Proceedings of the National Academy of Sciences, 109(24):9342–9347, 2012.

[93] Vivian K Lee, Diana Y Kim, Haygan Ngo, Young Lee, Lan Seo, Seung-Schik Yoo, Peter A Vincent, and Guohao Dai. Creating perfused functional vascular channels using 3d bio-printing technology. Biomaterials, 35(28):8092–8102, 2014.

[94] Eric S Comeau, Denise C Hocking, and Diane Dalecki. Ultrasound patterning technologies for studying vascular morphogenesis in 3d. J Cell Sci, pages jcs–188151, 2016.

[95] Hans H Ussing and K_ Zerahn. Active transport of sodium as the source of electric current in the short-circuited isolated frog skin. Acta physiologica Scandinavica, 23(2-3):110–127, 1951.

[96] YongTae Kim, Mark E Lobatto, Tomohiro Kawahara, Bomy Lee Chung, Aneta J Mieszawska, Brenda L Sanchez-Gaytan, Francois Fay, Max L Senders, Claudia Calcagno, Jacob Becraft, et al. Probing nanoparticle translocation across the permeable endothelium in experimental atherosclerosis. Proceedings of the National Academy of Sciences, 111(3):1078–1083, 2014.

[97] Nicholas Ferrell, Ravi R Desai, Aaron J Fleischman, Shuvo Roy, H David Humes, and William H Fissell. A microfluidic bioreactor with integrated transepithelial electrical resistance (teer) measurement electrodes for evaluation of renal epithelial cells. Biotechnology and bioengineering, 107(4): 707–716, 2010. ISSN 1097-0290.

[98] Paul A Vogel, Stephen T Halpin, R Scott Martin, and Dana M Spence. Microfluidic transendothelial electrical resistance measurement device that enables blood flow and postgrowth experiments. Analytical chemistry, 83(11):4296–4301, 2011. ISSN 0003-2700.

[99] J Yeste, X Illa, A Guimerà, and R Villa. A novel strategy to monitor microfluidic in-vitro blood-brain barrier models using impedance spectroscopy. In SPIE Microtechnologies, pages 95180N–95180N. International Society for Optics and Photonics, 2015.

[100] Tao Sun, Emily J Swindle, Jane E Collins, Judith A Holloway, Donna E Davies, and Hywel Morgan. On-chip epithelial barrier function assays using electrical impedance spectroscopy. Lab on a Chip, 10(12):1611–1617, 2010.

[101] Ying I Wang, Hasan Erbil Abaci, and Michael L Shuler. Microfluidic blood–brain barrier model provides in vivo-like barrier properties for drug permeability screening. Biotechnology and bioengineering, 114(1):184–194, 2017.

[102] Andries D ávan der Meer, Hyun JungáKim, Marinke W ávan der Helm, and Albertávan den Berg. Measuring direct current trans-epithelial electrical resistance in organ-on-a-chip microsystems. Lab on a Chip, 15(3):745–752, 2015.

[103] Olivier Henry, Remi Villenave, Michael Cronce, William Leineweber, Max Benz, and Donald Ingber. Organs-on-chips with integrated electrodes for trans-epithelial electrical resistance (teer) measurements of human epithelial barrier function. Lab on a Chip, 2017.

[104] Judith A Stolwijk, Khalid Matrougui, Christian W Renken, and Mohamed Trebak. Impedance analysis of gpcr-mediated changes in endothelial barrier function: overview and fundamental considerations for stable and reproducible measurements. Pflügers Archiv-European Journal of Physiology, 467(10):2193–2218, 2015.

[105] Nicholas J Douville, Yi-Chung Tung, Ran Li, Jack Dong Wang, Mohamed EH El-Sayed, and Shuichi Takayama. Fabrication of two-layered channel system with embedded electrodes to measure resistance across epithelial and endothelial barriers. Analytical chemistry, 82(6):2505, 2010.

[106] Balaji Srinivasan, Aditya Reddy Kolli, Mandy Brigitte Esch, Hasan Erbil Abaci, Michael L Shuler, and James J Hickman. Teer measurement techniques for in vitro barrier model systems. Journal of laboratory automation, 20(2):107–126, 2015. ISSN 2211-0682.

[107] Fruzsina R Walter, Sándor Valkai, András Kincses, András Petneházi, Tamás Czeller, Szilvia Veszelka, Pál Ormos, Mária A Deli, and András Dér. A versatile lab-on-a-chip tool for modeling biological barriers. Sensors and Actuators B: Chemical, 222:1209–1219, 2016. ISSN 0925-4005.

[108] Ross Booth and Hanseup Kim. Characterization of a microfluidic in vitro model of the blood-brain barrier (Îijbbb). Lab on a chip, 12(10):1784–1792, 2012.

[109] Christopher C Striemer, Thomas R Gaborski, James L McGrath, and Philippe M Fauchet. Charge- and size-based separation of macromolecules using ultrathin silicon membranes. Nature, 445(7129): 749–753, 2007. ISSN 0028-0836.

[110] Thomas R Gaborski, Jessica L Snyder, Christopher C Striemer, David Z Fang, Michael Hoffman, Philippe M Fauchet, and James L McGrath. High-performance separation of nanoparticles with ultrathin porous nanocrystalline silicon membranes. ACS nano, 4(11):6973–6981, 2010.

[111] JL Snyder, A Clark, DZ Fang, TR Gaborski, CC Striemer, PM Fauchet, and JL McGrath. An experimental and theoretical analysis of molecular separations by diffusion through ultrathin nanoporous membranes. Journal of membrane science, 369(1):119–129, 2011. ISSN 0376-7388.

[112] Ryoichi Ishimatsu, Jiyeon Kim, Ping Jing, Christopher C Striemer, David Z Fang, Philippe M Fauchet, James L McGrath, and Shigeru Amemiya. Ion-selective permeability of an ultrathin nanoporous silicon membrane as probed by scanning electrochemical microscopy using micropipet-supported ities tips. Analytical chemistry, 82(17):7127–7134, 2010.

[113] Karl JP Smith, Marina May, Ruth Baltus, and James L McGrath. A predictive model of separations in dead-end filtration with ultrathin membranes. Separation and Purification Technology, 189:40–47, 2017.

[114] Karl JP Smith, Joshua Winans, and James McGrath. Ultrathin membrane fouling mechanism transitions in dead-end filtration of protein. In ASME 2016 14th International Conference on Nanochannels, Microchannels, and Minichannels collocated with the ASME 2016 Heat Transfer Summer Conference and the ASME 2016 Fluids Engineering Division Summer Meeting, pages V001T15A001–V001T15A001. American Society of Mechanical Engineers, 2016.

[115] JD Winans, KJP Smith, TR Gaborski, JA Roussie, and JL McGrath. Membrane capacity and fouling mechanisms for ultrathin nanomembranes in dead-end filtration. Journal of Membrane Science, 499:282–289, 2016.

[116] Dean G Johnson, Tejas S Khire, Yekaterina L Lyubarskaya, Karl JP Smith, Jon-Paul S DesOrmeaux, Jeremy G Taylor, Thomas R Gaborski, Alexander A Shestopalov, Christopher C Striemer, and James L McGrath. Ultrathin silicon membranes for wearable dialysis. Advances in chronic kidney disease, 20(6):508–515, 2013.

[117] Dean G Johnson, Sabrina Pan, Andrew Hayden, and James L McGrath. Nanoporous membrane robustness/stability in small form factor microfluidic filtration system. In Engineering in Medicine and Biology Society (EMBC), 2016 IEEE 38th Annual International Conference of the, pages 1955–1958. IEEE, 2016.

[118] Tucker Burgin, Dean Johnson, Henry Chung, Alfred Clark, and James McGrath. Ultrathin silicon membranes for improving extracorporeal blood therapies. In ASME 2016 14th International Conference on Nanochannels, Microchannels, and Minichannels collocated with the ASME 2016 Heat Transfer Summer Conference and the ASME 2016 Fluids Engineering Division Summer Meeting, pages V001T15A003–V001T15A003. American Society of Mechanical Engineers, 2016.

[119] Jessica L Snyder, Jirachai Getpreecharsawas, David Z Fang, Thomas R Gaborski, Christopher C Striemer, Philippe M Fauchet, David A Borkholder, and James L McGrath. High-performance, low-voltage electroosmotic pumps with molecularly thin silicon nanomembranes. Proceedings of the National Academy of Sciences, 110(46):18425–18430, 2013.

[120] Hitomi Mukaibo, Tonghui Wang, Victor H Perez-Gonzalez, Jirachai Getpreecharsawas, Jack Wurzer, Blanca H Lapizco-Encinas, and James L McGrath. Ultrathin nanoporous membranes for insulator-based dielectrophoresis. Nanotechnology, 29(23):235704, 2018.

[121] Jirachai Getpreecharsawas, James L McGrath, and David A Borkholder. The electric field strength in orifice-like nanopores of ultrathin membranes. Nanotechnology, 26(4):045704, 2015.

[122] Kyle Briggs, Gregory Madejski, Martin Magill, Konstantinos Kastritis, Hendrick W de Haan, James L McGrath, and Vincent Tabard-Cossa. Dna translocations through nanopores under nanoscale preconfinement. Nano letters, 18(2):660–668, 2017.

[123] Gregory Madejski, Kilean Lucas, Flavius C Pascut, Kevin F Webb, and James L McGrath. Tem tomography of pores with application to computational nanoscale flows in nanoporous silicon nitride (npn). Membranes, 8(2):26, 2018.

[124] Henry H Chung, Charles K Chan, Tejas S Khire, Graham A Marsh, Alfred Clark, Richard E Waugh, and James L McGrath. Highly permeable silicon membranes for shear free chemotaxis and rapid cell labeling. Lab on a Chip, 14(14):2456–2468, 2014.

[125] Karen L de Mesy Bentley, Ryan Trombetta, Kohei Nishitani, Sheila N Bello-Irizarry, Mark Ninomiya, Longze Zhang, Hung Li Chung, James L McGrath, John L Daiss, Hani A Awad, et al. Evidence of staphylococcus aureus deformation, proliferation, and migration in canaliculi of live cortical bone in murine models of osteomyelitis. Journal of Bone and Mineral Research, 32(5): 985–990, 2017.

[126] N Joan Abbott, Adjanie AK Patabendige, Diana EM Dolman, Siti R Yusof, and David J Begley. Structure and function of the blood–brain barrier. Neurobiology of disease, 37(1):13–25, 2010.

[127] Richard Daneman and Alexandre Prat. The blood–brain barrier. Cold Spring Harbor perspectives in biology, 7(1):a020412, 2015.

[128] Richard Daneman. The blood–brain barrier in health and disease. Annals of neurology, 72(5): 648–672, 2012.

[129] N Joan Abbott. Blood–brain barrier structure and function and the challenges for cns drug delivery. Journal of inherited metabolic disease, 36(3):437–449, 2013.

[130] M. Diebold and T. Derfuss. Immunological treatment of multiple sclerosis. Semin Hematol, 53 Suppl 1:S54–7, 2016. ISSN 0037-1963. doi: 10.1053/j.seminhematol.2016.04.016.

[131] Igor J Koralnik, Renaud A Du Pasquier, and Norman L Letvin. Jc virus-specific cytotoxic t lymphocytes in individuals with progressive multifocal leukoencephalopathy. Journal of virology, 75(7): 3483–3487, 2001.

[132] R. Martin, M. Sospedra, M. Rosito, and B. Engelhardt. Current multiple sclerosis treatments have improved our understanding of ms autoimmune pathogenesis. Eur J Immunol, 46(9):2078–90, 2016. ISSN 1521-4141 (Electronic) 0014-2980 (Linking). doi: 10.1002/eji.201646485. URL https://www.ncbi.nlm.nih.gov/pubmed/27467894.

[133] R. Cecchelli, S. Aday, E. Sevin, C. Almeida, M. Culot, L. Dehouck, C. Coisne, B. Engelhardt, M. P. Dehouck, and L. Ferreira. A stable and reproducible human blood-brain barrier model derived from hematopoietic stem cells. PLoS One, 9(6):e99733, 2014. ISSN 1932-6203. doi: 10.1371/journal.pone.0099733. URL https://www.ncbi.nlm.nih.gov/pmc/articles/PMC4061029/pdf/pone.0099733.pdf.

[134] R. Lyck, M. A. Lecuyer, M. Abadier, C. B. Wyss, C. Matti, M. Rosito, G. Enzmann, T. Zeis, L. Michel, A. B. Garcia Martin, F. Sallusto, F. Gosselet, U. Deutsch, J. A. Weiner, N. Schaeren-Wiemers, A. Prat, and B. Engelhardt. Alcam (cd166) is involved in extravasation of monocytes rather than t cells across the blood-brain barrier. J Cereb Blood Flow Metab, 37(8):2894–2909, 2017. ISSN 0271-678x. doi: 10.1177/0271678x16678639.

[135] G. Cinamon, V. Shinder, and R. Alon. Shear forces promote lymphocyte migration across vascular endothelium bearing apical chemokines. Nat Immunol, 2(6):515–22, 2001. ISSN 1529-2908 (Print) 1529-2908. doi: 10.1038/88710.

[136] J Kreuter. Drug delivery to the central nervous system by polymeric nanoparticles: what do we know? Advanced drug delivery reviews, 71:2, 2014.

[137] Massimo Masserini. Nanoparticles for brain drug delivery. ISRN biochemistry, 2013, 2013.

[138] Angela R Jones and Eric V Shusta. Blood–brain barrier transport of therapeutics via receptor-mediation. Pharmaceutical research, 24(9):1759–1771, 2007.

[139] Devin T Wiley, Paul Webster, Aaron Gale, and Mark E Davis. Transcytosis and brain uptake of transferrin-containing nanoparticles by tuning avidity to transferrin receptor. Proceedings of the National Academy of Sciences, 110(21):8662–8667, 2013.

[140] Margaret L. Sutherland, Kristin M. Fabre, and Danilo A. Tagle. The national institutes of health microphysiological systems program focuses on a critical challenge in the drug discovery pipeline. Stem Cell Research And Therapy, 4(1):I1, 2013. ISSN 1757-6512. doi: 10.1186/scrt361. URL http://dx.doi.org/10.1186/scrt361.

[141] Barrett J Nehilla, Nakul Nataraj, Thomas R Gaborski, and James L McGrath. Endothelial vacuolization induced by highly permeable silicon membranes. Acta biomaterialia, 10(11):4670–4677, 2014. ISSN 1742-7061.

[142] JPS DesOrmeaux, JD Winans, SE Wayson, TR Gaborski, TS Khire, CC Striemer, and JL McGrath. Nanoporous silicon nitride membranes fabricated from porous nanocrystalline silicon templates. Nanoscale, 6(18):10798–10805, 2014.

[143] C Crone and SP Olesen. Electrical resistance of brain microvascular endothelium. Brain research, 241(1):49–55, 1982. ISSN 0006-8993.

[144] Christian Crone and Ove Christensen. Electrical resistance of a capillary endothelium. The Journal of general physiology, 77(4):349–371, 1981. ISSN 0022-1295.

[145] Robert S Eisenberg and Edward A Johnson. Three-dimensional electrical field problems in physiology. Progress in biophysics and molecular biology, 20:1–65, 1970. ISSN 0079-6107.

[146] Michael Bindschadler and James L McGrath. Sheet migration by wounded monolayers as an emergent property of single-cell dynamics. Journal of cell science, 120(5):876–884, 2007. ISSN 0021-9533.

[147] Eric A Jaffe. Cell biology of endothelial cells. Human pathology, 18(3):234–239, 1987.

[148] Courtney M Sakolish, Mandy B Esch, James J Hickman, Michael L Shuler, and Gretchen J Mahler. Modeling barrier tissues in vitro: methods, achievements, and challenges. EBioMedicine, 5:30–39, 2016.

[149] Melissa A Lopes Pinheiro, Gijs Kooij, Mark R Mizee, Alwin Kamermans, Gaby Enzmann, Ruth Lyck, Markus Schwaninger, Britta Engelhardt, and Helga E de Vries. Immune cell trafficking across the barriers of the central nervous system in multiple sclerosis and stroke. Biochimica et Biophysica Acta (BBA)-Molecular Basis of Disease, 1862(3):461–471, 2016. ISSN 0925-4439.

[150] Warren L Lee and Arthur S Slutsky. Sepsis and endothelial permeability. The New England journal of medicine, 363(7):689, 2010.

[151] IS Woolhouse, DL Bayley, P Lalor, DH Adams, and RA Stockley. Endothelial interactions of neutrophils under flow in chronic obstructive pulmonary disease. European Respiratory Journal, 25 (4):612–617, 2005. ISSN 0903-1936.

[152] Sangeeta N Bhatia and Donald E Ingber. Microfluidic organs-on-chips. Nature biotechnology, 32 (8):760–772, 2014.

[153] Luca Cucullo, Mohammed Hossain, William Tierney, and Damir Janigro. A new dynamic in vitro modular capillaries-venules modular system: cerebrovascular physiology in a box. BMC neuroscience, 14(1):18, 2013. ISSN 1471-2202.

[154] Hyun Jung Kim, Dongeun Huh, Geraldine Hamilton, and Donald E Ingber. Human gut-on-a-chip inhabited by microbial flora that experiences intestinal peristalsis-like motions and flow. Lab on a Chip, 12(12):2165–2174, 2012.

[155] Dongeun Huh, Daniel C Leslie, Benjamin D Matthews, Jacob P Fraser, Samuel Jurek, Geraldine A Hamilton, Kevin S Thorneloe, Michael Allen McAlexander, and Donald E Ingber. A human disease model of drug toxicity–induced pulmonary edema in a lung-on-a-chip microdevice. Science translational medicine, 4(159):159ra147–159ra147, 2012.

[156] Ross Booth, S Noh, and H Kim. A multiple-channel, multiple-assay platform for characterization of full-range shear stress effects on vascular endothelial cells. Lab on a Chip, 14(11):1880–1890, 2014.

[157] Nina Tandon, Anna Marsano, Robert Maidhof, Keiji Numata, Chrystina Montouri-Sorrentino, Christopher Cannizzaro, Joel Voldman, and Gordana Vunjak-Novakovic. Surface-patterned electrode bioreactor for electrical stimulation. Lab on a Chip, 10(6):692–700, 2010.

[158] Dmitry Gabrilovich. The neutrophils: new outlook for old cells. World Scientific, 2013. ISBN 1783262915.

[159] Melissa A Kovach and Theodore J Standiford. The function of neutrophils in sepsis. Current opinion in infectious diseases, 25(3):321–327, 2012. ISSN 0951-7375.

[160] F Dallegri and L Ottonello. Tissue injury in neutrophilic inflammation. Inflammation research: official journal of the European Histamine Research Society...[et al.], 46(10):382–391, 1997.

[161] Yulia Komarova and Asrar B Malik. Regulation of endothelial permeability via paracellular and transcellular transport pathways. Annual review of physiology, 72:463–493, 2010. ISSN 0066-4278.

[162] Ioannis Mitroulis and Triantafyllos Chavakis. $\alpha 3\beta 1$ is integral to septic neutrophils. Blood, 124 (24):3507–3508, 2014.

[163] Stephen F Rodrigues and D Neil Granger. Blood cells and endothelial barrier function. Tissue barriers, 3(1-2):e978720, 2015. ISSN 2168-8370.

[164] Stefano Santaguida, Damir Janigro, Mohammed Hossain, Emily Oby, Edward Rapp, and Luca Cucullo. Side by side comparison between dynamic versus static models of blood–brain barrier in vitro: a permeability study. Brain research, 1109(1):1–13, 2006. ISSN 0006-8993.

[165] Takashi Kei Kishimoto and Robert Rothlein. Integrins, icams, and selectins: role and regulation of adhesion molecules in neutrophil recruitment to inflammatory sites. Advances in pharmacology, 25:117–169, 1994. ISSN 1054-3589.

[166] Theodore G Papaioannou, Emmanouil N Karatzis, Manolis Vavuranakis, John P Lekakis, and Christodoulos Stefanadis. Assessment of vascular wall shear stress and implications for atherosclerotic disease. International journal of cardiology, 113(1):12–18, 2006.

[167] Michel E Safar. Peripheral pulse pressure, large arteries, and microvessels. Hypertension, 44(2): 121–122, 2004.

[168] CB Raub, AJ Putnam, BJ Tromberg, and SC George. Predicting bulk mechanical properties of cellularized collagen gels using multiphoton microscopy. Acta biomaterialia, 6(12):4657–4665, 2010.

[169] Ya-li Yang, Lindsay M Leone, and Laura J Kaufman. Elastic moduli of collagen gels can be predicted from two-dimensional confocal microscopy. Biophysical journal, 97(7):2051–2060, 2009.

[170] Joachim Werr, Einar E Eriksson, Per Hedqvist, and Lennart Lindbom. Engagement of $\beta 2$ integrins induces surface expression of $\beta 1$ integrin receptors in human neutrophils. Journal of Leukocyte Biology, 68(4):553–560, 2000.

[171] Andreas R Huber and Stephen J Weiss. Disruption of the subendothelial basement membrane during neutrophil diapedesis in an in vitro construct of a blood vessel wall. Journal of Clinical Investigation, 83(4):1122, 1989.

[172] Holly M Lauridsen, Jordan S Pober, and Anjelica L Gonzalez. A composite model of the human postcapillary venule for investigation of microvascular leukocyte recruitment. The FASEB Journal, 28(3):1166–1180, 2014.

[173] Robert Steadman, Patricia L St John, Rachel A Evans, Gareth J Thomas, Malcolm Davies, Louis W Heck, and Dale R Abrahamson. Human neutrophils do not degrade major basement membrane components during chemotactic migration. The international journal of biochemistry & cell biology, 29(7):993–1004, 1997.

[174] B. Engelhardt and R. M. Ransohoff. Capture, crawl, cross: the t cell code to breach the blood-brain barriers. Trends Immunol, 33(12):579–89, 2012. ISSN 1471-4906. doi: 10.1016/j.it.2012.07.004.

[175] M. Sospedra and R. Martin. Immunology of multiple sclerosis. Semin Neurol, 36(2):115–27, 2016. ISSN 0271-8235. doi: 10.1055/s-0036-1579739. URL `https://www.thieme-connect.com/DOI/DOI?10.1055/s-0036-1579739`.

[176] G. Krishnamoorthy and H. Wekerle. Eae: an immunologist's magic eye. Eur J Immunol, 39(8):2031–5, 2009. ISSN 0014-2980. doi: 10.1002/eji.200939568. URL `http://onlinelibrary.wiley.com/store/10.1002/eji.200939568/asset/2031_ftp.pdf?v=1&t=ixuposge&s=a8274961830b02677e4a2a6e871be18e5a938f24`.

[177] G. A. Grant, N. J. Abbott, and D. Janigro. Understanding the physiology of the blood-brain barrier: In vitro models. News Physiol Sci, 13:287–293, 1998. ISSN 0886-1714 (Print) 0886-1714.

[178] H. C. Helms, N. J. Abbott, M. Burek, R. Cecchelli, P. O. Couraud, M. A. Deli, C. Forster, H. J. Galla, I. A. Romero, E. V. Shusta, M. J. Stebbins, E. Vandenhaute, B. Weksler, and B. Brodin. In vitro models of the blood-brain barrier: An overview of commonly used brain endothelial cell culture models and guidelines for their use. J Cereb Blood Flow Metab, 36(5):862–90, 2016. ISSN 0271-678x. doi: 10.1177/0271678x16630991.

[179] O. Steiner, C. Coisne, B. Engelhardt, and R. Lyck. Comparison of immortalized bend5 and primary mouse brain microvascular endothelial cells as in vitro blood-brain barrier models for the study of t cell extravasation. J Cereb Blood Flow Metab, 31(1):315–27, 2011. ISSN 0271-678x. doi: 10.1038/jcbfm.2010.96.

[180] Romain Cayrol, Arsalan S. Haqqani, Igal Ifergan, Aurore Dodelet-Devillers, and Alexandre Prat. Isolation of Human Brain Endothelial Cells and Characterization of Lipid Raft-Associated Proteins by Mass Spectroscopy, pages 275–295. Humana Press, Totowa, NJ, 2011. ISBN 978-1-60761-938-3. doi: 10.1007/978-1-60761-938-3_13. URL https://doi.org/10.1007/978-1-60761-938-3_13.

[181] D. E. Eigenmann, G. Xue, K. S. Kim, A. V. Moses, M. Hamburger, and M. Oufir. Comparative study of four immortalized human brain capillary endothelial cell lines, hcmec/d3, hbmec, ty10, and bb19, and optimization of culture conditions, for an in vitro blood-brain barrier model for drug permeability studies. Fluids Barriers CNS, 10(1):33, 2013. ISSN 2045-8118. doi: 10.1186/2045-8118-10-33. URL https://www.ncbi.nlm.nih.gov/pmc/articles/PMC4176484/pdf/2045-8118-10-33.pdf.

[182] B. B. Weksler, E. A. Subileau, N. Perriere, P. Charneau, K. Holloway, M. Leveque, H. Tricoire-Leignel, A. Nicotra, S. Bourdoulous, P. Turowski, D. K. Male, F. Roux, J. Greenwood, I. A. Romero, and P. O. Couraud. Blood-brain barrier-specific properties of a human adult brain endothelial cell line. Faseb j, 19(13):1872–4, 2005. ISSN 0892-6638. doi: 10.1096/fj.04-3458fje.

[183] M. A. Deli, C. S. Abraham, Y. Kataoka, and M. Niwa. Permeability studies on in vitro blood-brain barrier models: physiology, pathology, and pharmacology. Cell Mol Neurobiol, 25(1):59–127, 2005. ISSN 0272-4340 (Print) 0272-4340.

[184] Scott G Canfield, Matthew J Stebbins, Bethsymarie Soto Morales, Shusaku W Asai, Gad D Vatine, Clive N Svendsen, Sean P Palecek, and Eric V Shusta. An isogenic blood–brain barrier model comprising brain endothelial cells, astrocytes, and neurons derived from human induced pluripotent stem cells. Journal of neurochemistry, 140(6):874–888, 2017.

[185] Ethan S Lippmann, Abraham Al-Ahmad, Sean P Palecek, and Eric V Shusta. Modeling the blood–brain barrier using stem cell sources. Fluids and Barriers of the CNS, 10(1):2, 2013. ISSN 2045-8118. doi: 10.1186/2045-8118-10-2. URL http://dx.doi.org/10.1186/2045-8118-10-2.

[186] Elodie Vandenhaute, Aurore Drolez, Emmanuel Sevin, Fabien Gosselet, Caroline Mysiorek, and Marie-Pierre Dehouck. Adapting coculture in vitro models of the blood–brain barrier for use in cancer research: maintaining an appropriate endothelial monolayer for the assessment of transendothelial migration. Laboratory Investigation, 96(5):588–598, Feb 2016. ISSN 1530-0307. doi: 10.1038/labinvest.2016.35. URL http://dx.doi.org/10.1038/labinvest.2016.35.

[187] C. Coisne, R. Lyck, and B. Engelhardt. Live cell imaging techniques to study t cell trafficking across the blood-brain barrier in vitro and in vivo. Fluids Barriers CNS, 10(1):7, 2013. ISSN 2045-8118. doi: 10.1186/2045-8118-10-7. URL https://www.ncbi.nlm.nih.gov/pmc/articles/PMC3560242/pdf/2045-8118-10-7.pdf.

[188] R. Martinelli, A. S. Zeiger, M. Whitfield, T. E. Sciuto, A. Dvorak, K. J. Van Vliet, J. Greenwood, and C. V. Carman. Probing the biomechanical contribution of the endothelium to lymphocyte migration: diapedesis by the path of least resistance. J Cell Sci, 127(Pt 17):3720–34, 2014. ISSN 0021-9533. doi: 10.1242/jcs.148619.

[189] H. Munir, G. E. Rainger, G. B. Nash, and H. McGettrick. Analyzing the effects of stromal cells on the recruitment of leukocytes from flow. J Vis Exp, (95):e52480, 2015. ISSN 1940-087x. doi: 10.3791/52480.

[190] Z. Shulman and R. Alon. Real-time analysis of integrin-dependent transendothelial migration and integrin-independent interstitial motility of leukocytes. Methods Mol Biol, 757:31–45, 2012. ISSN 1064-3745. doi: 10.1007/978-1-61779-166-6_3.

[191] G. Cinamon, V. Grabovsky, E. Winter, S. Franitza, S. Feigelson, R. Shamri, O. Dwir, and R. Alon. Novel chemokine functions in lymphocyte migration through vascular endothelium under shear flow. J Leukoc Biol, 69(6):860–6, 2001. ISSN 0741-5400 (Print) 0741-5400. URL `http://www.jleukbio.org/content/69/6/860.long`.

[192] N. T. Luu, G. E. Rainger, and G. B. Nash. Differential ability of exogenous chemotactic agents to disrupt transendothelial migration of flowing neutrophils. J Immunol, 164(11):5961–9, 2000. ISSN 0022-1767 (Print) 0022-1767.

[193] H. Rudolph, A. Klopstein, I. Gruber, C. Blatti, R. Lyck, and B. Engelhardt. Postarrest stalling rather than crawling favors cd8(+) over cd4(+) t-cell migration across the blood-brain barrier under flow in vitro. Eur J Immunol, 46(9):2187–203, 2016. ISSN 0014-2980. doi: 10.1002/eji.201546251.

[194] O. Steiner, C. Coisne, R. Cecchelli, R. Boscacci, U. Deutsch, B. Engelhardt, and R. Lyck. Differential roles for endothelial icam-1, icam-2, and vcam-1 in shear-resistant t cell arrest, polarization, and directed crawling on blood-brain barrier endothelium. J Immunol, 185(8):4846–55, 2010. ISSN 0022-1767. doi: 10.4049/jimmunol.0903732.

[195] S. K. Shaw, S. Ma, M. B. Kim, R. M. Rao, C. U. Hartman, R. M. Froio, L. Yang, T. Jones, Y. Liu, A. Nusrat, C. A. Parkos, and F. W. Luscinskas. Coordinated redistribution of leukocyte lfa-1 and endothelial cell icam-1 accompany neutrophil transmigration. J Exp Med, 200(12):1571–80, 2004. ISSN 0022-1007 (Print) 0022-1007. doi: 10.1084/jem.20040965.

[196] M. Abadier, N. Haghayegh Jahromi, L. Cardoso Alves, R. Boscacci, D. Vestweber, S. Barnum, U. Deutsch, B. Engelhardt, and R. Lyck. Cell surface levels of endothelial icam-1 influence the transcellular or paracellular t-cell diapedesis across the blood-brain barrier. Eur J Immunol, 45(4): 1043–58, 2015. ISSN 0014-2980. doi: 10.1002/eji.201445125.

[197] C. V. Carman, P. T. Sage, T. E. Sciuto, M. A. de la Fuente, R. S. Geha, H. D. Ochs, H. F. Dvorak, A. M. Dvorak, and T. A. Springer. Transcellular diapedesis is initiated by invasive podosomes. Immunity, 26(6):784–97, 2007. ISSN 1074-7613 (Print) 1074-7613. doi: 10.1016/j.immuni.2007.04.015.

[198] P. Garberg, M. Ball, N. Borg, R. Cecchelli, L. Fenart, R. D. Hurst, T. Lindmark, A. Mabondzo, J. E. Nilsson, T. J. Raub, D. Stanimirovic, T. Terasaki, J. O. Oberg, and T. Osterberg. In vitro models for the blood-brain barrier. Toxicol In Vitro, 19(3):299–334, 2005. ISSN 0887-2333 (Print) 0887-2333. doi: 10.1016/j.tiv.2004.06.011.

[199] N. J. Abbott, A. A. Patabendige, D. E. Dolman, S. R. Yusof, and D. J. Begley. Structure and function of the blood-brain barrier. Neurobiol Dis, 37(1):13–25, 2010. ISSN 0969-9961. doi: 10.1016/j.nbd.2009.07.030.

[200] Y. Reiss, G. Hoch, U. Deutsch, and B. Engelhardt. T cell interaction with icam-1-deficient endothelium in vitro: essential role for icam-1 and icam-2 in transendothelial migration of t cells. Eur J Immunol, 28(10):3086–99, 1998. ISSN 0014-2980 (Print) 0014-2980. doi: 10.1002/(sici)1521-4141(199810)28:10<3086::Aid-immu3086>3.0.Co;2-z.

[201] T. H. Schreiber, V. Shinder, D. W. Cain, R. Alon, and R. Sackstein. Shear flow-dependent integration of apical and subendothelial chemokines in t-cell transmigration: implications for locomotion and the multistep paradigm. Blood, 109(4):1381–6, 2007. ISSN 0006-4971 (Print) 0006-4971. doi: 10.1182/blood-2006-07-032995. URL `http://www.bloodjournal.org/content/bloodjournal/109/4/1381.full.pdf`.

[202] G. Enzmann, C. Mysiorek, R. Gorina, Y. J. Cheng, S. Ghavampour, M. J. Hannocks, V. Prinz, U. Dirnagl, M. Endres, M. Prinz, R. Beschorner, P. N. Harter, M. Mittelbronn, B. Engelhardt, and L. Sorokin. The neurovascular unit as a selective barrier to polymorphonuclear granulocyte (pmn) infiltration into the brain after ischemic injury. Acta Neuropathol, 125(3):395–412, 2013. ISSN 0001-6322. doi: 10.1007/s00401-012-1076-3.

[203] V. Goncharova and S. K. Khaldoyanidi. A novel three-dimensional flow chamber device to study chemokine-directed extravasation of cells circulating under physiological flow conditions. J Vis Exp, (77):e50959, 2013. ISSN 1940-087x. doi: 10.3791/50959.

[204] Y. Takeshita, B. Obermeier, A. Cotleur, Y. Sano, T. Kanda, and R. M. Ransohoff. An in vitro blood-brain barrier model combining shear stress and endothelial cell/astrocyte co-culture. J Neurosci Methods, 232:165–72, 2014. ISSN 0165-0270. doi: 10.1016/j.jneumeth.2014.05.013.

[205] H. Xu, Z. Li, Y. Yu, S. Sizdahkhani, W. S. Ho, F. Yin, L. Wang, G. Zhu, M. Zhang, L. Jiang, Z. Zhuang, and J. Qin. A dynamic in vivo-like organotypic blood-brain barrier model to probe metastatic brain tumors. Sci Rep, 6:36670, 2016. ISSN 2045-2322. doi: 10.1038/srep36670.

[206] L. Cucullo, P. O. Couraud, B. Weksler, I. A. Romero, M. Hossain, E. Rapp, and D. Janigro. Immortalized human brain endothelial cells and flow-based vascular modeling: a marriage of convenience for rational neurovascular studies. J Cereb Blood Flow Metab, 28(2):312–28, 2008. ISSN 0271-678X (Print) 0271-678x. doi: 10.1038/sj.jcbfm.9600525.

[207] A. Herland, A. D. van der Meer, E. A. FitzGerald, T. E. Park, J. J. Sleeboom, and D. E. Ingber. Distinct contributions of astrocytes and pericytes to neuroinflammation identified in a 3d human blood-brain barrier on a chip. PLoS One, 11(3):e0150360, 2016. ISSN 1932-6203. doi: 10.1371/journal.pone.0150360.

[208] W. Neuhaus, R. Lauer, S. Oelzant, U. P. Fringeli, G. F. Ecker, and C. R. Noe. A novel flow based hollow-fiber blood-brain barrier in vitro model with immortalised cell line pbmec/c1-2. J Biotechnol, 125(1):127–41, 2006. ISSN 0168-1656 (Print) 0168-1656. doi: 10.1016/j.jbiotec.2006.02.019.

[209] N. Erbeldinger, F. Rapp, S. Ktitareva, P. Wendel, A. S. Bothe, T. Dettmering, M. Durante, T. Friedrich, B. Bertulat, S. Meyer, M. C. Cardoso, S. Hehlgans, F. Rodel, and C. Fournier. Measuring leukocyte adhesion to (primary) endothelial cells after photon and charged particle exposure with a dedicated laminar flow chamber. Front Immunol, 8:627, 2017. ISSN 1664-3224 (Print) 1664-3224. doi: 10.3389/fimmu.2017.00627.

[210] R. Cecchelli, B. Dehouck, L. Descamps, L. Fenart, V. V. Buee-Scherrer, C. Duhem, S. Lundquist, M. Rentfel, G. Torpier, and M. P. Dehouck. In vitro model for evaluating drug transport across the blood-brain barrier. Adv Drug Deliv Rev, 36(2-3):165–178, 1999. ISSN 0169-409x.

[211] L. Bo, J. W. Peterson, S. Mork, P. A. Hoffman, W. M. Gallatin, R. M. Ransohoff, and B. D. Trapp. Distribution of immunoglobulin superfamily members icam-1, -2, -3, and the beta 2 integrin lfa-1 in multiple sclerosis lesions. J Neuropathol Exp Neurol, 55(10):1060–72, 1996. ISSN 0022-3069 (Print) 0022-3069.

[212] T. Collins, M. A. Read, A. S. Neish, M. Z. Whitley, D. Thanos, and T. Maniatis. Transcriptional regulation of endothelial cell adhesion molecules: Nf-kappa b and cytokine-inducible enhancers. Faseb j, 9(10):899–909, 1995. ISSN 0892-6638 (Print) 0892-6638.

[213] Aurore Drolez, Elodie Vandenhaute, Sylvain Julien, Fabien Gosselet, Joy Burchell, Roméo Cecchelli, Philippe Delannoy, Marie-Pierre Dehouck, and Caroline Mysiorek. Selection of a relevant in vitro blood-brain barrier model to investigate pro-metastatic features of human breast cancer cell lines. PloS one, 11(3):e0151155, 2016.

[214] W. Samuel, C. Jaworski, O. A. Postnikova, R. K. Kutty, T. Duncan, L. X. Tan, E. Poliakov, A. Lakkaraju, and T. M. Redmond. Appropriately differentiated arpe-19 cells regain phenotype and gene expression profiles similar to those of native rpe cells. Mol Vis, 23:60–89, 2017. ISSN 1090-0535 (Electronic) 1090-0535 (Linking). URL `https://www.ncbi.nlm.nih.gov/pubmed/28356702`.

[215] B. T. Hawkins and T. P. Davis. The blood-brain barrier/neurovascular unit in health and disease. Pharmacol Rev, 57(2):173–85, 2005. ISSN 0031-6997 (Print) 0031-6997. doi: 10.1124/pr.57.2.4.

[216] B. Engelhardt and S. Liebner. Novel insights into the development and maintenance of the blood-brain barrier. Cell Tissue Res, 355(3):687–99, 2014. ISSN 0302-766x. doi: 10.1007/s00441-014-1811-2.

[217] K. L. de Mesy Bentley, R. Trombetta, K. Nishitani, S. N. Bello-Irizarry, M. Ninomiya, L. Zhang, H. L. Chung, J. L. McGrath, J. L. Daiss, H. A. Awad, S. L. Kates, and E. M. Schwarz. Evidence of staphylococcus aureus deformation, proliferation, and migration in canaliculi of live cortical bone in murine models of osteomyelitis. J Bone Miner Res, 32(5):985–990, 2017. ISSN 0884-0431. doi: 10.1002/jbmr.3055.

[218] E. Kim, H. Xiong, C. C. Striemer, D. Z. Fang, P. M. Fauchet, J. L. McGrath, and S. Amemiya. A structure-permeability relationship of ultrathin nanoporous silicon membrane: a comparison with the nuclear envelope. J Am Chem Soc, 130(13):4230–1, 2008. ISSN 0002-7863. doi: 10.1021/ja711258w.

[219] Z. Shulman, V. Shinder, E. Klein, V. Grabovsky, O. Yeger, E. Geron, A. Montresor, M. Bolomini-Vittori, S. W. Feigelson, T. Kirchhausen, C. Laudanna, G. Shakhar, and R. Alon. Lymphocyte crawling and transendothelial migration require chemokine triggering of high-affinity lfa-1 integrin. Immunity, 30(3):384–96, 2009. ISSN 1074-7613. doi: 10.1016/j.immuni.2008.12.020.

[220] MJ Stebbins, HK Wilson, SG Canfield, T Qian, SP Palecek, and EV Shusta. Differentiation and characterization of human pluripotent stem cell-derived brain microvascular endothelial cells. Methods (San Diego, Calif.), 101:93 2016.

[221] D. C. Pedroso, A. Tellechea, L. Moura, I. Fidalgo-Carvalho, J. Duarte, E. Carvalho, and L. Ferreira. Improved survival, vascular differentiation and wound healing potential of stem cells co-cultured with endothelial cells. PLoS One, 6(1):e16114, 2011. ISSN 1932-6203. doi: 10.1371/journal.pone.0016114.

[222] C. Coisne, L. Dehouck, C. Faveeuw, Y. Delplace, F. Miller, C. Landry, C. Morissette, L. Fenart, R. Cecchelli, P. Tremblay, and B. Dehouck. Mouse syngenic in vitro blood-brain barrier model: a new tool to examine inflammatory events in cerebral endothelium. Lab Invest, 85(6):734–46, 2005. ISSN 0023-6837 (Print) 0023-6837. doi: 10.1038/labinvest.3700281.

[223] S. A. Engen, H. Valen Rukke, S. Becattini, D. Jarrossay, I. J. Blix, F. C. Petersen, F. Sallusto, and K. Schenck. The oral commensal streptococcus mitis shows a mixed memory th cell signature that is similar to and cross-reactive with streptococcus pneumoniae. PLoS One, 9(8):e104306, 2014. ISSN 1932-6203. doi: 10.1371/journal.pone.0104306. URL `https://www.ncbi.nlm.nih.gov/pmc/articles/PMC4131883/pdf/pone.0104306.pdf`.

[224] F. Sallusto, P. Schaerli, P. Loetscher, C. Schaniel, D. Lenig, C. R. Mackay, S. Qin, and A. Lanzavecchia. Rapid and coordinated switch in chemokine receptor expression during dendritic cell maturation. Eur J Immunol, 28(9):2760–9, 1998. ISSN 0014-2980 (Print) 0014-2980. doi: 10.1002/(sici)1521-4141(199809)28:09<2760::aid-immu2760>3.0.co;2-n.

[225] BB Weksler, EA Subileau, N Perriere, P Charneau, K Holloway, M Leveque, H Tricoire-Leignel, A Nicotra, S Bourdoulous, P Turowski, et al. Blood-brain barrier-specific properties of a human adult brain endothelial cell line. The FASEB journal, 19(13):1872–1874, 2005.

[226] Silvia Tietz and Britta Engelhardt. Brain barriers: crosstalk between complex tight junctions and adherens junctions. J Cell Biol, 209(4):493–506, 2015.

[227] Carola Förster, Malgorzata Burek, Ignacio A Romero, Babette Weksler, Pierre-Olivier Couraud, and Detlev Drenckhahn. Differential effects of hydrocortisone and tnfα on tight junction proteins in an in vitro model of the human blood–brain barrier. The Journal of physiology, 586(7):1937–1949, 2008.

[228] Babette Weksler, Ignacio A Romero, and Pierre-Olivier Couraud. The hcmec/d3 cell line as a model of the human blood brain barrier. Fluids and Barriers of the CNS, 10(1):16, 2013.

[229] N Joan Abbott, Lars Rönnbäck, and Elisabeth Hansson. Astrocyte–endothelial interactions at the blood–brain barrier. Nature Reviews Neuroscience, 7(1):41, 2006.

[230] Dong Ye, Michelle Nic Raghnaill, Mattia Bramini, Eugene Mahon, Christoffer Åberg, Anna Salvati, and Kenneth A Dawson. Nanoparticle accumulation and transcytosis in brain endothelial cell layers. Nanoscale, 5(22):11153–11165, 2013.

[231] Mattia Bramini, Dong Ye, Anna Hallerbach, Michelle Nic Raghnaill, Anna Salvati, Christoffer Åberg, and Kenneth A Dawson. Imaging approach to mechanistic study of nanoparticle interactions with the blood–brain barrier. ACS nano, 8(5):4304–4312, 2014.

[232] Michelle Nic Raghnaill, Mattia Bramini, Dong Ye, Pierre-Olivier Couraud, Ignacio A Romero, Babette Weksler, Christoffer Åberg, Anna Salvati, Iseult Lynch, and Kenneth A Dawson. Paracrine signalling of inflammatory cytokines from an in vitro blood brain barrier model upon exposure to polymeric nanoparticles. Analyst, 139(5):923–930, 2014.

[233] N Joan Abbott. Astrocyte–endothelial interactions and blood–brain barrier permeability. Journal of anatomy, 200(6):629–638, 2002.

[234] Cathrin J Czupalla, Stefan Liebner, and Kavi Devraj. In vitro models of the blood–brain barrier. In Cerebral Angiogenesis, pages 415–437. Springer, 2014.